

Oral Session I: Q-space Sampling, Local
Diffusion Models, and Microstructure Imaging

Real-time Rician noise correction applied to real-time HARDI and HYDI

Véronique Brion^{1,2}, Irina Kezele^{1,2}, Olivier Riff^{1,3}, Maxime Descoteaux⁴,
Jean-François Mangin^{1,2}, Cyril Poupon^{1,2} and Fabrice Poupon^{1,2}

¹ NeuroSpin, CEA, Gif-sur-Yvette, France

² IFR-49, Paris, France

³ Digiteo, Saint-Aubin, France

⁴ Sherbrooke University, Sherbrooke, Canada

Abstract. In this paper we addressed the problem of the correction of the Rician noise corrupting diffusion-weighted images at high b-values in real-time. We combined a Linear Minimum Mean Square Error Estimator (LMMSE) together with a Kalman framework in order to compute in real-time the noise-free diffusion data, as well as the diffusion maps stemming from any local high angular resolution diffusion (HARDI) or hybrid diffusion (HYDI) model. A feedback is retropropagated from the Kalman filter to the LMMSE in order to reinforce the influence of the local structure onto the noise correction in order to prevent smoothing effects. The technique was validated on synthetic and real data acquired at low signal to noise ratio (SNR) to assess its efficiency and the full pipeline was tested on the computation of fibre orientation distributions in real-time.

1 Introduction

Real-time diffusion-weighted (DW) Magnetic Resonance Imaging (rt-dMRI) was recently introduced to perform diffusion tensor (DTI) and Q-ball (QBI) imaging during the acquisition. First developed in 2008 by [1], this technique improves clinical protocols as it allows stopping and restarting acquisitions at any time without threatening the quality of the final data. Furthermore, inherited information stemming from DTI or QBI such as maps of the apparent diffusion coefficient (ADC), maps of the generalized fractional anisotropy (GFA), maps of the orientation distribution functions can be estimated at any step of the acquisition, thus saving time for clinicians since long post-processing tasks are no more required. Some original methods using optimized orientation sets for rt-dMRI have been proposed by [1] and [2]. More recently, further progress was achieved about on-line motion detection [3].

Along with motion, the noise present in data greatly decreases image quality, especially when using high b-values. The NMR signal is complex with two real and imaginary channels each corrupted by some Gaussian noise. Practically, only magnitude images are delivered by MRI systems, and contrary to individual channels, the magnitude signal does not follow a Gaussian distribution anymore, but it follows a Rician distribution [4] due to the non linear square root function used to get it. For high signal to noise ratios (SNR), Rician distributions can be approximated by Gaussian distributions, and least square estimators can be

used efficiently. At high b-values, the SNR drops and the signal depicts a systematic bias. Least square estimators cannot be used anymore because the mean operator does not converge to the noise-free magnitude. This makes Rician noise more difficult to correct than Gaussian noise. High Angular Resolution Diffusion Imaging (HARDI) or HYbrid Diffusion Imaging (HYDI) are usually performed at high b-values leading to large attenuation of the signal, generally yielding low SNR data on clinical systems. Several methods have been developed to correct the HARDI data from Rician noise, but, to our knowledge, Rician correction has never been performed in real-time for dMRI. In this paper, we propose to extend the method of [1] by combining Rician noise correction to rt-dMRI reconstruction of local diffusion models. A feedback mechanism is also developed to refine the noise correction taking benefits of the structural angular information estimated incrementally. We prove the efficacy of this novel technique applying it to the single-shell DTI and QBI models.

Current techniques for Rician noise correction operate off-line, using data acquired on the entire diffusion orientation set. A method using the Maximum Likelihood approach [5] has been proposed in 2007 to directly improve the Fiber Orientation Distribution Functions (FODs). This method was extended by [6] by using a decomposition of the diffusion signal in the modified Spherical Harmonics basis, so that it could be applied for the FODs and for the Orientation Distribution Functions (ODFs). Another correction technique developed for QBI incorporates the Rician noise model in a variational estimation of the ODFs [7]. These techniques are not compatible with real-time processing because they require the entire dataset to be acquired before starting computations. Another technique was proposed by [8] that is based on a Non-Local Means filter adapted to Rician noise for correcting HARDI data. It does not require measurements along all the diffusion orientations. Despite its ability to be implemented recursively for rt-dMRI, it suffers from a long computation time due to comparisons of spatial neighborhoods. A similar but faster to compute technique using a Linear Minimum Mean Square Error Estimator (LMMSE) approach to correct the magnitude from the Rician noise was introduced in [9] that is more compatible with real-time.

In this paper we present a novel approach to perform any noise-free HARDI or HYDI imaging in real-time that combines a LMMSE method with a rt-dMRI reconstruction algorithm. First, we describe the Rician noise correction based on a modified LMMSE approach. Then, we explain how to combine it with the incremental framework described in [1]. Finally, we validate the technique on simulated and real data, applying it to the Diffusion Tensor and analytical Q-ball models.

2 Methods

The proposed method is an extension of the rt-dMRI work of [1] based on a Kalman filter (KF), where a LMMSE technique is used in a primary step to remove Rician noise from the acquired data, and a feedback is added to adapt the weighting coefficients used in the neighboring loops of the LMMSE based on the refined output of the KF (Fig. 1).

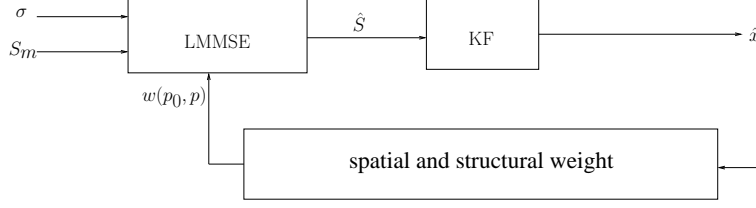


Fig. 1. Diagram of our rt-Rician noise correction method

2.1 Rician noise correction based on a modified LMMSE approach

In this subsection, we summarize the LMMSE estimator proposed in [9], and adapted for Rician noise correction. For any diffusion orientation, and any voxel, the measured magnitude S_m is assumed to follow a Rician distribution. Let S be the noise-free magnitude and σ the noise standard deviation. The LMMSE estimator \hat{S}^2 of S^2 is defined as (see [9] for the details):

$$\hat{S}^2 = \langle S_m^2 \rangle - 2\sigma^2 + (S_m^2 - \langle S_m^2 \rangle) \left(1 - \frac{4\sigma^2 (\langle S_m^2 \rangle - \sigma^2)}{\langle S_m^4 \rangle - \langle S_m^2 \rangle^2} \right). \quad (1)$$

To avoid smoothing effects, we replaced the isotropic averaging originally proposed by an anisotropic mean operator $\langle \cdot \rangle$ defined such that:

$$\langle I_{p_0} \rangle = \frac{\sum_{p \in \eta_{p_0}} w(p_0, p) I_p}{\sum_{p \in \eta_{p_0}} w(p_0, p)} \quad (2)$$

with η_{p_0} being the 3D neighborhood of the central voxel p_0 ; I_p is the intensity of the neighbor point p . For each neighbor point p , we define the weight:

$$w(p_0, p) = w_{spatial}(p_0, p) \cdot w_{structural}(p_0, p) \quad (3)$$

with

$$w_{spatial}(p_0, p) = \exp\left(-\frac{(p - p_0)^2}{2\alpha^2}\right), \quad (4)$$

and

$$w_{structural}(p_0, p) = \exp\left(-\frac{\sum_{j=1}^N (\hat{x}_p(j) - \hat{x}_{p_0}(j))^2}{2\beta^2}\right), \quad (5)$$

where \hat{x}_p is the current value of the Kalman filter state vector at voxel p (N being the length of the state vector), and α and β are two constants driving the magnitude of the spatial and structural weightings. The \hat{x}_p we use in our context corresponds to the vector of the decomposition of the normalized diffusion-weighted signal onto a modified Spherical Harmonics (SH) basis (see [10] for a detailed description of the modified SH basis) at point p , and will be detailed in next section. The global $w_{spatial}(p_0, p)$ weight therefore contains two terms:

- $w_{spatial}(p_0, p)$ modulate the influence of the neighboring points according to their distance from the central point, thus preserving resolution of thin structures,

- $w_{structural}(p_0, p)$ is based on a metric of ODF similarities introduced in [11] and favours neighboring points having similar ODFs.

This dual weighting removes the smoothing effects usually observed with an isotropic local mean.

Practically, employing equation (1) only requires the knowledge of a good estimate of the noise standard deviation σ . This can be achieved spatially using a region of interest located in the background of the image. In such a region, $S = 0$ and the Rician noise distribution is simplified to a Rayleigh distribution. In this case, the estimate $\hat{\sigma}$ of σ is given by:

$$\hat{\sigma} = \sqrt{\frac{2}{\pi}} \langle S_{m_{background}} \rangle \quad (6)$$

This Rician noise correction method is therefore easy to compute: the noise standard deviation is computed from the background signal, followed by the computation of the local means of the corrupted signal magnitudes based on neighborhoods, and finally we obtain the estimates of the corrected magnitudes using (1).

2.2 Rician noise correction in real-time

The idea is to improve and extend the real-time framework proposed in [1], to take Rician noise correction into account. The innovative point of the method is that at each iteration we use the result of the Kalman filter to adapt the weighting coefficients used in the LMMSE step. Our technique operates in five steps that consist of:

1. estimating the noise standard deviation $\hat{\sigma}$ from the background of the T2-weighted image, where the noise-free magnitude is equal to zero, using (6); in the following we will assume that $\hat{\sigma}$ remains the same on the entire dataset, thus assuming the independence of the noise with the diffusion directions,
2. denoising the T2-weighted magnitude data thanks to the technique described above, using $\hat{\sigma}$; to accelerate the computation, we only process points belonging to a brain mask defined robustly from the T2-weighted image; this yields the Rician noise free T2-weighted magnitude \hat{S}_0 ,
3. applying the Rician noise correction to any new diffusion-sensitized acquisition provided by the scanner, using the previous $\hat{\sigma}$ estimate; this yields the denoised DW magnitude image \hat{S} for the current diffusion direction,
4. updating the local signal decomposition of the normalized diffusion-weighted signal \hat{S}/\hat{S}_0 processed from the new Rician noise free DW magnitude and the previously corrected T2-weighted reference data; this step involves the use of a Kalman framework similar to the one described in [1] built upon a General Linear Model (GLM) of the form:

$$\mathbf{y} = \mathbf{A}\mathbf{x} + \boldsymbol{\epsilon}, \quad (7)$$

where we usually call $\mathbf{y} = [y(1), \dots, y(i), \dots, y(M)]^T$ the observations' vector and $\mathbf{x} = [x(1), \dots, x(N)]^T$ the state vector. $\boldsymbol{\epsilon} = [\epsilon(1), \dots, \epsilon(i), \dots, \epsilon(M)]^T$ represents a zero-mean Gaussian noise in the common Kalman framework.

Given a vector $\mathbf{a}(i) = [A_{i1}, \dots, A_{iN}]^T$ corresponding to the i^{th} row of \mathbf{A} , the Kalman recursion is as follows:

$$\begin{cases} \nu(i) = y(i) - \mathbf{a}(i)^T \hat{\mathbf{x}}(i-1), \\ \mathbf{k}(i) = (1 + \mathbf{a}(i)^T \mathbf{P}(i-1) \mathbf{a}(i))^{-1} \mathbf{P}(i-1) \mathbf{a}(i), \\ \hat{\mathbf{x}}(i) = \hat{\mathbf{x}}(i-1) + \nu(i) \mathbf{k}(i), \\ \mathbf{P}(i) = \mathbf{P}(i-1) - \mathbf{k}(i) \mathbf{a}(i)^T \mathbf{P}(i-1), \end{cases} \quad (8)$$

where $\nu(i)$ is the innovation, $\mathbf{k}(i)$ the Kalman gain, $\mathbf{P}(i)$ the normalized covariance matrix of \mathbf{x} , and $\hat{\mathbf{x}}(i)$ the updated estimate of the state vector \mathbf{x} . In the case of the decomposition of the normalized diffusion-weighted signal onto the SH basis, the GLM formulation is straightforward: $\mathbf{y} = \hat{\mathbf{S}}_m^{\text{NORM}} = [\hat{S}_{m_1}/\hat{S}_0, \dots, \hat{S}_{m_M}/\hat{S}_0]^T$ is the vector of normalized measurements, $\mathbf{x} = \mathbf{C}^{\text{DWI}}$ is the SH decomposition vector, and $\mathbf{A} = \mathbf{B}$ is the $M \times N$ matrix of the modified SH basis with $N = (O+1)(O+2)/2$ being the number of spherical harmonics, O being the SH order such that

$$\mathbf{B} = \begin{pmatrix} Y_1(\theta_1, \phi_1) & Y_2(\theta_1, \phi_1) & \dots & Y_N(\theta_1, \phi_1) \\ \vdots & \vdots & \ddots & \vdots \\ Y_1(\theta_M, \phi_M) & Y_2(\theta_M, \phi_M) & \dots & Y_N(\theta_M, \phi_M) \end{pmatrix}. \quad (9)$$

5. computing the new $w(p_0, p)$ coefficients to be used in step 3, following eq. (3).

Directly using measured data as in [1] is based on the assumption that the Rician noise present in the data can be approximated by a Gaussian distribution which is a rough approximation, especially for low signal values. In our method, we first denoise in real-time the current measurement data, and we then provide the result to the recursive Kalman process. The assumption we make here is that the noise residual follows a zero-mean Gaussian distribution after Rician noise correction, which is a good approximation that better fits the formulation of equation (7).

At this point, it is also important to highlight that the noise correction makes only one assumption about the Q-space: it corresponds to spherical shells. Consequently, it can be applied to many local diffusion models such as DTI, HARDI or HYDI.

2.3 Embedding with local diffusion modelling

The Kalman framework developed in the previous section works directly on the normalized diffusion-weighted signal. Its state vector corresponding to its SH decomposition is used as a feedback information to increase the influence of neighbors sharing similar attenuation profiles while decreasing the influence of neighbors depicting few similarities. The current framework is not restricted to the correction of the diffusion-weighted signal and can be used to incrementally map local diffusion models too. As an example, we embedded the real-time noise correction with the real-time computation of the ODF using the analytical Q-ball model published in [12], [13], [11]. We also implemented a similar framework to compute in real-time the inherited fibre orientation distributions (FOD) as proposed in [11] relying on the Sharpening Deconvolution

Transform (SDT). Thanks to the Funk-Hecke transform linking the SH decomposition of the normalized signal to the SH decomposition of the ODF, obtaining ODF maps is straightforward and corresponds to a GLM equation where $\mathbf{y} = \hat{\mathbf{S}}_{\mathbf{m}}^{\text{NORM}} = [\hat{S}_{m_1}/\hat{S}_0, \dots, \hat{S}_{m_M}/\hat{S}_0]^T$ is the vector of normalized measurements, $\mathbf{x} = \mathbf{C}^{\text{ODF}}$ is the SH decomposition vector of the ODF, and $\mathbf{A} = \mathbf{B} \times \mathbf{F}^{-1}$ is the $M \times N$ reconstruction matrix of the modified SH basis with $N = (O+1)(O+2)/2$ being the number of spherical harmonics, O being the SH order, \mathbf{F} being the Funk-Hecke matrix.

At any step of the recursion, the ODF $\Psi_{diffusion}$ can be reconstructed using the equation (10), whereas the FOD Ψ_{fibre} can be reconstructed using the equation (11) assuming that \mathbf{R} is the representation of the convolution kernel corresponding to the response of an homogeneous fibre bundle to the diffusion process (also estimated in real-time):

$$\Psi_{diffusion}(\mathbf{o}) = \sum_{k=1}^N C_k^{\text{ODF}} Y_k(\Theta(\mathbf{o}), \Phi(\mathbf{o})) \quad (10)$$

$$\Psi_{fibre}(\mathbf{o}) = \sum_{k=1}^N \frac{C_k^{\text{ODF}}}{R_k} Y_k(\Theta(\mathbf{o}), \Phi(\mathbf{o})) \quad (11)$$

2.4 Kalman filter initialization

In all cases, the initial guess $\hat{\mathbf{x}}(0)$ was set to the null vector. The initial covariance matrix was set to $\mathbf{P}(0) = (c\mathbf{I} + \lambda\mathbf{L})^{-1}$ with $c = 10^{-6}$, as suggested by [2] to optimize the convergence of the Kalman filter. \mathbf{I} represents the identity matrix, λ is a regularization factor, and \mathbf{L} is the Laplace-Beltrami operator. This operator regularizes the solution and prevents remaining noise peaks to contribute to the final solution. The initial weighting coefficients in equation (2) are set to $w(p_0, p) = w_{spatial}(p_0, p)$.

3 Results and discussion

3.1 Validation on synthetic data

Synthetic data. To validate our real-time correction method, we created 3D volumes of noise-free T2-weighted and DW data used as ground truth depicting a fibre crossing. The data was artificially corrupted at different Rician noise levels in order to perform validations. The noise-free diffusion data was modelled using a Gaussian mixture model to create two fibre bundles crossing at 60° :

$$S(b, \mathbf{o}) = S_0 \sum_{k=1}^n f_k e^{-b\mathbf{o}^T \mathbf{D}_k \mathbf{o}}, \quad (12)$$

with b representing the b-value, \mathbf{o} corresponding to the orientation, S_0 being the noise-free T2-weighted signal, f_k being the volume fraction ($\sum_{k=1}^n f_k = 1$), and \mathbf{D}_k being the diffusion tensor associated to the k^{th} bundle, assuming that

there is no water molecules' exchange between the n compartments. This hypothesis remains acceptable, as exchange time between compartments is much longer than the diffusion time used in dMRI experiments. In order to simulate two bundles crossing at 60° , we set the same $\{1.7 \times 10^{-9}; 0.3 \times 10^{-9}; 0.3 \times 10^{-9}\}$ eigenvalues (in $m^2.s^{-1}$) [14] to the two bundles and computed the eigenvectors to get the desired angle. The b-value was set to $b = 3000s.mm^{-2}$ in a first simulation, and then to $b = 6000s.mm^{-2}$. The maximum SH order was set to 8. The Rician noise was added using the non linear transform $S_{noisy} = \sqrt{(S_{noise-free} + n_{real})^2 + n_{imaginary}^2}$ where n_{real} and $n_{imaginary}$ are generated using a Gaussian noise distribution of standard deviation $\sigma = 100$ for a T2-weighted signal $S_0 = 1000$. We used 2 definitions of the SNR:

$$SNR_1 = \frac{\langle S_{noisy}(b, \mathbf{o}) \rangle}{\sigma} \text{ and } SNR_2 = \frac{\langle S_{noise-free}(b, \mathbf{o}) \rangle}{\sigma} \quad (13)$$

Tuning of parameters. Our Rician noise correction method is controlled by three tuning parameters: α , β , and η_{p_0} , defined respectively in equations (2), (4), and (5). α and β drive the influence of weights associated to distance and structural similarity of the considered neighbor. η_{p_0} defines the size of the neighborhood. The initial step consists in finding the optimal values of these parameters. This was achieved by measuring the quadratic error between the ODFs of the noise-free and the corrected data for several values of the parameters:

$$\epsilon = \sum_{j=1}^N (x_{p_0}^{NOISE-FREE}(j) - \hat{x}_{p_0}(j))^2. \quad (14)$$

We optimized the α and β parameters, assuming their independence. And, we tested 4 different neighborhood sizes: $3 \times 3 \times 3$, $5 \times 5 \times 5$, $7 \times 7 \times 7$, and $9 \times 9 \times 9$.

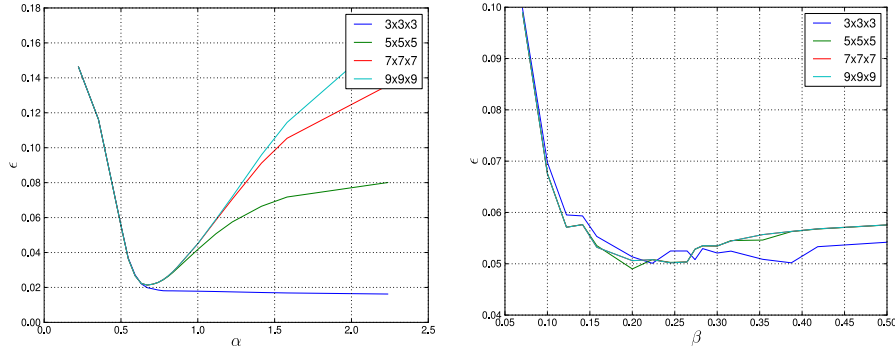


Fig. 2. Left:quadratic error $\epsilon(\alpha)$, using $w(p_0, p) = w_{spatial}$ only. Right:quadratic error $\epsilon(\beta)$, using $w(p_0, p) = w_{spatial}.w_{structural}$ and the optimal value of α .

In Fig. 2 the curves show that an optimal value of α and β can be obtained for a neighborhood size $\eta_{p_0} > 3 \times 3 \times 3$. The curve $\epsilon(\beta)$ on the left also shows

that there is no significant differences on the error relatively to the neighborhood size if we take $\eta_{p_0} > 3 \times 3 \times 3$. Hence, we took the optimal values $\alpha = 0.7$, $\beta = 0.22$, and $\eta_{p_0} = 5 \times 5 \times 5$.

Results. In order to validate the obtained optimal values, we evaluated the influence of the spatial and structural weights on 4 neighborhood sizes, and we compared our results with the Gaussian hypothesis method of [1] using the 60° crossing configuration described above. These tests were performed in severe signal to noise conditions to highlight the benefit of the Rician noise correction.

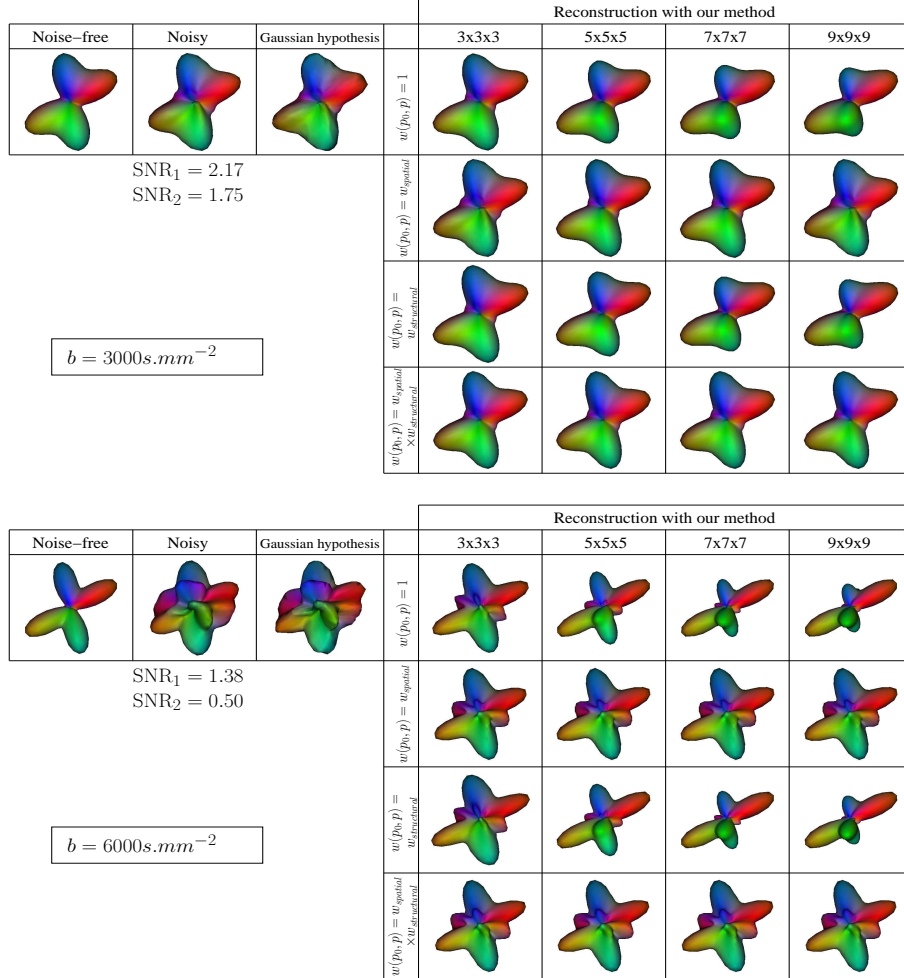


Fig. 3. Results obtained for a 60° crossing with two identical eigenvalues $\{1.7 \times 10^{-9}; 0.3 \times 10^{-9}; 0.3 \times 10^{-9}\}$ in $m^2.s^{-1}$ and two different b-values. From left to right: noise-free ODF, noisy ODF, reconstructed ODF under a Gaussian noise hypothesis, and table of reconstructed ODFs using our method for the four neighborhood sizes and four possible combinations of $w(p_0, p)$.

Figure 3 depicts the ODFs for the noise-free data, the corrupted data, and the corrected data using either the Gaussian noise hypothesis or the Rician noise hypothesis. The tables on the right show that the bias introduced by the Rician noise is efficiently removed in comparison to the standard real-time estimator limited to a Gaussian assumption, which is a significant improvement. Additionally, the bias decreases as the neighborhood size increases, but extra lobes are sometimes created depending on the weighting conditions (rows 1 and 3). They are coming from the influence of far neighboring ODFs that do not necessarily contain the same diffusion orientations as the ODF which is being corrected, and they are only observable in the absence of spatial weightings. The combination of spatial and structural weights induce a better bias reduction than the spatial weight taken alone. The figure shows that the combination of the spatial and structural weights in a $5 \times 5 \times 5$ neighborhood is a good compromise thus confirming this choice as an optimal parameter.

3.2 Application to human brain data

Multiple-shell DW data were collected on a Tim Trio 3T MRI system (Siemens, Erlangen), using a gradient sampling scheme of 64 orientations uniformly distributed over each shell at $b = 1000/3000/4000/6000s.mm^{-2}$. A further reference volume was acquired at $b = 0s.mm^{-2}$. The acquisition parameters were as follows: $T_E/T_R = 117ms/11.5s$, field of view $FOV = 192mm$, matrix 96×96 , slice thickness $TH = 2mm$, GRAPPA factor of 2, read bandwidth $RBW = 1410Hz/pixel$. Applying the definition of SNR_1 in equation (13), the SNR was evaluated for each b-value and was found close to 16/6/2/1.8, respectively.

The General Fractional Anisotropy (GFA) and the color-encoded (RGB) maps are shown in Fig. 4. The impact of the Rician noise correction increases with the b-value since the image’s SNR drops down for high b-values. The Rician noise corrected GFA images show an enhanced contrast, and the fiber details are preserved even if we make use of a LMMSE approach that is known to introduce smoothing effects. This proves the advantage of using a feedback loop to adapt and refine the structural weights during the local mean estimation.

Fig. 5 shows the effect of the Rician noise correction on FOD maps. The corrected FOD map presents an improved spatial and angular coherence leading to a better inference of the anatomical underlying connectivity (see the region corresponding to the yellow circle).

3.3 Efficient real-time implementation

A standard implementation of this method on a workstation takes approximately 37s per volume with dimensions equal to $96 \times 96 \times 60$ and using a spherical harmonics basis of order 6. It is not compatible with real-time because this computation time is greater than the repetition time ($T_R = 19s$).

To reach the real-time objective we parallelized the computation on a grid of 72 processors using the Message Passing Interface (MPI) library [15]. The input noisy volumes are split into slabs distributed on the nodes of the cluster, and then gathered and displayed on a workstation, leading to a huge reduction of the processing time to 0.9s per volume, now far below the repetition time. The grid implementation uses slabs with extra slices to ensure the continuity of the spatial neighboring information.

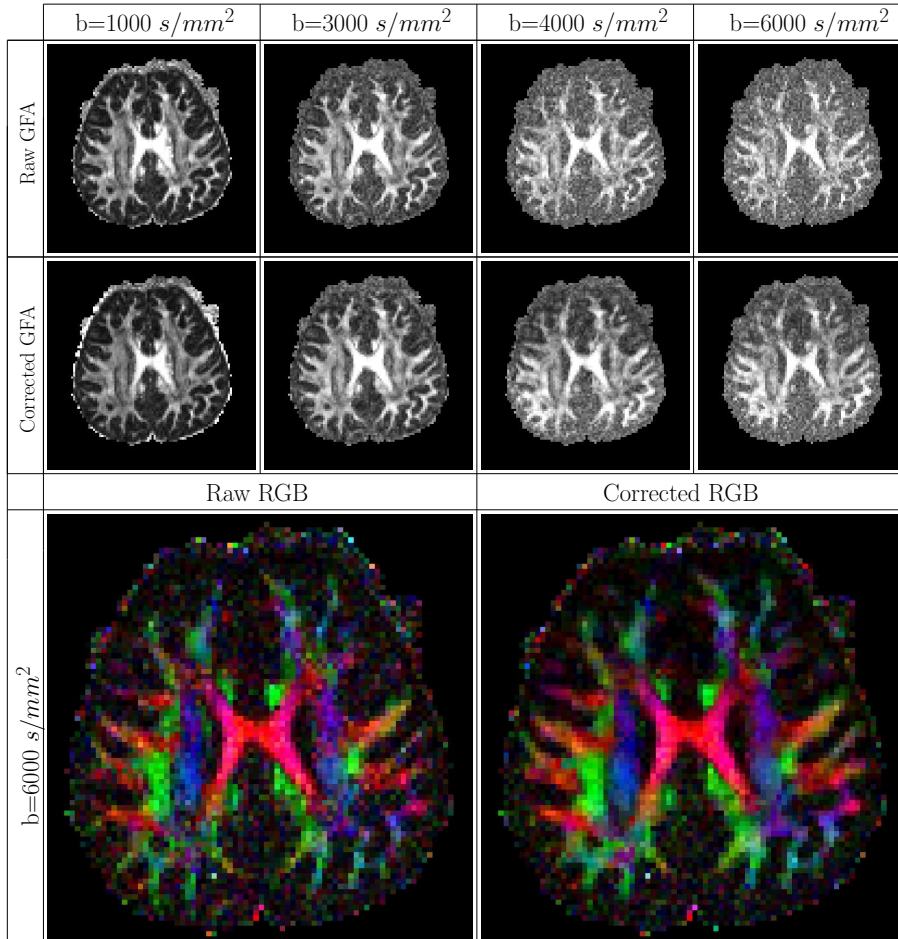


Fig. 4. Top rows: raw (up) and corrected (down) GFA maps for four different b-values. Bottom: raw and corrected RGB maps for $b = 6000 \text{ s.mm}^{-2}$.

4 Conclusion

We have proposed a novel algorithm to remove the Rician noise corrupting the diffusion-weighted data in real-time. This novel technique can be easily embedded with the real-time dMRI framework recently introduced in [1] and [2]. The method was employed to create a dedicated application that correct the Rician noise and process the fibre orientation distributions of the brain, as well as the standard diffusion maps used for clinical diagnosis. The tool was successfully validated on synthetic and ultra-low SNR DW data obtained during an in vivo experiment that was performed on a healthy volunteer. This tool definitely allows performing multiple-shell HYDI imaging at very high b-values that opens a plethora of new applications focused on the inference of the ensemble average propagator much more informative in terms of microstructure than the limited angular information stemming from orientation distribution functions or fibre

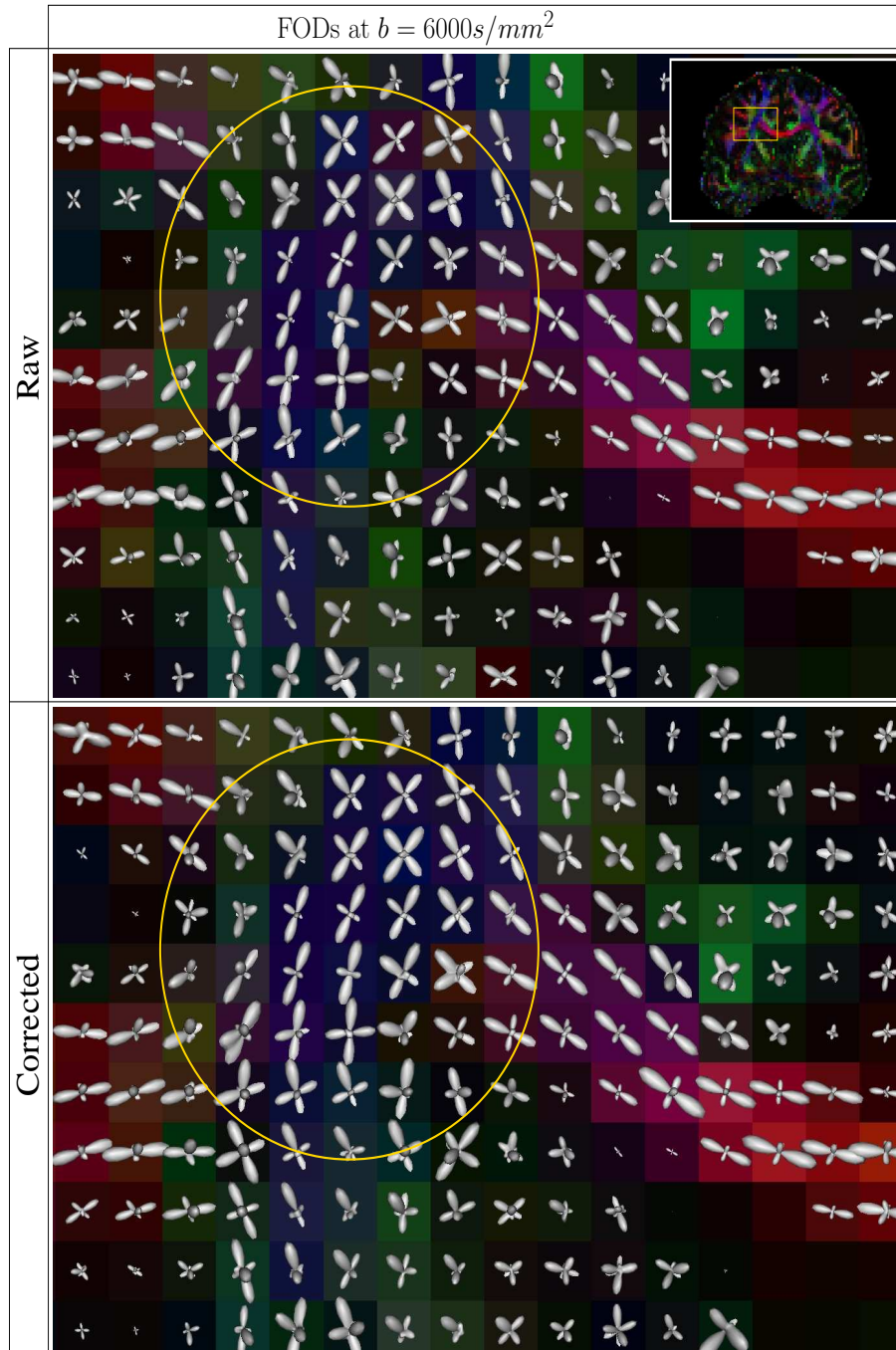


Fig. 5. Top: original FODs map; bottom: corrected FODs map. Both are superimposed to their underlying RGB map.

orientation distributions. Moreover, due to the efficacy of the parallel implementation of the tool, we are actually developing further improvements such as real-time motion and susceptibility artifact corrections that will be made available soon.

References

1. Poupon, C., Roche, A., Dubois, J., Mangin, J.F., Poupon, F.: Real-time MR diffusion tensor and Q-ball imaging using Kalman filtering. *Medical Image Analysis* **12** (2008) 527–534
2. Deriche, R., Calder, J., Descoteaux, M.: Optimal Real-Time Q-Ball Imaging using Regularized Kalman Filtering with Incremental Orientation Sets. *Medical Image Analysis* **13** (2009) 564–579
3. Caruyer, E., Aganj, I., Muetzel, R.L., Lenglet, C., Sapiro, G., Deriche, R.: Online Orientation Distribution Function Reconstruction in Constant Solid Angle and its Application to Motion Detection in HARDI. In: *Symposium on Biomedical Imaging: From Nano to Macro*. (April 2010)
4. Sijbers, J., Dekker, A.J.D., Scheunders, P., Dyck, D.V.: Maximum Likelihood estimation of Rician distribution parameters. *IEEE Transactions on Medical Imaging* **17** (1998) 357–361
5. Clarke, R.A., Scifo, P., Rizzo, G., Acqua, F.D., Scotti, G., Fazio, F.: Noise Correction on Rician Distributed Data for Fibre Orientation Estimators. *IEEE Transactions on Medical Imaging* **27** (2008) 1242–1251
6. Brion, V., Kezele, I., Descoteaux, M., Mangin, J.F., Poupon, C.: Rician denoising dedicated to single-shell diffusion-weighted MR data using spherical harmonics: impact on fibre orientation distribution maps. In: *ESMRMB*. (2009)
7. Assemblal, H.E., Tschumperlé, D., Brun, L.: Estimation variationnelle robuste de modèles complexes de diffusion en IRM à haute résolution angulaire et tractographie. In: *Colloque GRETSI*. (2007) 5–8
8. Descoteaux, M., Wiest-Daesslé, N., Prima, S., Barillot, C., Deriche, R.: Impact of Rician Adapted Non-Local Means Filtering on HARDI. In: *MICCAI*. (2008) 122–130
9. Aja-Fernández, S., Niethammer, M., Kubicki, M., Shenton, M.E., Westin, C.F.: Restoration of DWI Data Using a Rician LMMSE Estimator. *IEEE Transactions on Medical Imaging* **27** (2008) 1389–1403
10. Descoteaux, M., Angelino, E., Fitzgibbons, S., Deriche, R.: Regularized, Fast, and Robust Analytical Q-Ball Imaging. *Magnetic Resonance in Medicine* **58** (2007) 497–510
11. Descoteaux, M.: High Angular Resolution Diffusion MRI: from Local Estimation to Segmentation and Tractography. PhD thesis, Université de Nice-Sophia Antipolis (2008)
12. Frank, L.R.: Characterization of Anisotropy in High Angular Resolution Diffusion-Weighted MRI. *Magnetic Resonance in Medicine* **47** (2002) 1083–1099
13. Hess, C.P., Mukherjee, P., Han, E.T., Xu, D., Vigneron, D.B.: Q-Ball Reconstruction of Multimodal Fiber Orientations Using The Spherical Harmonic Basis. *Magnetic Resonance in Medicine* **56** (2006) 104–117
14. Tuch, D.: Diffusion MRI of complex tissue structure. PhD thesis, Harvard University–MIT Division of Health Sciences and Technology. (2002)
15. Gabriel, E., Fagg, G.E., Bosilca, G., Angskun, T., Dongarra, J.J., Squyres, J.M., Sahay, V., Kambadur, P., Barrett, B., Lumsdaine, A., Castain, R.H., Daniel, D.J., Graham, R.L., Woodall, T.S.: Open MPI: Goals, concept, and design of a next generation MPI implementation. In: *Proceedings, 11th European PVM/MPI Users Group Meeting*. (2004) 97–104

Compressed Sensing for Accelerated EAP Recovery in Diffusion MRI

Sylvain Merlet and Rachid Deriche

Athena Project-Team, INRIA Sophia Antipolis - Méditerranée, France

Abstract. Compressed Sensing (CS) or Compressive Sampling is a recent technique to accurately reconstruct sparse signals from under sampled measurements acquired below the Shannon-Nyquist rate. In this article, we present a CS based method for accelerating the reconstruction of the Ensemble Average Propagator (EAP), also known as the Propagator in Diffusion MRI (dMRI), by significantly reducing the number of measurements. Contrarily to the time consuming acquisition technique known as the Diffusion Spectrum Imaging (DSI), our method is developed and implemented to efficiently reconstruct the EAP from reduced and non uniformly under sampled Diffusion Weighted (DW) MRI images combined to an efficient and accurate l_1 norm based reconstruction algorithm. We illustrate in detail the artifacts occurring in a classical EAP reconstruction à la DSI, and qualitatively and quantitatively demonstrate good and better results in recovering the EAP and some of its important features such as the Orientation Distribution Function (ODF) from non-regularly undersampled and l_1 norm based reconstructed data. This opens an original and very interesting road to shorten the dMRI acquisition time and opens new opportunities to render High Angular Resolution Diffusion Imaging (HARDI) feasible in a clinical setting.

Key words: Diffusion MRI; Compressed sensing; Ensemble Average Propagator recovery; Propagator; Orientation Distribution Function

1 Introduction

Diffusion MRI (dMRI) is a recent Magnetic Resonance Imaging technique introduced by [13, 15, 19]. Since the first acquisitions of diffusion-weighted images (DWI) in vivo by [16, 17] and the development of the rigorous formalism of the diffusion tensor (DT) model by [3, 2], dMRI has become an established research tool for the investigation of tissue structure and orientation.

Using dMRI to infer the 3D Ensemble Average Propagator (EAP) also known as the diffusion probability displacement function or propagator (PDF) requires the acquisition of many diffusion images sensitized to different orientations in the sampling space. The number of diffusion weighted images (DWI) required depends on how the diffusion is modeled. The well known DT model assumes the PDF is Gaussian and requires at least 6 DWIs plus an additional unweighted image. However, the Gaussian assumption is an over-simplification of the diffusion of water molecules in the brain and thus has some limitations for voxels in which there is more complicated internal structure.

Therefore, it is of utmost importance to develop techniques that go beyond the limitations of diffusion tensor imaging (DTI). To do so, high angular resolution diffusion imaging (HARDI) has been proposed to measure the diffusion of water molecules along several directions. HARDI depends on the number of measurements N and the gradient strength (b -value), which will directly affect acquisition time and signal to noise ratio in the signal. One way to proceed for the acquisition in HARDI is to sample the whole q-space 3D Cartesian grid. In Diffusion Spectrum Imaging (DSI), a large number of q-space points are taken over the discrete grid and the inverse Fourier transform of the measured DWI signal is taken to obtain an estimate of the diffusion PDF P . The method requires very strong imaging gradients ($500 \leq b \leq 20000$ s/mm²) and a long time for acquisition (up to 60 minutes) depending on the number of sampling directions, which can be problematic for clinical studies involving children and people afflicted with certain diseases. A large number of acquisitions can force the patient to abort or render the diffusion weighted images useless. According to the literature [11], if established practice is followed, 515 diffusion-weighted images are acquired successively to obtain data of good quality. Each image corresponds to a different q vector, the effective diffusion gradient.

The visualization of 3D diffusion PDF at every voxel is computationally intensive. Hence, people either take an isosurface of the diffusion PDF for a certain radius \mathbf{r} or the diffusion Orientation Distribution Function (ODF) is computed. The diffusion ODF contains the full angular information of the diffusion PDF and is defined as [1, 20]

$$\Psi(\theta, \phi) = \int_0^\infty P(r, \theta, \phi)r^2 dr, \quad (1)$$

where (θ, ϕ) obey physics convention ($\theta \in [0, \pi], \phi \in [0, 2\pi]$).

This is a spherical function which is very useful to drive tractography since it overcomes the limitations of DTI in fiber crossing regions, especially for higher b -value acquisitions with $b \geq 1000$ s/mm² [11, 6]. One of the HARDI techniques known as the Q-ball imaging (QBI) [21, 5] consist in sampling the q-space on a single sphere in several directions instead of attempting to get the entire q-space. QBI aims to estimate the ODF directly from the measured signal by means of the Funk-Radon transform (FRT) [21, 1].

However, the ODF only captures angular information of the diffusion process. As explained above, the Diffusion Spectrum Imaging (DSI) technique approximates the ensemble average propagator P by taking samples on the whole q-space. It aims to estimate directly the PDF in a numerical way without any prior knowledge about the tissue shape. This results in estimating the diffusion PDF P in a more accurate fashion than any other methods. Both radial information from DTI and angular information from QBI are caught, that makes DSI a richer technique than QBI [21] or DTI. This method, first attempted by [23], considers that the measured signal, after normalization, is written as the 3-dimensional Fourier transform of the diffusion propagator P [18],

$$E(q) = F[P(r|r_0, \tau)] \quad (2)$$

where q and r are both 3D-vectors that represent respectively the effective gradient direction and the diffusion direction. $E(q) = S(q)/S_0$ is the normalized attenuated diffusion signal expressed as the ratio of the attenuated diffusion signal and the signal measured without any diffusion encoding gradient ($q = 0$). P is the probability that a molecule moves from a position r_0 to r after a delay τ . Using equation 2, it is straightforward to get P by taking the inverse 3D Fourier transform of the signal E measured in the q -space. Many measurements are necessary to obtain high-resolution PDF. In brief, while this technique has the advantage of a very good approximation of the diffusion propagator, it is limited by the long time for acquisition due to the large number of samples required.

Compressed Sensing (CS), a recent technique to accurately reconstruct sparse signals from under sampled measurements acquired below the Shannon-Nyquist rate, HARDI, DSI, the Ensemble Average Propagator and the diffusion ODF play a central role in this work which is focused on the development of CS based method for accelerating the reconstruction of the EAP by significantly reducing the number of acquisitions and measurements.

The method we propose combines the idea of randomly undersampling DW-MRI to the idea of using an efficient and accurate L_1 norm based EAP reconstruction algorithm. Significantly undersampling the q -space in a random fashion and then reconstructing the EAP by solving a convex optimization problem which exploits the sparsity in P is shown to lead to less measurements than needed in DSI and to qualitatively and quantitatively better results in recovering the EAP and some of its important features such as the ODF.

This allows to shorten the dMRI acquisition time, in particular when dealing with High Angular Resolution Diffusion MRI and opens new opportunities to render HARDI feasible in a clinical setting. The next section introduces the CS technique before presenting our L_1 norm based EAP reconstruction algorithm and the experimental results obtained.

2 Signal & Image Reconstruction via Compressed Sensing

The Compressed Sensing (CS) technique has been proving useful in recovering Magnetic resonance images by significantly undersampling their k -spaces [14] [10] [9] [4]. David Donoho described a complete mathematical framework [7] of CS theory. By analogy with the 2D-images case, we know that diffusion propagator P and the attenuated diffusion signal E are related by a 3D Fourier transform (see eq. 2). We use this relation combined with a regularized CS reconstruction to recover P from a small number of measured coefficients.

A fundamental result in signal theory is the Nyquist-Shannon sampling theorem. It indicates the minimum sampling frequency required to avoid aliasing, equal to twice the highest frequency contained within the signal. Undersampling a signal in the Fourier space regardless of this theorem does not enable

to reconstruct the signal that would have been given from all the Fourier coefficients. It produces regular shifted replicas typically resulting in an image of little diagnostic value that does not permit any reconstruction. However, the proposition is valid regarding a regular undersampling scheme. A random undersampling scheme results in incoherent artefacts spread all over the image as a random noise and an appropriate reconstruction method can allow the signal recovering. An example of this phenomenon on a 1-Dimensional signal is shown figure 1(a). We have generated eight signals. The original signal in the top-left is a discrete signal of length 500 and originally sampled at the frequency $f_s = 44100Hz$. We can visualize its Fourier transform on the top-right and see that the maximum frequency component is $f_m = 5000Hz$. Hence, according to the Nyquist-Shannon theorem, the sampling frequency has to respect $f_e > 2f_m$. By returning to the discrete domain, we obtain the Nyquist rate expressed as $N_e = \frac{f_e}{f_s} = \frac{2f_m}{f_s} = \frac{2*5000}{44100} = \frac{1}{4.41}$. It indicates the minimum sampling required rate to avoid aliasing. In figure 1 (a), the second and third lines show the signal regularly undersampled but with two different rates and the corresponding Fourier transforms. One respects the Nyquist condition and is undersampled at $N_{u1} = \frac{1}{2} > N_e$ (the second line) and the other violates this condition with a rate $N_{u2} = \frac{1}{6} < N_e$ (the third line). The non-respect of the Nyquist theorem in the second case causes aliasing in Fourier space. This non-reversible phenomenon appears when high frequency components shift and overlay the original frequency components. However, the fourth line of figure 1(a) show a signal undersampled at rate N_{u2} , that is to say without respecting the Nyquist condition, excepted it follows a random undersampling scheme. In this case, we do not see the previous shifted frequency components any more but random-like noise spread all over the signal Fourier transform.

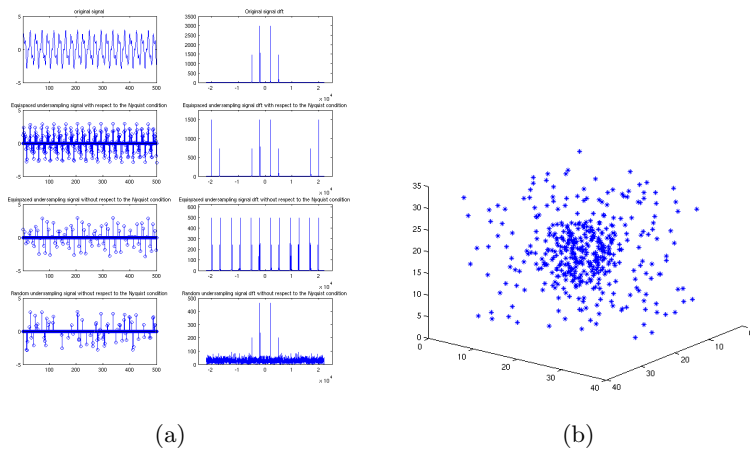


Fig. 1. (a) Illustration of the Nyquist theorem on a 1D signal and (b) Sampling scheme with 3D binomial distribution.

The possibility to acquire q-space samples in a random fashion is an important aspect in DSI that facilitates the application of the CS technique. We will exploit this property to recover the 3 dimensional propagator P .

Our reconstruction is based on the assumption that P has a sparse representation, that is composed by a small number of non-zero coefficients. If we know that most of the signal coefficients are zeros, why do not we exploit this information for reconstructing the signal? Considering the signal sparse, we can constrain most of its components to be zero by minimizing the number of non-zero elements, that is the l_0 norm defined by $\|x\|_0 = \sum_{i=1}^N x_i^0$. Nevertheless, minimizing the l_0 norm is difficult and requires combinatorial optimization so we prefer to minimize the l_1 norm defined by $\|x\|_1 = \sum_{i=1}^N |x_i|$. l_1 norm is just the sum of the absolute values of every element and [14] proved that when the l_0 -minimization have a sparse solution, the l_1 -minimization will find it. We need the solution to be sparse either in its original space or in another domain by applying a sparse transform. A sparse domain enables to represent a signal with a smaller number of non-zero elements than originally and thus enforce the sparsity constraint. Many transforms are known to make a signal sparse, for instance we can cite the Wavelet transform, the discrete cosine transform or simply a finite difference transform. It comes to promote sparsity by minimizing $\|\Psi x\|_1$ where Ψ is a sparse transform.

The solution x of our problem is given by solving the following convex optimization problem:

$$\operatorname{argmin}_x J(x) = \|TF_{u0}(x) - E_u\|_2^2 + \lambda\|\Psi x\|_1 \quad (3)$$

The first term is the data consistency constraint, $\|\Psi x\|_1$ is the sparsity constraint. λ is the Lagrange parameter that defines the confidence we put in the measured signal E_u . The data consistency constraint enables the solution to remain close to the raw data acquisition. TF_{u0} is the 3D undersampled Fourier operator defined by three operations. The first operation consists in applying a 3D Fourier transform. The latter is undersampled in a random manner. Then, the other coefficients are replaced by zero values. Hence, the acquired data are defined by $E_u = TF_{u0}(P)$ with P the propagator to be recovered. x is the estimated propagator so $TF_{u0}(x)$ is the undersampled Fourier transform of the estimated propagator. Equation (3) finds the sparsest solution that corresponds to the acquired data.

We have seen the three conditions necessary to reconstruct a signal using Compressed Sensing : (1) Possibility to acquire the measurements in a random fashion. (2) The signal has a sparse representation. (3) Reconstruction via a convex optimization problem. The next section reviews these three CS conditions in the case of a 3D signal : The diffusion propagator or EAP.

3 EAP reconstruction via Compressed Sensing

In this section, we present the CS based reconstruction method.

Undersampling Most of the propagator energy is focused on the origin of its Fourier space. This energy corresponds to the low-frequency components, that describes the main features. Hence, it is judicious to sample more these components, or even fully sample them, and take the higher frequency components in a random fashion. The choice of a well appropriate sampling scheme is a open problem that requires an in-depth study. An appropriate scheme can lead to really good reconstructions whereas a bad scheme can make the reconstruction inapplicable. The CS approach recommends to maximize the degree of incoherence during the undersampling process in order to produce noise-like artefact. A way to measure the incoherence is to compute the Point Spread Function [14]. We are currently working on this important problem and among many sampling scheme already tested, we use a density function compact in the centre and decreasing away from the origin. The Binomial and Gaussian distributions are good candidates for such sampling schemes. An example of 3D Binomial distribution is shown figure 1(b).

EAP natural sparsity The trajectory of water molecules can be described by a random walk, i.e. each molecule follows a random path in a 3D space. However, when looking at a set of molecules, one can see that, in a free medium, the averaged displacement follows a Gaussian distribution. It means most of the molecules remain confined around their initial positions. For example, in free water, at $37^{\circ}C$, with a diffusion coefficient $D = 3.10^9$, and a diffusion time of $50.10^{-3}s$. 32% of the molecules have moved at least at $17\mu m$ whereas only have passed $34\mu m$ [12].

At the scale of a voxel, one models the diffusion by the EAP, $P(r_0|r, \tau)$. P represents the probability that a molecule moves from an initial position r_0 to r after a delay τ . Because of the Gaussian particular nature, the EAP values decrease while moving away from its centre until falling to zero. Thereby, the propagator is already sparse in free medium. When the diffusion is hindered by biological obstacle, as the myelin in the white matter fibres, the molecules displacement is constrained to the milieu. Beside such hindrance the propagator values decrease to zero. This phenomenon emphasizes the sparsity in the original space of P.

Because of the EAP natural sparsity, we choose to not use any sparse transform for the signal reconstruction.

EAP Reconstruction For some reason explained in the previous paragraph, we consider the case where $\Psi = I$. This leads to the following functional to be minimized :

$$\operatorname{argmin}_x J(x) = \|TF_{u0}(x) - E_u\|_2^2 + \lambda\|x\|_1 \quad (4)$$

Many techniques have been recently proposed to solve this functional [8, 24]. We are in the process to test some of the most appropriate. Here, and for simplicity, we just illustrate the case where we find the minimizer of this problem by means of a iterative shrinkage-thresholding algorithm (ISTA), where each

iteration involves a shrinkage step. This method avoids the computation of the l_1 -norm gradient, and thus overcome the difficulties that occur when we want to compute the derivative of this norm at zero. The general step of ISTA is

$$x_{k+1} = S_\lambda(x_k - 2\alpha TF_{u0}^*(TF_{u0}(x) - E_u)) \quad (5)$$

where α is a suitable stepsize and $S_\lambda : \mathfrak{R}^3 \rightarrow \mathfrak{R}^3$ is the 3D soft-thresholding operator defined by

$$S_\lambda(x) = \begin{cases} 0 & \text{if } |x| \leq \lambda \\ x - \text{sign}(x)\lambda & \text{otherwise} \end{cases} \quad (6)$$

For more detail, we refer the interested reader to [8, 24].

4 Experimental results

In this section, we evaluate the performances of our algorithm on a set of synthetic propagator constructed on a Cartesian grid according to the multi-tensor model.

Propagator comparison. Letting P represent the propagator to be recovered and P' the estimated propagator, we compute the Euclidian distance between P and P' over all the q-space grid, normalized by the norm of P given by

$$\text{error}(P, P') = \frac{1}{MNL} \sum_{i=1}^M \sum_{j=1}^N \sum_{k=1}^L \frac{|P(i, j, k) - P'(i, j, k)|}{\|P\|_2^2} \quad (7)$$

where M,N,L are the q-space dimension. In this section, we use this criterion to follow the performances of the method.

Angular information. Because P is a $\mathfrak{R}^3 \rightarrow \mathfrak{R}$ function, we cannot observe it directly. Hence, We chose to visualize its ODF by integration of the probability values in a constant solid angle as expressed in eq. 1. This representation points up the angular information about the diffusion [22] [1].

Synthetic data generation The synthetic data are generated using the multi-tensor model. The diffusion signal S is, thus, described as,

$$S(g_i) = \sum_{k=1}^K p_k e^{-b_i g_i^T D_k g_i} \quad (8)$$

where a fibre k is defined by a tensor matrix D_k and a weight p_k . g_i and b_i are the encoding gradient direction and intensity, respectively, allowing to sample the entire q-space. This model enables to simulate multi-crossing fibre. The fibre orientations are defined by the tensor matrix D_k and the number of fibre is indicated by T .

In order to evaluate the performance of our algorithm, we need to generate the propagator P . Recalling that the attenuated diffusion signal $S(g)$ is directly related to the diffusion propagator $P(r)$ by a Fourier transform as expressed in equation 2, we need to compute the inverse Fourier transform of $S(g)$ in order to get $P(r)$. It happens that $P(r)$ is also a multi-Gaussian function expressed as

$$P(r) = \sum_{k=1}^K \frac{1}{\sqrt{(4\pi b)^3 |D_k|}} p_k e^{-\frac{r^T D_k^{-1} r}{4b}} \quad (9)$$

where r is a 3D vector representing the water molecule displacement.

Simulation The CS method is applied on three phantoms generated as described previously from three tensors $D_1 = \text{diag}(10^{-6} \times [150 \ 150 \ 1500])$, $D_2 = \text{diag}(10^{-6} \times [1500 \ 150 \ 150])$, $D_3 = \text{diag}(10^{-6} \times [150 \ 1500 \ 150])$ and three weights $p_1 = p_2 = p_3 = 1$. One is the diffusion propagator of one fibre made from D_1 and p_1 . The second corresponds to a 90° 2-crossing fibers made from D_1 , D_2 and the corresponding weights. The third one is the sum of three fibers that crosses each other with a 90° angle and each of the three fiber k is defined by one of the covariance matrix D_k and its p_k . All the synthetic propagators are generated on a $M * N * L = 16 * 16 * 16$ cartesian grid with sampling frequency $f_s = 1.5$. The ODFs corresponding to the radial integration over the entire grid ($K = 16 * 16 * 16 = 4096$ equispaced measurements) are shown in figure 2. The reconstruction is evaluated in the next section after taking N measurements within $K_1 = 5 * 5 * 5 = 125$, $K_2 = 6 * 6 * 6 = 216$, $K_3 = 7 * 7 * 7 = 343$ and $K_4 = 8 * 8 * 8 = 512$ on the initial grid. The corresponding rate are $N_{e1} = K/K_1 = 32.7680$, $N_{e2} = K/K_2 = 18.9630$, $N_{e3} = K/K_3 = 11.9417$ and $N_{e4} = K/K_4 = 8$.

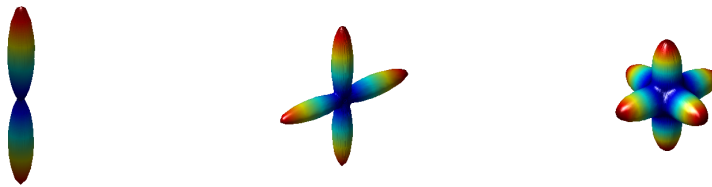


Fig. 2. ODF from 1, 2 and 3 90° crossing fibres propagator

In the first part of the simulation, we take equispaced samples on the grid and try to reconstruct the propagator by computing directly the inverse Fourier transform of the diffusion signal so-undersampled. Table 1 shows numerical results and figure 3 (a) represents the ODFs from the estimated propagator using

DSI. In the second part, the q-space is undersampled in an random fashion using an binomial density function. Then we apply the CS method to recover the propagator. Mean and standard deviation of the error between the true propagator and the estimated propagator are shown table 2 and examples of ODF estimated with our technique are displayed in figure 3 (b).

In a Matlab implementation, the technique proposed take no more than 20 seconds to reconstruct $16*16*16$ signal components, on a Intel Core 2 Duo CPU at 2.8 GHz.

The numerical results, shown table 1, indicates that the reconstruction error increases with decreasing number of measurements. We can still reconstruct the propagator in a correct manner with only $N = 512$, in the case of a regular sampling scheme. Below this level the reconstruction error diverges. This is due to the violation of the Nyquist condition. The maximal frequency component for both propagator is $f_m = 6$, so the Nyquist rate is $N_e = 2 * f_m / f_s = 9.333$. The only case where this rate is respected corresponds to the case $N = 512$ measurements.

After randomly undersampling the attenuated diffusion signal and then applying a CS reconstruction, the error between the true propagator and the estimated propagator does not diverge even for a smaller number of measurements (table 2). We note that the regular reconstruction is slightly better for $N = 512$ because the Nyquist theorem is respected. Nevertheless, the DSI reconstruction do not reach the accuracy of a CS reconstruction after this point. Our technique thus overcomes the limitation of DSI concerning the number of measurements.

Standard deviations remain low from $N = 512$ to $N = 216$, which indicates that the reconstruction is quite stable within this range. Below, the lack of precision is due to the random aspect of the method. Indeed, the reconstruction depends on the sampling scheme and we know that an appropriate scheme leads to correct recovering (see sec. 3, Undersampling).

The figure 3 (b) indicates that we can easily extract maxima from all the CS-based estimated ODFs while the DSI-based ODFs presented figure 3 (a) give corrupted angular information from $N = 216$. In spite of unwanted artefacts at $N = 343$ we can still detect maxima. They are regular shifted artefacts that appear when violating the Nyquist conditions. The random undersampling scheme results in incoherent artefacts spread all over the grid as a random noise and the l_1 - minimization enables to get rid of it. Once again, the CS reconstruction outperforms the DSI method regarding the recovering of the angular information.

The l_1 regularization problem gives large penalty to the small components and tends to produce a solution with a large number of coefficients equal to zero. It results in keeping the coarse features, i.e. the one characterized by the large components. It is exactly what we need to preserve if the signal has a compact, i.e. sparse, representation. The multi tensor model gives a non band-limited signal with many small values away from its centre, which are estimated by zeros after reconstruction. This is not important if we only look at the whole propagator because the small values can be replaced by zero without any prob-

lem. However this phenomenon is emphasized when integrating P values as ODF does. Thereby, the ODF look a bit flattened as an effect of the l1 regularization (fig. 3).

DSI with Regular undersampling				
	N=125	N=216	N=343	N=512
One fibre phantom ($\times 10^{-5}$)	9.742	7.8826	3.1254	1.9459
90° 2-crossing fibres phantom ($\times 10^{-5}$)	17.384	13.113	5.429	1.8143
90° 3-crossing fibres phantom ($\times 10^{-5}$)	16.624	12.944	7.7627	2.6951

Table 1. Error between the true propagator and the estimated propagator for regular undersampling.

DSI with Compressed Sensing based reconstruction and random undersampling				
	N=125	N=216	N=343	N=512
One fibre phantom ($\times 10^{-5}$)	2.8901 \pm 0.1413	2.7987 \pm 0.0758	2.6214 \pm 0.0292	2.5702 \pm 0.0178
90° 2-crossing fibres phantom ($\times 10^{-5}$)	3.1131 \pm 0.1527	3.007 \pm 0.0983	2.9332 \pm 0.0364	2.8873 \pm 0.0267
90° 3-crossing fibres phantom ($\times 10^{-5}$)	2.9094 \pm 0.0495	2.8074 \pm 0.0324	2.7239 \pm 0.0253	2.7021 \pm 0.0203

Table 2. Mean and standard deviation of the error between the true propagator and the estimated propagator.

5 Conclusion

In this article, we have presented a Compressed Sensing based method for accelerating the reconstruction of the Ensemble Average Propagator in Diffusion MRI (dMRI).

It paves the way for a new method to reconstruct the propagator and the subject has to be further developed. We are implementing several optimization techniques in order to solve (4) and some of these techniques seem really promising. The results presented in this article use synthetic data with no noise and, so, do not take in account the perturbations that occur during the acquisition. Hence, our current work considers noisy measurements.

The signal representation has to be compact if we want to reconstruct it. This condition is crucial when we want to decrease the number of measurements

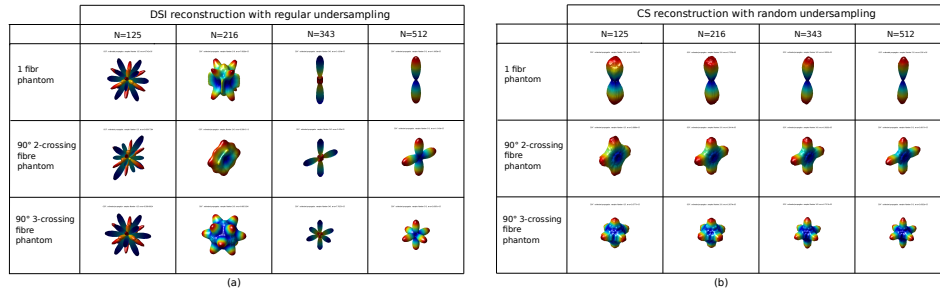


Fig. 3. ODF of the reconstructed propagator on the one fibre phantom and the 90° crossing fibre phantom. (a) CS reconstruction . (b) Direct reconstruction

needed to a good-quality reconstruction. In this paper we have undersampled P to 125 acquisitions because less coefficients are not sufficient to entirely described the propagator. An interesting issue would be to find the transforms which best sparsify P in order to go down the stage of 125 acquisitions.

Aside from these points that need reviews, our method allows to significantly reduce the number of measurements and outperforms the time consuming acquisition technique known as the Diffusion Spectrum Imaging (DSI). Our method efficiently reconstruct the EAP from reduced and non uniformly under sampled Diffusion Weighted (DW) MRI images combined to an efficient and accurate l_1 norm based reconstruction algorithm. This opens an original and very interesting road to shorten the dMRI acquisition time and opens new opportunities to render HARDI feasible in a clinical setting.

Acknowledgement: This work was partially supported by the ANR project NucleiPark.

References

1. i. Aganj, C. Lenglet, and G. Sapiro. Odf reconstruction in q-ball imaging with solid angle consideration., In *Proceedings of the Sixth IEEE International Symposium Biomedical Imaging, Boston, MA., June 2009.*
2. P.J. Basser, J. Mattiello, and D. Le Bihan. Estimation of the effective self-diffusion tensor from the nmr spin echo. *Journal of Magnetic Resonance*, B(103):247–254, 1994.
3. P.J. Basser, J. Mattiello, and D. Le Bihan. Mr diffusion tensor spectroscopy and imaging. *Biophysical Journal*, 66(1):259–267, 1994.
4. R. Chartrand. Fast algorithms for nonconvex compressive sensing: Mri reconstruction from very few data. *IEEE International Symposium on Biomedical Imaging (ISBI)*, 2009.
5. M. Descoteaux, E. Angelino, S. Fitzgibbons, and R. Deriche. Regularized, fast, and robust analytical q-ball imaging. *Magnetic Resonance in Medicine*, 58(3):497–510, 2007.

6. Maxime Descoteaux. *High Angular Resolution Diffusion MRI: From Local Estimation to Segmentation and Tractography*. PhD thesis, Nice Sophia Antipolis University,, February 2008.
7. David L. Donoho. Compressed sensing. *IEEE Trans on Information Theory*, 52(4):1, 2004.
8. M. Elad, B. Matalon, J. Shtok, and M. Zibulevsky. A wide-angle view at iterated shrinkage algorithms. In *in SPIE - Wavelet XII*, volume 6701, pages 26–29, August 2007.
9. A. Ganesh, VR Edward, et al. Reordering for improved constrained reconstruction from undersampled k-space data. *International Journal of Biomedical Imaging*, 2008.
10. W. Guoa and W. Yinb. Edgects: Edge guided compressive sensing reconstruction. 2009.
11. P. Hagmann, L. Jonasson, P. Maeder, J.P Thiran, Van J. Wedeen, and R. Neuli. Understanding diffusion mr imaging techniques: From scalar diffusion-weighted imaging to diffusion tensor imaging and beyond. *RadioGraphics*, 26:S205–S223, 2006.
12. D. Le Bihan. Looking into the functional architecture of the brain with diffusion MRI. *Nature Reviews Neuroscience*, 4(6):469–480, June 2003.
13. D. Le Bihan and E. Breton. Imagerie de diffusion it in vivo par résonance magnétique nucléaire. *CR Académie des Sciences*, (301):1109–1112, 1985.
14. M. Lustig, D. Donoho, and J.M. Pauly. Sparse mri: The application of compressed sensing for rapid mr imaging. *Magnetic Resonance in Medicine*, 58(6):1182–1195, 2007.
15. K.D. Merboldt, W. Hanicke, and J. Frahm. Self-diffusion nmr imaging using stimulated echoes. *J. Magn. Reson.*, 64:479–486, 1985.
16. M.E. Moseley, Y. Cohen, J. Mintorovitch, J. Kucharczyk, J. Tsuruda, P. Weinstein, and D. Norman. Evidence of anisotropic self-diffusion. *Radiology*, 176:439–445, 1990.
17. P.A. Osment, K.J. Packer, M.J. Taylor, J. J. Attard, T. A. Carpenter, L. D. Hall, S. J. Doran, and N. J. Herrod. Nmr imaging of fluids in porous solids. *Phil. Trans. Roy. Soc.*, 333:441–452, 1990.
18. E.O. Stejskal and J.E. Tanner. Spin diffusion measurements: spin echoes in the presence of a time-dependent field gradient. *Journal of Chemical Physics*, 42:288–292, 1965.
19. D.G. Taylor and M.C. Bushell. The spatial mapping of translational diffusion coefficients by the nmr imaging technique. *Phys. Med. Biol.*, 30:345–349, 1985.
20. A. Tristan-Vega, SC.F. Westin, and S. Aja-Fernandez. Estimation of fiber orientation probability density functions in high angular resolution diffusion imaging. *NeuroImage*, 47(2):638–650, August 2009.
21. D. Tuch. Q-ball imaging. *Magnetic Resonance in Medicine*, 52(6):1358–1372, 2004.
22. V.J. Wedeen, P. Hagmann, W. Tseng, T.G. Reese, and R.M. Weisskoff. Mapping complex tissue architecture with diffusion spectrum magnetic resonance imaging. *Magnetic Resonance in Medicine*, 54(6):1377–1386, 2005.
23. V.J. Wedeen, T. G. Reese, D.S. Tuch, M.R. Weigel, J.-G. Dou, R.M. Weisskoff, and D. Chessler. Mapping fiber orientation spectra in cerebral white matter with fourier-transform diffusion mri. In *Proceedings of the International Society for the Magnetic Resonance in Medecine: 8th Scientific Meeting and Exhibition*, number 82, 2000.
24. M. Zibulevsky and M. Elad. L1-l2 optimization in signal and image processing. *IEEE Signal Processing Magazine*, 27(3), May 2010.

Extrapolating fiber crossings from DTI data.

Can we infer similar fiber crossings as in HARDI?

V. Prčkovska, P.R. Rodrigues, R. Duits,
B.M. ter Haar Romeny, and A. Vilanova

Department of Biomedical Engineering, Eindhoven University of Technology

Abstract. High angular resolution diffusion imaging (HARDI) has proven to better characterize complex intra-voxel structures compared to its predecessor diffusion tensor imaging (DTI). However, the benefits from the modest acquisition costs and significantly higher signal-to-noise ratios (SNRs) of DTI make it more attractive for use in clinical research. In this work we use contextual information derived from DTI data, to obtain similar fiber crossings as the ones recovered with the HARDI reconstruction techniques. We conduct a synthetic phantom study under different angles of crossing and different SNRs. We compare the extrapolated crossings from contextual information with HARDI data. We qualitatively corroborate our findings from the phantom study to real human data. We show that with extrapolation of the contextual information, the obtained crossings are similar to the ones from the HARDI data, and the robustness to noise is significantly better.

1 Introduction

The recent diffusion weighted magnetic resonance imaging (DW-MRI) technique, diffusion tensor imaging (DTI) [1], is subject of intense research mainly due to its feasibility in clinical practice (number of gradients (NG) around 20, b-value of 1000 s/mm^2 and total acquisition time of 3-5 minutes [2]). DTI constitutes a valuable tool to inspect fibrous structures in a non-invasive way. Despite the great potential for clinical applications, DTI has one obvious disadvantage due to the crude assumption for modeling the underlying diffusion process as Gaussian. In other words, in the areas of complex intra-voxel heterogeneity the DTI model fails to distinguish multiple fiber populations. This limits the accurate description of the diffusion process locally, and influences the accuracy of the fiber tracking algorithms, an important application of this model. To overcome the limitations of DTI, more complex acquisition schemes known as high angular resolution diffusion imaging (HARDI) were introduced [3]. These acquisitions come coupled with more sophisticated reconstruction techniques that tend to avoid any assumptions for the probability density function (PDF) that describes the underlying diffusion process. Thus, locally more accurate models for the diffusion process, that allow the detection of multiple fibrous structures, were introduced [4–9]. However, the increased accuracy in HARDI comes along with a few drawbacks, mainly in more time consuming acquisitions (60 to few hundreds NG, higher b-values ($> 2000 \text{ s/mm}^2$) and total acquisition times from 20 minutes to a few hours) [3,10]. This is one of the biggest impediments in applying

HARDI in a clinical setting. Another major issue is the SNR in the images acquired by the typical DTI or HARDI acquisition protocols for clinical scanners. Despite the more accurate local modeling of the underlying diffusion process by the HARDI techniques, they require acquisitions at higher b-values and denser gradient sampling compared to DTI. Therefore, the acquired datasets have significantly lower SNRs than in DTI (especially in the diffusion weighted images which is sometimes a factor of 4 lower). The reconstructed diffusion profiles suffer from major noise pollution that often produces false or displaced maxima of the reconstructed diffusion functions and might notably disturb the fiber tracking algorithms. Proper regularization techniques on the domain of these datasets are thus important. Moreover, there is an additional issue with the accuracy of the DW-MRI data. Since the noise is very prominent in the phase of an MRI signal, it is common to discard this information, thus considering only the amplitude. This results in anti-podally symmetric profiles as pointed out by Liu et al. [11], that can only model single fiber or symmetric crossings of multiple fibers. However, this can not always be assumed to be the case in the white matter of the brain, especially in structures such as *optic chiasm*, *the hippocampus*, *the brain stem* and others. Since the data is ill defined, considering the contextual information (i.e., neighborhood) can be of utmost importance. There has been previous work on inter-voxel, contextual based filtering for estimating asymmetric diffusion functions [12], and cross-preserving smoothing of HARDI images [13] by modeling the stochastic processes of water molecules (i.e., diffusion) in oriented fibrous structures. However, these approaches increase the complexity of already complex and computationally heavy HARDI data. Rodrigues et al. [14], accelerated these complex convolutions enabling a fast framework for the noise removal, regularization and enhancement of HARDI datasets. Notwithstanding, contextual processing as described above has been applied only on HARDI models, due to the natural coupling of the space of positions and orientations that describe the diffusion process.

In this paper, we address some of the above mentioned issues. We use data from typical clinically obtained DTI acquisitions to build orientation distribution functions (ODF) that can be used for contextual processing of the data. The data initially comes with high SNR values making the local reconstruction of the ODFs reliable. The context information of well defined single direction fibers is extrapolated to areas where the fiber structure is considerably complex and therefore not defined in DTI. We analyze the difference of the contextually modified ODFs compared with the Qball reconstructions [15] without any regularization from the same data as the estimated extrapolated ODFs (E-ODFs). To be fair, we extend this comparison to Qball’s “best scenario” at high b-value ($3000s/mm^2$) and dense gradient sampling (121 number of gradients) and with Laplace-Beltrami smoothing as reported in Descoteaux et al. [15]. We do quantitative analysis on synthetic crossings of two fibers at different angles and qualitative analysis on *in-vivo* data with the same acquisition as in the synthetic data. We come to a few interesting conclusions, suggesting that E-ODFs contain similar information as Qball’s best scenario case. The E-ODFs could bring great

improvement to the DTI data, helping to overcome the limitations in crossing regions and enabling possibilities for streamline-based tractography.

2 Methods

In this section we present our method for creating extrapolated ODFs (E-ODFs) from diffusion tensors (DT) estimated from our DW-MRI data. We additionally give details on the contextual image processing and perform an evaluation.

2.1 Creating spherical diffusion functions from diffusion tensors

In DTI, the signal decay is assumed to be mono-exponential [16], and yields the equation:

$$S_g = S_0 \exp(-b\mathbf{g}^T \mathbf{D} \mathbf{g}) \quad (1)$$

where S_g is the signal in the presence of diffusion sensitizing gradient, and S_0 is the zero-weighted baseline signal, b is the b-value parameter of the scanner closely related to the effective diffusion time, and the strength of the gradient field, \mathbf{g} are the diffusion gradient unit vectors, and \mathbf{D} is the 2^{nd} order symmetric, positive definite diffusion tensor (DT). Once the DT is calculated per voxel, the orientation distribution function (ODF) can be reconstructed, and sampled on the sphere

$$ODF(\mathbf{n}) = \mathbf{n}^T \mathbf{D} \mathbf{n} \quad (2)$$

where \mathbf{n} is the direction vector defined by the tessellation. Figure 1 shows a typical linear DT and the corresponding diffusivity profile sampled on a sphere (in our case icosahedron of order 4, 642 points on a sphere). Note that this ODF, since it is derived from the DT, does not hold any crossing information and should not be confused with the apparent diffusion coefficient (ADC) whose crossing information does not necessarily coincide with the underlying fiber population as pointed out by Özarslan et al. [7].

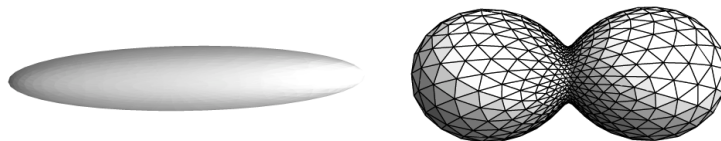


Fig. 1. A linear diffusion tensor (left) and the corresponding tessellated ODF (right).

From a tensor field we create an ODF field, i.e., a HARDI-like dataset \mathcal{U} defined on the coupled space of positions and orientations [13], meaning the local diffusion profiles are defined not only spatially, but also as a function of orientation:

$$\mathcal{U} : \mathbb{R}^3 \times S^2 \rightarrow \mathbb{R}^+ : \mathcal{U}(\mathbf{y}, \mathbf{n}(\beta, \gamma)) \quad (3)$$

This means that the probability density of a given water particle, starting at position \mathbf{y} , to have moved to a location with a certain direction $\mathbf{n}(\beta, \gamma)$ by the end of the diffusion time is given by the scalar $\mathcal{U}(\mathbf{y}, \mathbf{n}(\beta, \gamma))$. Here, β and γ are not the standard spherical coordinates. They are parametrized via a different chart, as described in Duits et al. [13]. To stress the coupling between orientations and positions, that comes along with the alignment of fiber fragments, we write $\mathbb{R}^3 \times S^2$ rather than $\mathbb{R}^3 \times S^2$. Such an image \mathcal{U} can now be enhanced. Throughout this article we consider DTI-data as the initial condition, which means that we set $\mathcal{U}(\mathbf{y}, \mathbf{n}) = \mathbf{n}^T \mathbf{D}(\mathbf{y}) \mathbf{n}$.

2.2 Kernels for contextual enhancing of orientation distribution functions

Duits et al. [13, 17] proposed a kernel implementation that solves the diffusion equation for HARDI images. The full derivation is beyond the scope of this manuscript. This kernel represents the Brownian motion kernel, on the coupled space $\mathbb{R}^3 \times S^2$ of positions and orientations. Next, we present a close analytic approximation of the Green's function. This approximation is a product of two 2D kernels on the coupled space $p_{2D} : \mathbb{R}^2 \times S^1 \rightarrow \mathbb{R}^+$ of 2D-positions and orientations:

$$p_{3D}^{D_{33}, D_{44}, t}((x, y, z)^T, \mathbf{n}(\beta, \gamma)) \approx N(D_{33}, D_{44}, t) \cdot p_{2D}^{D_{33}, D_{44}, t}((z/2, x), \beta) \cdot p_{2D}^{D_{33}, D_{44}, t}((z/2, -y), \gamma), \quad (4)$$

where $\mathbf{y} = (x, y, z)^T$, $N(D_{33}, D_{44}, t) \approx \frac{8}{\sqrt{2}} \sqrt{\pi t} \sqrt{t D_{33}} \sqrt{D_{33} D_{44}}$ takes care that the total integral over positions and orientations is 1.

The 2D kernel is given by:

$$p_{2D}^{D_{33}, D_{44}, t}(x, y, \theta) \equiv \frac{1}{32\pi t^2 c^4 D_{44} D_{33}} e^{-\frac{\sqrt{EN((x, y), \theta)}}{4c^2 t}} \quad (5)$$

where we use short notation

$$EN((x, y), \theta) = \left(\frac{\theta^2}{D_{44}} + \frac{\left(\frac{\theta y}{2} + \frac{\theta/2}{\tan(\theta/2)} x \right)^2}{D_{33}} \right)^2 + \frac{1}{D_{44} D_{33}} \left(\frac{-x\theta}{2} + \frac{\theta/2}{\tan(\theta/2)} y \right)^2$$

where one can use the estimate $\frac{\theta/2}{\tan(\theta/2)} \approx \frac{\cos(\theta/2)}{1 - (\theta^2/24)}$ for $|\theta| < \frac{\pi}{10}$ to avoid numerical errors. c is a positive constant for rescaling the diffusion time t . For details adhere to the work of Duits et al. [13, 17] and Rodrigues et al. [14].

The diffusion parameters D_{33} and D_{44} and stopping time t allow the adaptation of the kernels to different purposes:

1. $t > 0$ determines the overall size of the kernel, i.e., how relevant is the neighborhood;
2. $D_{33} > 0$, the diffusion along the principal axis, determines the width of the kernel;

3. $D_{44} > 0$ determines the angular diffusion, so the quotient D_{44}/D_{33} models the bending of the fibers along which diffusion takes place.

We can now convolve this kernel with the ODF image \mathcal{U} , using the HARDI convolution [14], as expressed in equation 6. We chose the parameters for the kernel in order to give a high relevance to the diffusion along the principal axis $D_{33} = 0.6, D_{44} = 0.01$ and $t = 1.4$.

$$\Phi(\mathcal{U})[\mathbf{y}, \mathbf{n}_k] = \sum_{\mathbf{y}' \in P} \sum_{\mathbf{n}' \in T} p_{\mathbf{y}, \mathbf{n}_k}(\mathbf{y}', \mathbf{n}') \mathcal{U}(\mathbf{y}', \mathbf{n}') \Delta \mathbf{y}' \Delta \mathbf{n}' \quad (6)$$

where $p_{\mathbf{y}, \mathbf{n}_k}$ is a kernel at position \mathbf{y} and orientation \mathbf{n}_k , such that

$$p(R_{\mathbf{n}'}^T(\mathbf{y} - \mathbf{y}'), R_{\mathbf{n}'}^T \mathbf{n}_k) = p_{\mathbf{y}, \mathbf{n}_k}(\mathbf{y}', \mathbf{n}') \quad (7)$$

and $R_{\mathbf{n}}$ is any rotation such that $R_{\mathbf{n}} \mathbf{e}_z = \mathbf{n}$. $\Delta \mathbf{y}'$ is the discrete volume measure and $\Delta \mathbf{n}'$ the discrete surface measure, which in case of (nearly) uniform sampling of the sphere, such as tessellations of icosahedrons, can reasonably be approximated by $\frac{4\pi}{|T|}$. P is the set of lattice positions neighboring to \mathbf{y} and T is the set of tessellation vectors. The convolution with such a kernel will result on the extrapolation of crossing profiles where the neighborhood information so indicates, i.e., the E-ODFs.

In order to achieve the desired results, care should be taken on the sharpness of the input image \mathcal{U} . Before applying the convolution, the ODFs are min-max normalized and sharpening is applied by a nonlinear transformation (i.e., power of 2) of the ODFs.

2.3 Data

Synthetic Data - To validate and analyse our methodology artificial datasets were generated. DT datasets were created where two fiber bundles forming “tubes” with radii of 2 voxels intersect each other. Here, the tensors, with eigenvalues $\lambda = [17, 3, 3] \times 10^{-3} mm^2/s$ and oriented tangentially to the center line of the tube, are estimated using a mixed tensor model [5]. Gaussian noise with different SNRs is added to the real and complex part of the signal reconstructed from equation 1. In order to evaluate the angular resolution we vary the angle between the two fiber tubes $\theta \in \{50^\circ, 60^\circ, 70^\circ\}$. We made a choice for these angles, given that the accuracy of Qball to detect multiple fiber orientations is around 60° [15, 18]. With these angle configurations we create two sets of data, with different acquisition parameters.

1. To evaluate the accuracy of E-ODFs we create datasets with $b = 1000s/mm^2$ and 49 gradient directions. We add Rician noise with SNR=20, given that this is the SNR found in literature for DTI acquisitions [2, 19]. From these datasets we estimate E-ODFs and Qballs without regularization.
2. To compare with the Qball’s best case scenario, as report by Descoteaux et al. [15], we create datasets at $b = 3000s/mm^2$ and 121 gradient direction. Since this kind of data is expected to have lower SNR, we add Rician

noise with $SNR = 10$. We estimate Qballs for these datasets and regularize with Laplace-Beltrami (LB) smoothing with $\lambda = 0.006$. This choice for the regularization parameter λ was made, since it was found to be the best at $b = 3000s/mm^2$ [15].

In order to evaluate the robustness to noise, we fix the angle to $\theta=70^\circ$, and we vary the SNR $\{5, 10, 20\}$. We make the same choices for b -values and number of gradients as previously described, and apply LB smoothing for the Qballs at $b = 3000s/mm^2$

Real Human Data - Diffusion acquisitions were performed using a twice focused spin-echo echo-planar imaging sequence on a Siemens Allegra 3T scanner, with FOV 208×208 mm, isotropic voxels of 2mm. 10 horizontal slices were positioned through the body of the *corpus callosum* and *centrum semiovale*. Uniform gradient direction scheme with 49 and 121 directions were generated with the electrostatic repulsion algorithm [20] and the diffusion-weighted volumes were interleaved with b_0 volumes every 12th scanned gradient direction. Datasets were acquired at b -values of 1000 s/mm² and 3000 s/mm².

2.4 Analysis of synthetic data

To analyze the accuracy of the E-ODFs compared to the Qballs in the synthetic data sets, we calculate the angular error and standard deviation of the voxels in the crossing region. We do not expect to obtain exactly the same profile, notwithstanding it should contain the same information concerning the amount of fiber populations and their angle. To do so, we use a simple scheme for determining the error between the detected maxima, and then report the angular difference between these maxima and the simulated (true) fiber directions. We detect the maxima as the local maxima of the normalized [0,1] profiles where the function surpasses a certain threshold (here, we use 0.5). To minimize the error related to the sphere tessellation, we use 4th order of tessellation of an icosahedron.

2.5 Analysis of human data

For qualitative analysis of the real data, we select an interesting region, the *centrum semiovale* (CS), where crossings are to be expected. This is a challenging region for DW-MRI analysis techniques, since fibers of the *corpus callosum* (CC), *corona radiata* (CR), and *superior longitudinal fasciculus* (SLF) form a three-fold crossing. A region-of-interest (ROI) was defined on a coronal slice (see figure 5(a)). We only do qualitative analysis for the real data, as we do not know the ground truth there.

3 Results

3.1 Phantom data results

The quantitative results of the found angular error and standard deviation of the different profiles in the crossing area from the synthetic data are presented in

Acquisition	Profiles	50°			60°			70°		
		$l=4$	$l=6$	$l=8$	$l=4$	$l=6$	$l=8$	$l=4$	$l=6$	$l=8$
$b=1000s/mm^2$ $NG=49; SNR=20$	E-ODF Qball	x	x			55.5°; 12°			12°; 5°	
		x	x	x	x	54.3°; 15°	37.9°; 21°	x	43°; 25.1°	24.4°; 7.5°
$b=3000s/mm^2$ $NG=121; SNR=10$	Regularized Qball	x	x	37.6°; 19.9°	x	38.5°; 26.9°	33°; 27°	14.1°; 32.1°	5.4°; 3°	19°; 31°

Table 1. Table of angular error and standard deviation of the different profiles in the crossing area of the synthetic data.

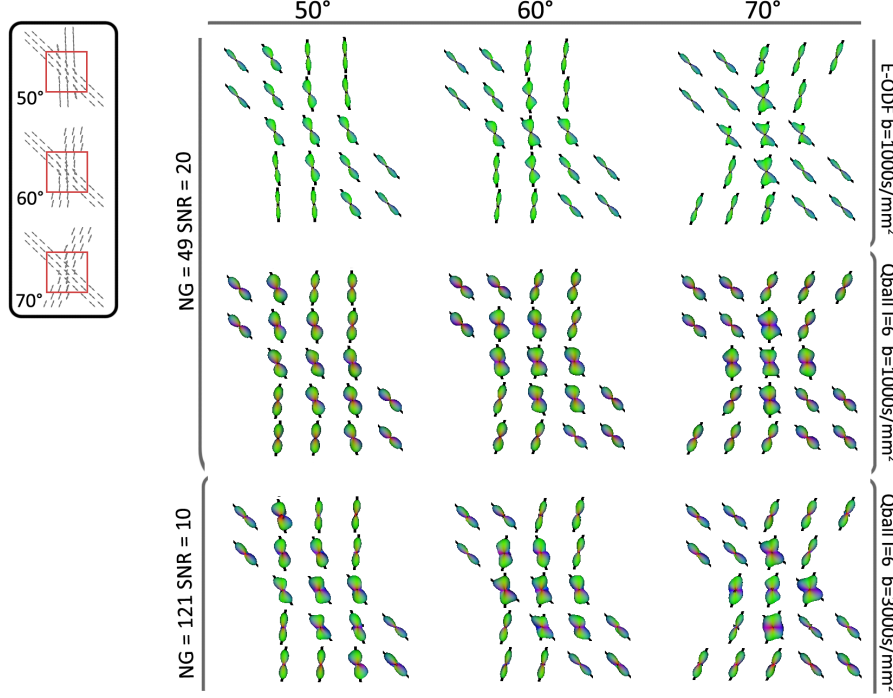


Fig. 2. E-ODFs and Qballs for different angles of crossing at fixed $SNR = 20$ for $b = 1000s/mm^2$, and $SNR=10$ for $b = 3000s/mm^2$. The Qballs at $b = 3000s/mm^2$ are regularized with LB smoothing with $\lambda = 0.006$.

table 1. In the following paragraphs we relate them to some figures of interesting parameter configurations and discuss the results. In figure 2, we present the results of the performance of the proposed E-ODFs compared to the Qballs [15] for different angles of crossings, and different simulation parameters: 49 gradient directions, b-value $1000 s/mm^2$ and SNR 20, (figure 2 middle row) ; 121 gradient directions, b-value $3000 s/mm^2$, LB smoothing with $\lambda = 0.006$ [15] and SNR 10 (figure 2 third row).

We observe that for the angle of 50° , E-ODFs and not regularized Qballs fail to find multiple maxima in the crossing areas. Only regularized Qball at high $b = 3000s/mm^2$ and high order $l = 8$, detects multiple maxima. For the

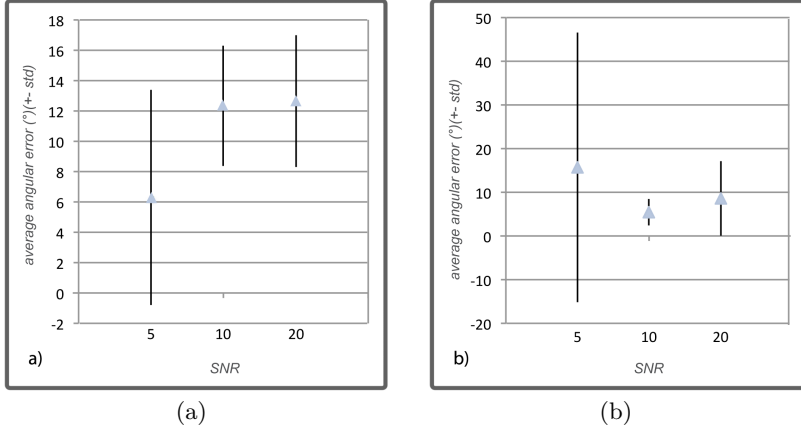


Fig. 3. Angular error and standard deviation for (a) E-ODFs at $b = 1000 \text{ s/mm}^2$ and 49 gradient directions (b) Regularized Qball with $\lambda = 0.006, b = 3000 \text{ s/mm}^2$ and 121 gradient directions.

angle of 60° the performance of E-ODFs is similar to the un-regularized Qball at $b = 1000 \text{ s/mm}^2$ and truncated at order of spherical harmonics $l = 6$. Regularized Qballs at $b = 3000 \text{ s/mm}^2$ outperform in this scenario. At an angle of 70° , the E-ODFs outperform the best (un-regularized) Qball scenario at order $l = 8$. Only regularized Qball at $l = 6$ outperforms in this scenario (see table of figure 1).

The plots of figure 3.1 report the relation between the angular error and change in SNR. We observe that the E-ODFs are more stable, regardless the noise level, whereas the regularized Qballs improve significantly at higher SNRs. However, it is important to note that in real data at high b -value $\approx 3000 \text{ s/mm}^2$ the SNR drops off to 5 (however, this might change depending on the type of scanner and imaging parameters). Figure 4 illustrates the previous conclusions. At higher order of truncation un-regularized Qball performs much worse, giving many false positives in the linear areas where the SNR is low.

We observe that regardless the SNR, the E-ODFs preserve the coherence of the linear and crossing regions, and preserve the angular error, to almost constant (see figure 3(a)). We also compared the E-ODFs, to Qball's best case scenario with LB regularization [15]. Here, for SNR 5, Qball performs worse (angular error of 14.9° and standard deviation 8.4°) than the E-ODFs. As noise decreases, E-ODFs' performance is similar to the regularized Qballs at $b = 3000 \text{ s/mm}^2$ (angular error 9.8° and standard deviation 9.15°). Regularized Qball outperforms E-ODFs, for SNR 20, with an angular error of 5.15° and standard deviation of 3.2° . However, this SNR is not realistic given nowadays acquisition protocols and machinery at b -values as high as 3000 s/mm^2 .

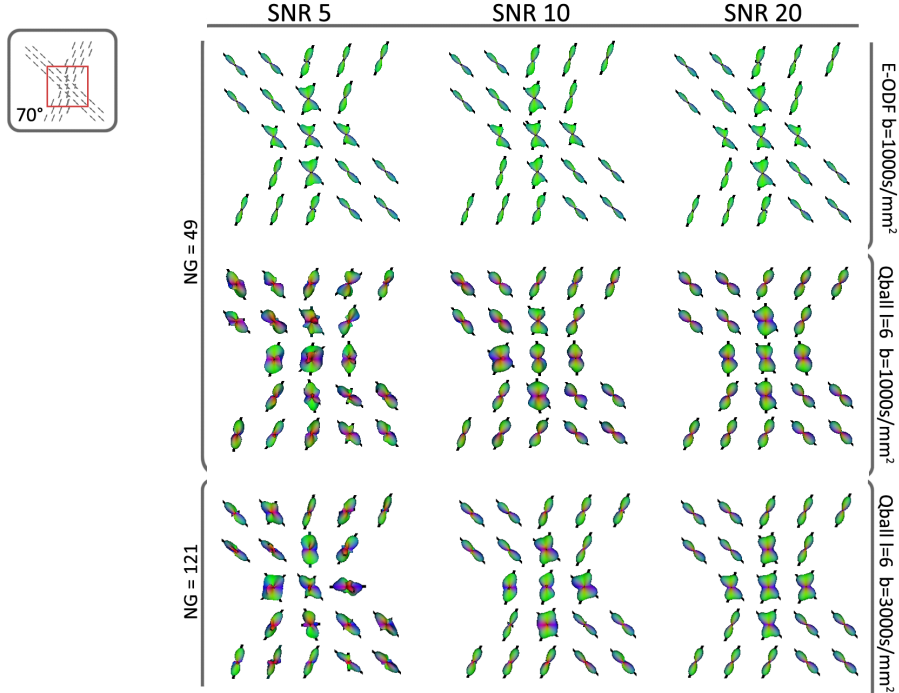


Fig. 4. E-ODFs and Qballs for different SNRs, and different b-value, at fixed angle of 70° .

3.2 Real data results

Even though crossing information is missing in the original DTI data, as well as in the created ODFs (as can be seen in figure 5(a) and figure 5(b)), we observe that after processing, crossing information is extrapolated (see figure 6(c)). The obtained crossings are very much comparable to the Qball reconstructions of $l = 6$, at $b = 3000s/mm^2$ and 121 gradient directions and regularized with LB smoothing of $\lambda = 0.006$ (figure 6(b)). The un-regularized Qballs at low b-value of $1000s/mm^2$ and low gradient sampling of 49 gradient directions, present less obvious structures of the CC and CR, and have more chaotically oriented crossings, figure 6(a).

All computations were conducted in an AMD Athlon X2 Dual 2.41GHz, with 3GB of RAM, taking 0.5 minutes per artificial tube dataset, and about 13 minutes for the real human brain dataset for estimating the E-ODFs.

4 Conclusions and Future Work

In this work we presented a method for extrapolating crossing information using image processing of the coupled space of positions and orientations in DTI data.

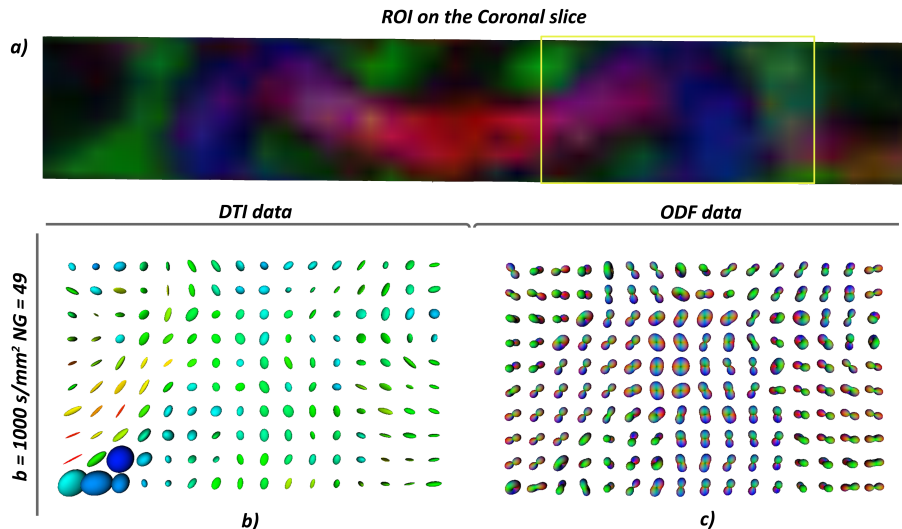


Fig. 5. The *centrum semiovale*. Left: the original DTI data, color coded by *FA*. Right: the ODFs from the DTI data, RGB color coded by orientation and min-max normalized.

We show that with typical acquisition schemes for DTI, the inferred fiber crossings are similar to the crossings from 6th order un-regularized Qball estimated from the same data. Furthermore we compare the E-ODFs to the best scenario of Qball at typical HARDI acquisition schemes, and we conclude that the information gain from the regularized Qball is similar at low SNR, but the Qballs improve when increasing the SNR. However, in practice HARDI acquisitions at high b-values result in very noisy datasets, and Qball reconstructions of poor quality including LB regularization. The robustness to noise of the presented method is significantly better than from the un-regularized Qballs reconstructed from the same data, and comparable to the Qball’s best scenario. The main contribution from this work lies on demonstrating similar quality of detected crossings with modest acquisitions modeled by DTI, and with the use of contextual information as in the popular HARDI reconstruction techniques that require more expensive acquisitions such as Qball. Future work addresses similar comparison to spherical deconvolution [8] as well as tensor decomposition techniques [21] which has proven to more reliably infer number and directions of fibers. The chosen kernel sets an overall reasonable probabilistic model that governs how the context of a fiber fragment is taken into account. Consequently, our framework lacks adaptivity. Future work will address more adaptive fiber context models to the data, such that context is only included where it is required by the data.

The method proposed has its limitations, it assumes that enough context is available for a correct extrapolation. The possible implications of this limitations for concrete brain structures should be studied. Future work should additionally bear more extensive validation to assess the exact differences between HARDI

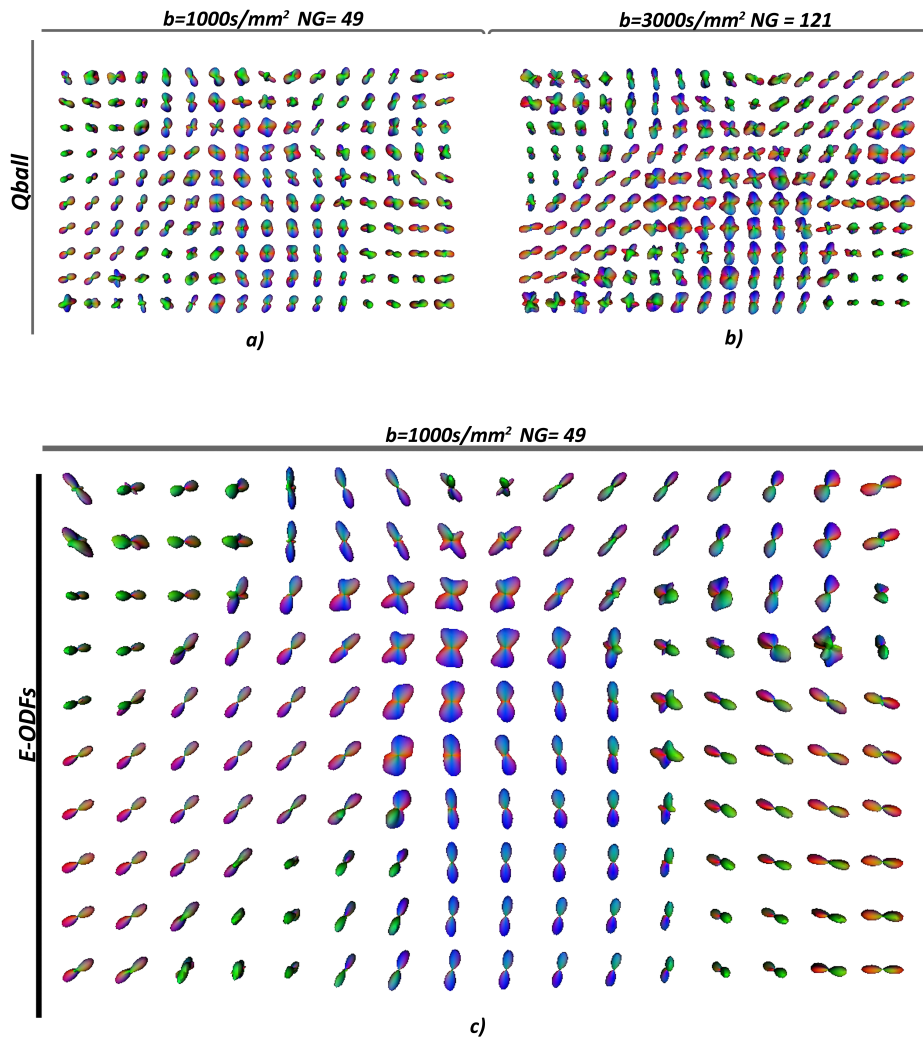


Fig. 6. Different profiles in the *centrum semiovale* a) un-regularized Qball of order 4 b) Regularized Qball with $\lambda = 0.006$ of order 6 from similar region as (a) c) E-ODFs of the same region as (a).

models and E-ODFs concerning acquisition parameters and anatomical areas of the brain. This includes synthetic data experiments with fibers of different configurations (e.g. curved bundles) and multiple crossings. As a conclusion, contextual processing of DTI data allows overcoming one of the main drawbacks of the DT model. The crossing information can be recovered with an acquisition that typically takes 3-6 minutes and modest post-processing (13 minutes for 10

slices of a human brain on a standard PC). This gives future work potential for applying more accurate stream-based tractography for DTI data.

References

1. Basser, P.J., Mattiello, J., Lebihan, D.: MR diffusion tensor spectroscopy and imaging. *Biophys. J.* **66**(1) (January 1994) 259–267
2. Jones, D.K.: The effect of gradient sampling schemes on measures derived from diffusion tensor mri: a monte carlo study. *MRM* **51**(4) (2004) 807–15
3. Tuch, D.S.: Diffusion MRI of complex tissue structure. PhD thesis, Harvard (2002)
4. Frank, L.R.: Characterization of anisotropy in high angular resolution diffusion-weighted MRI. *MRM* **47**(6) (2002) 1083–99
5. Alexander, D.C., Barker, G.J., Arridge, S.R.: Detection and modeling of non-gaussian apparent diffusion coefficient profiles in human brain data. *MRM* **48**(2) (2002) 331–40
6. Tuch, D.: Q-ball imaging. *MRM* **52** (2004) 1358–1372
7. Özarslan, E., Shepherd, T.M., Vemuri, B.C., Blackband, S.J., Mareci, T.H.: Resolution of complex tissue microarchitecture using the diffusion orientation transform (DOT). *NeuroImage* **36**(3) (July 2006) 1086–1103
8. Tournier, J.D., Calamante, F., Connelly, A.: Robust determination of the fibre orientation distribution in diffusion MRI: non-negativity constrained super-resolved spherical deconvolution. *NeuroImage* **35**(4) (2007) 1459–72
9. Jian, B., Vemuri, B.C.: A unified computational framework for deconvolution to reconstruct multiple fibers from Diffusion Weighted MRI. *IEEE Transactions on Medical Imaging* **26**(11) (2007) 1464–1471
10. Descoteaux, M.: High Angular Resolution Diffusion MRI: From Local Estimation to Segmentation and Tractography. PhD thesis, Universite de Nice - Sophia Antipolis (February 2008)
11. Liu, C., Bammer, R., Acar, B., Moseley, M.E.: Characterizing non-gaussian diffusion by using generalized diffusion tensors. *MRM* **51**(5) (2004) 924–37
12. A. Barmpoutis, B. C. Vemuri, D.H., Forder, J.R.: Extracting tractosemas from a displacement probability field for tractography in DW-MRI. In LNCS 5241, MICCAI (6-10 September 2008) 9–16
13. Duits, R., Franken, E.: Left-invariant diffusions on $\mathbb{R}^3 \times S^2$ and their application to crossing-preserving smoothing on HARDI-images. CASA report, TU/e, nr.18
14. Rodrigues, P.R., Duits, R., ter Haar Romeny, B., Vilanova, A.: Accelerated diffusion operators for enhancing DW-MRI. In: VCBM, Leipzig, Germany (2010)
15. Descoteaux, M., Angelino, E., Fitzgibbons, S., Deriche, R.: Regularized, fast and robust analytical Q-Ball imaging. *MRM* **58** (2007) 497–510
16. Basser, P.J., Mattiello, J., Lebihan, D.: Estimation of the effective self-diffusion tensor from the NMR spin echo. *J. of Magn. Res. Series B* **103** (1994) 247–254
17. Duits, R., Franken, E.: Left-invariant diffusions on the space of positions and orientations and their application to crossing-preserving smoothing of HARDI images. *International Journal of Computer Vision* 2010
18. Prčkovska, V., Roebroek, A.F., Pullens, W., Vilanova, A., ter Haar Romeny, B.M.: Optimal acquisition schemes in high angular resolution diffusion weighted imaging. In: MICCAI. Volume 5242 of LNCS., Springer (2008) 9–17
19. Lagana, M., Rovaris, M., Ceccarelli, A., Venturelli, C., Marini, S., Baselli, G.: DTI parameter optimisation for acquisition at 1.5T: SNR analysis and clinical application. *Comput Intell Neurosci NIL(NIL)* (2010) 254032
20. Jones, D., Horsfield, M., Simmons, A.: Optimal strategies for measuring diffusion in anisotropic systems by magnetic resonance imaging. *MRM* **42** (1999) 515–525
21. Schultz, T., Seidel, H.P.: Estimating crossing fibers: A tensor decomposition approach. *IEEE Transactions on Visualization and Computer Graphics* **14** (2008) 1635–1642

Inferring Microstructural Properties Using Angular Double Pulsed Gradient Spin Echo NMR in Orientationally Unknown Tissue

Wenjin Zhou¹, Matt G. Hall², and David H. Laidlaw¹

¹ Department of Computer Science, Brown University, USA.,

² Department of Computer Science, University College London, UK

Abstract. We present an analytical water diffusion model for inferring important microstructural properties such as axon radius, orientation, and packing density using low- q angular Double Pulsed Gradient Spin Echo (double-PGSE) NMR, taking into account finite gradient pulses. The MR signal attenuation obtained from Single Pulsed Gradient Spin Echo (single-PGSE) NMR reflects the underlying microstructural properties that restrict the molecular diffusion within. Estimating these properties using single-PGSE, however, requires prior knowledge of axon orientation and high q -values, inhibiting clinical application of these methods. Feasibility of estimating orientationally invariant fibers are emerging, although the acquisition protocol needs to be optimized for the specific axon radius to be estimated. Our simulation results are the first to use low- q angular double-PGSE experiments without prior knowledge of the axon orientation to demonstrate the feasibility of estimating axon radii of the typical human brain tissue range (1 to $5\mu m$). Along with axon radius, we were also able to infer other important microstructural properties such as axon orientation, axon packing density and water diffusivity.

1 Introduction

Diffusion MRI, which measures the diffusion of spins in tissues, is a popular technique in brain research for assessing a number of neurological disorders. Current diffusion MRI brain studies rely on indirect diffusivity-based measures such as fractional anisotropy (FA) as biomarkers for major microstructural changes [1, 2]. The fact that FA is a nonspecific summation index of the observed diffusion signal over the entire voxel makes it unable to distinguish between different microstructural changes in axon radius, orientation, packing density and myelin permeability [3]. Studies have shown that neuronal changes in these microstructural properties are detected in early stages of brain diseases [4, 5] and has been observed to be location specific and axon radius size selective [6, 7]. Measuring and analyzing these specific disease-affected microstructural changes *in vivo* may provide earlier indications of brain diseases such as multiple sclerosis (MS). Recently, various experiments have identified that axonal degeneration is the dominant cause of irreversible neurological disability in MS [8].

One approach to measure axon size uses diffraction patterns of diffusion MRI signals whose frequency is related to sample compartment size [9]. This approach imposes no geometric model. Weng [10], however, showed that the measurements from diffraction patterns did not match the microscope measurements in an excised rat brain. From simulation experiments, Lätt *et al.* [11] concluded that the lowest identifiable axon radius using current scanners is $10\mu m$, while human brain axon radii usually range from 0.3 to $5\mu m$ [12].

Alternatively, microstructural properties can be extracted by constructing a geometric model of the underlying tissue in which water molecules are diffusing and analyzing the experimental MR signals [13]. Different microstructural properties can be accounted for using the geometric model such as axon radius, packing density, orientation, etc. Assaf *et al.* [14] constructed a two-compartment CHARMED model for Single Pulsed Gradient Spin Echo (single-PGSE) experiments. In further work, they designed AxCaliber [15] to measure the Axon Diameter Distribution (ADD) of excised nerve tissues [15] and *in vivo* rat corpus callosum [16], assuming prior knowledge of axon orientation. Multi-diffusion DWI measurements let AxCaliber to classify axons using ADD since restricted diffusion is exhibited at different times relative to axon radius. Using single-PGSE approach, however, required prior knowledge of axon orientation, lengthy data acquisitions and high q -values (11 hr and $q_{max} = 51108m^{-1}$ in [15]), which can be difficult to achieve with current clinical scanners.

Feasibility of estimating orientationally invariant fibers with clinically achievable parameters are emerging [13]. However, the approach requires optimization of the acquisition protocol for the specific axon radius to be estimated. Good optimization results requires prior knowledge of the axon size which could be a problem in disease study where the underlying axonal change is hard to predict. Also, studies have shown that when a single optimized protocol is used for all axon radii range, small axon sizes ($R = 1, 2\mu m$) become indistinguishable.

The Double Pulsed Gradient Spin Echo (double-PGSE) sequence (Fig. 1a) first proposed by Cory [17] has been shown to reduce eddy current distortions [18]. It contains two pairs of diffusion gradients G_1 and G_2 separated by mixing time t_m that can be applied at any angle. Mitra [19] theoretically predicted the angular dependence of signal intensity on the angle between the two gradients G_1 and G_2 ; this makes it possible to distinguish restricted diffusion from Gaussian diffusion, and thus to determine the sizes of axons using moderate gradient strengths with angular double-PGSE experiments. Mitra’s theory, however, considered for only limiting cases of double-PGSE experiments, not taking into account finite duration of the diffusion time or mixing time. These limiting cases are difficult to achieve and Koch [20, 21] has shown that violating these conditions generally leads to underestimation of pore size and eccentricity. Özarlan [22] provided a theoretical solution for the angular dependence of NMR signal intensity in restricted geometries for arbitrary timing parameters. Shemesh [23] tested and verified this angular dependence of the signal decay [22] in well-controlled experiments using water-filled microcapillaries of known diameters ($5 - 20\mu m$).

Here, we propose an analytical water diffusion model based on Özarlan’s theory [22] for inferring microstructural properties by constructing a geometric model of the underlying microstructure using low- q angular double-PGSE experiments that accounts for finite gradient pulses. Unlike single-PGSE methods [15, 16], our model does not require prior knowledge of axon orientation. We demonstrate the feasibility of estimating axon radii in typical human brain tissue ranges (1 to $5\mu m$), along with axon orientation, axon packing density (using volume fraction), and water diffusivity with q_{max} of $25553m^{-1}$ using Monte Carlo simulation data from Camino [24, 25].

2 Methods

2.1 Analytical Model from double-PGSE

Geometric Axon Model We first construct a geometric model of the axons within which water molecules are diffusing in order to analyze the MR signal we obtain in double-PGSE experiments. Our geometric model has two compartments (Fig. 2): (1)

The intra-axonal compartment: the space inside the axons with radius a represented by non-abutting cylinders, and (2) *The extra-axonal compartment:* the homogeneous substrate space outside the axons. These two compartments are denoted as i and e below. The boundary of the axons is assumed to be impermeable (no exchange between the two compartments).

Double-PGSE Experiments The double-PGSE sequence (Fig. 1a) is the simplest form of multi-PGSE, first proposed by Cory [17]. The double-PGSE experiments are sensitive to restricted diffusion even in the condition of long diffusion wavelength $(\gamma\delta Ga)^2 \ll 1$, also known as small- q regime $(2\pi qa)^2 \ll 1$ (where a denotes axon radius, q denotes wave number defined as $q = \frac{\gamma\delta G}{2\pi}$, γ is the gyromagnetic ratio of the spins, δ is the pulse duration and G is the gradient strength). Özarslan [26] showed that when two diffusion gradient pulse pairs are used (as in double-PGSE), the wave number q necessary for nonmonotonicity is exactly half the wave number in single-PGSE experiments [27]. This sensitivity of the double-PGSE makes it possible to probe small compartments using relatively low wave numbers q . In a double-PGSE acquisition sequence, two encoding intervals of gradients G_1 and G_2 can be applied at any angle with an angle ψ between them. The two encoding intervals are separated by mixing time t_m with diffusion time Δ_1 and Δ_2 and pulse duration δ_1 and δ_2 . Özarslan [22] theoretic-

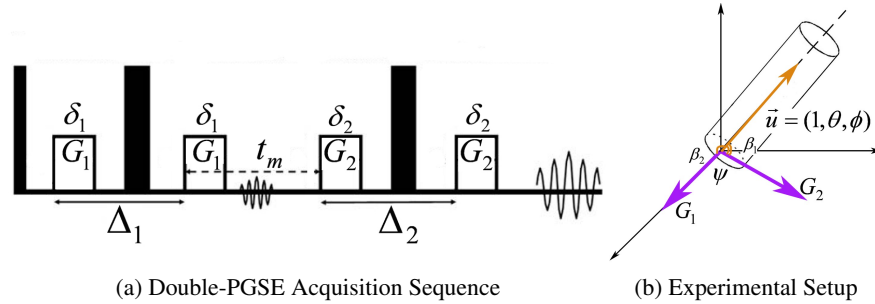


Fig. 1: (a) Double-PGSE acquisition sequence with two encoding intervals of gradient G_1 and G_2 . (b) Experimental setup. $u = (1, \theta, \phi)$ defines the arbitrary axon orientation. G_1 is fixed on the X-axis and G_2 angle varied linearly on the XOY plane. β_1 and β_2 denote the angle between G_1 , G_2 and u respectively.

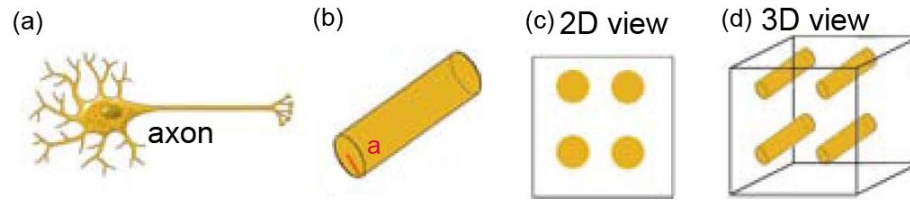


Fig. 2: Geometric axon model. (a) Schematic view of axon; (b) Single cylinder representing axon with radius a ; (c-d) 2D and 3D view of non-abutting rectangular arrangement of cylinders representing axons.

cally predicted the angular dependence of the signal intensity on the angle between the two gradients ψ for arbitrary parameters of the double-PGSE when the long diffusion wavelength condition $(\gamma\delta Ga)^2 \ll 1$ is met.

Analytical Model We propose an analytical water diffusion model aimed at estimating microstructural properties without prior knowledge of axon orientation, using angular double-PGSE based on [22]. The model analyzes the MR signal we obtain in double-PGSE experiments given the two-compartment geometric model described earlier. The intra-axonal compartment in the model exhibits restricted diffusion, while the extra-axonal compartment exhibits hindered diffusion. We model the combined normalized MR signal attenuation from these two compartments as:

$$E = (1 - f)E_e + fE_i \quad (1)$$

where E_e and E_i are the normalized MR signal attenuation in the extra- and intra-axonal compartments respectively, and f is the volume fraction of the intra-axonal compartment, reflecting axon packing density.

We model the normalized MR signal attenuation in the extra-axonal compartment with Gaussian diffusion distribution:

$$E_e = e^{-\gamma^2\delta^2 D_e (G_1^2 + G_2^2) (\Delta - \frac{\delta}{3})} \quad (2)$$

Here, we assume that the two encoding intervals of gradients G_1 and G_2 have the same pulse duration ($\delta_1 = \delta_2 = \delta$) and diffusion time ($\Delta_1 = \Delta_2 = \Delta$).

We further decompose the normalized MR signal attenuation in the intra-axonal compartment into two components: parallel ($E_{i//}$) and perpendicular ($E_{i\perp}$) to the axon orientation. Thus the combined MR signal attenuation in the intra-axonal compartment E_i is:

$$E_i = E_{i//} \times E_{i\perp} \quad (3)$$

By discretization of the gradient waveform, we can approximate it by a train of impulses using a series of propagators and derive:

$$E_{i//} = e^{-\gamma^2\delta^2 D_i (G_1^2 \cos^2 \beta_1 + G_2^2 \cos^2 \beta_2) (\Delta - \frac{\delta}{3})} \quad (4)$$

$$E_{i\perp} = C + A(G_1^2 \cos^2 \beta_1 + G_2^2 \cos^2 \beta_2) - B(G_1 G_2 \cos \beta_1 \cos \beta_2) \quad (5)$$

where,

$$C = 1 - A(G_1^2 + G_2^2) - B(G_1 G_2 \cos \psi) \quad (6)$$

$$A = 2\gamma^2 a^2 \sum_{n=1}^{\infty} S_n \left[\frac{2\delta}{\omega_n} - \frac{1}{\omega_n^2} (2 - 2e^{-\omega_n \delta} + e^{-\omega_n (\Delta - \delta)} - 2e^{-\omega_n \Delta} + e^{-\omega_n (\Delta + \delta)}) \right] \quad (7)$$

$$B = 2\gamma^2 a^2 \sum_{n=1}^{\infty} \frac{S_n}{\omega_n^2} \left[e^{-\omega_n (t_m - \delta)} - 2e^{-\omega_n t_m} + e^{-\omega_n (t_m + \delta)} - 2e^{-\omega_n (\Delta + t_m - \delta)} + 4e^{-\omega_n (\Delta + t_m)} - 2e^{-\omega_n (\Delta + t_m + \delta)} + e^{-\omega_n (2\Delta + t_m - \delta)} - 2e^{-\omega_n (2\Delta + t_m)} + e^{-\omega_n (2\Delta + t_m + \delta)} \right] \quad (8)$$

We define:

- $s_n = \frac{1}{\alpha_n^4 - \alpha_n^2}$; $w_n = \frac{\alpha_n^2 D_i}{a^2}$; α_n are the roots of the derivatives of the first-order Bessel functions satisfying the boundary condition: $J_1'(\alpha_n) = 0$
- $\cos \beta_1 = \mathbf{u} \cdot \mathbf{G}_1$ and $\cos \beta_2 = \mathbf{u} \cdot \mathbf{G}_2$, where $\mathbf{u} = (1, \theta, \phi)$ is the unit vector that defines the arbitrary orientation of the axon in polar coordinates (θ is the polar angle measured from the Z axis, and ϕ is the azimuth angle measured on the XOY plane from the X axis in the counter clockwise direction). β_1 and β_2 denote the angles between G_1, G_2 and \mathbf{u} respectively. (Fig. 1b)

The experimental parameters must satisfy two conditions:

- The long diffusion wavelength condition: $(\gamma \delta G a)^2 \ll 1$.
- The diffusion time condition: $\Delta > \frac{a^2}{2D_i}$, diffusion periods must be long enough for spins to probe the boundary and experience restricted diffusion.

The axon parameters we aim to extract from the model are:

- a , the axon radius
- $\mathbf{u} = (1, \theta, \phi)$, the axon orientation
- $f \in (0, 1)$, the volume fraction of the intra-axonal compartment
- D_i and D_e , the diffusivity of the intra- and extra-axonal compartments

2.2 Axon Parameter Estimation Procedure

Experimental Setup In order to estimate the underlying microstructural properties and validate our analytical model, we performed several simulation experiments. The benefit of using simulation data is that the ground truth about the microstructural properties is known and controllable. Figure 1a illustrates the double-PGSE sequence used in our experiment: the experimental parameters of this acquisition sequence were described in section 2.1. We assume an unknown arbitrary orientation vector $\mathbf{u} = (1, \theta, \phi)$ for the axon (Fig. 1b). The first gradient pair \mathbf{G}_1 is aligned on the x-axis and we varied the second gradient pair \mathbf{G}_2 in the XOY plane by changing the angle ψ between \mathbf{G}_1 and \mathbf{G}_2 and keeping their magnitude constant. In this setup, we can evaluate $\cos \beta_1 = \sin \theta \cos \phi$ and $\cos \beta_2 = \sin \theta \cos(\phi - \psi)$.

Simulation Data Our simulation data for double-PGSE experiments was derived from Monte Carlo simulation for 100,000 spins in our geometric model (section 2.1) using Camino [24, 25]. The double-PGSE sequence is simulated directly over the diffusive dynamics using a variety of scan parameters. These experiments were repeated with five different axon radii $a = (1, 2, 3, 4, 5)\mu\text{m}$ with the following axon parameters (which we later try to recover): axon orientation $\mathbf{u} = (1, 30^\circ, 60^\circ) = (1, \frac{\pi}{6}, \frac{\pi}{3})$; intra-axonal volume fraction $f = 0.7$; and the diffusivity of the intra- and extra-axonal compartments, assumed to be the same, $D_i = D_e = 2e^{-9}m^2/s$. Data were collected for three different q -values with experimental parameters: q_{max} of $25553m^{-1}$, pulse duration $\delta = 1.5ms$; diffusion time $\Delta = 40ms$; diffusion gradients $G_{1max} = G_{2max} = 0.4T/m$; mixing time $t_m = 5ms$; ψ varied in 10° increments; and SNR set to 40.

Parameter Estimation We used Bayesian inference using Markov Chain Monte Carlo (MCMC) to get samples of the posterior distribution of the axon parameters given the simulation data and experimental parameters. The estimation procedure was implemented in MATLAB® (R2009a, The MathWorks, Natick, MA) and openBUGS [28]

on Linux operating system. Our likelihood were Gaussian distribution with standard deviations chosen with respect to the difference between model and experimental data. We used uninformative gamma prior for a , beta prior for f , and broad uniform priors for all the other axon model parameters. We ran MCMC for 1 million iterations with 10 sets of initial values for various parameters to ensure convergence (burn-in period = 900,000 iterations). We gathered 100,000 independent samples from the marginal posterior distribution of the model parameters as our estimates.

3 Results

Figure 3 demonstrates the accuracy of the analytical model and shows that the predicted signals from our model match the physical simulation data well in our experimental setting. Note that (Fig. 3b) the maximum signal intensity is observed when G_2 is perpendicular to the axon ($\beta_2 = 90^\circ$), as expected [22], while holding G_1 fixed on the x-axis.

Table 1 and Fig. 4 show our main results. Table 1 summarizes our estimated *mean* and standard deviation (*std*) values for axon radius a , orientation θ and ϕ , intra-axonal volume fraction f , and diffusivity D . The *mean* and *std* were calculated by averaging 100,000 samples drawn from the marginal posterior distribution of Markov Chain Monte Carlo (MCMC) (section 2.2). Figure 4 shows the histogram of axon parameter estimate packing density: a, θ, ϕ, f, D for each of the various true $a = (1, 2, 3, 4, 5)\mu m$ using MCMC. For comparison, in Fig. 4(b-e), the orange vertical lines in the graph show the true values of the corresponding axon parameters from simulation data.

We observed a slight underestimation for axons whose radius less than $3\mu m$, $a = (1, 2)\mu m$; this was also observed in [20, 21] when the SGP limits were not met using Mitra's theory [19]. It is important, however, to note that these two small axon radii recovered were still distinguishable regardless of the underestimation. We were able to

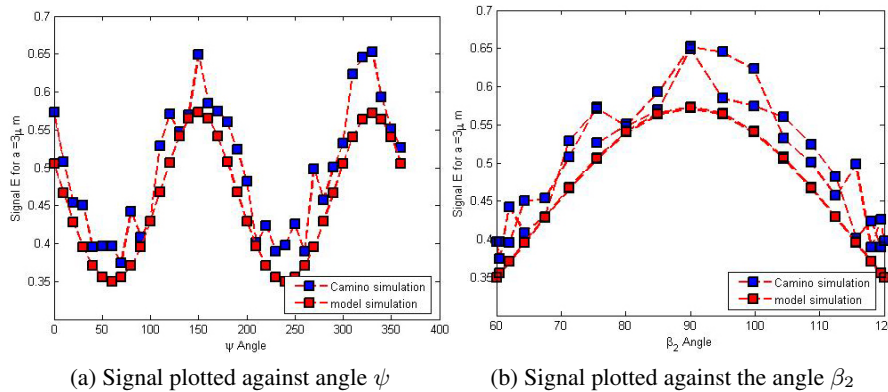


Fig. 3: Signal predicted by our model compared with Camino simulation data [29]. (a) Signal plotted against angle ψ between G_1 and G_2 . Angle ψ ranged from $0 - 360^\circ$ with 10° increments. (b) Signal plotted against the angle β_2 between G_2 and axon orientation u . Angle β_2 had two repeated cycles ranged from $60 - 120^\circ$. In this data, axon radius $a = 3\mu m$, experimental parameters were: $G = 0.4T/m$, $\delta = 1.5ms$, $\Delta = 40ms$, $t_m = 5ms$, SNR = 40.

recover axon radii $a = (3, 4, 5)\mu m$ with high accuracy and averaged $std = 0.0747$. As shown in table 1, the estimated values for θ , ϕ , f and D were in close agreement with their true value with $std = (0.0039, 0.0081, 0.0059, 0.0293)$ respectively. Overall, our estimation results demonstrated the feasibility of recovering axon radii in the typical human brain tissue range without prior knowledge of axon orientation.

Axon radius (μm)		Axon Orientation (rad)		Volume Fraction	Diffusivity $1e^{-9}(m^2/s)$
Ground truth	Estimate	$\theta = 0.5236 = 30^\circ$	$\phi = 1.0472 = 60^\circ$	$f = 0.7$	$D = 2$
1	0.754 ± 0.084	0.507 ± 0.005	1.068 ± 0.005	0.716 ± 0.004	2.170 ± 0.013
2	1.757 ± 0.082	0.512 ± 0.005	1.037 ± 0.013	0.724 ± 0.007	2.074 ± 0.027
3	2.943 ± 0.107	0.519 ± 0.004	1.087 ± 0.013	0.705 ± 0.002	2.115 ± 0.037
4	3.983 ± 0.067	0.493 ± 0.003	1.039 ± 0.005	0.838 ± 0.007	2.071 ± 0.049
5	5.004 ± 0.049	0.490 ± 0.002	1.013 ± 0.003	0.741 ± 0.008	1.945 ± 0.019

Table 1: Summary of estimated mean values of axon parameters from the model. Ground truth from simulation are: (a) Axon radii $a = (1, 2, 3, 4, 5)\mu m$; (b) Axon orientation; $\mathbf{u} = (1, 30^\circ, 60^\circ) = (1, \frac{\pi}{6}, \frac{\pi}{3})$; (c) Intra-axonal volume fraction $f = 0.7$; (d) Diffusivity $D = 2e^{-9}m^2/s$.

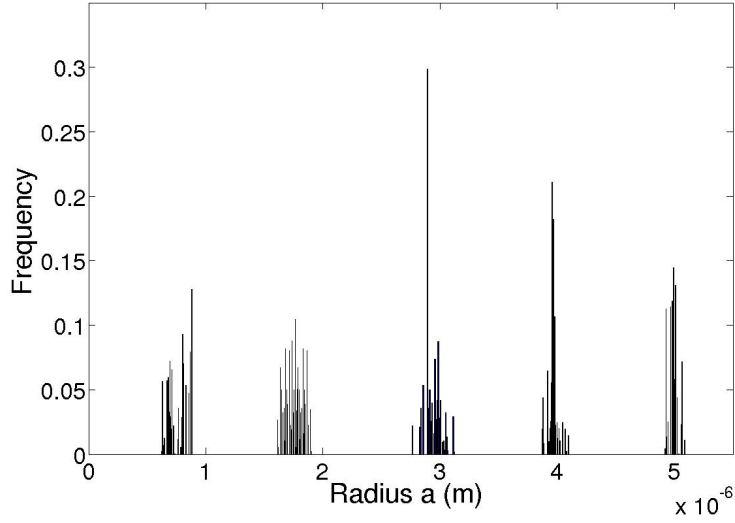
4 Discussions

We currently run Markov Chain Monte Carlo (MCMC) sampling algorithm for 1 million iterations in order to ensure convergence for all initial values tested for each axon parameter. We could speed up MCMC chain convergence if we initialize the parameters to the true values of the simulation. We chose a longer MCMC chain to ensure convergence when we draw the last 100,000 samples of the posterior distribution regardless of the initial value, since the true parameter values are uncertain for complex white matter structures in clinical cases.

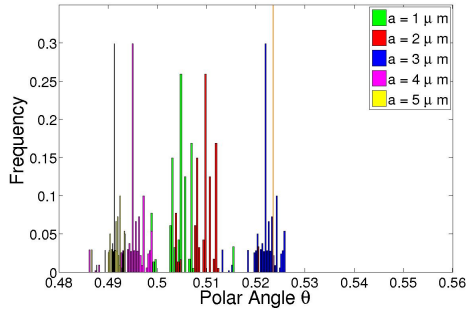
The simulation data presented in this paper uses a small pulse duration of 1.5ms to ensure that the long diffusion wavelength condition $(\gamma\delta Ga)^2 \ll 1$ is satisfied. Also, we used a maximum gradient of $G_{max} = 400mT/m$ in this simulation in order to obtain data with higher angular resolution and signal to noise ratio. In fact, preliminary experiments (data not shown) suggest the feasibility of axon property recovery at a much lower gradient of $G_{max} = 70mT/m$ and longer diffusion pulse duration of 10 – 15ms, which are commonly achievable on clinical scanners.

The intra-axonal volume fraction we estimate from the model is an important parameter relative to axon packing density. However, it may not directly reflect the volume fraction of the axons since only relative fractions of the axon compartment are weighted by MRI T1 and T2 relaxation [16].

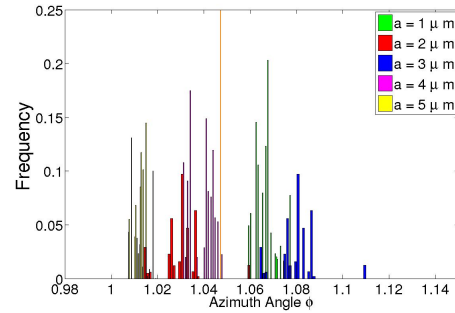
The axon orientation in our model is assumed to be arbitrarily unknown but uniform based on the parallel fibers observed in the midsection of the corpus callosum. It would be interesting to look into cases of fiber crossing and kissing using spherical harmonics decomposition. In future work, we will extend our model to account for non-uniform axon caliber distribution using gamma distribution, as it has been observed in electron microscopy images. Although simple models like the diffusion tensor could describe the general axon orientation, such a model can not be used to estimate important microstructural properties such as axon radius and intra-axonal volume fraction, as the model does not encode restricted diffusion information.



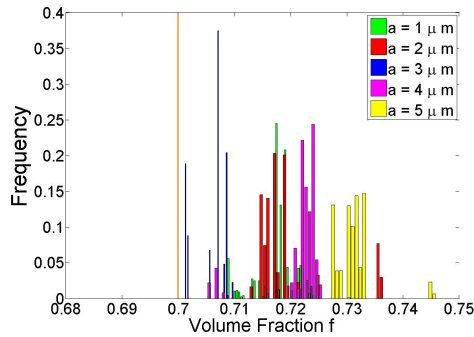
(a) Axon radius $a = (1, 2, 3, 4, 5)\mu m$



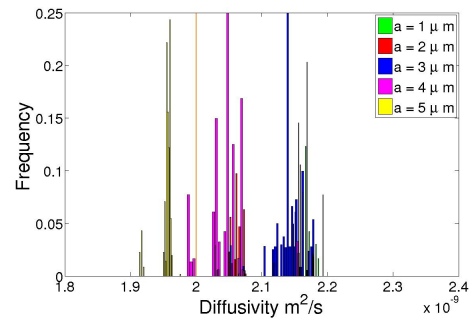
(b) Axon Polar Angle $\theta = 0.5236rad$



(c) Axon Azimuth Angle $\phi = 1.0472rad$



(d) Intra-axonal volume Fraction $f = 0.7$



(e) Diffusivity $D = 2e^{-9}m^2/s$

Fig. 4: Histograms of 100,000 samples drawn from posterior distributions on (a) axon radius a ; (b-c) axon orientation (θ and ϕ); (d) intra-axonal volume fraction $f = 0.7$; and (e) diffusivity D for each of the various true a values using Markov Chain Monte Carlo (MCMC). Orange vertical lines show the true values in simulation: $a = (1, 2, 3, 4, 5)\mu m$, $\theta = \frac{\pi}{6}rad = 30^\circ$, $\phi = \frac{\pi}{3}rad = 60^\circ$, $f = 0.7$, $D = 2e^{-9}m^2/s$. The *mean* and *std* values of parameter estimates are shown in table 1. Note that some overlapping bars may not be visible in the figure.

5 Conclusions

We have demonstrated, for the first time without prior knowledge of the axon orientation using low- q angular double-PGSE experiments, the feasibility of estimating axon radii of the typical human brain tissue range (1 to $5\mu m$); other important underlying microstructural properties such as axon packing density and diffusivity can be extracted from the analytical model as well. Although many angles are required to achieve high angular double-PGSE resolution, these can be collected in considerably less time than multiple high- q single-PGSE experiments using the current hardware [23]. We conclude that modeling microstructural properties using double-PGSE acquisition may be advantageous in extracting underlying microstructural properties as it requires lower q -values and has an inherently higher signal-to-noise ratio (SNR).

Acknowledgments

This work has been supported in part by NIH grant 1R01EB00415501A1 and the Reisman Fellowship of the Brown Institute for Brain Sciences. Matt G. Hall is supported by EPSRC grant EP/E06490/1. The simulation code used is available as part of Camino <http://www.camino.org.uk>.

References

1. Pierpaoli, C., Basser, P.: Toward a quantitative assessment of diffusion anisotropy. *Magnetic Resonance in Medicine* **36**(6) (1996) 893–906
2. Westin, C., Maier, S., Mamata, H., Nabavi, A., Jolesz, F., Kikinis, R.: Processing and visualization for diffusion tensor MRI. *Medical Image Analysis* **6**(2) (2002) 93–108
3. Assaf, Y., Cohen, Y.: Inferring Microstructural Information of White Matter from Diffusion MRI. *Diffusion MRI: From Quantitative Measurement to In-vivo Neuroanatomy* (2009) 127
4. Lovas, G., Szilagyi, N., Majtenyi, K., Palkovits, M., Komoly, S.: Axonal changes in chronic demyelinated cervical spinal cord plaques. *Brain* **123**(2) (2000) 308
5. Kure, K., Weidenheim, K., Lyman, W., Dickson, D.: Morphology and distribution of HIV-1 gp41-positive microglia in subacute AIDS encephalitis. *Acta Neuropathologica* **80**(4) (1990) 393–400
6. Evangelou, N., Konz, D., Esiri, M., Smith, S., Palace, J., Matthews, P.: Regional axonal loss in the corpus callosum correlates with cerebral white matter lesion volume and distribution in multiple sclerosis. *Brain* **123**(9) (2000) 1845
7. Ganter, P., Prince, C., Esiri, M.: Spinal cord axonal loss in multiple sclerosis: a post-mortem study. *Neuropathology and Applied Neurobiology* **25**(6) (1999) 459–467
8. Bjartmar, C., Kinkel, R., Kidd, G., Rudick, R., Trapp, B.: Axonal loss in normal-appearing white matter in a patient with acute MS. *Neurology* **57**(7) (2001) 1248
9. Avram, L., Assaf, Y., Cohen, Y.: The effect of rotational angle and experimental parameters on the diffraction patterns and micro-structural information obtained from q -space diffusion NMR: implication for diffusion in white matter fibers. *Journal of Magnetic Resonance* **169**(1) (2004) 30–38
10. Weng, J., Chen, J., Kuo, L., Wedeen, V., Tseng, W.: Maturation-dependent microstructure length scale in the corpus callosum of fixed rat brains by magnetic resonance diffusion-diffraction. *Magnetic resonance imaging* **25**(1) (2007) 78–86
11. Lätt, J., Nilsson, M., Malmberg, C., Rosquist, H., Wirestam, R., Stahlberg, F., Topgaard, D., Brockstedt, S.: Accuracy of q -space related parameters in MRI: simulations and phantom measurements. *IEEE Transactions on Medical Imaging* **26**(11) (2007) 1437
12. Edgar, J., Griffiths, I.: White Matter Structure: A Microscopists View. *Diffusion MRI: From Quantitative Measurement to In-vivo Neuroanatomy* (2009) 75
13. Alexander, D.: A general framework for experiment design in diffusion MRI and its application in measuring direct tissue-microstructure features. *Magnetic Resonance in Medicine* **60**(2) (2008) 439–448

14. Assaf, Y., Freidlin, R., Rohde, G., Basser, P.: New modeling and experimental framework to characterize hindered and restricted water diffusion in brain white matter. *Magnetic Resonance in Medicine* **52**(5) (2004) 965–978
15. Assaf, Y., Blumenfeld-Katzir, T., Yovel, Y., Basser, P.: AxCaliber: a method for measuring axon diameter distribution from diffusion MRI. *Magnetic Resonance in Medicine* **59**(6) (2008)
16. Barazany, D., Basser, P.J., Assaf, Y.: In vivo measurement of axon diameter distribution in the corpus callosum of rat brain. *Brain* **132** (2009) 1210–1220
17. Cory, D.G.: Applications of spin transport as a probe of local geometry. *Polym. Preprints* **31** **149** (1990)
18. Reese, T., Heid, O., Weisskoff, R., Wedeen, V.: Reduction of eddy-current-induced distortion in diffusion MRI using a twice-refocused spin echo. *Magnetic Resonance in Medicine* **49**(1) (2003) 177–182
19. Mitra, P.: Multiple wave-vector extensions of the NMR pulsed-field-gradient spin-echo diffusion measurement. *Physical Review B* **51**(21) (1995) 15074–15078
20. Koch, M., Finsterbusch, J.: Compartment size estimation with double wave vector diffusion-weighted imaging. *Magnetic Resonance in Medicine* **60**(1) (2008) 90–101
21. Koch, M., Finsterbusch, J.: Numerical simulation of double-wave vector experiments investigating diffusion in randomly oriented ellipsoidal pores. *Magnetic resonance in medicine: official journal of the Society of Magnetic Resonance in Medicine/Society of Magnetic Resonance in Medicine* (2009)
22. Özarlan, E., Basser, P.: Microscopic anisotropy revealed by NMR double pulsed field gradient experiments with arbitrary timing parameters. *The Journal of Chemical Physics* **128** (2008) 154511
23. Shemesh, N., Özarlan, E., Basser, P., Cohen, Y.: Measuring small compartmental dimensions with low-q angular double-PGSE NMR: The effect of experimental parameters on signal decay. *Journal of Magnetic Resonance* **198**(1) (2009) 15–23
24. Cook, P., Bai, Y., Nedjati-Gilani, S., Seunarine, K., Hall, M., Parker, G., Alexander, D.: Camino: open-source diffusion-MRI reconstruction and processing. In: 14th Scientific Meeting of the International Society for Magnetic Resonance in Medicine. (2006) 2759
25. Hall, M., Alexander, D.: Finite pulse widths improve fibre orientation estimates in diffusion tensor MRI. In: *Proc. Intl. Soc. Mag. Reson. Med.* Volume 14. (2006) 1076
26. Özarlan, E., Basser, P.: MR diffusion–diffraction phenomenon in multi-pulse-field-gradient experiments. *Journal of Magnetic Resonance* **188**(2) (2007) 285–294
27. Callaghan, P., Coy, A., MacGowan, D., Packer, K., Zelaya, F.: Diffraction-like effects in NMR diffusion studies of fluids in porous solids (1991)
28. Lunn, D., Spiegelhalter, D., Thomas, A., Best, N.: The BUGS project: Evolution, critique and future directions. *Statistics in medicine* **28**(25) (2009) 3049–3067
29. Hall, M., Alexander, D.: Convergence and Parameter Choice for Monte-Carlo Simulations for Diffusion MRI. *IEEE transactions on medical imaging* (2009)

Oral Session II: Group Analysis and
Applications of Diffusion MRI

Procrustes Analysis for Diffusion Tensor Imaging

Diwei Zhou¹, Ian Dryden², Alexey Koloydenko³, and Li Bai⁴

¹ School of Technology, University of Wolverhampton, UK
D.Zhou@wlv.ac.uk

² School of Mathematical Sciences, University of Nottingham, UK

³ Mathematics Department, Royal Holloway, University of London, UK

⁴ School of Computer Sciences, University of Nottingham, UK

Abstract. There is an increasing need to develop processing tools for diffusion tensor image data with the consideration of the non-Euclidean nature of the tensor space. In this paper Procrustes analysis, a non-Euclidean shape analysis tool under similarity transformations (rotation, scaling and translation), is proposed to redefine sample statistics of diffusion tensors. A new anisotropy measure Procrustes Anisotropy (PA) is defined with the full ordinary Procrustes analysis. Comparisons are made with other anisotropy measures including Fractional Anisotropy and Geodesic Anisotropy. The partial generalized Procrustes analysis is extended to a weighted generalized Procrustes framework for averaging sample tensors with different fractions of contributions to the mean tensor. Applications of Procrustes methods to diffusion tensor interpolation and smoothing are compared with Euclidean, Log-Euclidean and Riemannian methods.

Keywords: Non-Euclidean metrics, Procrustes analysis, interpolation, smoothing, anisotropy measure

1 Introduction

Diffusion tensor imaging (DTI) is an advance non-invasive method for providing a unique insight into tissue structure and organization in vivo. In DTI, displacement of water molecules over time is modeled by a zero-mean trivariate Gaussian distribution [1] with covariance matrix evolving linearly with time and determined by the diffusion tensor (DT), a 3x3 symmetric positive-definite matrix. DT inference from observed diffusion MRI data has been commonly carried out using least squares [2][3] and Bayesian [4][5] methods. At each location (voxel) of interest, the principal eigenvector of the tensor estimates the dominant fibre orientation whereas various tensor-derived diffusion anisotropy indices measure local anisotropy. DTI has been applied into the study of diseases such as multiple sclerosis, schizophrenia, and stroke [6]. White matter tractography [7][8][9] is another promising application of DTI for investigating brain connectivity.

However, the estimation of diffusion tensor is noise-sensitive due to artifacts and limitations resulting from DTI measurements [10]. There is an increasing need to develop processing tools for diffusion tensor data. With the consideration

of positive semi-definiteness and symmetry of diffusion tensor, non-Euclidean methods [11][12][13][14][15] have been proposed for diffusion tensor processing and anisotropy study.

Recall that \mathbf{D} is a 3×3 real matrix with symmetric positive semi-definiteness, i.e. $\mathbf{D} = \mathbf{D}^T$ and $\mathbf{x}\mathbf{D}\mathbf{x}^T \geq 0$ for all $\mathbf{x} \in \mathbb{R}^3$. Let $f(\mathbf{D})$ be a probability density function of a diffusion tensor \mathbf{D} on a Riemannian metric space. The Fréchet mean [15][16][17] of \mathbf{D} is defined as

$$\mathbf{T} = \arg \inf_{\mathbf{T}} \frac{1}{2} \int d(\mathbf{D}, \mathbf{T})^2 f(\mathbf{D}) d\mathbf{D}, \quad (1)$$

where d is a metric. A Fréchet mean is not necessarily unique. However, it is possible to prove the uniqueness with sufficient conditions. For example, for non-Euclidean spaces with negative sectional curvature, the Fréchet mean is always unique [18].

Now we consider a sample of N diffusion tensors $\mathbf{D}_1, \dots, \mathbf{D}_N$. The Fréchet mean of $\mathbf{D}_1, \dots, \mathbf{D}_N$ is given by

$$\hat{\mathbf{T}} = \arg \inf_{\mathbf{T}} \sum_{i=1}^N d(\mathbf{D}_i, \mathbf{T})^2. \quad (2)$$

And the *sample variance* of $\mathbf{D}_1, \dots, \mathbf{D}_N$ is defined as

$$\sigma_{\mathbf{D}_1, \dots, \mathbf{D}_N}^2 = \frac{1}{N} \sum_{i=1}^N d(\mathbf{D}_i, \hat{\mathbf{T}})^2. \quad (3)$$

The Euclidean [19], Log-Euclidean [20] and Riemannian [15][21] metrics, denoted by d_E , d_L and d_R respectively, have been proposed for defining the sample mean of diffusion tensors.

The motivation for the work is to define new statistics of diffusion tensor sample with the non-Euclidean method Procrustes analysis for tensor field processing and anisotropy study.

2 Procrustes Estimators of Mean Tensor

In this section, we will define the mean diffusion tensor given a sample of tensors using Procrustes analysis.

2.1 Full ordinary Procrustes analysis

Full ordinary Procrustes analysis (FOPA)[22][23] is used to match two objects as closely as possible with similarity transformations (translation, rotation and scale). Let us first consider a pair of diffusion tensors \mathbf{D}_1 and \mathbf{D}_2 . To ensure the positive semi-definiteness of \mathbf{D}_i , $i = 1, 2$, we use a reparameterization $\mathbf{D}_i = \mathbf{Q}_i \mathbf{Q}_i^T$, where \mathbf{Q}_i is a 3×3 real matrix. For example, $\mathbf{Q}_i = \text{chol}(\mathbf{D}_i)$ is the

Cholesky decomposition, or $\mathbf{Q}_i = \mathbf{D}_i^{1/2}$ is the matrix square root. In our computation we shall choose the Cholesky decomposition. Note that \mathbf{Q}_i and any rotation of it $\mathbf{Q}_i\mathbf{R}$ ($\mathbf{R} \in O(3)$) result in the same \mathbf{D}_i , i.e. $\mathbf{D}_i = \mathbf{Q}_i\mathbf{Q}_i^T = \mathbf{Q}_i\mathbf{R}(\mathbf{Q}_i\mathbf{R})^T$.

The objective of FOPA is to minimize $S_{FOPA}(\mathbf{D}_1, \mathbf{D}_2)^2$ in (4) the squared Euclidean distance between \mathbf{D}_1 and \mathbf{D}_2 under the similarity transformations. The squared Euclidean distance is given by

$$S_{FOPA}(\mathbf{D}_1, \mathbf{D}_2)^2 = \| \mathbf{Q}_1 - \beta\mathbf{Q}_2\mathbf{R} - \mathbf{1}_3\boldsymbol{\gamma}^T \|^2, \quad (4)$$

where a 3×3 rotation matrix $\mathbf{R} \in O(3)$, a scale parameter $\beta > 0$, and a 3×1 location vector $\boldsymbol{\gamma}$ represent three similarity transformations. Note $\mathbf{1}_3$ is the 3×1 vector of ones.

The solution $(\hat{\boldsymbol{\gamma}}, \hat{\beta}, \hat{\mathbf{R}})$ to the minimization of Equation (4) is given by [22]

$$\hat{\boldsymbol{\gamma}} = \mathbf{0}_3 \quad (5)$$

where $\mathbf{0}_3$ is the 3×1 vector of zeros,

$$\hat{\mathbf{R}} = \mathbf{U}\mathbf{V}^T, \quad (6)$$

where $\mathbf{U}, \mathbf{V} \in O(3)$ are obtained from a singular value decomposition:

$$\mathbf{Q}_1^T\mathbf{Q}_2 = \mathbf{V}\boldsymbol{\Delta}\mathbf{U}^T, \quad (7)$$

with $\boldsymbol{\Delta}$ a diagonal 3×3 matrix of singular values. Furthermore,

$$\hat{\beta} = \frac{\text{trace}(\mathbf{Q}_1^T\mathbf{Q}_2\hat{\mathbf{R}})}{\text{trace}(\mathbf{Q}_2^T\mathbf{Q}_2)}. \quad (8)$$

The full Procrustes shape metric between \mathbf{D}_1 and \mathbf{D}_2 is given by

$$\begin{aligned} d_F(\mathbf{D}_1, \mathbf{D}_2) &= \inf_{\mathbf{R} \in O(3), \beta \in \mathbb{R}} \| \mathbf{Q}_1 - \beta\mathbf{Q}_2\mathbf{R} \| \\ &= \| \mathbf{Q}_1 - \hat{\beta}\mathbf{Q}_2\hat{\mathbf{R}} \| \end{aligned} \quad (9)$$

2.2 Procrustes size-and-shape distance

In DTI study, we wish to match \mathbf{Q}_1 (from \mathbf{D}_1) and \mathbf{Q}_2 (from \mathbf{D}_2) under location, rotation and reflection while often preserving scale information. Then the joint study of size-and-shape is of interest. Size-and-shape spaces were introduced by [24]. The definition of the size-and-shape of a configuration matrix was given by [22].

The Procrustes size-and-shape distance between two diffusion tensors is defined as

$$d_S(\mathbf{D}_1, \mathbf{D}_2) = \inf_{\mathbf{R} \in O(3)} \| \mathbf{Q}_1 - \mathbf{Q}_2\mathbf{R} \|. \quad (10)$$

The Procrustes solution $\hat{\mathbf{R}}$ for matching \mathbf{Q}_1 to \mathbf{Q}_2 is

$$\begin{aligned} \hat{\mathbf{R}} &= \arg \inf_{\mathbf{R} \in O(3)} \| \mathbf{Q}_1 - \mathbf{Q}_2\mathbf{R} \| \\ &= \mathbf{U}\mathbf{V}^T \end{aligned} \quad (11)$$

where \mathbf{U} and \mathbf{V} are from the singular value decomposition in Equation (7).

2.3 Procrustes estimators

Consider the general case where there are $N \geq 2$ diffusion tensors $\mathbf{D}_1, \dots, \mathbf{D}_N$, and $\mathbf{D}_i = \mathbf{Q}_i \mathbf{Q}_i^T$, $i = 1, \dots, N$. Now the aim is to calculate the Fréchet mean using the full Procrustes shape metric in Equation (9) and the Procrustes size-and-shape metric in Equation (10).

The sample Fréchet mean relative to the full Procrustes shape metric $d_F(\cdot)$ is given by

$$\hat{\mathbf{T}}_F = \hat{\mathbf{Q}}_F \hat{\mathbf{Q}}_F^T, \quad (12)$$

where

$$\hat{\mathbf{Q}}_F = \arg \inf_{\mathbf{Q}} \sum_{i=1}^N \inf_{\mathbf{R}_i \in O(k)} \|\beta_i \mathbf{Q}_i \mathbf{R}_i - \mathbf{Q}\|^2. \quad (13)$$

The sample Fréchet mean relative to the Procrustes size-and-shape distance $d_S(\cdot)$ is given by

$$\hat{\mathbf{T}}_S = \arg \inf_{\mathbf{T}} \sum_{i=1}^N d(\mathbf{D}_i, \mathbf{T})^2. \quad (14)$$

where $d(\cdot)$ can be $d_F(\cdot)$ or $d_S(\cdot)$. Specifically,

$$\hat{\mathbf{T}}_S = \hat{\mathbf{Q}}_S \hat{\mathbf{Q}}_S^T, \quad (15)$$

where

$$\hat{\mathbf{Q}}_S = \arg \inf_{\mathbf{\Delta}} \sum_{i=1}^N \inf_{\mathbf{R}_i \in O(k)} \|\mathbf{Q}_i \mathbf{R}_i - \mathbf{\Delta}\|^2. \quad (16)$$

2.4 Procrustes anisotropy

We define a new anisotropy measure Procrustes anisotropy (PA) with the full Procrustes shape metric. The definition of PA is given by

$$\begin{aligned} PA(\mathbf{D}) &= \sqrt{\frac{3}{2}} d_F\left(\frac{\mathbf{I}_{3 \times 3}}{\sqrt{3}}, \mathbf{D}\right) \\ &= \sqrt{\frac{3}{2} \sum_{i=1}^3 (\sqrt{\lambda_i} - \sqrt{\bar{\lambda}})^2 / \sum_{i=1}^3 \lambda_i} \end{aligned} \quad (17)$$

where $\sqrt{\bar{\lambda}} = \sum_{i=1}^3 \sqrt{\lambda_i} / 3$. It is clear that PA is a normalization of the FOPA distance from any given diffusion tensor \mathbf{D} to the identity tensor, representing the case of ideal isotropy. The range of PA is $[0, 1]$ with PA = 0 indicating full isotropy and PA ≈ 1 representing the extremely strong anisotropy. PA is invariant to the uniform scaling of a diffusion tensor.

3 Generalized Procrustes Methods

Diffusion MRI has become an established technique for health care and neuroscience. However, it still suffers from some limitations and artifacts, especially in terms of eddy currents and sensitivity to motion [10]. It is therefore important to process the diffusion tensor data that can capture and resample important diffusion information in the data while leaving out the noise. In this section, diffusion tensor processing methods including smoothing and interpolation are developed with consideration of contributions from more than two neighbouring tensors.

3.1 Partial generalized Procrustes analysis with rotations

Consider the general case that there are $N \geq 2$ diffusion tensors $\mathbf{D}_1, \dots, \mathbf{D}_N$, and $\mathbf{D}_i = \mathbf{Q}_i \mathbf{Q}_i^T$, $i = 1, \dots, N$. Consider the partial generalized Procrustes analysis (PGPA) [22] which minimizes the total sum $S_{PGPA}(\mathbf{D}_1, \dots, \mathbf{D}_N)$ of the squared Euclidean distances between all pairs $\mathbf{Q}_i \mathbf{R}_i$ and $\mathbf{Q}_j \mathbf{R}_j$ over the orthogonal transformations $\mathbf{R}_1, \mathbf{R}_2, \dots, \mathbf{R}_N \in O(3)$. The minimization of the sum of squares is given by

$$\begin{aligned} S_{PGPA}(\mathbf{D}_1, \dots, \mathbf{D}_N) &= \inf_{\mathbf{R}_1, \dots, \mathbf{R}_N} \frac{1}{N} \sum_{i=1}^{N-1} \sum_{j=i+1}^N \|\mathbf{Q}_i \mathbf{R}_i - \mathbf{Q}_j \mathbf{R}_j\|^2 \\ &= \inf_{\mathbf{R}_1, \dots, \mathbf{R}_N} \sum_{i=1}^N \|\mathbf{Q}_i \mathbf{R}_i - \frac{1}{N} \sum_{j=1}^N \mathbf{Q}_j \mathbf{R}_j\|^2. \end{aligned} \quad (18)$$

Let $\hat{\mathbf{R}}_i$, $i = 1, \dots, N$ be the estimates of rotations which minimizing Equation (18). The Generalized Procrustes Algorithm has been described by [23] and [22].

Hence, the Fréchet mean of $\mathbf{D}_1, \dots, \mathbf{D}_N$ with generalized Procrustes analysis is given by

$$\hat{\mathbf{T}}_{PGPA} = \hat{\mathbf{Q}}_{PGPA} \hat{\mathbf{Q}}_{PGPA}^T, \quad (19)$$

where

$$\hat{\mathbf{Q}}_{PGPA} = \frac{1}{N} \sum_{i=1}^N \mathbf{Q} \hat{\mathbf{R}}_i. \quad (20)$$

3.2 Weighted generalized Procrustes method

For processing a sample of diffusion tensors at voxels distributed in three-dimensional space, a more general case appears that the contributions from $\mathbf{D}_1, \dots, \mathbf{D}_N$ are different to the mean diffusion tensor. Therefore, we need to consider a weighted problem to obtain the weighted mean diffusion tensor.

Given a suitable distance function d , the weighted Fréchet sample mean of $\mathbf{D}_1, \dots, \mathbf{D}_N$ is defined by:

$$\mathbf{T} = \arg \inf_{\mathbf{D}} \sum_{i=1}^N w_i d(\mathbf{D}_i, \mathbf{D})^2, \quad (21)$$

where the weights w_i satisfy $w_i \geq 0$ and $\sum_{i=1}^N w_i = 1$, and in applications can be, for example, a function of the Euclidean distance from the location of interest to the sampling locations (e.g., voxels).

Weighted generalized Procrustes analysis (WGPA) is proposed to estimate $\hat{\mathbf{T}}$ when $d = d_S$ is the size-and-shape distance [14]. It can then be shown that the *WGPA mean tensor* is given by

$$\hat{\mathbf{T}}_{WGPA} = \hat{\mathbf{Q}}_{WGPA} \hat{\mathbf{Q}}_{WGPA}^T, \quad (22)$$

where $\hat{\mathbf{Q}}_{WGPA} = \sum_{i=1}^N w_i \mathbf{Q}_i \hat{\mathbf{R}}_i$ and the orthogonal matrices $\hat{\mathbf{R}}_i, i = 1, \dots, N$ minimize S_{WGPA} , the sum of weighted squared Euclidean norms, which is given by

$$\begin{aligned} S_{WGPA}(\mathbf{D}_1, \dots, \mathbf{D}_N) &= \inf_{\mathbf{R}_1, \dots, \mathbf{R}_N} \sum_{i=1}^N w_i \left\| \mathbf{Q}_i \mathbf{R}_i - \sum_{j=1}^n w_j \mathbf{Q}_j \mathbf{R}_j \right\|^2 \\ &= \inf_{\mathbf{R}_1, \dots, \mathbf{R}_N} \sum_{i=1}^N w_i \left\| (1 - w_i) \mathbf{Q}_i \mathbf{R}_i - \sum_{j \neq i} w_j \mathbf{Q}_j \mathbf{R}_j \right\|^2 \\ &= \inf_{\mathbf{R}_1, \dots, \mathbf{R}_N} \sum_{i=1}^n \frac{w_i}{(1 - w_i)^2} \left\| \mathbf{Q}_i \mathbf{R}_i - \frac{1}{(1 - w_i)} \sum_{j \neq i} w_j \mathbf{Q}_j \mathbf{R}_j \right\|^2. \end{aligned} \quad (23)$$

Below we give Algorithm 1 for computing $\hat{\mathbf{Q}}_{WGPA}$:

Algorithm 1 Weighted Generalized Procrustes Method

- 1: **Initial setting:** $\mathbf{Q}_i^P \leftarrow \text{chol}(\mathbf{D}_i), i = 1, \dots, N$
 - 2: S_{WGPA} from previous iteration: $S_p \leftarrow 0$
 - 3: S_{WGPA} from current iteration: $S_c \leftarrow \sum_{i=1}^N w_i \left\| \mathbf{Q}_i^P - \sum_{j=1}^N w_j \mathbf{Q}_j^P \right\|^2$
 - 4: **while** $|S_p - S_c| > \text{tolerance}$ **do**
 - 5: **for** $i = 1$ to N **do**
 - 6: $\hat{\mathbf{Q}}_i = \frac{1}{1 - w_i} \sum_{j \neq i} w_j \mathbf{Q}_j^P$
 - 7: Calculate the $\hat{\mathbf{R}}_i$ minimizing $\left\| \hat{\mathbf{Q}}_i - \mathbf{Q}_i^P \mathbf{R}_i \right\|$ (partial ordinary Procrustes analysis)
 - 8: $\mathbf{Q}_i^P \leftarrow \mathbf{Q}_i^P \hat{\mathbf{R}}_i$
 - 9: **end for**
 - 10: $S_p \leftarrow S_c$
 - 11: $S_c \leftarrow \sum_{i=1}^N w_i \left\| \mathbf{Q}_i^P - \sum_{j=1}^N w_j \mathbf{Q}_j^P \right\|^2$
 - 12: **end while**
 - 13: $\hat{\mathbf{Q}}_{WGPA} \leftarrow \sum_{i=1}^N w_i \mathbf{Q}_i^P$
 - 14: **return** $\hat{\mathbf{Q}}_{WGPA}$
-

In WGPA we assume that the weights $w_i, i = 1, \dots, N$ are a function of the Euclidean distance from the voxel of interest to the sampling voxel. An exponential weight function is proposed as follows:

$$w_i = \frac{\exp(-Ad_i^2) + B}{\sum_{j=1}^N [\exp(-Ad_j^2) + B]}, i = 1, \dots, N \quad (24)$$

where $A, B \geq 0$ are used to control the change of the weight as the distance changes. For example, with $A = 1$ and $B = 0.01$ the weight changes more steadily than the weight with $A = 20$ and $B = 0.01$.

4 Applications

4.1 Material

A set of diffusion weighted MR images acquired with the Uniform 32 DTI diffusion gradient direction scheme [25] from a healthy human brain has been used for this study. The MR images were acquired using a spin echo EPI (echo planar imaging) sequence with diffusion weighting gradients applied with a weighting factor of $b=1000$ s/mm² in a Philips 3T Achieva clinical imaging system (Philips Medical Systems, Best, The Netherlands). Throughout the subject's head, 52 interleaved contiguous transaxial slices were acquired in a matrix of 112x112 (interpolated to 224x224) with an acquisition voxel size of 1x1x2 mm³. For each slice, the acquisition was repeated for each of the 32 non-collinear directions according to the Uniform 32 direction scheme, and once with no diffusion weighting ($b = 0$). A Bayesian estimation method [5] has been employed to compute the tensor field and all methods of this paper are programmed with MATLAB (The Mathworks, Inc., R2008a).

4.2 Anisotropy study

Now let us compare PA with Fractional Anisotropy (FA) [26], and the hyperbolic tangent function of Geodesic Anisotropy ($\tanh(GA)$) [13] from real data. Figure 1 shows FA, PA and $\tanh(GA)$ maps (axial slices). Since PA of diffusion tensor is always smaller than FA and $\tanh(GA)$ values, the PA map gives a darker color overall. The splenium in corpus callosum is one of the regions where the overall anisotropy is strongly high [27]. We take FA, PA and $\tanh(GA)$ values along the green line in the splenium and show them in Figure 2. PA has significantly higher variation than FA and $\tanh(GA)$. In general, PA offers better contrast in highly anisotropic regions.

4.3 Geodesic interpolation

Now we carry out an experiments to investigate the geometric nature of geodesic paths obtained with different metrics. Two syntectic tensors are defined as fol-

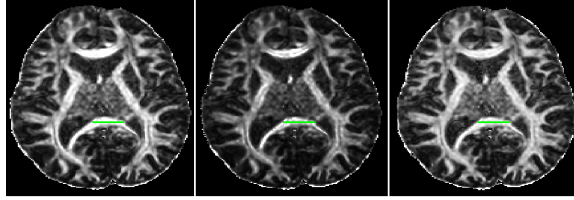


Fig. 1. Anisotropy maps from axial view. Left: FA map. Middle: PA map. Right: tanh(GA) map.

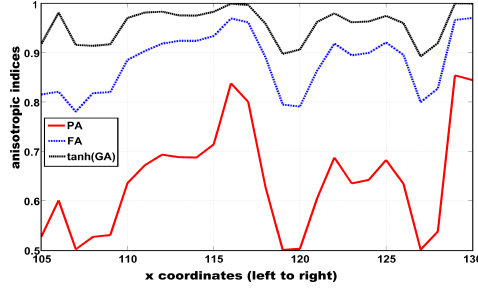


Fig. 2. Comparison of FA, PA and tanh(GA) values. FA, PA and tanh(GA) values are from tensors at voxels along the green line in Figure 1. PA value is more sensitive than FA and tanh(GA) with significantly higher variation.

lows

$$\mathbf{D}_1 = \begin{pmatrix} 5.5 & 4.5 & 0 \\ 4.5 & 5.5 & 0 \\ 0 & 0 & 1 \end{pmatrix}, \mathbf{D}_2 = \begin{pmatrix} 4.7242 & -11.4618 & 0 \\ -11.4618 & 36.2758 & 0 \\ 0 & 0 & 4 \end{pmatrix}. \quad (25)$$

These two tensors \mathbf{D}_1 and \mathbf{D}_2 are not orthogonal and are of different shape and size.

To compare interpolations with different metrics in size, orientation and anisotropy of tensor, we use four measures: the determinant $|\mathbf{D}|$ (volume of the diffusion ellipsoid), ϕ , FA and PA, where the angle ϕ measures the difference of orientations from the synthetic \mathbf{D}_1 to a interpolated tensor in the geodesic path. The angle ϕ is the smaller angle between the principal eigenvectors of \mathbf{D}_1 and the interpolated tensor. The angle ϕ is defined as

$$\phi = \arcsin(\|\mathbf{p}\mathbf{v}_1 \times \mathbf{p}\mathbf{v}_i\|), i = 1, \dots, 9 \quad (26)$$

where $\mathbf{p}\mathbf{v}_1$ is the principal eigenvector of \mathbf{D}_1 , and $\mathbf{p}\mathbf{v}_i$ is the principal eigenvector of the i th interpolated tensor (including two synthetic diffusion tensors), and $i = 1, \dots, 9$, with $i = 1$ and $i = 9$ corresponding to the synthetic tensors \mathbf{D}_1 and \mathbf{D}_2 , respectively.

Figure 3 shows four different geodesic paths between \mathbf{D}_1 and \mathbf{D}_2 , namely, the Euclidean (d_E), log-Euclidean (d_L), Riemannian (d_R) and Procrustes size-and-shape (d_S) metrics. From a variety of examples it does seem clear that

the Euclidean metric is very problematic, especially due to the parabolic interpolation of the determinant. The Procrustes metric offers somewhat better interpolation in the tensor’s orientation and anisotropy (see graphs of $|\mathbf{D}|$ and ϕ). In general, the log-Euclidean and Procrustes size-and-shape methods seem preferable.

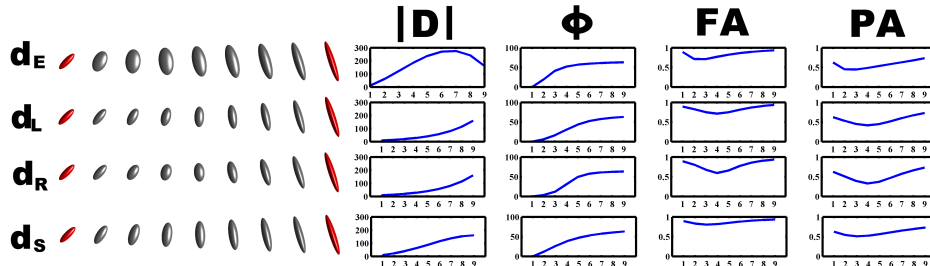


Fig. 3. Geodesic paths in experiment 5 between two general tensors. Two tensors \mathbf{D}_1 (left in red) and \mathbf{D}_2 (right in red) with general (i.e. non-collinear non-orthogonal) orientation, different shape and size. The geodesic paths are obtained with $d_E(\cdot)$, $d_L(\cdot)$, $d_R(\cdot)$ and $d_S(\cdot)$.

4.4 Interpolation and smoothing of real data

We smooth and interpolate (with 2 interpolations between each pair of original voxels) the diffusion tensor data from a normal human brain, and calculate the FA and PA maps shown in Figure 4. Obviously, FA and PA maps from the processed tensor data are much smoother than the ones without processing. The feature that the cingulum (cg) is distinct from the corpus callosum (cc) is clearer in the anisotropy maps from the processed data than those without processing in Figure 4.

5 Conclusion

In this work, we have used the full ordinary Procrustes analysis to match two diffusion tensors. The solution to the full ordinary Procrustes problem of a diffusion tensor and an isotropy has been normalized to be a new anisotropy index-Procrustes Anisotropy (PA). PA provides better contrast in highly anisotropic region of the brain. For a more general case with more than two tensors, the weighted generalized Procrustes framework has been developed for averaging $N > 2$ diffusion tensors with different fractions of contributions to the mean tensor. The weighted generalized Procrustes method has also been adapted for tensor field smoothing and interpolation. It will be interesting to apply Procrustes methods to other processing situations such as regularization of diffusion tensors [28] for the future work.

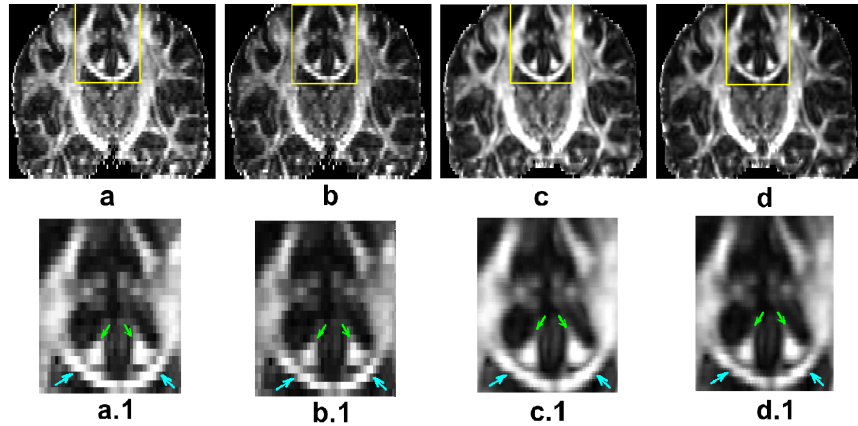


Fig. 4. FA (a) and PA (b) maps based on Bayesian estimates without post-processing. FA (c) and PA (d) maps from smoothed and interpolated tensor data obtained with the weighted generalized Procrustes method. (a.1), (b.1), (c.1) and (d.1) are zoomed inset regions in yellow box.

References

1. Alexander, D. C. (2005). Multiple-fibre reconstruction algorithms for diffusion MRI. *Annals of the New York Academy of Sciences*, 1046:113–133
2. Kingsley, P. B. (2006). Introduction to diffusion tensor imaging mathematics: Part iii. tensor calculation, noise, simulations, and optimisation. *Concepts in Magnetic Resonance Part A*, 28A:155–179
3. Koay, C. G., Carew, J. D., Alexander, A. L., Basser, P. J., and Meyerand, M. E. (2006). Investigation of anomalous estimates of tensor-derived quantities in diffusion tensor imaging. *Magnetic Resonance in Medicine*, 55:930–936
4. Behrens, T., Woolrich, M., Jenkinson, M., Johansen-Berg, H., Nunes, R., Clare, S., Matthews, P., Brady, J., and Smith, S. (2003). Characterisation and propagation of uncertainty in diffusion-weighted MR imaging. *Magnetic Resonance in Medicine*, 50:1077–1088
5. Zhou, D., Dryden, I. L., Koloydenko, A., and Bai, L. (2008). A Bayesian method with reparameterisation for diffusion tensor imaging. In *Proceedings of SPIE Medical Imaging 2008: Image Processing*, 69142J. Edited by J. M. Reinhardt and J. P. W. Pluim
6. Le Bihan, D., Mangin, J. F., Poupon, C., Clark, C. A., Pappata, S., Molko, N., and Chabriat, H. (2001). Diffusion tensor imaging: concepts and applications. *Journal of Magnetic Resonance Imaging*, 13:534–546
7. Basser, P. J., Pajevic, S., Pierpaoli, C., Duda, J., and Aldroubi, A. (2000). In vivo fibre tractography using DT-MRI data. *Magnetic Resonance in Medicine*, 44:625–632
8. Jbabdi S, Woolrich M. W., Andersson J. L., Behrens T.E. (2007). A Bayesian framework for global tractography. *Neuroimage*, 37:116–29
9. Sun, H., Yushkevich, P. A., Zhang, H., Cook, P. A., Duda, J. T., Simon, T. J., and Gee, J. C. (2007). Shape-based normalization of the corpus callosum for (DTI) connectivity analysis. *IEEE Transactions on Medical Imaging*, 26:1166–1178

10. Le Bihan, D., Poupon, C., Amadon, A., and Lethimonnier, F. (2006). Artifacts and pitfalls in diffusion MRI. *Journal of Magnetic Resonance Imaging*, 24:478–488
11. Arsigny, V., Fillard, P., Pennec, X., and Ayache, N. (2006). Log-Euclidean metrics for fast and simple calculus on diffusion tensors. *Magnetic Resonance in Medicine*, 56:411–421
12. Arsigny, V., Fillard, P., Pennec, X., and Ayache N. (2007). Geometric means in a novel vector space structure on symmetric positive-definite matrices. *SIAM Journal on Matrix Analysis and Applications*, 29:328–347
13. Batchelor, P. G., Moakher, M., Atkinson, D., Calamante, F., and Connelly, A. (2004). A rigorous framework for diffusion tensor calculus. *Magnetic Resonance in Medicine*, 53(1):221–225
14. Dryden, I., Koloydenko, A., and Zhou, D.(2009). Non-Euclidean statistics for covariance matrices, with applications to diffusion tensor imaging. *Annals of Applied Statistics.*, 3:1102–1123
15. Fletcher, P. T. and Joshi, S. (2007). Riemannian geometry for the statistical analysis of diffusion tensor data. *Signal Process*, 87(2):250–262
16. Fréchet, M. (1948). Les éléments aléatoires de nature quelconque dans un espace distancié. *Annales de l’institut Henri Poincaré*, 10(4):215–310
17. Koenker, R. (2006). The median is the message: toward the Fréchet median. *Journal de la Société Française de Statistique*, 147:61–64
18. Le, H. (1995). Mean Size-and-Shapes and Mean Shapes: A Geometric Point of View *Advances in Applied Probability*, 27(1):44–55
19. Moakher, M. and Batchelor, P. G. (2006). *Visualization and Processing of Tensor Fields*, chapter Symmetric Positive-Definite Matrices From Geometry to Applications and Visualization, pages 291–295. Springer.
20. Fillard, P., Pennec, X., Arsigny, V., and Ayache, N. (2007). Clinical DT-MRI estimation, smoothing, and fiber tracking with Log-Euclidean metrics. *IEEE Transactions on Medical Imaging*, 26(11):1472–1482
21. Pennec, X., Fillard, P., and Ayache, N. (2006). A Riemannian framework for tensor computing. *International Journal of Computer Vision*, 66:41–66
22. Dryden, I. and Mardia, K. (1998). *Statistical Shape Analysis*. Wiley & Sons, Chichester
23. Gower, J. C. (1975). Generalized Procrustes analysis. *Psychometrika*, 40:33–50
24. Kendall, David G. (1989). A Survey of the Statistical Theory of Shape. *Statistical Science*, 28A:87–120
25. Sotiropoulos, S., Bai, L., Morgan, P., Auer, D., Constantinescu, C., Tench, C. (2008). A regularized two-tensor model fit to low angular resolution diffusion images using basis directions. *Journal of Magnetic Resonance Imaging* , 28(1):199-209
26. Basser, P. J., Mattiello, J., and Le Bihan, D. (1994). Estimation of the effective self-diffusion tensor from the NMR spin echo. *Journal of Magnetic Resonance. Series B*, 103:247–254
27. Lee, C. E. C., Danielian, L. E., Thomasson, D., and Baker, E. H. (2009). Normal regional fractional anisotropy and apparent diffusion coefficient of the brain measured on a 3 T MR scanner. *Neuroradiology*, 51:3–9
28. Coulon, O., Alexander, D. C., Arridge, S. R. (2004). Diffusion tensor magnetic resonance image regularisation. *Medical Image Analysis*, 8:47–67

Genetic Analysis of High Angular Resolution Diffusion Images (HARDI)

Liang Zhan¹, Alex D. Leow^{2,3}, Neda Jahanshad¹, Agatha D. Lee¹, Marina Barysheva¹, Arthur W. Toga¹, Katie L. McMahon⁴, Greig I. de Zubicaray⁴, Nicholas G. Martin⁵, Margaret J. Wright⁵, Paul M. Thompson¹

¹ Laboratory of Neuro Imaging, Dept. of Neurology, University of California, Los Angeles, USA

² Departments of Psychiatry, Bio-engineering and Radiology, University of Illinois Medical Center at Chicago, USA

³ Community Psychiatry Associates, USA

⁴ Centre for Magnetic Resonance, University of Queensland, Brisbane, Australia

⁵ Queensland Institute of Medical Research, Brisbane, Australia

Abstract. Imaging genetics is a new field that extends methods from quantitative genetics to handle brain images. Its goal is to identify features of the brain that are genetically influenced, and then find specific variations at the genomic level that contribute to them. Recent studies using diffusion tensor imaging (DTI) in twins have discovered specific genomic variations that influence standard DTI-derived measures, such as fractional anisotropy (FA). As these associations require hundreds of scans to detect, genetic analyses will be accelerated if some measure could be derived from diffusion images that is more highly genetically influenced than FA. To test this, we scanned 116 young adult twins (29 identical and 29 fraternal twin pairs) with high-angular resolution diffusion imaging (HARDI) at 4 Tesla. We fitted tensor distribution functions (TDFs) to the full HARDI signal at each point in the brain. We then computed TDF-FA, a fiber-crossing/mixing corrected FA using the TDF, and the tensor orientation distribution (TOD), whose spherical integral encodes the volume fraction of fibers detected in each direction. We fitted structural equation models voxel-wise, using multivariate correlation for genetic analysis of vector-valued measures. Fiber directions, expressed using the 3-vector of TOD projections along each axis, were more highly heritable than standard scalar anisotropy measures (e.g., standard FA). FA_{TDF} gave higher inter-twin correlations than standard FA, avoiding errors where fibers cross or mix. Due to their higher heritability, these HARDI measures show promise for genome-wide association studies of diffusion images, and are expected to accelerate the search for specific genetic causes of variations in fiber integrity and connectivity in large human populations.

Keywords: High-Angular Resolution Diffusion Imaging, tensor distribution function, structural equation model, twins, quantitative genetics, fractional anisotropy

1. Introduction

Modeling genetic effects on the brain through neuroimaging is a rapidly growing subspecialty in the field of imaging genetics. However, genetic effects on the white matter microstructure of the brain are still largely unknown. Localization of genes associated with differences in white matter integrity and connectivity using diffusion tensor imaging (DTI) may shed light on molecular mechanisms associated with cognition and risk for disease [1]. In genetics, several models have been established to estimate the genetic and environmental contributions to a phenotype, e.g., by comparing correlations in monozygotic twins (MZs, who share 100% of their genes) to those found between dizygotic twins (DZs, who share 50% of their genes on average). Among these, the A/C/E structural equation model uses information from both types of twins to distinguish between sources of variance attributable to additive genetic factors (A), common environment (C) and environmental factors unique to each individual (E) [2]. Voxelwise fitting of these models to databases of DTI scans found that FA, its asymmetry, and scalar maps of fiber connectivity are all under strong genetic control [3, 4].

Recently, voxelwise genetic analysis of DTI was used to discover several commonly carried genes that affect fiber anisotropy (FA) in healthy adults [5-7]. One analysis performed voxelwise genome-wide association scanning (vGWAS) to identify candidate genes that affect DTI signals [8]. Even so, many of these studies required data from over 400 subjects. If we could identify other measures from HARDI scans that were more highly genetically influenced, then gene discovery and replication may be more efficient.

As genetic analyses often require the computation of correlations and estimation of variance components for structural equation models, Lee et al. [9] developed a method for multivariate genetic analysis of the full diffusion tensor, using log-Euclidean transformation to flatten the tensor manifold. The required intra-class correlations between vector- and tensor-valued signals were computed using a variant of canonical correlation analysis that seeks optimal projections of the high-dimensional data to maximize correlations between the signals. The heritability of the full 6D diffusion tensor was found to be higher than that of the standard DTI-derived scalars, such as FA and GA (geodesic anisotropy). The 3-component vector of the diffusion tensor eigenvalues, sorted in rank order, was also found to be more heritable than FA. This further suggests the promise of extending genetic analysis to higher-dimensional DTI signals than FA.

Prior studies show that single-tensor DTI models severely underestimate fiber anisotropy in brain regions where fibers mix or cross [10]. The full orientation distribution functions computable from high angular resolution diffusion imaging (HARDI), can capture additional information about aspects of fiber microstructure relevant to cognition [11]. To date, genetic contributions to HARDI-derived signals have yet to be explored.

The Tensor Distribution Function (TDF) was recently proposed in [12, 13] to model multidirectional diffusion at each point as a probabilistic mixture of symmetric positive definite tensors. The TDF models the diffusion signal more flexibly, as a unit-mass

probability density on the 6D manifold of symmetric positive definite tensors, yielding a TDF, or continuous mixture of tensors, at each point in the brain. Using the calculus of variations, the TDF approach separates different dominant fiber directions within each voxel and computes their individual eigenvalues, and anisotropy measures are weighted by the proportional contribution of each fiber component. From the TDF, one can derive analytic formulae for the orientation distribution function (ODF), the tensor orientation distribution (TOD), and their corresponding anisotropy measures. In this study, we set out to find HARDI-derived univariate and multivariate measures that are more sensitive for detecting genetic effects on the brain. We hypothesized that (1) higher-dimensional HARDI signals, such as the TOD, would be more strongly genetically influenced than FA, and (2) intraclass correlations would be higher for FA measures derived from the TDF than for the tensor.

2. Methods

2.1 Subjects and image acquisition

3D structural brain MRI scans and diffusion-weighted scans were acquired from 116 healthy young adult subjects: 29 pairs of monozygotic twins (MZ; 30 men/28 women; 25.1 ± 1.7 SD years old) and 29 pairs of same-sex dizygotic twins (DZ; 28 men/30 women; 23.8 ± 1.9 SD years old) on a 4 Tesla Bruker Medspec MRI scanner with an optimized diffusion sequence [14]. Diffusion weighted imaging (DWI) parameters were: TE/TR 92.3/8250 ms, 55 x 2mm contiguous slices, FOV = 23 cm. 105 gradient images were collected: 11 baseline (b_0) images with no diffusion sensitization (i.e., T2-weighted images) and 94 diffusion-weighted images (b -value: 1159 s/mm^2) with gradient directions evenly distributed on the hemisphere. The reconstruction matrix was 128×128 , yielding a $1.8 \times 1.8 \text{ mm}^2$ in-plane resolution. Total scan time was 14.5 minutes. T1-weighted scan parameters were: TI/TR/TE = 1500/2500/3.83 msec; flip angle=15 degrees; slice thickness = 0.9 mm, with a $256 \times 256 \times 256$ acquisition matrix.

2.2. Image Preprocessing and Registration

Raw DWIs were corrected for eddy current distortions using FSL software (www.fmrib.ox.ac.uk/fsl/). Diffusion tensors and the TDFs were calculated in the raw image space after distortion correction, prior to computing derived scalars and vectors (Sect. 2.3).

Non-brain regions were removed from the T1-weighted MR and DWI b_0 images, also using FSL. All T1-weighted images were linearly aligned with a 9-DOF global transform to a common space. The 11 b_0 images were averaged, linearly aligned, and resampled to their corresponding T1 image. Transformation matrices (1) were retained for each subject.

Each subject's average b_0 maps were then elastically registered to the individual common space T1-weighted scans using a mutual information cost function [15] to control for EPI induced susceptibility artifacts. The resulting deformation fields (2) from the EPI distortion corrections were retained. A mean deformation template (MDT) was created from the T1 images of randomly selected unrelated subjects using 3D nonlinear fluid registration [15]. To ensure co-registration between subjects, individual T1 maps were registered to the final population averaged T1-based MDT using a 3D elastic warping technique with a mutual information cost function [15]. Deformation fields from this inter-subject registration (3) were also retained. Global transformation matrices (1) and deformation fields (2 and 3) were then applied to the scalar and vector parameters (derived in raw image space) from the eddy distortion corrected DWI so that all maps were aligned anatomically.

2.3 Parameter calculation

Several parameters (defined below) were computed from the diffusion tensors and TDFs: (1) fractional anisotropy derived from the tensor or the TDF (FA_{DTI} , FA_{TDF}), (2) the principal eigenvector, or dominant direction of the fitted diffusion tensor (TDD); and (3) a spherical function called the tensor orientation density (TOD), defined below. FA_{DTI} was calculated from eigenvalues (λ_1 , λ_2 , and λ_3) of the single-tensor model (Eq. 1). TDD is the principal eigenvector - corresponding to the largest eigenvalue, λ_1 .

$$\left\{ \begin{array}{l} FA_{DTI} = \sqrt{\frac{3}{2} \left(\frac{(\lambda_1 - \langle \lambda \rangle)^2 + (\lambda_2 - \langle \lambda \rangle)^2 + (\lambda_3 - \langle \lambda \rangle)^2}{\lambda_1^2 + \lambda_2^2 + \lambda_3^2} \right)} \\ \langle \lambda \rangle = \frac{\lambda_1 + \lambda_2 + \lambda_3}{3} \end{array} \right. \quad (1)$$

The Tensor Distribution Function (TDF) framework was applied to compute a probabilistic ensemble of 3D Gaussian diffusion processes at each voxel that best describes the observed signal [12]. We represent the manifold of 3x3 symmetric positive definite tensors by \bar{D} . The probabilistic ensemble of tensors, as represented by the TDF P , is defined on the tensor space \bar{D} that best explains the observed diffusion-weighted signals. To solve for an optimal TDF P^* , we use the multiple diffusion-sensitized gradient directions q_i and arrive at P^* using the least-squares principle with a gradient descent algorithm defined in [12] (Eq. 2):

$$\left\{ \begin{array}{l} S_{calculated}(q) = \int_{D \in \bar{D}} P(D) \exp(-bq^T D q) dD \\ P^* = \underset{P}{\operatorname{argmin}} \sum_i (S_{obs}(q_i) - S_{calculated}(q_i))^2 \end{array} \right. \quad (2)$$

By parameterizing the tensor space using eigenvalues (λ) and Euler angles (θ), the dominant fiber directions may be estimated from Eq. 3 by thresholding the TOD as a function of spherical angle:

$$TOD(\theta) = \int_{\lambda} P(D(\lambda, \theta)) d\lambda \quad (3)$$

The FA_{TDF} is defined as a weighted average of FA based on the fitted distribution of component signals in the tensor space \bar{D} (Eq. 4). It can be considered as a HARDI-derived version of FA, corrected for the multiple fibers or tissue types that contribute to the diffusion propagator in each voxel.

$$\left\{ \begin{array}{l} FA_{TDF} = \int_{\theta} TOD(\theta) \times FA(\theta, \lambda) d\theta \\ FA(\theta, \lambda) = \sqrt{\frac{3}{2} \left(\frac{(\lambda_1 - \langle \lambda \rangle)^2 + (\lambda_2 - \langle \lambda \rangle)^2 + (\lambda_3 - \langle \lambda \rangle)^2}{\lambda_1^2 + \lambda_2^2 + \lambda_3^2} \right)} \\ \lambda_k = \frac{\int_{\lambda_k} P(D(\lambda_k, \theta)) \lambda_k d\lambda_k}{\int_{\lambda_k} P(D(\lambda_k, \theta)) d\lambda_k} \quad (k = 1, 2, 3) \\ \langle \lambda \rangle = \frac{\lambda_1 + \lambda_2 + \lambda_3}{3} \end{array} \right. \quad (4)$$

For visualization, we also projected the TOD spherical function and TDD vector onto the cardinal x , y and z axes to get six scalar maps: TOD- x , TOD- y , TOD- z and TDD- x , TDD- y , TDD- z respectively.

2.4 Heritability and structural equation models

For each subject, we computed maps of the univariate scalars FA_{DTI} , FA_{TDF} , and 3×1 multivariate vectors representing the principal eigenvector (TDD) and projections of the TOD on the 3-cardinal axes (assembled into a 3-component vector). Two sets of voxel-wise covariance matrices for the MZ pairs and DZ pairs were computed for all the measures. For each statistic, we estimated the intraclass correlation (ICC), heritability (i.e., proportion of the observed variance due to genetic differences among individuals), and computed the best-fitting A/C/E model, which partitions the observed variance into components due to genetic factors (A) as well as common or unique environmental factors (C,E).

An initial estimate of heritability can be computed from the ICC in both types of twins (r_{MZ} and r_{DZ}) for both univariate and multivariate maps [9]. Here we used Falconer's heritability estimate [2]:

$$h^2 = 2(r_{MZ} - r_{DZ}) \quad (5)$$

This heritability estimate, ranging from 0 (no genetic effect) to 1 (total genetic control), is expected to vary across brain regions and across different parameters. The multivariate ICC [17] is defined as:

$$\Gamma = \Sigma^{-1/2} \Omega \Sigma^{-1/2} \quad (6)$$

where Σ , Ω are the expected values of $(t_1 - \mu)(t_1 - \mu)^T$ and $(t_2 - \mu)(t_2 - \mu)^T$ respectively. Here, μ is the sample mean of all of the t_1 and t_2 vectors. t_1 and t_2 are 3-dimensional vectors (representing with the TOD or the TDD) defined at each voxel for each twin in the pair. This implies that $\Sigma - \Omega$, which basically estimates the within-pair correlation, is

positive semi-definite. The maximum eigenvalue of this ICC matrix Γ is considered to be the multivariate ICC value.

A structural equation model (SEM) may be fitted to the covariances to infer how much of the population variance is attributable to additive gene effects (A), environmental factors that are shared, or common, between twins (C), and unique environmental factors coupled with measurement errors (E). Measurement errors or inter-subject registration errors will both be classified as part of the E component of variance. Any measure Z in the twins, such as FA or TOD at a given voxel, may be modeled as arising from contributions of 3 factors with different weights:

$$Z = aA + cC + eE \quad (7)$$

Here A/C/E are latent variables and a , c , e are the weights of each parameter to be estimated. A maximum-likelihood estimate (MLE) [18] is used to estimate the proportion of the voxel-based intersubject variance that is attributable to each of the 3 free model parameters. The 3 variance components combine to create the total observed inter-individual variance, so that $a^2 + c^2 + e^2 = 1$. The weights $\Theta = (a, c, e)$ are estimated by comparing the covariance matrix implied by the model, $\Sigma(\Theta)$, and the sample covariance matrix of the observed variables, S , using maximum-likelihood fitting.

The covariance matrix, $\Sigma(\theta)$, for observations (Z_1, Z_2) in a given twin pair, is specified by the A/C/E model to be:

$$\Sigma(\theta) = \begin{pmatrix} \text{cov}(Z_1, Z_1) & \text{cov}(Z_1, Z_2) \\ \text{cov}(Z_1, Z_2) & \text{cov}(Z_2, Z_2) \end{pmatrix} = \begin{pmatrix} a^2 + c^2 + e^2 & \alpha a^2 + c^2 \\ \alpha a^2 + c^2 & a^2 + c^2 + e^2 \end{pmatrix} \quad (8)$$

where $\alpha=1$ for MZ twins and $\alpha=0.5$ for DZ twins, as MZ twins share all the same genes and DZ twins share half of their genes on average. The maximum-likelihood, $F_{LM,\theta}$, is modeled as follows:

$$F_{LM,\beta} = \log|\Sigma(\Theta)| + \text{trace}(\Sigma^{-1}(\Theta)S) - \log|S| - p \quad (9)$$

where $p = 2$ is the number of observed variables. Under the null hypothesis that Z is multivariate normal (i.e., each of A, C and E is normally distributed), the MLE model approximately follows a χ^2 distribution with $p(p+1) - t$ degrees of freedom, where t is number of model parameters (3 in our case). We used the Broyden-Fletcher-Goldfarb-Shannon method [1] to obtain the minimum $F_{LM,\beta}$.

In SEM, the χ^2 goodness of fit measure determines a p -value for all specified regions of interest where the test is performed. This value indicates that the model is a *good* fit to the data if $p > 0.05$ (note this is the opposite of the usual convention). To determine the significance of a particular factor, specifically the A or C, the χ^2 goodness-of-fit values of the model may be compared to those for a reduced model that does not include that factor (e.g., to a C/E model to determine the significance of the additional A factor) giving:

$$p(A) = \chi^2_{1DF}^{-1}[\chi^2(ACE) - \chi^2(CE)] \quad (10)$$

Here $\chi^2_{1DF}^{-1}$ denotes the inverse of the cumulative distribution function for a chi-squared distributed variable with one degree of freedom. In this case, low p -values express significant improvements when adding a factor, consistent with the more standard convention for p -values. This allows the effect size and overall significance of the

resulting uncorrected p -value maps to be assessed using standard false discovery rate (FDR) methods which have proven to be powerful in neuroimaging applications [18].

3. Results and Discussion

Figure 1 shows the set of scalar maps derived for a single subject. FA_{DTI} clearly suffers from partial volume effects and fiber crossings. Visually, TDD projections are also noisy and inconclusive when compared to TOD projections. **Figure 2** shows cumulative distribution plots for ICC probability values mapped for vectors (TOD and TDD) and scalars (FA_{TDF} and FA_{DTI}). All maps show significant ICCs for each type of twin after multiple comparisons correction that controls the FDR at the 5% level (shown by $y=20x$ line). For investigating the heritability of white matter directional microstructure, we found that the TOD projection vector shows higher intraclass correlations than the TDD. For the corresponding ACE analyses, **Figure 4b** plots the difference in the genetic components of variance attributable to the TOD and the TDD; a greater genetic contribution was detected for the TOD measures. For measures of anisotropy, FA_{DTI} and FA_{TDF} show similar patterns of effects, but FA_{TDF} outperforms FA_{DTI} in its power to detect genetic effects on FA variance in fiber crossing regions (**Figures 3b** and **3c**). **Figure 4a** shows the results of ACE analyses comparing FA_{TDF} and FA_{DTI} . Here we see that the ACE model is a significantly better fit for capturing the full genetic and environmental components of the variance in the entire brain for FA_{TDF} as compared to FA_{DTI} .

4. Conclusion

Here we showed how to estimate genetic effects on HARDI-derived measures of white matter microstructure in the brain. Prior studies estimated the fractional anisotropy from the diffusion tensor, but that measure is known to be incorrect where fibers mix or cross (**Figure 3a**). When a continuous mixture of tensors is fitted to HARDI data (here using the TDF framework), the FA is higher where fibers cross, and in any voxels where multiple principal directions of diffusion are present. The TDF model recovers maps of dominant fiber directions that are less noisy and more highly heritable than maps derived from the standard diffusion tensor. Moreover, it also de-convolves the fiber wiring pattern (i.e., orientational information; represented by the TOD) from the individual fiber anisotropy. TDF-derived measures showed higher heritability and greater effect sizes, both for the intraclass correlations and additive genetic effects. Both of these effects are depleted by known sources of error in the standard diffusion tensor model.

This study has several strengths. We found that the tensor distribution function, which uses the full diffusion gradient data, boosts power in genetic studies. We also showed, perhaps surprisingly, that the dominant fiber direction is more highly heritable than the

FA, which has been the primary focus of most prior genetic studies of DTI. More research is needed to determine whether the heritability of fiber directions in the brain simply reflects heritable differences in overall brain shape, or a locally varying genetic control of fiber trajectories. A “cross-twin cross-trait” design could disentangle whether aspects of brain shape (encoded in the registration fields) have a partially overlapping genetic basis with that of the local dominant fiber directions, or whether they are independent.

Some caveats are needed. Our HARDI-derived measures avoid sources of bias that affect comparable measures from the diffusion tensor. However, this does not imply that all HARDI-derived measures are more heritable. The information on the diffusion propagator that is missed by the tensor model may be affected by an unknown mix of genetic and non-genetic factors. This may tend to enhance or reduce their heritability and promise of association in genome-wide studies.

Even so, given the greater effect sizes for our HARDI-based measures of anisotropy and fiber directions, HARDI-based measures are likely to reduce the sample sizes needed for genetic studies. This may accelerate the search for specific genes that affect brain integrity and connectivity. It may also make results easier and faster to verify. With this in mind, genome-wide searches have recently been extended to entire images [6]. Efforts to replicate promising genetic hits in independent datasets will likely be facilitated by multinational consortia such as the Enigma project (enigma.ionu.ucla.edu).

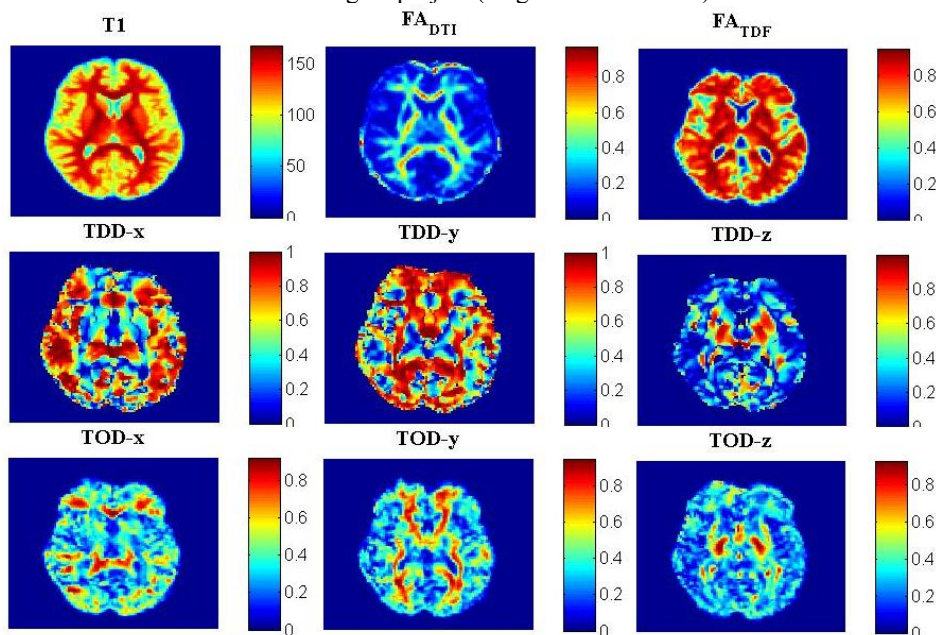


Figure 1. Single subject scalar maps. T1 denotes the T1-weighted image (in arbitrary units). FA_{DTI} tends to underestimate the true FA of the component fibers and is incorrect when fibers cross or mix

in the same voxel. It agrees more with FA_{TDF} in highly coherent tracts with a single dominant fiber direction (e.g., in the corpus callosum). TDD projections show the components of the principal eigenvector of the diffusion tensor. These components are higher in regions where the dominant fiber direction is aligned with that axis. TOD projections are less noisy, as they are computed from the full spherical diffusion function; they can also accommodate multiple fiber directions per voxel.

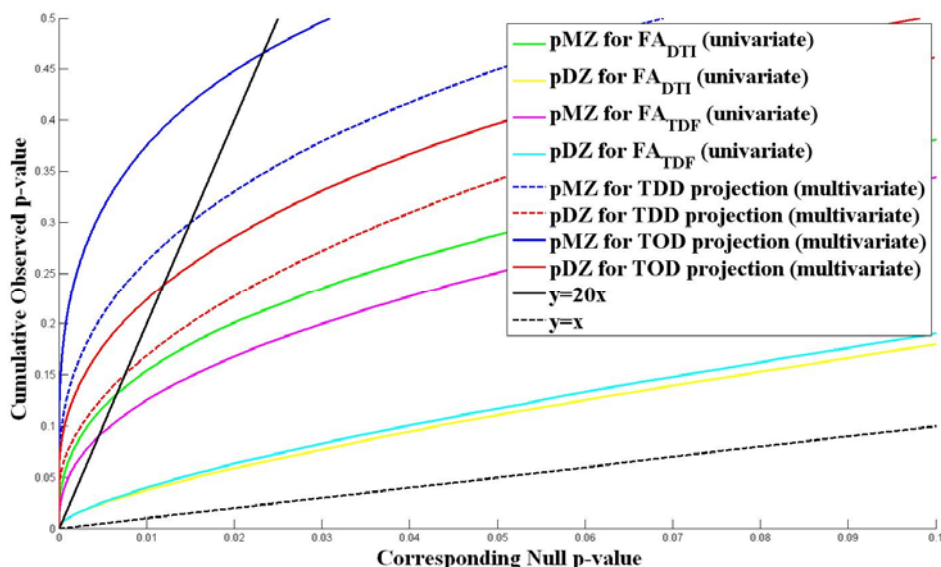


Figure 2. Cumulative distribution functions for the significance of intraclass correlations. When similarities between twins are assessed using the ICC (for scalar- or vector-valued signals), any measurement errors tend to deplete the observed correlations. For different DTI- or HARDI-derived measures, we computed a map of the significance of the ICC between twins. We made a cumulative distribution function from the resulting uncorrected p -values (*colored curves*). For null data, uncorrected p -values are uniformly distributed on the unit interval $[0,1]$, and their CDF approximately follows the line $y=x$. Using the standard FDR method, curves that rise more steeply at the origin show greater effect sizes. If the CDFs cross the line $y=20x$ other than at the original, the FDR is successfully controlled at the conventional 5% level. The power to detect significant correlations between twins follows a rank order. Greatest effect sizes were found for the TOD projection (multivariate) $>$ TDD projection (multivariate) $>$ FA_{DTI} (univariate) $>$ FA_{TDF} (univariate). The TOD projection reflects the fiber direction, which may be more genetically influenced than the anisotropy. As expected, the correlation for MZ twins is always greater than that for DZ twins, which gives evidence for genetic influences on all the measures (confirmed below).

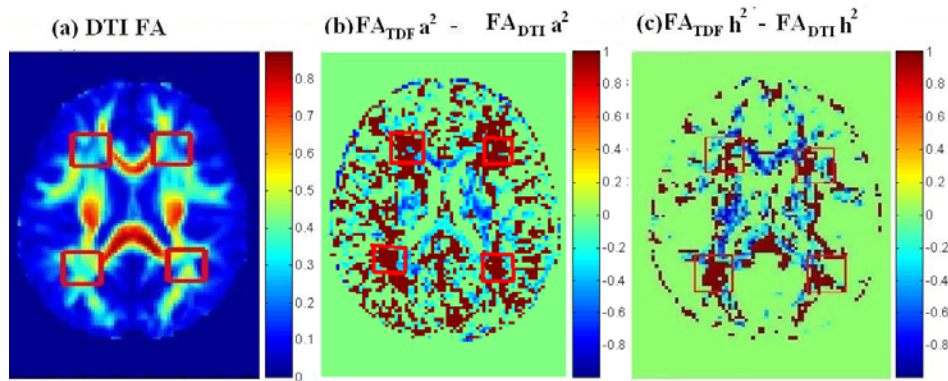


Figure 3. FA_{TDF} vs. FA_{DTI} . (a) When fractional anisotropy is computed from the diffusion tensor, it underestimates component fiber FA (too low) in regions where fibers cross (*red boxes*). These are effectively measurement errors, and FA_{TDF} can correct for them, as it estimates FA from a multi-fiber model fitted at each voxel. A rough but widely-used estimate of the proportion of variance due to genetic factors, h^2 (Falconer's heritability statistic), tends to be higher for FA_{TDF} than FA_{DTI} . This is clearly evident in fiber crossing regions (*red boxes*). Red colors indicate generally greater heritability for FA_{TDF} , but not for the entire white matter.

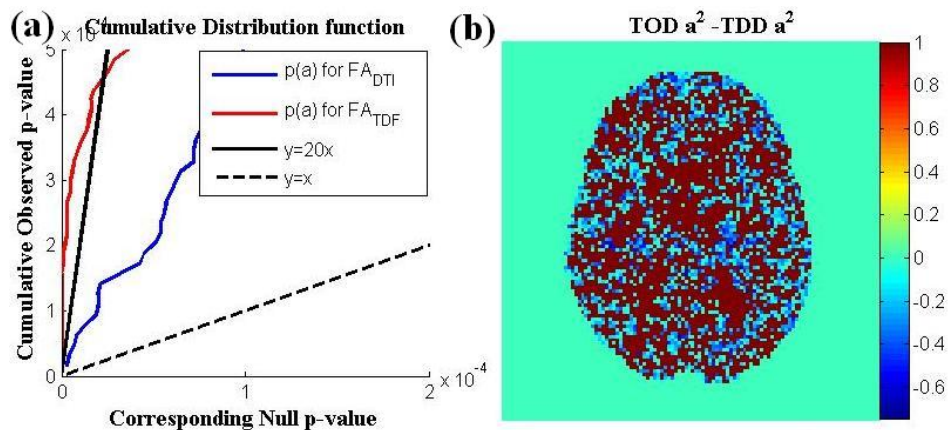


Figure 4. ACE analysis results. (a) CDF plot for the significance of the genetic effect, $p(a)$, on measures of fractional anisotropy derived from the diffusion tensor (FA_{DTI}) and from the tensor distribution function (FA_{TDF}). The FA_{TDF} is more accurate when fibers mix or cross. As expected, the CDF rises more sharply at the origin for the FA_{TDF} , so genetic effects are detected with greater effect sizes. (b) Voxelwise statistics showing $(TOD a^2 - TDD a^2)$. Red colors indicate that $TOD a^2 > TDD a^2$, in most white matter regions. This suggests that the dominant fiber directions are more highly heritable when estimated from the tensor distribution function (which is more accurate) than from the single-tensor model, which is incorrect when fibers mix or cross. This is reasonable, as any measurement errors will tend to deplete the observed correlations between twins. Measurement

errors, so long as they are not correlated between the two twins in a pair, also tend to reduce the a^2 term (and inflate the e^2 term) in the ACE variance-components model.

5. References

1. Chiang MC, Barysheva M, Lee AD, Madsen SK, Klunder AD, Toga AW, McMahon KL, de Zubicaray GI, Wright MJ, Srivastava A, Balov N, Thompson PM (2009). *Genetics of Brain Fiber Architecture and Intelligence*, **Journal of Neuroscience**, 2009 Feb 18;29(7):2212-24.
2. Falconer D, Mackay TF (1995). *Introduction to Quantitative Genetics*, 4th Edition. Addison Wesley Longman (Pearson Education).
3. Jahanshad N, Lee AD, Barysheva M, McMahon KL, de Zubicaray GI, Martin NG, Wright MJ, Toga AW, Thompson PM (2010). *Genetics Influences on Brain Asymmetry: A DTI Study of 374 Twins and Siblings*, **NeuroImage**, May 2010.
4. Patel V, Chiang MC, Thompson PM, McMahon KL, de Zubicaray GI, Hansell NK, Martin NG, Wright MJ, Toga AW (2010). *Scalar Connectivity Measures from Fast Marching Tractography Reveal Heritability of White Matter Architecture*, **ISBI 2010**, Rotterdam, The Netherlands.
5. Chiang MC, Avedissian C, Barysheva M, Toga AW, McMahon KL, de Zubicaray GI, Wright MJ, Thompson PM (2009). *Extending Genetic Linkage Analysis to Diffusion Tensor Images to Map Single Gene Effects on Brain Fiber Architecture*, **Medical Image Computing and Computer Assisted Intervention (MICCAI2009)**, London, UK, Sept. 2009
6. Jahanshad N, Stein JL, McMahon KL, de Zubicaray GI, Hansell NK, Martin NG, Wright MJ, Toga AW, Thompson PM (2010). *Commonly-carried variants in a visual pathway gene are associated with reduced white matter integrity in 451 young twins imaged with DTI*. **Proc. Soc. Neuroscience**, San Diego, CA, Nov. 2010.
7. Braskie MN,* Jahanshad N,* Stein JL,* Barysheva M, McMahon KL, de Zubicaray GI, Martin NG, Wright MJ, Ringman JM, Toga AW, Thompson PM (2010). *Common Alzheimer's disease risk variant affects white matter microstructure in young adults*, submitted. [*equal contribution].
8. Hibar DP, Stein JL, Jahanshad N, Barysheva M, Feng A, Kogachi S, McMahon KL, de Zubicaray GI, Hansell NK, Martin NG, Wright MJ, Toga AW, Thompson PM (2010). *Voxelwise genome-wide association of Diffusion Tensor Images identifies putative novel variants influencing white matter integrity in 467 related young adults*, **Proc. Soc. Neuroscience**, San Diego, CA, 2010.
9. Lee AD, Lepore N, de Leeuw J, Brun CC, Barysheva M, McMahon KL, de Zubicaray GI, Martin NG, Wright MJ, Thompson PM (2010). *Multivariate Variance-Components Analysis in DTI*, **ISBI 2010**, Rotterdam, The Netherlands, April 14-17, 2010.
10. Liang Zhan, Alex D. Leow, Neda Jahanshad, Arthur W. Toga, Thompson PM (2010). *Fiber Demixing with the Tensor Distribution Function avoids errors in Fractional Anisotropy maps*, Organization for Human Brain Mapping, Barcelona, Barcelona, Spain, June 2010.
11. Aganj I, Jahanshad N, Lenglet C, Toga AW, McMahon KL, de Zubicaray GI, Wright MJ, Sapiro G, Thompson PM. *Relating Fiber Crossing in HARDI to Intellectual Function*, Proc. 16th Annual Meeting of the **Organization for Human Brain Mapping**, Barcelona, June 6-10, 2010.
12. Leow AD, Zhu S, Zhan L, McMahon K, de Zubicaray GI, Meredith M, Wright MJ, Toga AW, Thompson PM. *The tensor distribution function*. **Magn Reson Med**. 2009 Jan;61(1):205-14.
13. Zhan L, Leow AD, Jahanshad N, Chiang MC, Barysheva M, Lee AD, Toga AW, McMahon KL, de Zubicaray GI, Wright MJ, Thompson PM. *How does angular resolution affect diffusion imaging measures?* **Neuroimage**. 2010 Jan 15;49(2):1357-71. Epub 2009 Oct 9.

14. Jones DK, Horsfield MA, Simmons A. Optimal strategies for measuring diffusion in anisotropic systems by magnetic resonance imaging. **Magn Reson Med** 42(3), 515–525 (1999)
15. Leow AD, Huang SC, Geng A, Becker JT, Davis SW, Toga AW, Thompson PM. *Inverse Consistent Mapping in 3D Deformable Image Registration: Its Construction and Statistical Properties*. **IPMI 2005**: 493-503 (2005)
16. Leporé N, Chou YY, Lopez OL, Aizenstein HJ, Becker JT, Toga AW, Thompson PM. *Fast 3D fluid registration of brain magnetic resonance images*. **SPIE Medical Imaging 2008**: Physiology, Function, and Structure from Medical Images. San Diego, CA, USA.
17. Rao CR. *Familial Correlations or the Multivariate Generalization of the Intraclass Correlation*. **Current Science**, 14:66–67 (1945).
18. Genovese CR, Lazar NA, Nichols T. *Thresholding of statistical maps in functional neuroimaging using the false discovery rate*. **NeuroImage** 15 (4), 870 – 878 (2002).

Oral Session III: Spatial Normalization and Segmentation

Spatial Transformations of High Angular Resolution Diffusion Imaging Data in Q-space

Thijs Dhollander^{1,2}, Wim Van Hecke^{1,3,4}, Frederik Maes^{1,2}, Stefan Sunaert^{1,3},
and Paul Suetens^{1,2}

¹ Medical Imaging Research Center (MIRC), K.U.Leuven, Leuven, Belgium

² Center for Processing Speech and Images (PSI), Department of Electrical Engineering (ESAT), Faculty of Engineering, K.U.Leuven, Leuven, Belgium

³ Department of Radiology, University Hospitals of the K.U.Leuven, Leuven, Belgium

⁴ Department of Radiology, University Hospital Antwerp, Antwerp, Belgium

Abstract. A crucial operation in every image registration algorithm is the application of a spatial transformation to an image. For scalar valued images, this particular operation is rather trivial. For diffusion weighted imaging (DWI) data however, the problem is more complex due to the information in every voxel being dependent on the angular structure of the underlying tissue. Methods for transforming the diffusion tensor and the fiber orientation distribution function from high angular resolution diffusion imaging have already been proposed. In order to perform registration of DWI data irrespectively of (i.e. *before* the application of) any particular reconstruction method, it should be done straight on the signal functions in q-space. In this work, we specifically consider the problem of transforming the signal functions in q-space. We develop a plausible method to accomplish this. The proposed method preserves anisotropic as well as isotropic volume fractions.

1 Introduction

Diffusion weighted imaging (DWI) is a magnetic resonance imaging (MRI) technique that allows to study the oriented microstructure of tissue *in vivo* through the assessment of the self-diffusion of water within this tissue. In high angular resolution diffusion imaging (HARDI), many volumes are acquired using different gradient directions. From these data, higher order reconstructions can be made, including, but not limited to the apparent diffusion coefficient (ADC) profile [1, 5], the diffusion orientation distribution function (dODF) from Q-Ball imaging (QBI) [2, 6] and the fiber orientation distribution function (fODF) from spherical deconvolution (SD) of the data [3, 4] or the dODF [7]. An advantage of higher order models is the ability to represent more complex fiber structures, where the diffusion tensor (DT) obtained from diffusion tensor imaging (DTI) is unable to do so. The methods of Descoteaux et al. [5–7] are notable because they yield simple relations between the signals in q-space, the dODF and the fODF using a symmetric, real, orthonormal spherical harmonics (SH) basis.

The application of a spatial transformation is a crucial operation in any registration / normalization algorithm. For DWI data or any of the previously

mentioned reconstructions, this is a challenge of its own since the information in every voxel is angularly dependent on the microstructure of the underlying tissue. In the case of a non-rigid deformation field, the Jacobian matrix can be calculated at the position of each voxel. This provides a local affine model, and as such reduces the problem to *affine transformation of the information in a single voxel*.

For DTI, it has been argued that the DT should only undergo a rigid rotation so as to preserve the properties of the tissue [8]. Through strategies such as finite strain (FS) or preservation of principal direction (PPD), the rigid rotation matrix can be obtained. Barmpoutis et al. [9] represent diffusion by a 4th order tensor and show how this can be affinely transformed. Both Hong et al. [12] and Raffelt et al. [13] tackle the problem of transforming the fODF. Their assumption of the final result is the same: applying the affine transformation to the directions while preserving the volume fractions of the fiber populations (this is reasonable, as the fODF is a probability distribution function). Although their methods to accomplish this goal are different, similar results should theoretically be obtained.

If we want to perform registration of images containing DWI data independently of a particular model and reconstruction method (such as the DT, dODF, fODF, ... from different reconstruction methods), it should be done *before* reconstruction, i.e. on the signal functions in q-space. This leads us to the problem of transforming these signal functions in q-space. In the literature, we found a method where the (local) affine transformation is simply applied straight to the gradient directions, whereafter they are normalized again [10]. Very recently, this approach showed up again [11]. While this works fine for a rigid rotation, we will show that it produces wrong results for affine transformations. We will also mention how this method can be easily fixed. However, this result is still not sufficient because volume fractions are not preserved. We will then start off from the method of Raffelt et al. [13]. Using the relations of Descoteaux et al. [5–7], we will translate this method back to the signals in q-space. We add upon this by including an isotropic volume fraction (IVF), so as to preserve its isotropic nature. As such, our new method is able to handle the transformation of full images (i.e. no threshold on anisotropy needed) containing DWI data in q-space while preserving anisotropic as well as isotropic volume fractions.

In the results section, we show the impact of (not) accounting for the IVF on quantitative measures that are also calculated straight on the signals in q-space. The qualitative impact on, for instance, reconstructed fODF's is also briefly discussed.

2 Methods

2.1 About reorienting the gradient directions

A very straightforward method to perform the (local) affine transformation can be found in the literature [10, 11]. It simply consists of applying the transformation to the gradient directions and normalizing the result so as to obtain a new

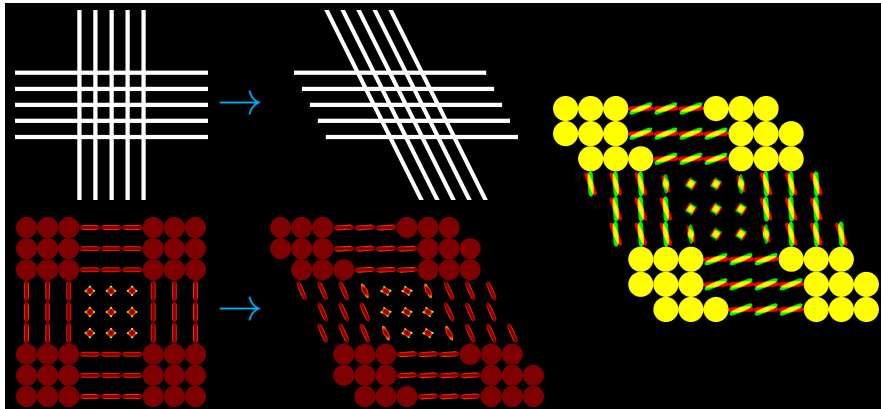


Fig. 1. A set of crossing fibers (*top left*) is being sheared (*top middle*). The sampling directions of the corresponding signal functions (*bottom left*) are sheared in the same way (*bottom middle*). The result is however highly inconsistent with the sheared fibers. This method (*red*) is overlaid with our fixed version (*green*) (*right*).

set of gradient directions for the voxel in question. In case of an affine transformation matrix M and gradient directions g , the new gradient directions g' can thus be found by $g' = Mg/\|Mg\|$. While it may intuitively seem a good idea to apply the transformation to the sampling directions of something like an fODF, this can however *not* be done in the same way to the signal functions to obtain a similar result! An example clarifies this statement. In Fig. 1, a small patch of crossing fibers is shown being sheared. This particular shearing changes the orientation of the vertical bundle, but leaves the orientation of the horizontal bundle unaffected. If we apply the same shearing to the sampling directions of the signal function (i.e. to the gradient directions), the outcome is highly inconsistent with the sheared fiber structure. The voxels in the vertical bundle barely changed, while the ones in the horizontal bundle were reoriented quite a lot.

After some reasoning, we could fix this method: the new gradient directions can actually be obtained by $g' = Ng/\|Ng\|$ instead, where the matrix N can be calculated as $N = (M^T)^{-1}$. A comparison of this fixed method and the original one is also presented in Fig. 1. We won't go into further details about this reasoning, as this result is still not satisfactory: while it changes sampling directions, it does in no way preserve volume fractions.

2.2 Preserving volume fractions

Signals in q-space, the dODF and the fODF in a single voxel are angular functions, which can be represented by functions on the unit sphere. SH functions provide a basis for complex functions on the unit sphere. They are defined as

$$Y_\ell^m(\theta, \phi) = \sqrt{\frac{2\ell + 1}{4\pi} \frac{(\ell - m)!}{(\ell + m)!}} P_\ell^m(\cos \theta) e^{im\phi} \quad (1)$$

where P_ℓ^m is an associated Legendre polynomial. The nonnegative integer ℓ denotes the order and the integer $m \in [-\ell, \ell]$ is a phase factor. Using only even orders ℓ , a new basis with index $j = (\ell^2 + \ell + 2)/2 + m$ can be constructed as

$$Y_j = \begin{cases} \sqrt{2} \cdot \text{Re}(Y_\ell^m) & \text{if } -\ell \leq m < 0 \\ Y_\ell^0 & \text{if } m = 0 \\ \sqrt{2} \cdot \text{Im}(Y_\ell^m) & \text{if } 0 < m \leq \ell \end{cases} \quad (2)$$

which consists of $T = (n+1)(n+2)/2$ terms, where n is the maximum order [5]. This basis has the useful properties of being real-valued, antipodally symmetric and orthonormal with respect to the inner product. We can now express the measured signal S for gradient direction (θ_i, ϕ_i) in a single voxel as a function

$$S(\theta_i, \phi_i) = \sum_{j=1}^T c_j Y_j(\theta_i, \phi_i) \quad (3)$$

of which the coefficients c_j can be estimated using a linear least-squares method while directly incorporating a local Laplace-Beltrami regularization [5].

The dODF can be estimated from the signal on a single sphere of q-space by the Funk-Radon transform (FRT), of which the value in direction u equals the integral over the corresponding equator [2]. Representing both S and the dODF in the SH basis allows for a simplification of the FRT given by

$$\text{FRT}[S](u) = \int_{w \perp u} S(w) dw = \sum_{j=1}^T 2\pi P_{\ell_j}(0) c_j Y_j(u) = \sum_{j=1}^T c'_j Y_j(u) \quad (4)$$

where ℓ_j is the order of Y_j and P_{ℓ_j} is the Legendre polynomial of degree ℓ_j [6]. This means the coefficient vector C' of the dODF can be obtained through a linear transformation of the coefficient vector C of the signals by $C' = FC$ where F is a diagonal matrix.

In a similar manner, the fODF can be estimated from the dODF by the sharpening deconvolution transform (SDT), which is a SD of the dODF with the single fiber dODF kernel R' (shaped by the b -value and eigenvalues λ_1 and $\lambda_2 = \lambda_3$) [7]. A simplified analytical solution is now given by

$$\text{SDT}[\text{FRT}[S]](u) = \sum_{j=1}^T \frac{c'_j}{2\pi \int_{-1}^1 P_{\ell_j}(t) R'(t) dt} Y_j(u) = \sum_{j=1}^T c''_j Y_j(u) \quad (5)$$

allowing for the calculation of the coefficient vector C'' of the fODF by $C'' = DC'$ where D is a diagonal matrix. An important property of both the FRT and the SDT is that they are linear and invertible within the context of our symmetric SH basis.

Raffelt et al. [13] start off from the fODF represented in a SH basis. They then approximate the fODF by a weighted sum of SH delta functions. Due to

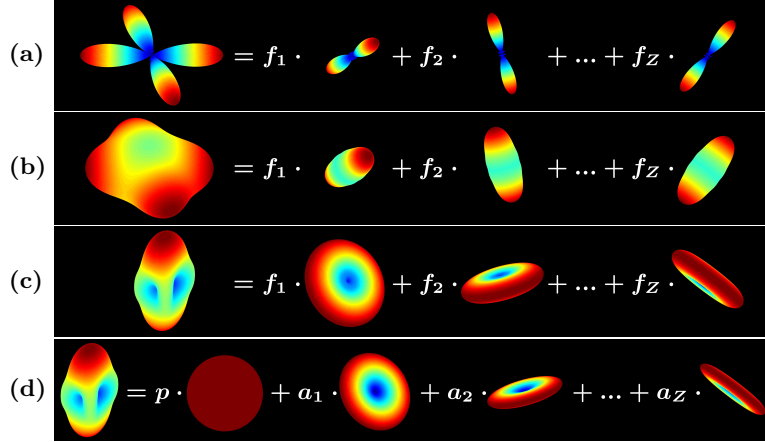


Fig. 2. Transformation-friendly representation (a) of the fODF, (b) of the dODF, (c) of S in q-space and (d) also accounting for isotropic volume fractions.

orthonormality of the SH basis, a delta function $\delta(\theta, \phi)$ can be projected into the elements of the coefficient vector E'' of a SH delta function by

$$e_j'' = \int_{\Omega} \delta(\theta, \phi) Y_j(\theta, \phi) d\Omega \quad (6)$$

Denoting the SH delta function of maximum order n with its main axis along direction z by δ_n^z , the fODF can then be approximated as shown in Fig. 2a by

$$\text{SDT}[\text{FRT}[S]](u) = \sum_{i=1}^Z f_i \delta_n^{z_i}(u) \quad (7)$$

using $Z > T$ uniformly distributed directions z_i and obtaining the fractions f_i . An affine transformation of the fODF is then achieved by subjecting the directions z_i to this transformation, while maintaining the fractions f_i . This can in a way be seen as a natural extension of the PPD approach in DTI: each $f_i \delta_n^{z_i}$ is independently subjected to a rigid PPD (z_i) transformation. We will call a representation such as (7) a transformation-friendly representation (TFR).

Because the SDT and FRT are linear and invertible, we can rewrite (7) as

$$S(u) = \sum_{i=1}^Z f_i \text{FRT}^{-1}[\text{SDT}^{-1}[\delta_n^{z_i}]](u) = \sum_{i=1}^Z f_i \beta_n^{z_i}(u) \quad (8)$$

so as to obtain an equivalent TFR of S in q-space, as shown in Fig. 2c. The elements of the coefficient vector E of a SH β_n^z function can be calculated from E'' of a SH delta function by $E = (DF)^{-1} E''$. This TFR of S should theoretically have the same fractions f_i as TFR (7) of the fODF and subjecting either of both TFR's to any affine transformation should produce the same result.

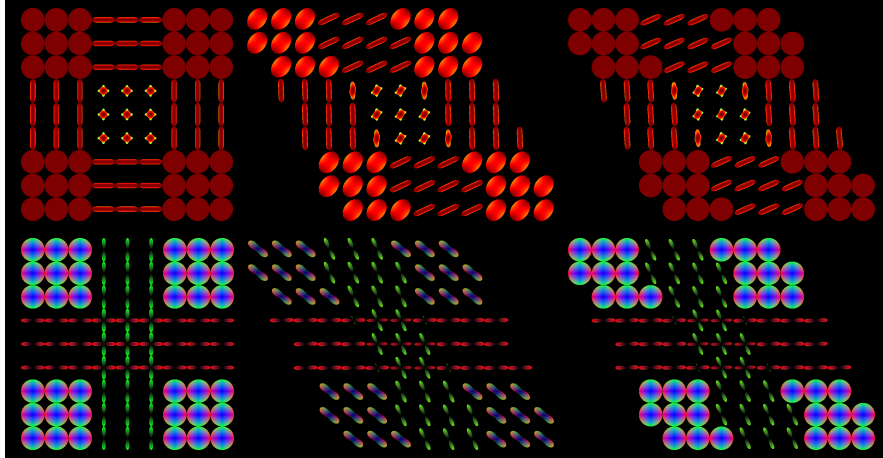


Fig. 3. The signal functions (*top left*) are sheared using TFR (8) (*top middle*). This however causes isotropic diffusion to become anisotropic. When using the new TFR (9), the problem is solved (*top right*). Corresponding fODF's calculated from the top row are also shown (*bottom row*).

However, examples can be found where the outcome will not satisfy. For instance, when shearing a voxel containing isotropic diffusion, we would like the outcome to still be isotropic, but this will not be the case due to the preservation of volume fractions. This example is also shown in Fig. 3. The problem is neither with the method nor the general idea of preserving volume fractions, but rather with the choice of fractions. We therefore suggest a new TFR of S as shown in Fig. 2d, which we define as

$$S(u) = pY_1 + \sum_{i=1}^Z a_i \alpha_n^{z_i}(u) \quad (9)$$

where the coefficient vector of a SH α_n^z function is $[0, e_2, e_3, \dots, e_T]^T$ (with $e_2 - e_T$ from the coefficient vector E of the corresponding SH β_n^z function). Because $Y_1 = Y_0^0$ is a constant function, we now obtain a single isotropic volume fraction (IVF) p and Z anisotropic volume fractions a_i . The result of using this new TFR in the case of the previous example can be seen in Fig. 3.

3 Results

We choose to focus on presenting a selection of results on the comparison of TFR (8) of S (Fig. 2c) – which is a translation of the method of Raffelt et al. [13] to q-space – and the new TFR (9) of S that accounts for IVF's (Fig. 2d).

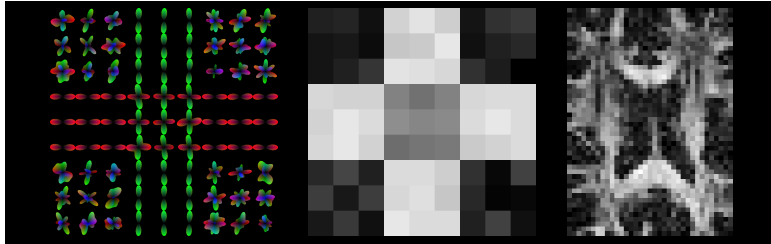


Fig. 4. The data: reconstructed fODF's (*left*) and GFA (*middle*) of the simulated data; GFA of the real data (*right*)

3.1 Data

Simulated data of a crossing was constructed for 75 gradient directions at $b = 3000s/mm^2$ using the multi-tensor model (anisotropic tensors with $\lambda_1 = 0.0018$ and $\lambda_2 = \lambda_3 = 0.0006$; isotropic tensors with $\lambda_1 = \lambda_2 = \lambda_3 = 0.0020$), after which Rician noise (SNR = 50) was added. Fig. 4 shows reconstructed fODF's from these data, as well as a generalized fractional anisotropy (GFA) image. GFA is calculated by

$$\text{GFA}(S) = \frac{\text{std}(S)}{\text{rms}(S)} = \sqrt{1 - \frac{c_1^2}{\sum_{j=1}^T c_j^2}} \quad (10)$$

straight on the SH coefficients of a signal function S .

Real data were acquired from a single healthy subject on a Siemens 3T scanner, with a $2.5mm$ isotropic voxel size, 75 gradient directions at $b = 2800s/mm^2$ and 10 repetitions of $b = 0$ (averaged). Fig. 4 shows a GFA image of the patch for which results are presented.

For both datasets, the SH coefficients of S were calculated up to order 6. To account for the noise, Laplace-Beltrami regularization was applied. From the SH representations of S , we then calculated both TFR's (8) and (9) (assuming a single fiber dODF kernel R' shaped by $\lambda_1 = 0.0018$ and $\lambda_2 = \lambda_3 = 0.0003$ to obtain the coefficient vectors of the SH β_n^z and α_n^z functions), with $Z = 300$ uniformly distributed directions z_i (obtained through electrostatic repulsion). Using each of both TFR's, 2 transformations were applied (a shear $[1, 0.5, 0; 0, 1, 0; 0, 0, 1]$ and a stretch $[1.5, 0, 0; 0, 1, 0; 0, 0, 1]$), after which the SH coefficients of the transformed S were again calculated. These were then compared in different ways.

3.2 Angular similarity

To compare the angular similarity between 2 signal functions, an angular similarity measure can be obtained by normalizing both SH coefficient vectors ($C_a^T C_a = C_b^T C_b = 1$) and calculating the inner product $C_a^T C_b$. It may as such vary between 0 and 1. We calculated this measure between the outcomes of using both TFR's. The results are shown in Fig. 5.

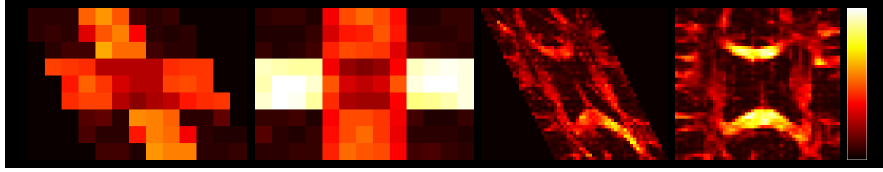


Fig. 5. Angular similarity after using both TFR's for the shearing and stretching of the simulated and real data. The color scale varies from 0.9966 (*dark*, less similar) to 0.9978 (*bright*, more similar).

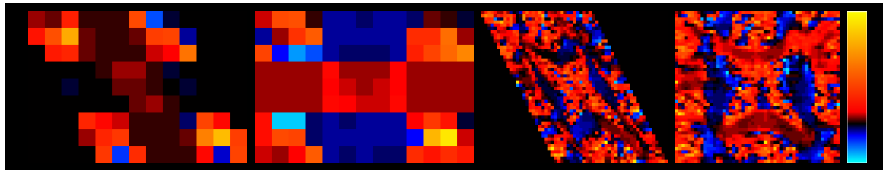


Fig. 6. Relative GFA difference after using both TFR's for the shearing and stretching of the simulated and real data. The color scale varies from 1/3 (*cyan*) over 1 (*black*) to 3 (*yellow*).

The first thing to notice is that the absolute values of the measure are very high. This makes sense, as the voxels compared should actually represent the same data, apart from the TFR used. Large differences in the angular structure itself are not expected. We are however interested in the relative difference between different tissue types: where does accounting for IVF's matter the most? The difference is clearly the largest in the more isotropic parts (this was also quite expected). However, the difference also seems to be dependent on the orientation of fibers relative to the transformation (this can most easily be seen in the stretching of the simulated data).

3.3 Relative GFA difference

GFA was calculated from the results of using TFR (8) and TFR (9) and relative GFA difference was defined as the division of the former (*not* accounting for IVF's) by the latter (accounting for IVF's). The results are shown in Fig. 6.

Not accounting for IVF's causes GFA to mostly go up in the isotropic parts. In the results of both simulated and real data, we also see that it is lowered in a few voxels of the isotropic parts. This can probably be attributed to specific interactions with the noise. In the other (more anisotropic) parts, the relative difference of GFA between both outcomes is clearly dependent on the specific combination of the local angular structure and the applied transformation: in some regions it goes up while in others it is lowered. The largest differences we could spot went up to a factor 3.

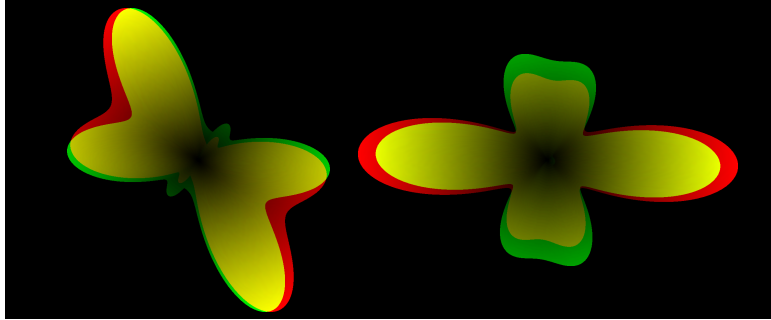


Fig. 7. Qualitative comparison after using both TFR’s for the shearing and stretching of the simulated data. fODF’s are calculated for a voxel in the crossing. The results after accounting (*green*) and not accounting for IVF’s (*red*) are overlaid.

3.4 Qualitative assessment

We also performed qualitative assessment on the signal functions as well as on fODF’s that were calculated from them. Due to the presence of IVF’s in many (if not all) voxels, we could spot differences in all voxels, of which the amount and nature corresponded to the earlier quantitative findings. As a clear example, we picked out a voxel in the crossing of the simulated data and calculated its fODF after applying the shearing as well as the stretching with both TFR’s. The results of accounting and not accounting for IVF’s were overlaid for comparison of shape. The results are shown in Fig. 7.

Not accounting for IVF’s caused the peaks to be less clearly separated in the case of the shearing. In the case of the stretching, we noticed that the peaks ended up with different relative sizes. It’s clear that the difference between accounting and not accounting for IVF’s in general can be seen in the end result as a difference in relative sizes between different volume fractions. In the case of a decreasing in angle between some peaks, an IVF that gets not accounted for (i.e. gets deformed) might cause peaks that are less clearly separated from each other than if the IVF would have been accounted for.

4 Discussion and Conclusion

In this work, we studied the problem of spatially transforming DWI data in q -space. Our main motivation is that it will enable us to perform registration on DWI data *before* the reconstruction of any particular model (a tensor, a dODF, a fODF, ... amongst others) while making maximum use of the information in the original data. We reasoned that the problem could be reduced to *affine transformation of the information in a single voxel*, because in the case of a non-rigid deformation field, the Jacobian matrix provides a local affine model for each voxel.

We started by looking into a simple method that is found in the literature [10, 11], which basically consists of applying the (local) affine transformation to

the gradient directions (and normalizing again) to obtain a new set of gradient directions. However, by use of a clear example, we showed that this method causes wrong results for affine transformations. The method could easily be fixed by not using the transformation matrix itself, but rather the inverse of its transpose, to reorient the gradient directions. This makes for a major difference in the end result. As the inverse of the transpose of a rigid rotation matrix equals again the original matrix, both the method and the fixed version give the same results for that specific case. We presume this fact to be the cause of why the issue could have been overlooked in the past.

But even this fixed method is not satisfactory, because it only reorients sampling directions (i.e. the magnitude of the samples itself is unaffected) and as such does not preserve volume fractions. Using (reversing) the methods of Descoteaux et al. [5–7] and starting from the representation of the fODF by a sum of SH delta functions as introduced by Raffelt et al. [13], we have shown how affine transformation of the fODF with preservation of volume fractions can be translated to equivalent approaches for transforming the dODF and the signals S in q -space. These approaches can in a way be seen as a natural extension of PPD, because each of the components of a TFR (Fig. 2) is independently subjected to a rigid PPD transformation.

Again reasoning on a simple example, we found our newly translated TFR (8) (Fig. 2c) not yet able to deal correctly with the case of isotropic diffusion. Therefore, we defined a new TFR (9) (Fig. 2d) of S by including an IVF, while preventing the other (anisotropic) volume fractions to represent any isotropic part (Fig. 2d). Using this new TFR for affine transformation, the IVF in each voxel is automatically preserved (as well as all the anisotropic volume fractions are). The impact of improvement is proportional to the magnitude of the IVF (i.e. inversely proportional to an anisotropy measure). While accounting for IVF’s mostly improves the outcome for the voxels containing less anisotropic tissue, it also has an impact on all other voxels in a real(istic) dataset, so just using an anisotropy mask doesn’t avoid the problem.

Because one of the major motivations for doing image registration might be a quantitative voxel based analysis, it is of high importance that the information inside each voxel gets transformed in the most correct way possible. We have shown that not accounting for the IVF has a clear impact on, for instance, a GFA measure that is calculated from the end result. There were also differences in angular structure as well as qualitative differences. These differences might even grow more severe if specific reconstruction schemes are applied after registration.

As our method can naturally deal with all voxels, be they anywhere in the spectrum between isotropic and highly anisotropic, no anisotropy mask is needed during registration and the information in all voxels can be put to good use. The method is mostly suited for HARDI data that consist of one or more shells in q -space. Each shell containing enough samples can then be represented in a SH basis, whereafter the method can be performed on the different shells. While we are as such able to spatially transform the data before the reconstruction of any particular model of diffusion, our method does however depend on a suitable

choice of the single fiber kernel. Using the SDT [7], the assumption of a tensor model is made for the construction of the kernel. In practice, it is also possible to estimate the single fiber signal response function from the data itself [3, 4]. This response function can then be used as the β function for TFR (8) (Fig. 2c), and the α function for TFR (9) (Fig. 2d) is easily obtained from the β function in the same way as we explained before. Using the methods of Descoteaux et al. [5–7] provides an insight that transcends the representation of HARDI data.

Future work will focus on incorporating this new model for transforming S in q-space while accounting for IVF’s in a coregistration algorithm, using the (angular) information in all voxels of the full brain volumes. This might then allow for better precision of the coregistration outcome, more reliable voxel-based analyses or the construction of a high quality full brain HARDI (q-space) atlas.

References

1. Tuch, D.S., Reese, T.G., Wiegell, M.R., Makris, N., Belliveau, J.W., Wedeen, V.J.: High Angular Resolution Diffusion Imaging Reveals Intravoxel White Matter Fiber Heterogeneity. *MRM* 48(4), 577–582 (2002)
2. Tuch, D.S.: Q-Ball Imaging. *MRM* 52(6), 1358–1372 (2004)
3. Tournier, J.D., Calamante, F., Gadian, D.G., Connelly, A.: Direct Estimation of the Fiber Orientation Density Function from Diffusion-Weighted MRI Data using Spherical Deconvolution. *NeuroImage* 23(3), 1176–1185 (2004)
4. Tournier, J.D., Calamante, F., Connelly, A.: Robust Determination of the Fibre Orientation Distribution in Diffusion MRI: Non-negativity Constrained Super-resolved Spherical Deconvolution. *NeuroImage* 35(4), 1459–1472 (2007)
5. Descoteaux, M., Angelino, E., Fitzgibbons, S., Deriche, R.: Apparent Diffusion Coefficients from High Angular Resolution Diffusion Imaging: Estimation and Applications. *MRM* 56(2), 395–410 (2006)
6. Descoteaux, M., Angelino, E., Fitzgibbons, S., Deriche, R.: Regularized, Fast, and Robust Analytical Q-Ball Imaging. *MRM* 58(3), 497–510 (2007)
7. Descoteaux, M., Deriche, R., Knösche, T.R., Anwander, A.: Deterministic and Probabilistic Tractography based on Complex Fibre Orientation Distributions. *IEEE TMI* 28(2), 269–286 (2009)
8. Alexander, D.C., Pierpaoli, C., Basser, P.J., Gee, J.C.: Spatial Transformations of Diffusion Tensor Magnetic Resonance Images. *IEEE TMI* 20(11), 1131–1139 (2001)
9. Barmpoutis, A., Vemuri, B.C., Forder, J.R.: Registration of High Angular Resolution Diffusion MRI Images using 4th Order Tensors. *MICCAI* 10(1), 908–915 (2007)
10. Tao, X., Miller, J.V.: A Method for Registering Diffusion Weighted Magnetic Resonance Images. *MICCAI* 9(2), 594–602 (2006)
11. Yap, P.T., Chen, Y., An, H., Gilmore, J.H., Lin, W., Shen, D.: Non-Parametric Deformable Registration of High Angular Resolution Diffusion Data using Diffusion Profile Statistics. *ISMRM* 18, 3968 (2010)
12. Hong, X., Arlinghaus, L.R., Anderson, A.W.: Spatial Normalization of the Fiber Orientation Distribution Based on High Angular Resolution Diffusion Imaging. *MRM* 61(6), 1520–1527 (2009)
13. Raffelt, D., Tournier, J.D., Fripp, J., Crozier, S., Connelly, A., Salvado, O.: Non-Linear Spatial Normalization of High Angular Resolution Diffusion Imaging Data using Fiber Orientation Distributions. *MICCAI* 12, DMFC Workshop (2009)

Building an Average Population HARDI Atlas

Sylvain Bouix¹, Yogesh Rathi¹, and Mert Sabuncu²

¹ Psychiatry Neuroimaging Laboratory, Brigham and Women’s Hospital, Harvard Medical School, Boston, MA, USA.

² A. A. Martinos Center for Biomedical Imaging, Massachusetts General Hospital, Harvard Medical School, Charlestown, MA, USA.

Abstract. We present a framework to build a High Angular Resolution Diffusion Image (HARDI) Atlas based on a population of HARDIs from different subjects. The method relies on a non-linear group-wise registration algorithm as well as a set of tools to re-orient the gradient directions of individual subjects and re-interpolate their diffusion weighted signal in a canonical gradient direction set in atlas space. We test the technique on a population of forty six HARDIs acquired on a 3 Tesla scanner. Our experiments show that our atlas can capture information beyond that of a single tensor, even with the inherent smoothing effect of averaging many different brains together.

1 Introduction

Diffusion Magnetic Resonance Imaging (dMRI) needs no introduction. It is one of the most active research areas in medical image analysis in particular in neuroimaging, where its ability to provide information about the location, orientation and “integrity” of white matter has become indispensable [1]. One popular technique for neuroimaging studies is the use of an atlas to describe a population, and several methods have been proposed to build a dMRI atlas from a population of subjects [2–4]. To our knowledge, all of these techniques use the Diffusion Tensor (DT) model to represent the diffusion information captured in the diffusion signal [5]. While DT imaging is still the *de facto* standard for neuroimaging analysis, more accurate diffusion models, capable of capturing more than a single primary orientation of diffusion, have been proposed and are becoming more prevalent [6–8].

In this article, we introduce a framework to build an *average population atlas of the original diffusion signal* without the use of a parametric model such as the DT (see for example [2, 9]). To our knowledge, only a couple attempts have been made to work with higher order signal [10, 11]. In [10] the authors rely on the 4th order tensor model to represent diffusion, whereas [11] uses a single tensor registration pipeline to transform the original dMRIs that are later used to fit a two tensor model. In contrast, we build a template of the diffusion signal directly, without the need for a model. Our work is inspired by the DT atlas building framework of [2] where an unbiased atlas building method designed for scalar data is used to compute diffeomorphic maps from each subject’s space to

template space and diffusion tensor images are resampled and reoriented using the diffeomorphic maps. The main challenge when working with HARDI data is that one does not have a model such as DT that can be reoriented easily through the diffeomorphic map. Our approach, described in detail in section 2, is to, for each voxel in each subject: (i) transform the original signal through the diffeomorphic maps; (ii) reorient the gradient directions associated with this voxel; (iii) estimate a spherical harmonic representation of the signal; and (iv) resample the diffusion signal in a canonical set of gradient directions. Our experiments show (section 3) that building a HARDI atlas from a large population of subjects can capture enough information to represent complex neuronal fiber architecture, which cannot be handled by a single diffusion tensor model.

2 Methods

2.1 Group-wise Non-linear Registration

In order to establish correspondence between all subjects, we use the Asymmetric Image-Template Registration method presented in [12]. This algorithm performs a non-linear alignment between a scalar individual image and a scalar template image that represents a population average. The heart of the method lies in using a bi-directional objective function that takes the asymmetric relationship between the individual image I and the template T into account by introducing a correction factor: the Jacobian that quantifies the deformation of the spatial grid. In mathematical terms, given an image I and a template T , the following objective function is minimized:

$$\hat{\Phi} = \arg \min_{\Phi} \frac{1}{2} \int_{\mathbb{R}^3} ([I(x) - T(\Phi(x))]^2 + [I(\Phi^{-1}(x)) - T(x)]^2 \det[\nabla\Phi^{-1}(x)]) dx + \text{Reg}(\Phi), \quad (1)$$

where $\Phi : \mathbb{R}^3 \mapsto \mathbb{R}^3$ is a smooth and invertible (i.e., diffeomorphic) transformation from the atlas coordinates to the coordinates of the individual image, ∇ denotes the Jacobian operator with respect to spatial coordinates, \det denotes the determinant, and Reg is a regularization term that penalizes non-smooth transformations. The transformation Φ is parametrized using a stationary velocity field via an ordinary differential equation [12]. An efficient solution to Eq. 1 is then computed by adapting the so-called “log-domain diffeomorphic demons” registration framework of [13].

For a given population of images $\{I_i\}$ and transformations $\{\Phi_i\}$ from the atlas coordinates to the corresponding image coordinates, an estimate of a template image that reflects the population average can be computed as [14]:

$$T(x) = \frac{\sum_i I_i(\Phi_i^{-1}(x)) \det(\nabla\Phi_i^{-1}(x))}{\sum_i \det(\nabla\Phi_i^{-1}(x))}. \quad (2)$$

Our *group-wise* registration procedure co-registers a population of images by iterating between computing the individual registrations by optimizing Eq. (1) and updating the template image using Eq. (2) and the latest estimates of the transformations. Crucially, at the end of each iteration we perform a normalization on the current transformation estimates so that the average transformation across the subjects is identity, i.e., $\sum_i \Phi_i(x) = x, \forall x$. These steps are repeated until convergence. The final result consists of a template image T and a set of diffeomorphic transformations $\{\Phi_i\}$ from the atlas coordinates to the individual image coordinates. In our experiments, similarly to [15], we used the scalar Fractional Anisotropy (FA) images derived from the individual dMRIs to perform the group-wise registration.

2.2 Transforming Individual HARDIs into Template space

If we were working with scalar images, our atlas would simply be the template computed in the previous section. However, when dealing with HARDI signal, one must perform additional steps.

Firstly, the rotational component of the non-linear transform must be extracted at each location in the input image, so that the gradient directions associated with this location can be rotated accordingly. We extract this rotation R by computing the finite strain of the Jacobian of the transformation as described in [16]:

$$R(x) = [\nabla\Phi(x)(\nabla\Phi(x))^T]^{\frac{1}{2}}\nabla\Phi(x). \quad (3)$$

Note that there is a *different rotation for each voxel* in the image.

Secondly, we transform and resample each gradient weighted component of the subject’s HARDI into atlas space as we would resample a scalar image, including scaling the MR signal by $\det(\nabla\Phi^{-1}(x))$.

The final result for each subject consists of: (i) the original set of gradient directions, (ii) R a 3D volume containing a rotation at each voxel, and (iii) the 4D HARDI signal transformed and resampled into atlas space.

2.3 Averaging the Resampled HARDIs

Since the HARDI signal at a voxel is a function defined on the sphere, an appropriate representation has to be used to compute the “average” signal. Spherical harmonics [17] provide one such basis in which averaging becomes a linear operation. The method works by first computing the coefficients of the spherical harmonic (SH) basis of order L that best fits the measured signal. Given any bandlimited signal S defined on the sphere, one can write it as an expansion in terms of the SH basis as: $S(\theta, \phi) = \sum_{l=0}^L \sum_{m=-l}^l c_{l,m} Y_{l,m}$, for any direction (θ, ϕ) , where $Y_{l,m}$ are the basis functions given by:

$$Y_{l,m}(\theta, \phi) = \sqrt{\frac{(2l+1)(l-m)!}{4\pi(l+m)!}} P_{l,m}(\cos\theta) e^{im\phi},$$

where $P_{l,m}$ is the associated Legendre polynomial. The above equations can be written as a linear system of equations and $c_{l,m}$ can be computed using the Moore-Penrose pseudo inverse. If needed, a regularization term can be added as shown in [17].

Let \mathbf{C}_i be the vector of coefficients $c_{l,m}$ that represents signal at a voxel for the i^{th} subject. Then, the average signal over M subjects can be computed by linear averaging: $\bar{\mathbf{C}} = \frac{1}{M} \sum_{i=1}^M \mathbf{C}_i$. Thus, the average signal at each voxel of the atlas is computed using the SH coefficients. Next, the average HARDI's of the atlas are computed by evaluating the signal (in the SH basis) in a specified set of directions. Our gradient direction scheme results from sampling the sphere on the vertices of a second order tessellation of the icosahedron, leading to 81 unique directions on the unit hemisphere.

3 Experiments and Results

3.1 Subjects

Forty-six HARDI scans from our Normal Control (NC) database were selected as input to our atlas building framework. The dataset contains 8 females and 38 males, the average age is 34.63 ± 12.13 years. Diffusion-weighted images were acquired on a 3T scanner (General Electric Company, Milwaukee, WI, USA) using an echo planar imaging (EPI) sequence, with a double echo option to reduce eddy-current related distortions. To reduce the impact of EPI spatial distortion, an 8 Channel coil and ASSET with a SENSE-factor of 2 were used. The acquisition consisted of 51 directions with $b = 900s/mm^2$, and 8 baseline images with $b = 0s/mm^2$. The scan parameters were: $TR = 17000ms$, $TE = 78ms$, $FOV = 24cm$, 144×144 encoding steps, $1.7mm$ slice thickness. A total of 85 axial slices covering the whole brain were acquired.

3.2 Building the atlas

We estimated Fractional Anisotropy (FA) maps for each HARDI scan and *rigidly* registered all FA maps to a randomly selected subject using FSL³ linear registration with six degrees of freedom. For each subject, the resulting transformation was applied to the HARDI scan, and the gradient directions were reoriented to account for the rotation introduced by the rigid alignment. We acknowledge here that we could have used an un-biased groupwise linear registration, the bias introduced in this step using a simpler rigid registration tool is clearly minimal. We then applied our atlas building pipeline as described in Section 2, using FA maps to compute the diffeomorphic maps and estimate the group template space.

Figure 1 shows the resulting atlas. As expected, the main white matter tracts are apparent, whereas the regions closer to neocortical areas are blurrier due to the variability of the anatomy between individuals.

³ <http://www.fmrib.ox.ac.uk/fsl/>

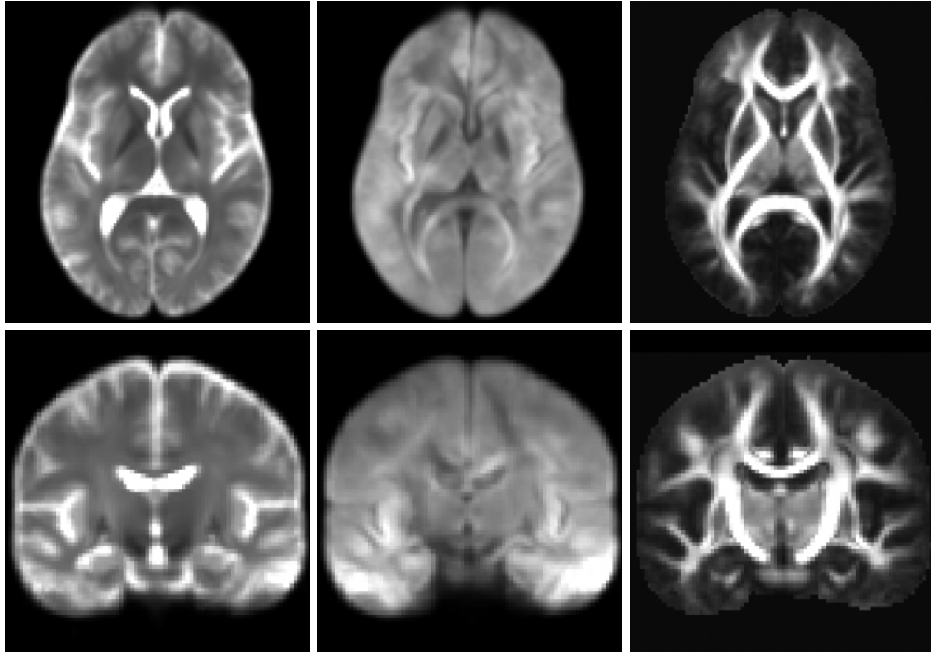


Fig. 1. An axial (top) and coronal (bottom) slice of the population HARDI atlas. Left: $b=0$ image, center: one of the resampled gradient directions, right: FA map of the tensor map estimated from the HARDI atlas.

3.3 Evaluation with tractography

In order to evaluate the benefits of building a HARDI instead of a DT template, we ran single tensor as well as two-tensor tractography on the atlas. The algorithm we used simultaneously estimates the diffusion model and performs tractography. Starting from a seed point, each fiber is traced to its termination using an un-scented Kalman filter to simultaneously fit the local model of diffusion and propagate in the most consistent direction [18].

We seeded the tractography in the midsagittal slice of the corpus callosum. The experiment was run twice, the first time using a single tensor as the diffusion model and the second time using two-tensor as the diffusion model. Results are shown in figure 2. We are pleased to report that although averaging over many subjects significantly smoothes the diffusion signal, the atlas captures enough information for the two-tensor tractography to accurately handle fiber crossings.

We further illustrate the accuracy of the estimation in figure 3. Observe that the algorithm correctly aligns both the first and second tensor to the same direction in the central section of the corpus callosum (fig. 3 center). Additionally, and perhaps most importantly, in the area where the cortico-spinal tract and the corpus callosum fibers intersect, one can see that the first and second tensor are

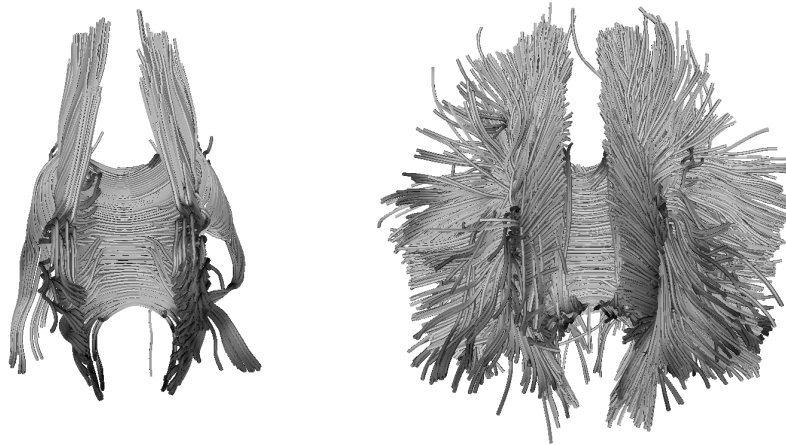


Fig. 2. Tractography of the Corpus Callosum of the atlas using single tensor tractography (left) and two tensor tractography (right). Note the atlas captures enough information for the two tensor tractography to resolve fiber crossings.

in perpendicular directions, thus correctly reflecting the anatomy in this region (fig. 3 right).

4 Discussion

In this paper, we present a framework to build a HARDI atlas from a population of individual HARDIs. Our method relies on an unbiased, bi-directional, asymmetric group-wise registration algorithm which computes a template space and a set of diffeomorphic maps to bring individual subjects into this template space. The resulting maps are used to transform and resample the original HARDIs into template space and extract rotation maps which capture the rigid transformation that needs to be applied to the gradient direction set at each voxel in each subject. In order to average the diffusion signal in template space, we first estimate a spherical harmonic representation of the HARDI signal for each *transformed* subject and resample the signal in a canonical set of gradient directions. The resulting image is a 4D HARDI volume, which can then be used for further processing using *any* model to describe the Orientation Distribution Function.

There are some limitations to such an atlas. Firstly, using a scalar image to derive the diffeomorphic maps may be suboptimal, although recent work suggest that using a high Contrast to Noise Ratio image (such as a high resolution anatomical T1 weighted) can lead to very accurate dMRI registrations [19]. The use of FA in particular is controversial as it is often used as a primary measure in further statistical analyses. In such cases, we would likely use a different measure such as Goodlett’s “C” measure [2]. Secondly, no matter how accurate

the registration is, averaging over a large number of subjects inevitably leads to smoothing the diffusion signal and losing some of the sharpness of the ODF in particular in regions close to the neocortex. Nevertheless, we have shown that sufficient information is captured in the atlas to resolve complex fiber architecture. Thirdly, our registration procedure utilized a method originally derived for scalar images. Obviously, here we are dealing with HARDIs and a rigorous derivation of an appropriate cost function for this type of signal for group-wise registration and template estimation is left to future work.

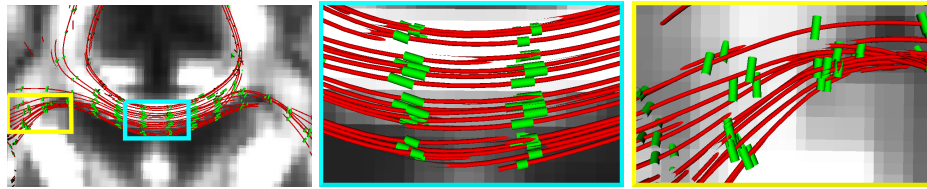


Fig. 3. Close up views of two tensor tractography on a coronal slice of the atlas. The green tubes represent the estimation of the second tensor superimposed on the (red) streamline obtained by tracking along the first tensor. In the central section of the CC, the first and second tensors are aligned (center), whereas at the location where cortico-spinal tract and CC intersect, the second tensor is perpendicular to the first (right).

To summarize, we have presented in this article a new method to build an unbiased group-wise HARDI population atlas. We believe such a template to be of great relevance in the dMRI world, especially in neuroimaging studies where statistics of diffusion properties over clinical populations are of the utmost interest. Deriving meaningful statistics from our HARDI atlas will be the focus of our future work.

Acknowledgements. Support for this research was provided in part by the National Institutes of Health Roadmap for Medical Research (U54EB005149), the National Center for Research Resources (P41RR14075), the National Institute for Biomedical Imaging and Bioengineering (R01EB006758), the National Institute on Aging (AG02238), and the National Institute for Neurological Disorders and Stroke (R01NS052585), the National Institute of Mental Health (R01MH50740, K05MH070047, P50MH080272, R01MH082918, R03TW008134), Department of Veteran Affairs Merit Awards, VA Schizophrenia Center grant, and Center for Integration of Medicine and Innovative Technology Soldier in Medicine Award.

References

1. Bihan, D.L.: Looking into the functional architecture of the brain with diffusion mri. *Nature Reviews Neuroscience* **4** (2003) 469–480

2. Goodlett, C., Davis, B., Jean, R., Gilmore, J., Gerig, G.: Improved correspondence for dti population studies via unbiased atlas building. In: MICCAI. Volume 4191. (2006) 260–267
3. O’Donnell, L., Westin, C.: Automatic tractography segmentation using a high dimensional white matter atlas. *IEEE Trans Med Imaging* **11**(26) (2007) 1562–75
4. Maddah, M., Grimson, W., Warfield, S., Wells, W.: A unified framework for clustering and quantitative analysis of white matter fiber tracts. *Med Imag Anal* **12**(2) (2008) 191–202
5. Basser, P., Mattiello, J., LeBihan, J.: Estimation of the effective self-diffusion tensor from the nmr spin echo. *J. Magn. Reson. B* **103**(3) (1994) 247–54
6. Peled, S., Friman, O., Jolesz, F., Westin, C.: Geometrically constrained two-tensor model for crossing tracts in dwi. *Magn. Reson. Imaging* **24**(9) (2006) 1263–70
7. Descoteaux, M., Deriche, R., Knosche, T., Anwander, A.: Deterministic and probabilist tractography based on complex fibre orientation distribution. *IEEE Trans. Med. Imaging* **28**(2) (2009) 269–86
8. Jian, B., Vemuri, B.: A unified computational framework for deconvolution to reconstruct multiple fibers from diffusion weighted mri. *IEEE Trans. Med. Imaging* **26**(11) (2007) 1464–71
9. Zhang, H., Yushkevich, P., Rueckert, D., Gee, J.: Unbiased white matter atlas construction using diffusion tensor images. In: MICCAI. Volume 4792. (2007) 211–18
10. Barmputis, A., Vemuri, B.C.: Groupwise registration and atlas construction of 4th-order tensor fields using the \mathbb{R}^+ riemannian metric. In: MICCAI. Volume 5761. (2009) 640–47
11. Caan, M., Sage, C., van der Graaf, M., Grimbergen, C., Sunaert, S., van Vliet, L., Vos, F.: Dual tensor atlas generation based on a cohort of coregistered non-hardi datasets. In: MICCAI. Volume 5761. (2009) 869–76
12. Sabuncu, M.R., Yeo, B.T.T., Leemput, K.V., Vercauteren, T., Golland, P.: Asymmetric image-template registration. In: MICCAI. Volume 5761. (2009) 565–573
13. Vercauteren, T., Pennec, X., Perchant, A., Ayache, N.: Symmetric log-domain diffeomorphic registration: A demons-based approach. In: MICCAI. Volume 5241. (2008) 754–61
14. Ashburner, J., Friston, K.: Computing average shaped tissue probability templates. *Neuroimage* **45**(2) (2009) 333–341
15. Smith, S., Jenkinson, M., Johansen-Berg, H., Rueckert, D., Nichols, T., Mackay, C., Watkins, K., Ciccarelli, O., Cader, M., Matthews, P., Behrens, T.: Tract-based spatial statistics: Voxelwise analysis of multi-subject diffusion data. *NeuroImage* **31** (2006) 1487–505
16. Alexander, D., Pierpaoli, C., Basser, P., Gee, J.: Spatial transformations of diffusion tensor magnetic resonance images. *IEEE Trans. Med. Imaging* **20**(11) (2001) 1131–39
17. Descoteaux, M., Angelino, E., Fitzgibbons, S., Deriche, R.: Regularized, fast and robust analytical q-ball imaging. *Magnetic Resonance in Medicine* **58**(3) (2007) 497–510
18. Malcolm, J.G., Shenton, M., Rathi, Y.: Two-tensor tractography using a constrained filter. In: MICCAI. Volume 5761. (2009) 894–902
19. Zollei, L., Stevens, A., Huber, K., Kakunoori, S., Fischl, B.: Improved tractography alignment using combined volumetric and surface registration. *Neuroimage* **51** (2010) 206–213

DTI Registration for Atlas Based Fiber Tract Analysis in Infantile Krabbe Disease

Yi Wang^{1,2}, Zhexing Liu², Maria L. Escolar³, Michele Poe³, Hui Zhang⁴, John H. Gilmore², Eric Maltbie², Casey Goodlett⁵, Guido Gerig⁵, Martin Styner^{2,6}

¹ School of Electronics and Information, Northwestern Polytechnical University, Xi'an, Shaanxi, China ² Dept. of Psychiatry, ³ Clinical Center for the Study of Development and Learning and ⁶ Depts. of Computer Science, University of North Carolina at Chapel Hill, NC, USA ⁴ Centre for Medical Image Computing, Department of Computer Science, University College London, UK ⁵ Scientific Computing and Imaging Institute, School of Computing, University of Utah, Salt Lake City, Utah, USA

Abstract. Diffusion tensor imaging (DTI) has become the modality of choice to investigate white matter pathology in the developing brain. In this work, we evaluate a series of DTI registration algorithms for the explicit use with our atlas based fiber tract analysis framework in order to study neonate Krabbe's disease. We first created a neonate atlas based on 377 healthy control subjects. Then we mapped DTI scans of 10 age-matched neonates with infantile Krabbe's disease into this normative atlas. One linear and five nonlinear commonly used registration algorithms for DTI registration were investigated. We propose the use of two novel evaluation metrics: an atlas based, regional matching quality criterion incorporating the local orientation match, as well as a fiber tract profile based metric using normative correlation. Our experimental results indicate that most of the registration tools were performing similarly well, but that the whole tensor registration "DTI-TK" seems to perform best for our purpose.

Keywords: Diffusion tensor imaging, Registration, Fiber tracking, Krabbe disease

1 Introduction

Diffusion tensor imaging (DTI) is a relatively new technique, but has become increasingly important for studies of anatomical and functional connectivity, as well as of fiber architecture in the living human brain via DTI tractography. DTI has proven especially of value in clinical studies of white matter (WM) integrity in the developing brain for diseases such as Cerebral Palsy or leukodystrophies[1,2,3,4].

Krabbe disease (also called globoid cell leukodystrophy) is a rare, often fatal genetic disorder of the nervous system caused by a deficiency of an enzyme called galactocerebrosidase, which aids in the breakdown and removal of galactolipids found

2 Yi Wang^{1,2}, Zhexiong Liu², Maria L. Escolar³, Michele Poe³, Hui Zhang⁴, John H. Gilmore², Eric Maltbie², Casey Goodlett⁵, Guido Gerig⁵, Martin Styner^{2,6}

in myelin. If left untreated, Krabbe is usually fatal within the first 2 years of life [5]. Treatment at asymptomatic, neonate stage has shown to stop disease progression [5]. Previous research also showed that patients with infantile Krabbe disease have lower FA across the corpus callosum [2] and along the DTI fiber bundle of internal capsules (IC) [1] compared with healthy controls. The results in [1] also show a correlation of pretreatment FA measurements with posttreatment gross motor function.

One of the goals of our ongoing clinical studies in Krabbe is the use of atlas based fiber tract analysis of DTI properties [1,6]. In this procedure the proper establishment of registration based voxel-wise correspondence between an existing normal control neonate DTI atlas that includes prior information of fiber tract locations and the Krabbe subject DTI images is crucial for an appropriate analysis. The research presented highlights our work to find the best state-of-the-art approach to individually register DTI image of Krabbe subjects into the atlas space at neonate stage.

According to [7], DTI registration algorithms can be categorized into two groups. One of them uses scalar images derived from DTI images and performs deformable registration with traditional image registration algorithm [8,9,10]. The other group of DTI registration algorithms directly uses higher order information of diffusion tensor images, e.g. corresponding principal eigenvectors [11], or the full tensor [7,12].

We investigate 6 DTI registration approaches available either in-house or publicly:

- 1) Affine registration [13] using normalized mutual information as a registration metric within the Image Registration Toolkit¹ (referred to as “Affine” in this paper);
- 2) B-spline based registration [8] using normalized mutual information as a registration metric within the Image Registration Toolkit (referred to as “B-spline”);
- 3) B-spline based registration [9] using weighted sum-of-squared differences as a registration metric via the “fnirt” implementation within FSL² (referred to as “FSL”);
- 4) Diffeomorphic demons [14] using sum-of-squared differences as a registration metric³ (referred to as “Demons”);
- 5) Fluid registration [10] using sum-of-squared differences as a registration metric (referred to as “Fluid”);
- 6) Tensor-based registration [7] using explicit optimization of tensor reorientation in an analytic manner within the DTI ToolKit⁴ (referred to as “DTI-TK”).

For the evaluation, we introduce two novel evaluation metrics. The first is a matching quality metric that incorporates the local tensor orientation and atlas anisotropy. The voxel-wise metric values are averaged over predetermined regions within the atlas (genu, splenium, internal capsule). The second evaluation metric employs a normative fiber tract profile based criterion, which computes the correlation of the fiber FA profile along the major tracts in the registered dataset and the atlas.

Since FA values of neonates are significantly lower than those of adults and moreover FA values of Krabbe patients are lower than those of healthy controls, the

¹ <http://www.doc.ic.ac.uk/~dr/software>

² <http://www.fmrib.ox.ac.uk/fsl/fnirt>

³ <http://hdl.handle.net/1926/510>

⁴ <http://www.nitrc.org/projects/dtitk>

presented setup poses a rather tough challenge to the selected registration algorithms due to the low SNR settings and the presence of pathological white matter.

2 Materials and methods

2.1 Subjects and scans

For the difficulty of acquisition of such data, ten neonates with Krabbe disease identified by family history or through the New York State screening program were referred to the Program for Neuro developmental Function in Rare Disorders for assessment of baseline neurologic function before receiving unrelated umbilical cord blood transplantation. The assessment included a detailed neuro developmental evaluation concurrent with a brain MR imaging within the first four weeks of life. 377 age-matched neonatal controls were recruited in a separate, unrelated study of brain development in normal controls and high risk offsprings as part of the UNC Conte center [15].

All neonates (control and Krabbe subjects) were scanned without sedation on an Allegra 3T head-only MR scanner (Magnetom Allegra; Siemens, Erlangen, Germany). Two separate DTI protocols were employed. Protocol 1 acquired seven images, one without diffusion gradient ($b=0$) and six diffusion weighted images along unique gradient directions with $b=1000 \text{ s/mm}^2$ (TR= 4219 ms; TE=92.2 ms; in-plane resolution = $2 \times 2 \text{ mm}^2$, slice thickness 2 mm, five averages). A newer protocol, Protocol 2, acquired 49 images, seven without diffusion gradients ($b=0$) and 42 diffusion weighted images along unique gradient directions with $b=1000 \text{ s/mm}^2$ (TR= 7680 ms; TE=82 ms; in-plane resolution = $2 \times 2 \text{ mm}^2$, slice thickness 2 mm, one average). The first seven Krabbe neonates as well as all healthy control subjects were scanned with protocol 1 (K1 to K7). The three final Krabbe neonates were scanned with protocol 2 (K8~K10.) No sedation was used; all scans were performed with subjects fully asleep. Neonates were fed before scanning, then swaddled, fell asleep and were fitted with ear protection and had their heads secured in a vacuum-fixation device. A physician or nurse was present during each scan; a pulse oximeter was used to monitor heart rate and oxygen saturation.

2.2 DTI atlas building

In order to build the normative DTI atlas, we used a scalar, unbiased diffeomorphic atlas building method based on a nonlinear high-dimensional fluid deformation method [10]. Based on studies in [16], the DTI derived feature selected for atlas building is the intensity-histogram normalized Fractional Anisotropy (FA). We did not investigate the use of alternative atlas building methods as part of this paper.

4 Yi Wang^{1,2}, Zhexiong Liu², Maria L. Escobar³, Michele Poe³, Hui Zhang⁴, John H. Gilmore², Eric Maltbie², Casey Goodlett⁵, Guido Gerig⁵, Martin Styner^{2,6}

2.3 Pre-processing of Krabbe datasets

We performed quality control (QC) on all datasets using the DTIPrep⁵ tool, which can detect artifacts in diffusion weighted images (DWI) data before DTI estimation and also cropped or embedded all datasets into consistent image dimensions. The diffusion tensors were estimated for each dataset from the QC'ed DWIs using weighted least squares tensor estimation [17]. Skull stripping was performed semi-automatically for all Krabbe datasets by a trained expert.

2.4 Registration Methods

In this section, we summarize six evaluated registration methods. The first five methods are based on intensity-histogram normalized FA images, while the last one is based on the whole tensor. In order to be consistent across methods, we only adopted the deformation fields from each registration method and performed DTI reorientation and interpolation using the same software for all methods via standard a finite strain tensor realignment [18].

“Affine” registration is a linear transform method that is commonly used as initialization for most deformable registrations [11], as is the case for all other methods evaluated in this paper. The affine registration used in this paper optimizes the 15 linear parameters by maximization of normalized mutual information in a multi-resolution framework using Gaussian smoothing to compute lower resolution steps.

“B-spline” is a parametric, non-rigid image registration method based on a multi-resolution adaptable free-form deformations using B-splines [8]. As for “Affine”, this method also maximizes normalized mutual information in a multi-resolution framework using Gaussian smoothing to compute lower resolution steps.

“FSL” (or rather “FSL-B-Spline”) is similar to the previous method, in that it represents displacement fields as B-splines on a regular grid [9]. The regularization of the field is though based on membrane energy, and the registration criterion uses the weighted sum of the sum-of-squared intensity differences and the membrane energy.

“Demons” is a non-parametric, diffeomorphic deformable image registration algorithm [14]. The deformation model is based on optical flow and the registration criterion employs the sum-of-squared intensity differences.

“Fluid” is a non-parametric, diffeomorphic deformable image registration that employs a dilatational-viscous fluid flow formulation [10] with sum-of-squared intensity differences as the registration criterion.

“DTI-TK” is a non-parametric, diffeomorphic deformable image registration [19] that incrementally estimates its displacement field using a tensor-based registration formulation [7]. It is designed to take advantage of similarity measures comparing tensors as a whole via explicit optimization of tensor reorientation [7].

⁵ <http://www.nitrc.org/projects/dtiprep>

2.5 Evaluation of Registration Accuracy

In central white matter (WM), FA values in DTI of neonates are considerably lower than those of subject at older ages [6]. Meanwhile, white matter pathology causes the FA values of Krabbe patients to be even lower than those of healthy controls. In addition, Krabbe subjects are likely to have regionally differing levels of white matter pathology. All of these observations indicate that the presented evaluation is a challenging test for the registration tools, as well as its results may not easily be generalized to other settings.

For our evaluation, we tested one linear and five nonlinear algorithms to determine the most suitable method for our application. We mainly focused on tracts of the genu and the splenium of the corpus callosum as well as both hemispheric internal capsule tracts, but the same tests can be extended to a larger selection of tracts.

While there are several ongoing initiatives towards an unbiased evaluation of deformable registration algorithms, there is currently no widely accepted metric standard for the evaluation of nonlinear registration algorithms, even more so for DTI registration. The first step of our evaluation strategy consists in a qualitative, visual quality control. For that purpose, we visualize FA and color-oriented FA images of all the registered datasets using a multi-dataset overview with MRIWatcher⁶. This kind of assessment is subjective and cannot detect minor differences. But significant errors are easily spotted and the dataset is marked as a failure for the registration.

Regional matching quality criterion: For the second step in our evaluation framework, we proposed a novel regional matching criterion that is tailored to atlas based analysis methods. In our specific setting, we have the following conditions: 1) the streamline fiber tractography employed in our fiber based analysis framework is purely based on the local principal eigenvectors \mathbf{e}_P (i.e. the vector associated with the largest of the three principal directions of the diffusion tensor: $\lambda_1 \geq \lambda_2 \geq \lambda_3$); 2) based on prior studies, we focus on fiber tracts of the genu and splenium in the corpus callosum as well as both hemispheric internal capsule tracts, which all have higher intensity in the FA images as compared to their neighboring tracts.

For the proposed criterion, the orientation agreement between principal eigenvectors of the source, i.e. the individual subject, and the target, i.e. the atlas, is the main focus. In order to enhance the specific regions associated with our tracts, as well as to render the method stable against small changes in the regional definition, we aimed to use the FA value of the atlas as a weight on local orientation criterion. Thus, the proposed similarity value s_v is defined for each voxel as follows:

$$s_v = |\mathbf{e}_{PI} \cdot \mathbf{e}_{PA}|FA_A \quad (1)$$

where \mathbf{e}_{PI} is the subject's principal eigenvector, \mathbf{e}_{PA} is the atlas' principal eigenvector, and $FA_A \in (0, 1)$ is the atlas FA value. Notation $[\cdot]$ indicates the dot product. In case that the principal eigenvectors of the individual subject and the atlas are oriented in similar or fully opposite direction, $|\mathbf{e}_{PI} \cdot \mathbf{e}_{PA}|$ will equal to $|\mathbf{e}_{PA}|^2$,

⁶ <https://www.ia.unc.edu/dev/download/mriwatcher>

6 Yi Wang^{1,2}, Zhexiong Liu², Maria L. Escobar³, Michele Poe³, Hui Zhang⁴, John H. Gilmore², Eric Maltbie², Casey Goodlett⁵, Guido Gerig⁵, Martin Styner^{2,6}

which is 1, and s_v will equal to FA_A . Using this local criterion, we compute a scalar matching image representing the registration quality at each voxel.

Using prior definitions of regions of interest (ROI) on the atlas that represent the major areas of our target fiber tracts, the average regional similarity values represents the regional matching quality criterion. Thus for region r , the average similarity value \bar{s}_r is computed as

$$\bar{s}_r = \frac{1}{N_r} \sum_{i=1}^{N_r} s_{v,i} \quad (2)$$

where N_r is the number of voxels in region r , $s_{v,i}$ is the similarity value at voxel i . Larger values of \bar{s}_r represent higher values of registration accuracy in our settings.

Fiber tract property profile based criterion: As a last and third step in our evaluation framework, we propose another novel matching criterion that evaluates the DTI property measurements along the fiber tracts, called tract profiles, as detailed by Goodlett et al. [6]. In brief, prior fiber tracts, which were tracked in atlas space, are resampled in each registered DTI dataset. Using a prior definition of a tract origin plane, which defines a curvilinear re-parameterization of the tracts, corresponding average tract property profiles (we focus on FA profiles here) are extracted from each individual fiber tract. The average is thereby computed across the individual streamlines and the profile is plotted along the fiber tract.

For the evaluation, we calculated the normative correlation between each average tract profile in the registered subjects' DTI datasets and the mean of all the healthy control datasets in atlas space. For this criterion we expect larger values to represent better accuracy in registration. It is further noteworthy that high degrees of white matter pathology are likely to decrease this evaluation metric, though that does not lessens its comparative merit in the presented work here.

3 Experimental Results

We present detailed results for an individual, representative case, K8, as well as the summary results across the whole Krabbe population of 10 subjects. As illustrated in Fig 1, qualitative inspection of the registration results of K8 indicates that all deformable registration algorithms seem to do show appropriate results, whereas affine registration does not fully represent the atlas anatomy. When we consider the orientation-coded color FA images, Fig. 2, several qualitative differences become apparent, as "B-spline" captures the local anatomy and orientations less well than the others. No major visual differences are detectable between the latter four methods.

For the regional matching criterion, we manually defined four regions on the atlas. The regions were selected as representative of the four main tracts of interest. We repeated the full evaluation (details not shown here due to space limitations) with slightly modified regional definitions (independently and manually redefined these four regions), and the results show that the computed regional matching criterion is stable and reliable.

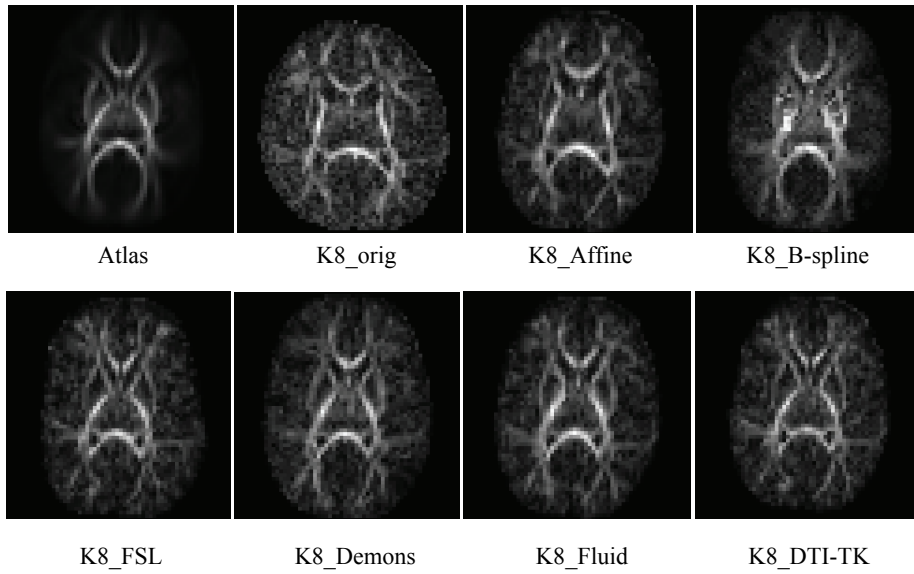


Fig. 1. FA images of atlas, K8 and its five registration results

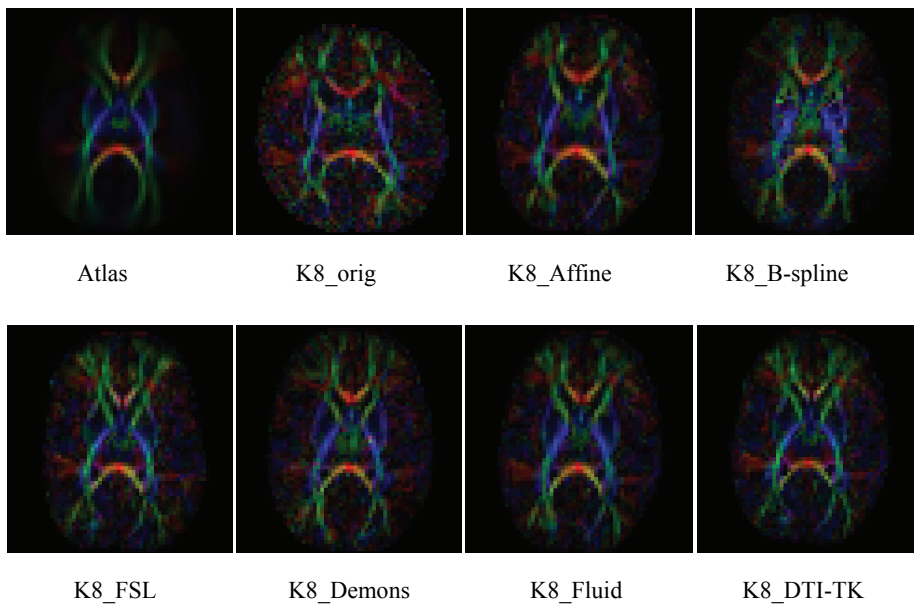


Fig. 2. Color-oriented FA images of atlas, K8 and its five registration results

K8’s regional matching values are shown for each region and registration method in Table 1. The table illustrates the effectiveness of our regional matching quality criterion to be useful both for potential quality control of DTI registration, as well as a valid evaluation measure that highlights differences across methods.

The mean and standard deviation of the regional similarity values and the correlation coefficients of each region across all subjects are shown in Table 2. The results in Table 2 indicate that “DTI-TK” gives the best results on average and is in the group of best for all tracts, although none of the six registration methods gives optimal result in each region and subject.

Table 3 shows the mean and standard deviation of the normative tract profile correlation values of the selected 4 fiber tracts. The results in Table 3 indicate that “DTI-TK” is performing best in the splenium, only slightly worse than “FSL” in the genu, while slightly worse than both “Demos” and “Fluid” in both hemispheres of internal capsule. It is thus harder to identify the best method for the normative tract profile correlation evaluation, though summarized over all fiber tracts “DTI-TK” seems to do best.

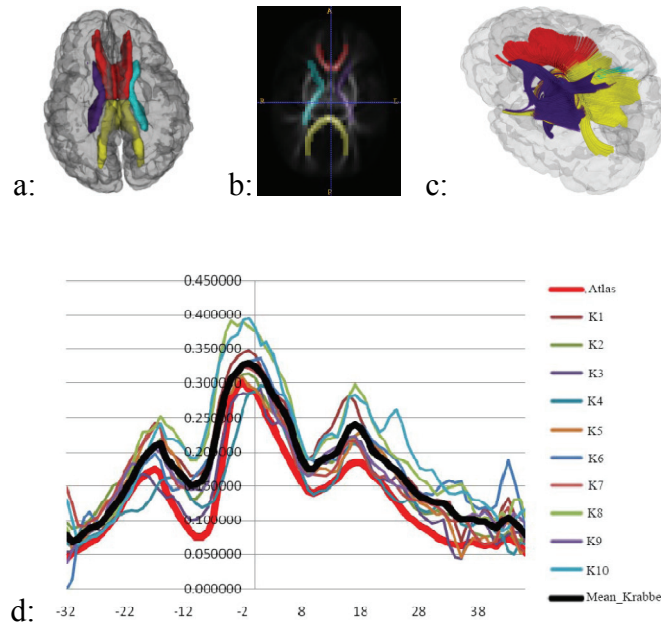


Fig. 3. Regional definition in 3D (a) and on an axial FA slice (b) (Red = genu. Yellow = splenium. Purple & Blue = left and right internal capsule). c: 3D visualization of target fiber tracts colored by ROIs. d: Example fiber profile (average FA value along the fiber) for all subjects of the right internal capsule tract.

Table 1. K8's average similarity value of each ROI and registration method

	Genu	Splenium	IC_left	IC_right
Affine	0.113	0.142	0.133	0.117
B-spline	0.115	0.142	0.170	0.163
FSL	0.123	0.151	0.190	0.187
Demons	0.120	0.145	0.180	0.177
Fluid	0.123	0.151	0.184	0.183
DTI-TK	0.126	0.152	0.193	0.192

Table 2. Mean and standard deviation of average similarity values of each ROI and registration method. "DTI-TK" performs best on average. Results that were significantly different as compared to "DTI-TK" were labeled with * (p<5%) and ** (p<1%).

	Genu	Splenium	IC_left	IC_right
Affine	0.118/0.006**	0.141/0.006**	0.133/0.009**	0.131/0.020**
B-spline	0.110/0.006**	0.132/0.007**	0.150/0.017**	0.148/0.017**
FSL	0.126/0.003*	0.151/0.003	0.191/0.003	0.187/0.007
Demons	0.121/0.004*	0.146/0.003**	0.183/0.004**	0.181/0.006**
Fluid	0.124/0.003*	0.148/0.003**	0.184/0.002**	0.180/0.005**
DTI-TK	0.127/0.003	0.152/0.004	0.193/0.003	0.191/0.003

Table 3. Mean and standard deviation of correlation coefficients of each tract and registration method. "DTI-TK" is performing best in the splenium, only slightly worse than "FSL" in the genu, while slightly worse than both "Demons" and "Fluid" in both hemispheres of internal capsule. Results that were significantly different as compared to "DTI-TK" were labeled with * (p<5%) and ** (p<1%).

	Genu	Splenium	IC_left	IC_right
Affine	0.508/0.285**	0.643/0.288*	0.571/0.095**	0.670/0.056**
B-spline	0.906/0.069	0.859/0.071	0.845/0.146*	0.919/0.058
FSL	0.951/0.033	0.887/0.063	0.945/0.022	0.929/0.043
Demons	0.877/0.083*	0.799/0.147*	0.954/0.016	0.950/0.023
Fluid	0.926/0.068	0.865/0.095	0.958/0.011	0.953/0.018
DTI-TK	0.949/0.032	0.893/0.048	0.950/0.012	0.936/0.028

4 Conclusion

In this paper, we evaluated one linear and five nonlinear popular registration methods for use in an atlas based DTI fiber analysis framework on 10 neonates with infantile Krabbe disease. Our results show that all registration algorithms do a fairly good job when we only inspect FA images. But when considering the local orientation, which is highly relevant to fiber tracking based analyses, several methods underperformed,

10 Yi Wang^{1,2}, Zhexing Liu², Maria L. Escolar³, Michele Poe³, Hui Zhang⁴, John H. Gilmore², Eric Maltbie², Casey Goodlett⁵, Guido Gerig⁵, Martin Styner^{2,6}

while the whole tensor registration using explicit optimization of tensor reorientation in an analytic manner performed best on average, though by a slim margin.

In one word, “Affine” is not “deformable” enough for our setting. Choice of deformation model seems to influence, i.e. highly deformable is better (thus when using b-spline, use a fine sampling of control points). Choice of scalar metric, e.g. SSD (sum of squared difference) or MI (mutual information), does not seem to make a difference for our setting. Results of different choice of scalar or tensor difference show that using full tensor or more than simple scalar measures is better for fiber tract analysis.

As is the case with any evaluation metric, the question can be raised, why this measure could not be used for the purpose of registration itself. The answer of this question with respect to the regional matching criterion, which can be represented in a voxel-wise manner, is currently under investigation in our lab.

5 Acknowledgments

This work was supported by the National Natural Science Foundation of China (Grant No.60903127); the National Alliance for Medical Image Computing (NAMIC, NIH U54 EB005149); the Autism Centers of Excellence Network at UNC-CH (NIH R01 HD055741), the Neurodevelopmental Research Center at UNC-CH (NIH P30 HD031110); and the National Institute of Mental Health Conte Center at UNC-CH (MH064065).

We also thank Daniel Rueckert and IXICO. The Image Registration Toolkit was used under Licence from Ixico Ltd.

References

1. Escolar, M.L., Poe, M.D., Smith, J.K., Gilmore, J.H., Kurtzberg, J., Lin, W., Styner, M.: Diffusion tensor imaging detects abnormalities in the corticospinal tracts of neonates with infantile Krabbe Disease. *AJNR* 30, 1017--1021 (2009)
2. Guo, A.C., Petrella, J.R., Kurtzberg, J., Provenzale, J.M.: Evaluation of white matter anisotropy in Krabbe disease with diffusion tensor MR imaging: initial experience. *Radiology* 218 (3), 809--815 (2001)
3. Yoshida, S., Hayakawa, K., Yamamoto, A., Okano, A., Kanda, T., Yamori, Y., Yoshida, N., Hirota, H. Quantitative diffusion tensor tractography of the motor and sensory tract in children with cerebral palsy. *Developmental medicine and child neurology* (2010) in print
4. Huang, H., Zhang, J., Wakana, S., Zhang, W., Ren, T., Richards, L.J., Yarowsky, P., Donohue, P., Graham, E., van Zijl, P.M.C., Mori, S. White and gray matter development in human fetal, newborn and pediatric brains. *Neuroimage* 33 (1), 27--38 (2006)
5. Escolar, M., Poe, M.D., Provenzale, J.M., Richards, K.C., Allison, J., Wood, S., Wenger, D.A., Pietryga, D., Wall, D., Champagne, M., Morse, R., Krivit, W., Kurtzberg, J. Transplantation of umbilical-cord blood in babies with infantile Krabbe's disease. *N Engl J Med* 352(20), 2069--2081 (2005)

6. Goodlett, C.B., Fletcher, P.T., Gilmore, J.H., Gerig, G.: Group analysis of DTI fiber tract statistics with application to neurodevelopment. *NeuroImage* 45, 133--142 (2009)
7. Zhang, H., Yushkevich, P.A., Alexander, D.C., Gee, J.C.: Deformable registration of diffusion tensor MR images with explicit orientation optimization. *Medical Image Analysis* 10(5), 764--785 (2006)
8. Schnabel, J.A., Rueckert, D., Quist, M., Blackall, J.M., Castellano-Smith, A.D., Hartkens, T., Penney, G.P., Hall, W.A., Liu, H., Truwit, C.L., Gerritsen, F.A., Hill, D.L.G., Hawkes, D.J.: A generic framework for non-rigid registration based on non-uniform multi-level free-form deformations. *MICCAI*, 573--581 (2001)
9. Andersson, J.L.R., Jenkinson, M., Smith, S.: Non-linear registration, aka Spatial normalization. FMRIB technical report TR07JA2 (2007)
10. Joshi, S., Davis, B., Jomier, M., Gerig, G.: Unbiased diffeomorphic atlas construction for computational anatomy. *NeuroImage* 23, 151--160 (2004)
11. Yap, P., Wu, G., Zhu, H., Lin, W., Shen D.: Fast Tensor Image Morphing for Elastic Registration. *MICCAI*, 721--729 (2009)
12. Yeo, B.T.T., Vercauteren, T., Fillard, P., Pennec, X., Golland, P., Ayache, N., Clatz, O.: DTI registration with exact finite-strain differential. *IEEE International Symposium on Biomedical Imaging (ISBI)*, 700--703 (2008)
13. Studholme, C., Hill, D.L.G., Hawkes, D.J.: An overlap invariant entropy measure of 3D medical image alignment, *Pattern Recognition* 32(1), 71--86 (1999)
14. Vercauteren, T., Pennec, X., Perchant, A. Ayache, N.: Non-parameteric Diffeomorphic Image Registration with the Demons Algorithm. *MICCAI*, 319--326 (2007)
15. Knickmeyer, R.C., Gouttard, S., Kang, C., Evans, D., Wilber, K., Smith, J.K., Hamer, R., Lin, W., Gerig, G., Gilmore, J.H. A structural MRI study of human brain development from birth to 2 years. *J Neurosci* 28(47), 12176--12182 (2008)
16. Liu, Z., Goodlett, C., Gerig, G., Styner, M. 2010. Evaluation of DTI property maps as basis of DTI atlas building. *SPIE*, 762325--762327 (2010)
17. Salvador, R., Peña, A., Menon, D.K., Carpenter, T.A., Pickard, J.D., Bullmore, E.T.: Formal characterization and extension of the linearized diffusion tensor model. *Hum. Brain Mapp.* 24 (2), 144--155 (2005)
18. Alexander, D.C., Pierpaoli, C., Basser, P.J., Gee, J.C.. Spatial transformations of diffusion tensor magnetic resonance images. *IEEE Transactions on Medical Imaging* 20(11), 1131--1139 (2001).
19. Zhang, H., Avants, B.B., Yushkevich, P.A., Woo, J.H., Wang, S., McCluskey, L.F., Elman, L.B., Melhem, E.R., Gee, J.C. High-dimensional spatial normalization of diffusion tensor images improves the detection of white matter differences in amyotrophic lateral sclerosis. *IEEE Transactions on Medical Imaging - Special Issue on Computational Diffusion MRI*, 26(11), 1585--1597 (2007).

A Combined Label Fusion and Connectivity Based Parcellation Approach for Anatomical Brain Segmentation

Emma C. Robinson¹, A. David Edwards³ and Daniel Rueckert¹

¹ Department of Computing, Imperial College, London. SW7 2BZ, UK

² MRC Clinical Sciences Centre and Division of Neuroscience, Faculty of Medicine, Imperial College, London. W12 ONN, UK

³ Department of Paediatrics, Imperial College, London. W12 ONN, UK

Abstract. Atlas-based segmentation, performed by propagation and fusion of labels from multiple manually delineated templates, has been shown to be a robust and consistent means of segmenting new subjects. Nevertheless, at boundaries between different regions there is typically a lack of certainty regarding the correct labelling. In addition, even the manual delineation of the templates sometimes contains arbitrary boundaries between regions, especially if there is no distinct feature in the images indicating the exact location of the boundaries. On the other hand, neuronal connections have been shown to strongly correlate to functional brain regions and connectivity profiles obtained from tractography in diffusion tensor MRI have been previously used to parcellate the cortex. This paper presents a framework for combining atlas-based segmentation with additional connectivity information provided by probabilistic tractography. We use atlas-based segmentations based on label fusion to perform tractography. The resulting connectivity profiles are used as feature vectors in a subsequent classification step. The results suggest that connectivity information can be used to improve the accuracy of atlas-based segmentation approaches.

1 Introduction

There is a growing requirement within structural and functional neuroimaging studies for techniques that can automatically segment brain images into anatomically meaningful regions. These regions should correspond across subjects and correlate to functional areas of the brain.

One popular approach for anatomical brain segmentation is atlas-based segmentation. In this approach labels from a template image that has been expertly annotated are transformed to the co-ordinate frame of a previously unseen subject [1]. The main limitation of the approach is the ability of the registration algorithm to register the template and target images. However, segmentation accuracy can be improved by transforming multiple templates and fusing the labels according to, for example, a majority vote rule [2, 3]. In addition, further improvement can be obtained by selecting those templates that have the greatest

similarity to the target [4] or by weighting the contribution of each template [5]. Nevertheless, at the boundaries of regions there is still an inherent uncertainty regarding the true labelling of each voxel, in particular in areas where there is no clear image feature to indicate the location of the boundary. Furthermore, for brain images which include pathologies or where there are systematic differences between the target images and the available templates, the label fusion approach can be problematic.

The underlying connectivity structure of the brain underpins brain function and influences cortical folding. Equivalent functional regions can be correlated across subjects through comparison of their connectivity profiles. This has been demonstrated by connectivity-based parcellation of the thalamus [6], where parcellations have been shown to correspond with histology. In addition Roca et al. perform cortical segmentation via clustering of whole-brain connectivity matrices, and derive clusters which reflect recognisable functional sub-units [7].

One limitation of the above cortical clustering approach is that it cannot consistently reproduce clusters across subjects. By contrast atlas-based approaches constrain segmentations to reproduce the same clusters across subjects. We therefore propose a combined approach. Atlas-based segmentation and label fusion is used to provide an initial estimate of the anatomical segmentation. We then perform probabilistic tractography using the regions segmented by atlas-based segmentation and label fusion as seeds, and assign targets from all voxels on the white-grey matter boundary of the cortex and inner structures. The segmentation labelling is then updated and voxels are re-classified using each voxels connectivity profile as a feature in a GentleBoost classification step. To train the GentleBoost classifier, training vectors are formed from all voxels with a high probability of belonging to each region according to the initial segmentation. These are then used to re-classify voxels whose label membership is uncertain.

In the next section we describe the atlas-based segmentation and label fusion approach used to generate an initial segmentation estimate and explain the connectivity parcellation approach. Section 2.3 describes how the output of the tractography is used to train a classifier which is subsequently tested on query voxels whose label membership is uncertain. In Section 3.1 we evaluate the approach for a situation where a large number of voxels from one region are wrongly assigned to a neighbouring region. We demonstrate that classifier is able to successfully re-label the majority of these voxels correctly, and show improved results that suggest that the approach also has the potential to improve on the initial estimate provided by the atlas-based segmentation.

2 Methods

2.1 Atlas-based segmentation and label fusion

Atlas-based segmentation of T1-weighted MR images was performed using 30 T1 template images. These were manually segmented by an expert into 83 anatomical regions, following an augmented version of approach proposed in [8]. The segmentations include both cortical and subcortical regions.

Propagation of labels from template images to the query subject was achieved by performing a non-rigid registration between each of the 30 template T1 images to the T1 images of each of the target subjects. Registration was performed using a free-form deformation approach [9] over four resolution levels with control point spacings of 40mm, 20mm, 10mm and 5mm. We used normalised mutual information (NMI) as a similarity metric. Following this step, the labels of each template were transformed to the co-ordinate frame of the target, and fused using a majority vote rule [2, 3]. This means that the labels assigned at each voxel correspond to the most common label across all transformed templates at that position. The probabilities of each voxel belonging to any of the 83 possible regions were also retained. These were used to highlight possible query voxels for re-classification.

2.2 Cortical parcellation using probabilistic tractography

The atlas-based segmentation framework described above was used to provide an initial starting point estimation of functional sub regions throughout the brain. Updates were then made following examination of the connectivity profiles obtained from probabilistic tractography between grey matter tissues only (Fig. 1 a). This is because neurological connections are known to initiate within nerve cell bodies in grey matter structures and propagate through axons in the white matter. Seed regions were obtained by eroding the anatomical segmentation to remove all voxels corresponding to cortical white tissue, as indicated by tissue probability maps obtained using SPM [10].

Targets (T) for the target mask for the tractography were formed from all voxels from the white-grey matter boundary of the cortex and those contained within the internal grey matter structures (e.g. thalamus, putamen and caudate, see Fig. 1 b). All segmentations were transformed from T1 to diffusion space where tractography is conventionally performed. We performed non-rigid registration of the bias-corrected T1 image to the non-diffusion weighted B_0 image [9], where initially the T1 image was blurred and downsampled to a similar resolution to the diffusion data. Registration was performed over four resolution levels (initial control point spacing 40mm) where image similarity was again assessed in terms of NMI metrics. In addition, a regularisation term ($\lambda = 0.001$) was used to ensure inversion of the transformation such that the final transformations can be transformed back from the diffusion image to the T1 image for visual inspection.

Probabilistic tractography was performed using the approach proposed by Behrens et al. [11]. This approach fits a partial volume model of diffusion at each voxel where anisotropic diffusion components are represented as single vectors along the principal fibre directions (θ, ϕ), and the number of fibre directions per voxel are estimated using Automatic Relevance Determination (ARD). This assumes a multiple fibre model at each voxel, but ensures (through the use of shrinkage priors) that the magnitudes of any additional directions are forced to zero where there is little evidence for them in the data. Posterior distributions on the key parameters of the diffusion mode (θ, ϕ and f) are estimated using

Bayesian inference, and samples are drawn from the posterior distributions using Markov Chain Monte Carlo (MCMC) sampling. The maximum number of fibres per voxel was set at two.

Tractography was performed by seeding multiple streamlines from each seed voxel. These sample from the posterior distributions on the principal diffusion direction at each step, leading to a distribution of possible targets from each seed voxel. Tracts were seeded from all voxels labelled in the atlas-based segmentation, and propagated through the image. Tracts were terminated where curvature $> \cos^{-1}(0.2)$ or if they propagated across CSF. This was constrained using tissue class information obtained from SPM, and prevents tracts from passing across sulci in areas with significant partial volume effects.

Finally, the connectivity profile (C_i) for each seed voxel ($s_i \in S$) was determined by summing the number of initialised streamlines ($n_{s_i \rightarrow t_j}$) that reach each target (t_j) with a correction term, d_j , which corrects for the falling off in the number of streamlines with length:

$$C_{ij} = n_{s_i \rightarrow t_j} + d_j \quad (1)$$

For each target, d_j is calculated from the total number of steps propagated between it and the seed (s_i). These connectivity profiles were used to generate feature vectors for a subsequent re-classification step.

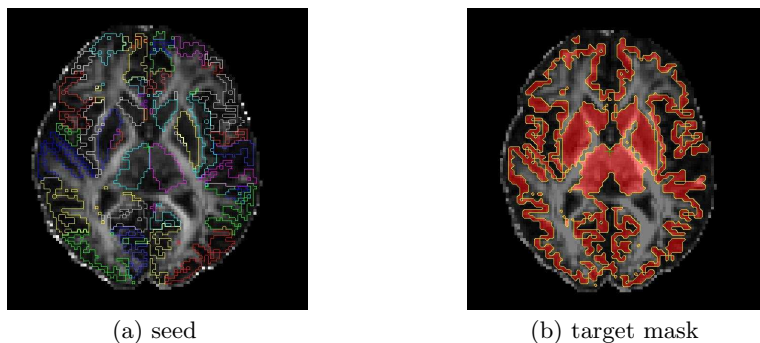


Fig. 1. Seed and target masks for tractography. a) Seed regions represent anatomical regions of interest in the brain and were formed from the output of the atlas-based segmentation fused with tissue segmentation; b) A target mask was formed from all voxels on the white-grey matter boundary of the cortex and internal structures (shown in red). All voxels in the target mask present individual targets. These were independently indexed within feature vectors allowing the connectivity profile from each seed voxel to be compared in a subsequent re-classification step

2.3 Classification of Voxels using GentleBoost

The outcome of tractography is a feature vector, for each seed voxel, representing the probability of it being connected to each target voxel. Therefore using the atlas-based segmentation as a starting point, feature vectors from seed voxels with a high probability of belonging particular labels can be used to learn the label memberships of query voxels using boosting.

Boosting works by sequentially re-training weak classifiers on weighted data ($x \in X$). All data sets are initially given a uniform weighting (w_i) and a weak classifier is used to classify the data. The weak classifier examines a single dimension (target voxel feature) of the data across all subjects and separates the subjects using a simple classification rule. Typically the weak classifier is chosen to act on the feature which gives best class separation for the current distribution of weights. Following this, examples are re-weighted such that miss-classified examples are given higher weight and therefore higher precedence for correct classification in the next round. A new weak classifier, trained on a different feature, is then added and the process is repeated until all training vectors have been correctly classified.

In this framework, we have used two-class GentleBoost (gentle AdaBoost [12]) with decision stumps as the weak classifier. We use GentleBoost as it has been shown to be most robust to noise and outliers. This is because it re-weights examples directly from the weighted class probabilities (P_w rather than using as log ratio (as for conventional AdaBoost) which has been shown to be numerically unstable. Weights are adjusted as:

$$w_i \leftarrow w_i e^{-y_i f_t(x_i)} , \quad (2)$$

where $f_t(x_i) = P_w(y = 1|x) - P_w(y = -1|x)$, and $y_i \in \mathbf{Y} = \{-1, +1\}$ are the labels. Decision stumps are single level decision trees, where examples are separated using a threshold and Boolean statement which indicates whether examples below the threshold are positive or negative.

The output from boosting is a strong classifier, calculated by combining the results of weak classifiers over many rounds.

$$F(x) = \text{sign} \sum_{t=1}^{t=T} f_t(x_i). \quad (3)$$

3 Experiments and Results

The algorithm is tested on healthy adult data, consisting of high-resolution T1-weighted whole-brain structural images, and 64 gradient direction diffusion data, acquired using the following parameters: TR 12000ms, TE 51ms, slice thickness 2mm, voxel size = 1.75 x 1.75 x 2mm³, b value 1000s/mm². The data includes four non-diffusion weighted images.

The results are visualized by projecting the segmentation result onto 3D renderings of the cortical surface extracted from the subjects T1 images. Therefore

corrected labels have been projected back the subject's non-diffusion weighted image by inverse transformation.

3.1 Experiments

In a proof of concept study we re-assigned a large number of voxels from one region in the atlas-based segmentation to an adjacent region and tested whether the approach was able to re-classify these voxels correctly. We used all voxels from one cortical fold of the inferior frontal gyrus and manually relabelled them as motor cortex. These voxels are clearly visible on the 3D rendering (Fig.2 a). In total 771 voxels were changed.

We then ran probabilistic tractography to obtain feature vectors for classification and trained the GentleBoost classifier on voxels labelled as positive, if the atlas-based segmentation indicated that $\geq 90\%$ of all templates agreed that they belonged to the motor cortex gyrus, and negative if the atlas-based segmentation indicated that $\geq 90\%$ of all templates agreed that they belonged to region inferior frontal gyrus. Features vectors were selected from each region for testing if the atlas segmentation indicated that they had a $\geq 0\%$ probability of belonging to the opposite region. Voxels that were re-classified as a result of the boosting were then relabelled in the segmentation. Training and re-classification were performed iteratively with each new set of training vectors until re-labelling converges.

The results of the reclassification are shown in Figure 2. These show that after several rounds most voxels manually re-labelled as belonging to the motor cortex are correctly re-classified as belonging to the inferior frontal gyrus. The exact percentage of voxels correctly re-classified as belonging to the inferior frontal gyrus was 94.8% (sensitivity = 95.5 %; specificity 94.8%). In addition 94.7% of the voxels from the initial atlas-based estimate of the motor cortex are retained.

We hypothesised that the discrepancy between the final output of the boosting and the initial atlas-based segmentation may reflect the fact that the ground truth is not fully known. Specifically, visual inspection suggested that remaining voxels (not re-classified as inferior frontal gyrus) may in fact belong to the middle frontal gyrus (Fig.3 a). Therefore, we trained a GentleBoost classifier on voxels from the motor cortex and middle frontal gyrus and tested it on query voxels, assigned as before. The results show that as expected many of the remaining voxels are re-classified as middle frontal gyrus (Fig.3 b). This labelling improves the agreement between the segmentation and the sulcal boundary between motor and middle frontal regions. This suggests that re-classifying voxels on the basis of their connectivity profiles may improve segmentation accuracy. We now hope to apply the technique to improve the accuracy of the segmentation for a whole brain.

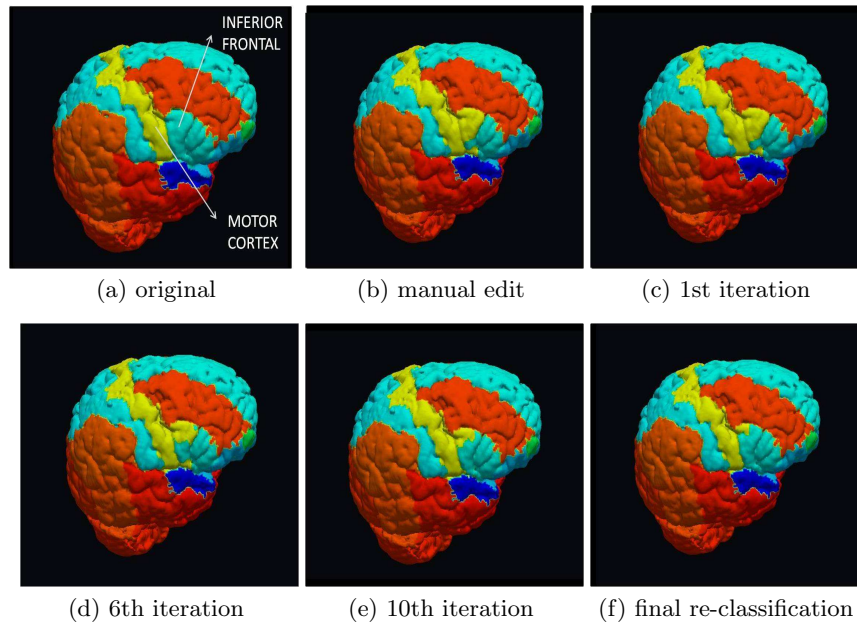


Fig. 2. Correction of segmentation after manual relabelling. a) shows the original segmentation propagated to a 3D rendering of a T1 image of the brain. The motor cortex and inferior frontal cortex are labelled; b) shows the results of manual relabelling of one fold of the inferior frontal gyrus; c) Results after one iteration of re-classification using only connectivity information; d) after 6 iterations; e) after 10 iterations; f) final segmentation after re-classification of all labels using the boosting approach

4 Discussion

In this paper we have presented a framework for improving atlas-based segmentation of the brain using additional information obtained from probabilistic tractography. The approach uses GentleBoost classification to train a classifier from the connectivity profiles of voxels whose label memberships are highly certain and uses this to test class membership for voxels whose true membership is considered uncertain from the atlas-segmentation alone. We have included preliminary results that test the approach on two regions with known mis-labelings and demonstrate that re-classification via connectivity profiles is capable of correcting segmentation error. In addition, inclusion of additional neighbouring regions appears to improve the accuracy of the segmentation at sulcal boundaries.

There are some limitations with the present framework. First, accuracy of the method is dependent on the accuracy of the registrations, both from the segmentation to the diffusion space, and its successful inversion back to the T1 image for analysis. This may be solved using a surface-based strategy which identifies each position on the T1 surface volume with a unique starting for tractography.

The approach also uses a 2-class classifier. Therefore re-labelling of the whole brain must be performed by boosting separately between all pairs of neighbours, and this process must be iterated until stability is met. This is time consuming. In future this will be extended to a multi-class solution where all neighbouring regions can be compared simultaneously.

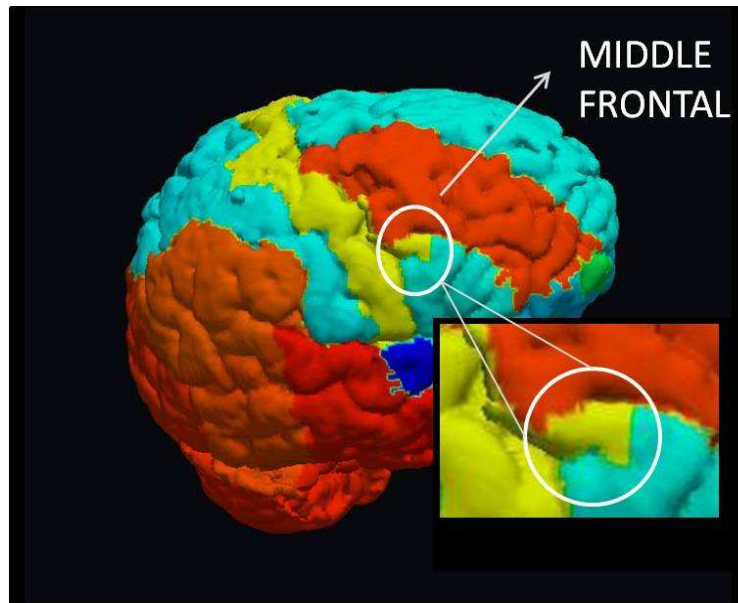
Another question that should be investigated is whether the atlas segmentation might be further subdivided. Many of the anatomical sub regions used cover large areas of cortex and therefore it is likely that many of the voxels within these regions have distinct connectivity profiles. The advantage of using boosting is that it builds up a collection of features, or connectivity targets that characterise each seed region. As such a variety of connectivity profiles can be accommodated for each region. Nevertheless future work may look at clustering schemes to separate the seed regions into further cliques.

Finally it will also be necessary to devise a method for validation. This is complicated by the fact that the ground truth is not known. However, One solution may be to investigate whether improving the accuracy of anatomical segmentations will increase cross-subject similarity of whole-brain connectivity networks. This is because, at this macroscopic scale, we expect connectivity matrices to be consistent.

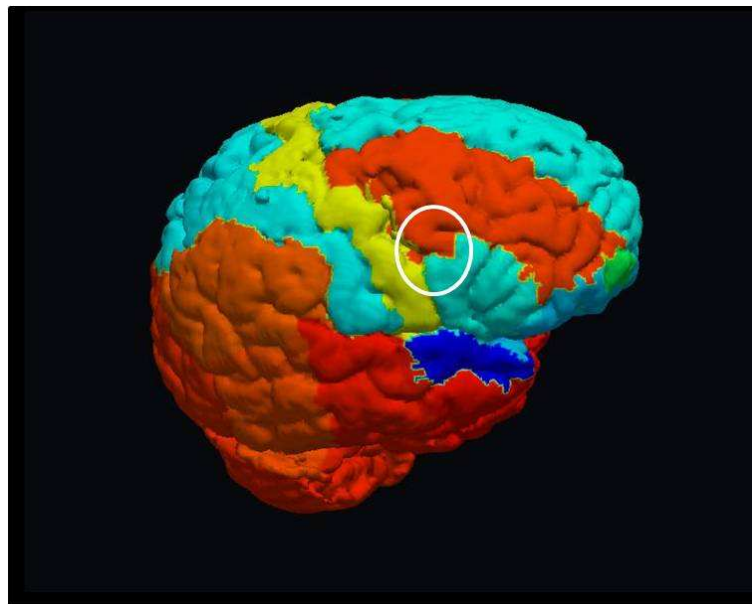
In conclusion, atlas-segmentation approaches based on label propagation and fusion have been shown to be very successful at segmenting brains if the templates used closely match the topology of the target subjects. Nevertheless, for very deformed brains, for example during ageing, or early development, the approach is unreliable. In these instances we propose using connectivity information improve the accuracy of the segmentation. In future we intend to use this approach to segment neonatal brain images from estimates provided by adult templates. Work will also be performed to investigate whether training feature vectors for one region over multiple subjects will allow the improved segmentation of new data.

References

1. Iosifescu, D., Shenton, M., Warfield, S., Kikinis, R., Dengler, J., Jolesz, F., Mccarley, R.: An automated registration algorithm for measuring mri subcortical structures. *NeuroImage* **6** (1997) 13–25
2. Rohlfing, T., Brandt, R., Menzel, R., Jr, C.M.: Evaluation of atlas selection strategies for atlas-based segmentation with application to confocal microscopy of bee brains. *NeuroImage* **21** (2004) 1428–1442
3. Heckemann, R., Hajnal, J., Aljabar, P., Rueckert, D., Hammers, A.: Automatic anatomical brain mri segmentation combining label propagation and decision fusion. *NeuroImage* **33** (2006) 115–126
4. Aljabar, P., Heckemann, R., Hammers, A., J.V., H., Rueckert, D.: Classifier selection strategies for label fusion using large scale atlas databases. In: *Medical Image Computing and Computer-Assisted Intervention*. (2006) 523–531
5. Warfield, S., Zou, K., Wells, W.: Simultaneous truth and performance level estimation (staple): an algorithm for the validation of image segmentation. *IEEE Trans. Med. Imaging* **23** (2004) 904–921
6. Behrens, T., Johansen-berg, H., Woolrich, M., Smith, S., Wheeler-Kingshott, C., Boulby, P., Barker, G., Sillery, E., Skeehan, K., Cicarelli, O., Thompson, A., Brady, J., Matthews, P.: Non-invasive mapping of connections between human thalamus and cortex using diffusion imaging. *Nat. Neurosci.* **6(7)** (2003) 750–757
7. Roca, P., Rivière, D., Guevara, P., Poupon, C., Mangin, F.F.: Tractography based parcellation of the cortex using a spatially-informed dimension reduction of the connectivity matrix. In: *Medical Imaging Computing and Computer assisted Intervention (MICCAI), Lecture Notes in Computer Science* (2009) 935–942
8. Hammers, A., Allom, R., Koeppe, M., Free, S., Myers, R., Lemieux, L., Mitchell, T., Brookes, D., Duncan, J.: Three-dimensional maximum probability atlas with particular reference to the temporal lobe. *Hum. Brain. Mapp* **19(4)** (2003) 224–247
9. Rueckert, D., Sonoda, L., Hayes, C., Hill, D., Leach, M., Hawkes, D.: Non-rigid registration using free-form deformations: Application to breast mr images. *IEEE Trans on Med Imaging* **18(8)** (1999) 712–721
10. Ashburner, J., Friston, K.: Unified segmentation. *Neuroimage* **26** (2005) 839–851
11. T.E.J. Behrens, H.J.B., Jbabdi, S., Rushworth, M., Woolrich, M.: Probabilistic diffusion tractography with multiple fibre orientations: What can we gain? *NeuroImage* **34** (2007) 144–155
12. Friedman, J., Hastie, T., Tibshirani, R.: Additive logistic regression: a statistical view of boosting. *The Annals of Statistics* **28** (2000) 337–407



(a)



(b)

Fig. 3. Correction of segmentation after inclusion of middle frontal gyrus. a) Shows region of manually re-labelled voxels not re-classified as Inferior Frontal gyrus; b) GentleBoost re-classification of the middle frontal gyrus versus the motor cortex shows that these voxels actually belong to the middle frontal region.

Poster Session

Characterizing brain connectivity using ϵ -radial nodes: application to autism classification

Nagesh Adluru*, Moo K. Chung, Kim M. Dalton
Andrew L. Alexander, and Richard J. Davidson

University of Wisconsin, Madison, WI, USA

Abstract. Whole brain tractography studies can generate up to and over half-a-million tracts per brain which form the basis for constructing edges in an extremely large 3D graph. Currently there is no agreed-upon method for constructing the brain anatomical connectivity graphs out of large number of white matter tracts. In this paper, we present an efficient framework for building and analyzing graphs using tractography in a normalized space. We then apply the constructed graphs in a classification setting of autistic vs. typically developing individuals and obtain prediction accuracy of 87%. This suggests that efficiently characterizing anatomical connectivities of the brain may be used to characterize discriminant patterns in different populations.

1 Introduction

White matter which forms the basis of structural connectivity has been shown to be abnormal for example in regions like corpus callosum, in various autism studies [1, 2]. Characterizing global anatomical connectivity will significantly impact the study of brain pathology and such developmental disorders [3]. There is a growing interest of mapping out anatomical connectivity at a macroscale *in vivo* with the advancement of various Diffusion MRI acquisition techniques. A graph is a mathematical representation of a real-world complex system and is defined by a collection of nodes (vertices) and edges (links) between pairs of nodes. The nature of nodes and links in individual brain networks may be determined by combinations of brain mapping methods, anatomical parcellation schemes, and measures of connectivity. The nature of nodes and edges largely determines the neurobiological interpretation of network topology [4, 5].

Streamline tractography is typically used to characterize structural connectivity between two regions (nodes) in the brain. Here we propose that streamlines can be used to construct the nodes as well. Currently there is no agreed-upon method for constructing brain connectivity graphs out of a large number of white matter tracts. In this paper, we present an efficient, scalable and automated framework for building and analyzing ϵ -radial anatomical connectivity matrices (ϵ -acms) in a normalized space. Automatically identifying nodes using

* Contact author: adluru@wisc.edu. The authors are with Waisman Laboratory for Brain Imaging and Behavior at University of Wisconsin, Madison, WI, USA.

tract data has several advantages: (1) Cross-modality registration, which can have limitations when acquisition parameters vary, can be avoided. (2) Large scale studies become feasible with automated methods.

By using state-of-the-art spatial normalization ([6]) and tractography tools ([7]) the ϵ -acms show promising discriminative power in the context of classifying autism. The source code in MATLAB implementation is available on an accompanying website¹.

2 Related Work

Improved methods for mapping anatomical connectivity is an important step in exploring causal relationships in functional correlations [8, 9]. Fonteijn et. al. [10] attempt at providing anatomical basis for functional networks but they point out the problem of normalization of tracts and that there is no agreed-upon way of transferring anatomical landmarks into subject space without affecting tractography. Gong et. al. [11] applied DTI to map a network of anatomical connections between 78 cortical regions. Hagmann et. al. [12] constructed a connection matrix from fiber densities measured between homogeneously distributed and equal-sized regions of interest (ROIs) numbering between 500 and 4000. They identify ROIs by a heuristical two-phase “region growing” of voxels in the white/grey matter boundary. They show results on only two human subjects where they find that their individual brain networks have an exponential node degree distribution and that their global organization is in the form of a small world. Skudlarski et. al. [9] present an approach in which they use tractography to first estimate the strength of anatomical connection for any two white matter voxels and then using the neighboring white matter voxels they extend the connectivity information between pairs of grey matter voxels by using the information from neighboring white matter voxels. They perform tractography in the native space and use only up to 40000 tracts on average per subject. Further they use B0 images for non-linear registration for performing statistical analyses which does not guarantee that the underlying fiber architecture (defined by FA or λ_1) is in register [13].

In addition to using state-of-the-art tensor based normalization scheme, our framework is scalable up to a million tracts and we perform graph based classification on a dataset of 31 subjects. Fig. 1 shows the overview of the construction and analyses of ϵ -radial anatomical connectivity matrices (ϵ -acms). The next section describes the details of our ϵ -radial node and edge construction algorithms followed by experimental results and conclusions.

3 ϵ -radial anatomical connectivity

In this section we describe how to construct an anatomical connectivity matrix using streamlines without parcellations of the grey or white matter. The method uses the end points of the tracts to define the nodes by clustering neighboring

¹ <http://brainimaging.waisman.wisc.edu/~adluru/ERG/eacm.htm>

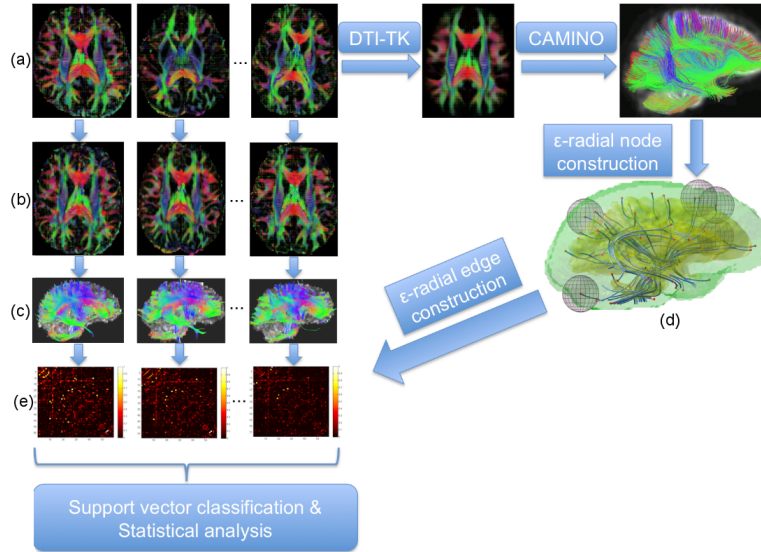


Fig. 1. (a) The input tensor volumes are used to generate a population specific atlas using DTI-TK. Tractography is performed on the atlas volume. (b) The individual subjects are transformed into the normalized space. (c) Tractography is performed on the individual volumes in the normalized space. (d) ϵ -radial nodes are constructed using Alg. 1. (e) ϵ -acms are constructed using Alg. 2, which can be used for classification and other statistical analyses.

tract end points into a set of spheres of ϵ radius. These spheres form the nodes for constructing a connectivity matrix. We call the resulting connectivity as ϵ -radial connectivity. Using tract endpoint clusters as nodes allows to focus on regions where there is structural connectivity. The nodes although sphere shaped can be useful in localizing important regions of the brain. These ϵ -radial nodes are typically near the grey matter/white matter interface (useful to study connectivities between functional areas [12]) where the FA drops below 0.15, the tractography stopping criterion. The lower the stopping threshold, the more nodes will be in grey matter.

The following two algorithms describe how to identify the ϵ -radial nodes (\mathcal{N}) and edges efficiently. We would like to note that the connectivity matrices are currently built using the presence of *end points* in these spheres but can be extended to “passing through/way point” connectivity. Sample tracts connecting two different pairs of nodes, a set of ϵ -radial nodes and sample ϵ -radial anatomical connectivity are shown in Fig. 2.

Time complexity: If there are n tracts, the construction of kd -tree and ϵ -radial nodes takes $O(n \log^2 n)$. The construction of the ϵ -acm (with N nodes) takes $O(N \log^2 N + n \log^2 N)$ time. Most connectivity matrix algorithms estimate connectivity between nodes pairwise and are not scalable in the number of nodes and tracts as $O(nN^2) \gg O(N \log^2 N + n \log^2 N)$. The proposed algorithm can

Algorithm 1 Construction of ϵ -radial nodes (\mathcal{N})

- 1: **Input:** Set of n tracts in population specific atlas
 - 2: $\mathcal{N} \leftarrow \Phi$ (empty set)
 - 3: Build a kd -tree ($\mathcal{K}_{\mathcal{P}}$) on the end points, $\mathcal{P} = \{p_i\}_{i=1}^{2n}$ of the tracts
 - 4: **repeat**
 - 5: Pick an element $p_k \in \mathcal{P}$
 - 6: $\mathcal{N} \leftarrow \mathcal{N} \cup \{p_k\}$
 - 7: $\mathcal{P} \leftarrow \mathcal{P} - \{p_j\}$ (set minus), where $\{p_j\}$ in ϵ -radius of p_k using $\mathcal{K}_{\mathcal{P}}$
 - 8: **until** $\mathcal{P} = \Phi$
 - 9: **Output:** \mathcal{N}
-

Algorithm 2 Construction of ϵ -radial anatomical connectivity matrix (ϵ -acm)

- 1: **Input:** Set of tracts, $\{t_i\}_{i=1}^n$ of the input volume in the normalized space and \mathcal{N}
 - 2: Build a kd -tree ($\mathcal{K}_{\mathcal{N}}$) on the ϵ -radial nodes, \mathcal{N}
 - 3: Initialize the square matrix $\epsilon\text{-acm}[N][N]$ to zeros, where $N = |\mathcal{N}|$
 - 4: **for** $i = 1$ to n **do**
 - 5: $n_1 \leftarrow$ node indices in ϵ radius of the first end point of t_i using $\mathcal{K}_{\mathcal{N}}$
 - 6: $n_2 \leftarrow$ node indices in ϵ radius of the second end point of t_i using $\mathcal{K}_{\mathcal{N}}$
 - 7: $n_1 \leftarrow n_1 - n_2$ (set minus)
 - 8: $\epsilon\text{-acm}[n_1, n_2] \leftarrow \epsilon\text{-acm}[n_1, n_2] + 1$
 - 9: **end for**
 - 10: $\epsilon\text{-acm} \leftarrow \epsilon\text{-acm} + \epsilon\text{-acm}^T$ (transpose)
 - 11: **Output:** $\epsilon\text{-acm}$
-

scale up to a million tracts very easily as the connectivity matrix is populated in *one pass* through the tracts. Connectivity matrices using about 200000 tracts take less than a minute on a typical machine and in MATLAB implementation.

Different resolutions of ϵ produce different sets of nodes and connectivity matrices. Sample ϵ -acms for a subject at different resolutions can be seen in Fig 3. As $\epsilon \rightarrow 0$, $N \rightarrow 2n$ where each tract end point becomes an ϵ -radial node and the connectivity matrix becomes very sparse and has unit entries. Using very large sparse connectivity matrices for any reasonable statistical analysis is very hard with the small sizes of datasets used in various studies. For the experiments presented we chose $\epsilon = 8mm$, which produced 58 nodes. We used $\epsilon = 8mm$ following the heuristics of Fonteijn et. al. [10], where they state "In most of the original studies [15-19,22], the ROIs that were used for effective connectivity analysis were all spheres of 8mm radius." in Sec. 2.3.

Alg. 1 is dependent on the order of points $p_k \in \mathcal{P}$. Our initial experiments suggest that although there is slight variance in spatial locations of the nodes, some global properties like histograms of node-degrees and edge-weights are stable. There seem to be some interesting connections between ϵ -acms and approximate neighborhood graphs used in simplicial complexes ([14]) which need further exploration. Simplicial complexes extract topological representations underlying point cloud data. In our case the tract end points form the point cloud data.

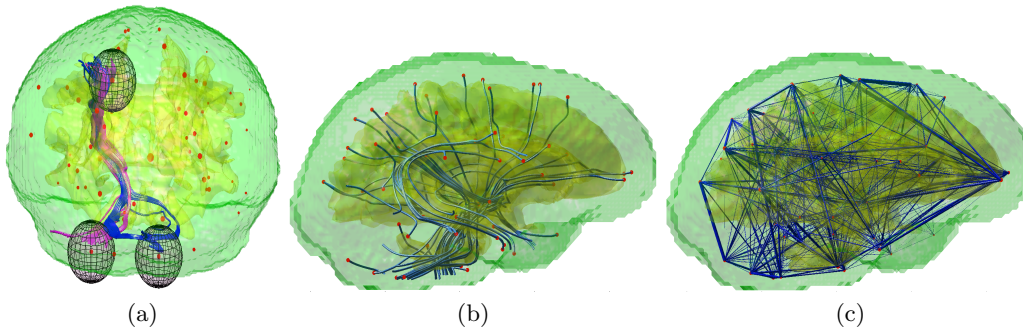


Fig. 2. Tracts whose end points are within the ϵ -radial spheres characterize the edges. (a) Tracts between two pairs of nodes are shown in different color. Size of the nodes is proportional to the degree of the nodes. (b) ϵ -radial node locations (red) on the template volume with the tracts that are responsible in identifying them. The nodes and tracts are overlaid on white matter (yellow) and grey matter (green). (c) Connectivities of the ϵ -radial nodes are shown using edges. The thickness of an edge is proportional to the number of tracts connecting two nodes.

4 Experimental results

Pre-processing and spatial normalization: DTI data from 31 subjects were used: 17 subjects with autism spectrum disorders (ASD) and 14 control subjects matched for age, handedness, IQ, and head size. The diffusion weighted images were acquired in 12 non-collinear diffusion encoding directions with diffusion weighting factor of $b = 1000s/mm^2$ in addition to a single ($b = 0$) reference image. Eddy current related distortion and head motion of each data set were corrected using AIR [15] and distortions from field inhomogeneities were corrected using field maps. The tensor elements were calculated using non-linear estimation using CAMINO [7].

Spatial normalization of diffusion tensor images plays a key role in constructing brain network graphs with identical nodes in the template. The quality of spatial normalization determines the extent to which white matter tracts are aligned. It has direct impact on the successful removal of shape confounds and consequently on the validity, specificity, and sensitivity of the subsequent statistical inferences of group differences. State-of-the-art diffusion tensor image registration DTI-TK [6] was used for spatial normalization of the subjects. Tensor volumes, with axial dimension equal to a power of 2, are better suited for registration algorithms that require the construction of standard multi-resolution image pyramids. Hence the tensor volumes were resampled to a voxel space of $128 \times 128 \times 64$ with voxel dimensions equal to $1.5mm \times 1.75mm \times 2.25mm$. Streamline tractography based on TENSOR Deflection (TEND, implemented in CAMINO [7]) was then used to generate the fiber tracts in the individual subjects transformed to the normalized space. The summary of the pre-processing can also be seen in Fig. 1.

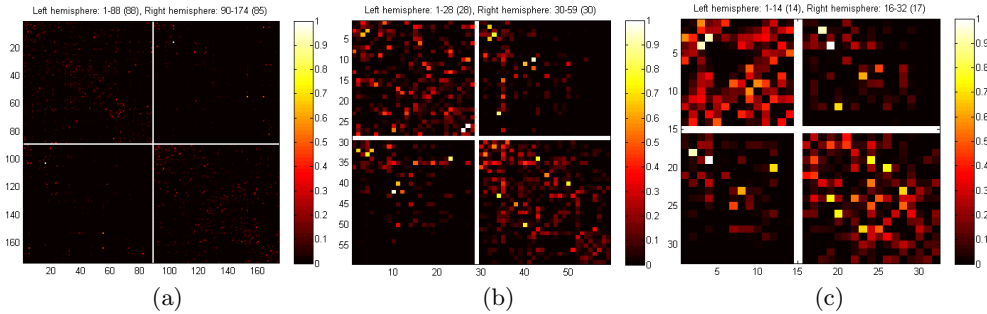


Fig. 3. ϵ -anatomical connectivity matrices (acms) of a sample subject at different resolutions of ϵ . (a) $\epsilon = 5mm$, $N = 173$ (b) $\epsilon = 8mm$, $N = 58$ (c) $\epsilon = 10mm$, $N = 31$. As ϵ decreases the number of nodes increases and the connectivity matrix becomes sparser. The ϵ -acms are normalized as $\epsilon\text{-acm} \leftarrow \frac{\epsilon\text{-acm} - \min(\epsilon\text{-acm})}{\max(\epsilon\text{-acm}) - \min(\epsilon\text{-acm})}$. The bright lines separate the hemispheric connectivities.

Support vector classification: The ϵ -radial nodes were identified in the population specific template as described in Alg. 1. Then for each of the individual subjects in the normalized space, ϵ -radial anatomical connectivity is obtained using Alg. 2. We filtered out tracts having fewer than 50 points to avoid the influence of spurious tracts. On average there were about 92000 tracts in each subject and the average longest tract had about 1500 points. On average the graph construction per subject takes about 18 seconds including file I/O on a 64-bit machine and using MATLAB implementation. Based on our survey of the existing tools for connectivity construction ours is the fastest automatic method. We explored two feature vectors viz. degree of nodes and weights of edges, for the classification experiments. Degree of nodes is simply calculated by summing up the rows or columns of adjacency matrices. The node-degree feature vector is N long while the edge-weight feature vector is $\frac{N(N-1)}{2}$ long. We use the popular support vector machines [16] with radial basis kernel as a classifier.

Since we have only 31 examples we evaluate our classifier performance using leave-one-out cross-validation scheme. For each fold we perform feature selection using simple t -tests (only on training data) and keep features that have p -values below a certain threshold. When using edge weight distributions as feature vectors, the average accuracy over 31 folds is 87% with 84% specificity and 94% sensitivity. When using degree of nodes the results are 84% accuracy, 83% specificity and 88% sensitivity. The classifier output values and the corresponding receiver operating characteristic (ROC) curves are shown in Fig. 4². The average areas under curve (AUC) for the two features are 0.912 and 0.811 respectively.

Although edge weight distribution has higher cross-validation accuracy, there are more samples that fall inside the margin which could imply that degree

² One of the TD samples (subject 11 of the 14) in (c) although correctly classified, is not shown because the corresponding output made the figure out of scale.

of nodes is more generalizable feature. Increased discriminative power of edge-weights could be attributed to the “pair-wise” interactions while increased generalizability of node-degrees to lower dimensionality of the feature vector. Further exploration on sensitivity to ϵ , different feature extractions (e.g. hemispheric connectivities) and combinations (e.g. multi-kernel setting) is part of our future work.

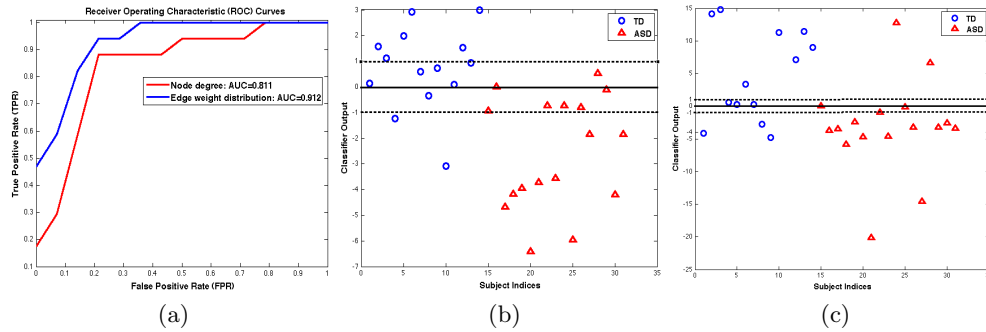


Fig. 4. (a) ROC curve shows for the two features. Edge weight distribution (blue) performs better than degree of nodes (red). (b,c) Classifier output values for the two classes. The thick line is the classification boundary and the dotted lines are the margins. Values above the thick line are classified as controls and those below as individuals with ASD. Blue circles represent Typically Developing (TD) individuals and the red triangles represent individuals diagnosed with Autism Spectrum Disorder (ASD). Edge weight distribution (b) has more examples in the margin compared to that using node degrees (c).

5 Discussion and conclusions

In this paper we proposed an automated and efficient way to build and analyze anatomical connectivities of brains. Our method of connectivity matrix construction could be applied to cases where the nodes are manually identified as well. The ϵ -radial connectivity method revealed significant group differences between ASD and controls and is consistent with current hypotheses of abnormal brain connectivity in autism [3, 17, 18]. Ideally, connectome maps acquired through the use of diffusion imaging should be cross-validated with anatomical data collected by histological techniques.

Acknowledgments

We thank Jee Eun Lee for eddy current correcting and field map correcting the DWI volumes. This work was partially supported by NIH grants MH62015, MH084051, MH080826 and CIBM-MIR fellowship.

References

1. Alexander, A., Lee, J., Lazar, M., et. al.: Diffusion tensor imaging of the corpus callosum in autism. *Neuroimage* **34**(1) (2007) 61–73

2. Pardini, M., Garaci, F., Bonzano, L., et. al.: White matter reduced streamline coherence in young men with autism and mental retardation. *Eur. J. Neurol* **16**(11) (2009) 1185–1190
3. Just, M., Cherkassky, V., Keller, T., et. al.: Functional and anatomical cortical underconnectivity in autism: Evidence from an fMRI study of an executive function task and corpus callosum morphometry. *Cerebral Cortex* **17** (2007) 951–961
4. Butts, C.: Revisiting the foundations of network analysis. *Science* **325** (2009) 414–416
5. Zalesky, A., Fornito, A., Harding, I., et. al.: Whole-brain anatomical networks: Does the choice of nodes matter? *Neuroimage* **50**(3) (April 2010) 970–983
6. Zhang, H., Yushkevich, P., Alexander, D., Gee, J.: Deformable registration of diffusion tensor MR images with explicit orientation optimization. **10** (2006) 764–785
7. Cook, P., Bai, Y., Nedjati-Gilani, S., et. al.: Camino: Open-source Diffusion-MRI reconstruction and processing. In: ISMRM. (2006) 2759
8. Sporns, O., Tononi, G., Kotter, R.: The human connectome: A structural description of the human brain. *PLOS Computational Biology* **1**(4) (2005)
9. Skudlarski, P., Jagannathan, K., Calhoun, V., et. al.: Measuring brain connectivity: diffusion tensor imaging validates resting state temporal correlations. *Neuroimage* **43**(3) (2008) 554–561
10. Fonteijn, H., Norris, D., Verstraten, F.: Exploring the anatomical basis of effective connectivity models with DTI-based fiber tractography. *Journal of Biomedical Imaging* **2008**(3) (2008) 1–9
11. Gong, G., He, Y., Concha, L., et. al.: Mapping anatomical connectivity patterns of human cerebral cortex using in vivo diffusion tensor imaging tractography. *Cereb Cortex* **19**(3) (2009) 524–536
12. Hagmann, P., Kurant, M., Gigandet, X., et. al.: Mapping human whole-brain structural networks with Diffusion MRI. *PLoS one* **2**(7) (2007)
13. Alexander, A., Lobaugh, N. In: *Insights into Brain Connectivity Using Quantitative MRI Measures of White Matter*. Springer Berlin (2007) 221–273
14. Zomorodian, A.: Fast construction of the Vietoris-Rips complex. *Computer and Graphics* **34**(3) (June 2010) 263–271
15. Woods, R., Grafton, S., Holmes, C., et. al.: Automated image registration: I. general methods and intrasubject, intramodality validation. *Journal of Computer Assisted Tomography* **22** (1998) 139–152
16. Chang, C., Lin, C.: LIBSVM: a library for support vector machines. (2001) Software available at <http://www.csie.ntu.edu.tw/~cjlin/libsvm>.
17. Kana, R., Keller, T., Minshew, N., Just, M.: Inhibitory control in high functioning autism: Decreased activation and underconnectivity in inhibition networks. *Biological Psychiatry* **62** (2007) 198–206
18. Sahyoun, C., Belliveau, J., Soulières, I., et. al.: Neuroimaging of the functional and structural networks underlying visuospatial vs. linguistic reasoning in high-functioning autism. *Neuropsychologia* **48**(1) (2010) 86–95

Tract Atrophy in Alzheimer's Disease Measured Using Probabilistic Tractography

H. Azadbakht^{1,2}, D. M. Morris^{1,2}, H. A. Haroon^{1,2}, K. V. Embleton^{1,2,3},
S. F. Carter⁴, B. Whitcher⁵, J. Snowden⁶, and G. J. M. Parker^{1,2}.

¹Imaging Science and Biomedical Engineering, School of Cancer and Imaging Sciences, University of Manchester, Oxford Road, Manchester M13 9PT. ²The University of Manchester Biomedical Imaging Institute, University of Manchester, Oxford Road, Manchester M13 9PT. ³School of Psychological Science, University of Manchester, Oxford Road, Manchester M13 9PT. ⁴Wolfson Molecular Imaging Centre, University of Manchester, Withington, Manchester, M20 3LJ, ⁵Clinical Imaging Centre, GlaxoSmithKline, Hammersmith Hospital, London W12 0HS. ⁶Greater Manchester Neuroscience Centre, Salford Royal NHS Trust, Salford.

Abstract. In this paper we propose a novel algorithm for quantifying the width of WM tracts in the brain. First we extract the Uncinate Fasciculus (*UF*) and Inferior Longitudinal Fasciculus (*ILF*) from both hemispheres of healthy aged, mild cognitive impairment (MCI) and Alzheimer's disease (AD) subjects using the *PiCo* probabilistic tractography algorithm. Then, we apply a novel algorithm for automatically identifying the optimum threshold values for the probability of connectivity maps generated by *PiCo*. Curve-skeletons of the tracts are generated by an electric field model and the widths of the tracts are computed as a function of position along these curve-skeletons. The results reveal right hemisphere lateralization for the UF in all normal-aged and seven out of eight MCI subjects. There was no consistent pattern of lateralization in the AD group. The findings demonstrate the sensitivity of our method in detecting tract-specific white matter tract width differences between healthy and patient groups.

Keywords: Tractography, Diffusion, White Matter, Alzheimer's Disease, Mild Cognitive Impairment, Atrophy, Width Measurement, Neurodegeneration.

1. Introduction

Brain atrophy is a common feature of many neurological conditions such as Alzheimer's Disease (*AD*). Atrophy of cerebral grey and white matter (*WM*) is related to normal ageing, at a rate of approximately 0.2 – 0.3 % per year [1], the rate of which is increased by neurodegenerative diseases such as *AD*. Various researchers in the literature have introduced magnetic resonance imaging (*MRI*) based methods that determine global brain atrophy and localised tissue atrophy and enable the assessment of prognosis and the monitoring of treatment effects in *AD*.

Current literature on the measurement of atrophy aims to characterise the atrophy of the whole brain, global grey and/or white matter, specific lobes, or specific grey matter structures such as the hippocampus. However, in order to provide a sensitive

biomarker that points to disease-related alterations within these structures, and by taking into account the fact that the resulting atrophy caused by such conditions also affects the *WM* tracts of the brain via degenerative processes, there may be utility in measuring atrophy of the *WM* tracts that connect these structures. If specific tract systems are more prone to atrophy than others, then there is the potential that tract-specific atrophy measurements may be more sensitive than less targeted methods.

With this aim in mind, this work presents a novel method for quantifying the width of *WM* tracts that may be used to differentiate between normal and patient groups or in the assessment of changes in the rate of disease progression due to pharmaceutical intervention.

2. DATA ACQUISITION

All imaging was performed on a 3 T Philips Achieva scanner (Philips Medical Systems, Best, Netherlands) using an 8-element phased array head coil.

Diffusion weighted imaging was performed using a PGSE EPI sequence with $TE = 54$ ms, $TR = 11884$ ms, $G = 62$ mTm⁻¹, half scan factor = 0.679, 112×112 image matrix reconstructed to 128×128 using zero padding, reconstructed resolution 1.875×1.875 mm, slice thickness 2.1 mm, 60 contiguous slices, 43 non-collinear diffusion sensitisation directions at $b = 1200$ smm⁻² ($\Delta, \delta = 29.8, 13.1$ ms), 1 at $b = 0$, SENSE acceleration factor = 2.5. Each diffusion-weighted volume was acquired entirely before starting on the next diffusion weighting resulting in 44 temporally-spaced volumes with different direction diffusion gradients. Acquisitions were cardiac gated using a peripheral pulse unit positioned over the subject's index finger to reduce artefacts associated with pulsatile movements in the brain. Correction for susceptibility-induced distortion was performed as described in [2].

Data were acquired from 8 *AD*, 8 Mild Cognitive Impairment (*MCI*) and 8 *Normal-Aged* subjects. Handedness was not recorded.

3. METHODS

3.1. ROI specification and tractography

After processing the acquired data using q-ball and model-based residual bootstrapping [3,4], to determine probability density functions (*PDFs*) of multiple fibre orientations in every voxel, the tracts of interest must be extracted from each subject. We made use of the multi-*ROI* specification approach outlined in [5], which is suited for the extraction of cerebral *WM* pathways that are a part of fibre bundles that are composed of different kissing or touching fasciculi. These pathways are aligned closely to one another, but connections between different gray matter regions. In this approach a secondary *ROI* is defined at a distance from the first *ROI* so that it

includes at least a section of the desired fasciculus but not any fibres from unwanted fasciculi that pass through the first *ROI*.

The Probabilistic Index of Connectivity (*PICo*) multi-fibre probabilistic tractography method [6,7] was then used to extract the Uncinate Fasciculus (*UF*), Inferior Longitudinal Fasciculus (*ILF*) and Superior Longitudinal Fasciculus (*SLF*) from both hemispheres of all subjects. This algorithm considers multiple pathways emanating from a *ROI* [7,8]. Due to noise in the measurements, there is uncertainty associated with estimating the principal direction of diffusion. This is modeled by generating a *PDF* of fibre directions based on the diffusion model at each voxel. The *PDF* provides voxel-wise approximations of the uncertainty in fibre tract alignment. Using the generated *PDFs*, streamline-based tracking was repeated via a Monte Carlo approach, with random sampling of the *PDFs* on each iteration. For the studies included in this work we chose 1000 iterations to generate connectivity maps that estimate the probability of streamline connection of every voxel in the brain to a given seed point or region [7]. Streamlines are propagated using trilinear interpolation of the *PDFs*, and are terminated if they exit the brain [6].

The *UF* and *ILF* were successfully extracted in both hemispheres of all individuals, however, the *SLF* were successfully extracted in both hemispheres of Normal-Aged and MCI subjects but proved impossible to extract in many AD subjects in either hemisphere and so it is not considered further.

3.2. Automated Thresholding

After the extraction of the tracts of interest using *PICo*, the resulting connectivity maps are thresholded so that pathways and branches with a low probability of connection, which are assumed to be false positives, are excluded. As our aim is to measure tract width, each set of extracted tracts are thresholded at a given connection probability value, which is applied across all subjects and all groups. This avoids inter-individual bias in the tract width measurement.

In this work we introduce a method for the automatic identification of the optimum threshold value in order to minimise any user-introduced bias (Figure 1). Given N datasets and $2 \times N$ instances of a given tract extracted from both hemispheres of the individuals, the unthresholded tracts from a given hemisphere of all the subjects are used to form a training set. Our thresholding algorithm starts by randomly selecting a tract from one of the subjects as the target tract. Then, using affine registration [8] with 12 degrees of freedom, we register all the corresponding tracts from the other subjects to this target tract. The algorithm then creates an initial average probability of connectivity map or average tract of all the registered tracts. The initial average is then used to again register all the individuals' tracts from their native space into the initial average tract's space, resulting in a secondary average tract. The secondary average tract is then presented to the user who identifies an optimum threshold value for the average tract. The algorithm still requires some level of anatomical knowledge in order to estimate the true topology of the tract of interest. The secondary average tract is then used as the template tract for determining the optimum group threshold.

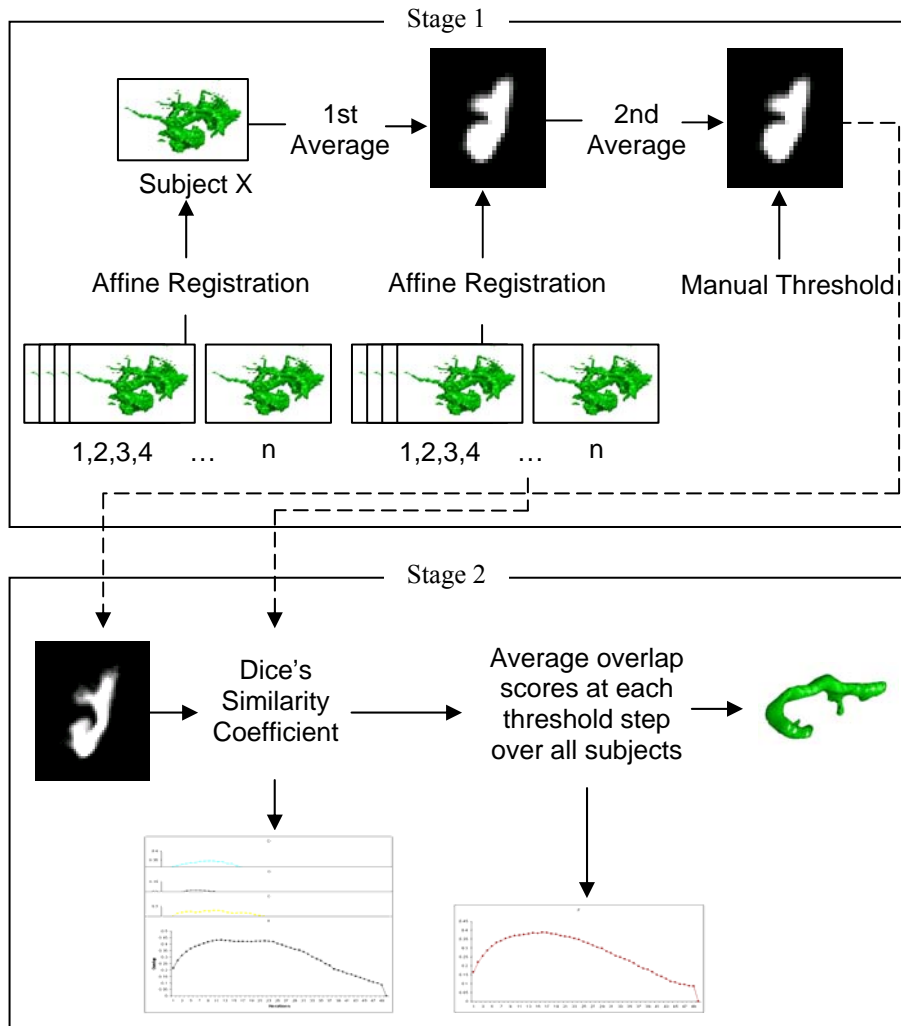


Fig. 1. Flow diagram of the steps involved in the automated thresholding algorithm.

The algorithm iteratively applies a threshold value, which ranges from a probability of 0 to 1 in steps of 0.01 and applies this to each individual's tract. At each thresholding step the algorithm computes the Dice's similarity coefficient [9] between the thresholded tract and the secondary average image in 3D space. The overlap scores at each candidate threshold are averaged over all subjects and the threshold value with the highest average percentage overlap score is identified as the optimum group threshold. After thresholding the tracts using the optimum threshold value, they are filtered using a median kernel of size 3x3x3 to remove isolated voxels that have not been effectively thresholded out and are not attached to the main body of the tract (Figure 2).

3.3 Object Triangulation

In this work the Matlab Isosurface algorithm was used to create triangulated surfaces of the binarised tracts. This algorithm takes a binarised object and outputs a series of vertex coordinates and a table that contains the information on how these vertices are connected together to form the faces of the triangles forming the isosurface representation.

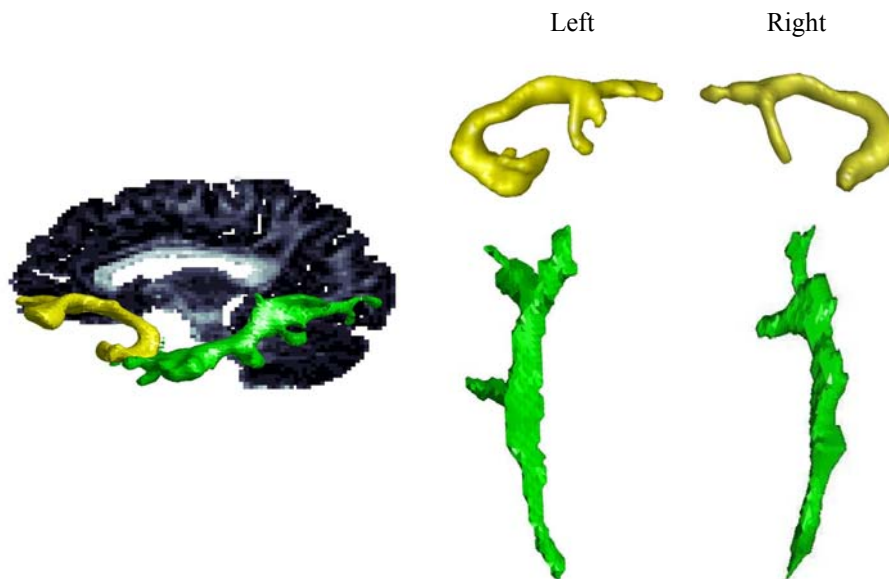


Fig. 2. Left: The UF (yellow) and ILF (green) overlaid on a sagittal slice. Right: The left and right UF tracts (yellow), and the left and right ILF tracts (green) which are extracted from a subject and pre-processed using the described steps.

The use of binarised/voxalised surface representations increases the likelihood of partial voluming at the boundaries of object. The initial mesh that is created is sparse and follows the rigid boundary of the binarised object. In order to generate a more refined representation of curvature at the boundary of objects, a series of mesh refinements steps were carried out.

3.3.1 Loop Subdivision and Mesh Refinement

The process of triangulation and mesh refinement results in a smoother and more natural representation of the boundary of the tracts. One of the most commonly used methods for mesh refinement is loop subdivision [10], which creates a sequence of successively finer meshes which converge to a continuous limit surface [11].

In this framework, given a triangle/face that is made of three vertices A, B and C, four smaller and triangles of equal area are created by locating the midpoints a, b and c along the vectors connecting each of the vertices to the other two, such that (Figure 3):

$$a = (A+B)/2, b = (B+C)/2 \text{ and } c = (C+A)/2 . \quad (1)$$

A weakness of the standard loop subdivision approach is that the area of the faces that form two different triangulated surfaces may vary, and so this difference in area still exists in the area of the refined faces of the finer meshes. This is an important point as the vertices of the meshes are going to be used as reference points for the measurement of the widths of the tracts, and so faces of equal areas forming the mesh representation of our tracts is desired, hence leading to an unbiased and uniform sampling of width values across a tract and subjects.

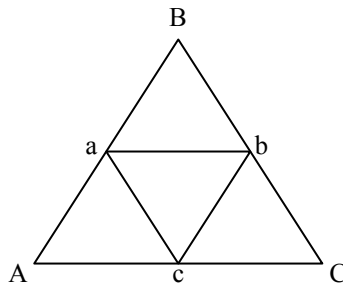


Fig. 3. An illustration of the loop subdivision process (see also Eq. 1).

To accommodate for this potential bias we introduce a novel solution in which a constant weighing factor, D , is used, which controls how many levels of subdivision are needed for each object. D is set to be the minimal distance of the mean distance between vertices of a triangle. To identify the optimum value for D , a triangulated representation of a unit sphere was successively refined and at each iteration the surface area of the triangulated surface was calculated and compared with the known surface area of the sphere. This was repeated until the surface area of the refined triangulated surface was so close to that of the unit sphere's that the percentage error between the actual surface area and the triangulated sphere's surface area was less than 0.5%. D was then set to be the mean distance between the vertices of the triangles forming the optimally refined mesh (0.14 mm).

In practice, when refining the triangulated tract meshes, only three to four levels of subdivisions were required to reach the optimum value for D .

3.4. Skeletonization

In this work we implemented the methodology described by Cornea et al [12] for the generation of *curve-skeletons*. This algorithm begins by computing a repulsive force field over the entire object, resulting in a 3D dataset where each voxel contains a virtual force vector. Topological characteristics of this vector field, such as critical points are used to generate the skeleton.

3.4.1. Repulsive Force Function

The repulsive force function is generated by placing charges on the thresholded tract object's boundary, which results in the generation of a force field within the object (Figure 4).



Fig. 4. The sagittal view of an UF tract with charge nodes (depicted using red points) placed on its boundary.

As the objects being processed in this work are 3D triangulated objects, the vertices of the surface triangles can be considered as point charges that are used to generate the repulsive force vector field. The repulsive force at a given point due to a given point charge is defined as a force pushing the point away from the charge with a force that is inversely proportional to a power of the distance between the point and the charge node and is defined as [12]:

$$\overrightarrow{F_{PC}} = \frac{\overrightarrow{CP}}{R^m}, \quad (2)$$

where $\overrightarrow{F_{PC}}$ is the repulsive force at a given point, P , as a result of the point charge C , \overrightarrow{CP} represents the normalized vector from C to P indicating the direction of the force, R is the distance between the point P and the charge C and m is the order of the force function ($m=2$ for the Newtonian force).

Equation 2 can be used to compute the force at a point P , which is generated by the effect of numerous point charges on that given point [12]:

$$\overline{F_P} = \sum_i \overline{F_{PC_i}}, \quad (3)$$

where $\overline{F_P}$ is the sum of the forces at point P and $\overline{F_{PC_i}}$ are the forces resulting from each point charge C_i .

3.4.2. Generating the Curve Skeleton

Curve skeleton segments are identified by first finding the critical points in the force field – points with zero net force vector magnitude. As described by [13], the occurrence of a zero in the vector field is a product of the absence of the three components of the force vector (x , y and z), and so, by identifying regions in which each vector component changes sign, one can predict that the given region contains a critical point. It is possible to make use of the real and imaginary components of the eigenvalues of the Jacobian matrix of the vector-field at the critical point to classify critical points. A positive real part of an eigenvalue points to the existence of a repelling critical point, a negative part points to an attracting critical point and, an imaginary part denotes a spiralling motion around the point [12]. In the event of the eigenvalues having the same sign, and the critical point being negative, it is classified as attracting, and if the critical point is positive, it is classified as repelling. A critical point is classified as a saddle point when two of the real eigenvalues have the same sign and the third having an opposite sign. Saddle points are important in the extraction of a curve-skeleton. They occur in between attracting and repelling critical points and are used to form a connection between them. As the vector field is directed towards the interior of the object, the flow leading away from a saddle point can only reach another critical point, which in turn can be an attracting critical point or another saddle point. Streamlines are then initiated from the saddle points and are propagated in the direction of the eigenvectors that relate the positive eigenvalues which represent the outward flow. A streamline force-following algorithm is used which terminates if it arrives at another critical point or if it revisits a previous location within the vector field. This algorithm operates on the basis of examining the force value at each point and moving along the force direction in small step sizes (0.1 of the greatest voxel dimension in the dataset). Samples along the integration path which is initiated away from a saddle point make up a skeleton segment and in turn skeleton segments that connect all the critical points within the force field would define the critical-curves which form the core skeleton (Fig. 5: A).

3.5. Tract Width Measurement

The generated curve-skeletons are used as references against which the tract widths are measured. In this work we devise a new method for the sampling and measurement of width. This approach makes use of the repulsive force fields that were calculated for the generation of the curve-skeletons and the vertices of the triangulated meshes as seeds for a second force-following algorithm that tracks through the vector field. Using the vertices of the mesh as opposed to the centroids of the boundary voxels to act as the starting seed points for the force following algorithm

leads to the initiation of more streamlines and hence ensures a better sampling of the vector field and in turn width.

Starting from the triangulated mesh vertices, streamlines are propagated using trilinear interpolation with the step size again set to 0.1 of the greatest dimension of the voxels in the dataset and terminate when reaching a skeleton voxel. By following the force field vectors through the tract object a unique mapping of each boundary point to the skeleton is achieved. We term these paths geodesics as they represent the minimum cost line integral between two points through the force field.

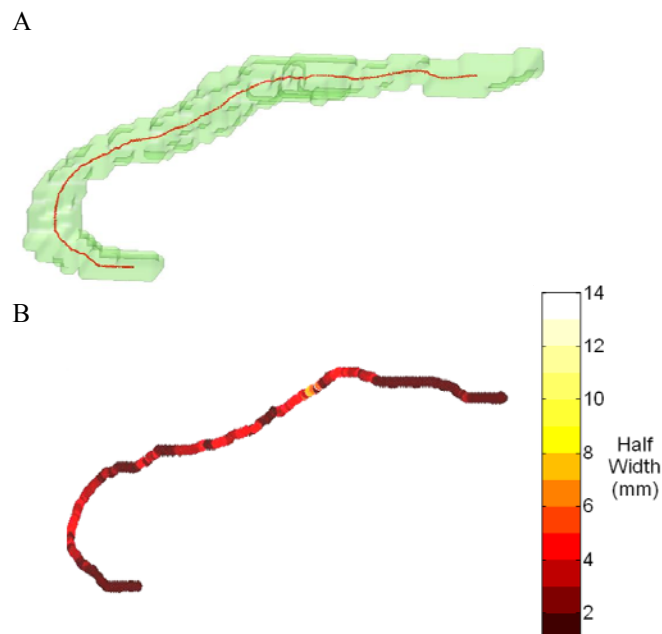


Fig. 5. A) The Isosurface representation of a tract (green) overlaid with its skeleton (red). B) Tract skeleton colour-coded by half-width values.

The mean length of geodesics terminating at a given skeleton voxel defines the mean half-width at that voxel. By repeating this for every skeleton voxel, the widths of the tracts are calculated as a function of position along the tracts (Fig. 5: B).

4. Results

For the *UF*, in the *Normal-Aged* group all eight subjects demonstrated right hemisphere lateralization where the right *UF* had a higher mean width than the left. This lateralization was statistically significant at the group level (paired *t*-test $p =$

0.0005). In the *MCI* group seven out of eight subjects also demonstrated right hemisphere lateralization; and this was also significant at group level ($p = 0.0057$). As for the *AD* group there was no such clear pattern of lateralization in the group and the paired *t*-test also did not reveal any significance ($p = 0.6815$).

Figure 6 shows normalized group histograms of width values of the left and the right *UF* and *ILF* of all eight subjects for each group. It can be seen that for the *UF* there is a shift towards higher width values in the right hemisphere. It can also be seen that the mean *UF* half-width values for both the *Normal-Aged* and *MCI* groups are higher than that of the *AD* group. The right-lateralization absence in the *AD* group is clearly visible.

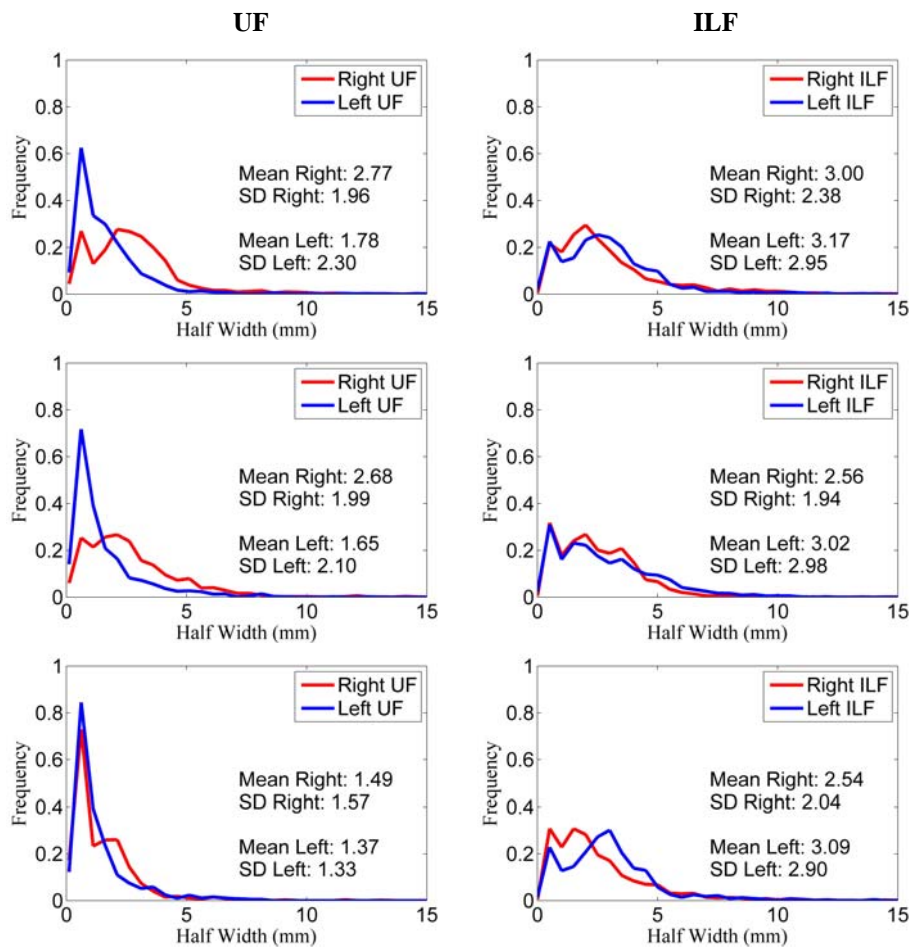


Fig. 6. Normalised histogram plot of the half-width values of the left and right *UF* (left column) and *ILF* (right column) tracts of all the subjects in the *Normal-Aged*, *MCI* and *AD* groups.

As illustrated in table 1, cross-group comparisons performed using unpaired *t*-tests also demonstrate the reduction in the right *UF* thickness in *AD*.

For the *ILF*, across the *Normal-Aged*, *MCI* and *AD* groups there was no pattern of lateralization between the left and right *ILF* tracts ($p=0.9046$, $p=0.1979$ and $p=0.7750$ respectively).

Table 1. Cross-group comparisons performed using unpaired *t*-tests on the mean half-width values of the *UF*.

Groups	Statistically Significant Difference	p-value
Normal-Aged ↔ MCI	No	0.5126
Normal-Aged ↔ AD	Yes	0.0071
MCI ↔ AD	Yes	0.015

5. Discussion & Conclusions

This work introduces a method to quantify the geodesic width of the *WM* tracts, and generates results that are consistent with known neuroanatomy. The evidence of possible right hemisphere lateralization for the *UF* in the *Normal-Aged* and *MCI* groups is comparable to published *in vitro* work [14], which found right hemisphere lateralization in the *UF* in 80% of their subjects.

We have presented evidence that the *UF* reduces in thickness in *AD* and that the lateralization of this tract is lost. Furthermore, the fact that the *SLF* proved impossible to be extracted in all subjects in the *AD* group is probably due to tract-specific atrophy as well. To our knowledge this is the first time that specific tract atrophy relating to *AD* has been reported. The lack of atrophy in the *ILF* indicates that the measurement has a degree of specificity to individual tracts and therefore to the affects of atrophy on specific connections and networks. This is important for two reasons. Firstly, the lack of change in the *ILF* provides confidence that the method is not simply reflecting whole-brain atrophy, and is therefore adding new information. Secondly, this specificity may help in understanding the pattern of disease progression and the relationships between functional decline and tissue alterations.

The proposed method may be used to quantify tract-specific white matter atrophy that results from conditions such as *AD*, and may be used to differentiate width variations between normal and patient groups or as an imaging biomarker in clinical trials to assess the performance of a given treatment on the rate of atrophy.

Acknowledgements. This work is funded by GlaxoSmithKline (GSK) and the UK EPSRC via a CASE award, the UK BBSRC (BB/E002226/1) and the UK MRC (G0501632).

REFERENCES

1. Parker, G.J.M., Chard, D.T.: Volume and atrophy, in *Quantitative MRI of the Brain: Measuring changes caused by Disease*. John Wiley & Sons Ltd (2003).
2. Embleton, K.V., Haroon, H.A., Morris, D.M., Lambon Ralph, M.A., Parker, G.J.M.: Distortion correction for diffusion-weighted MRI tractography and fMRI in the temporal lobes, *Human Brain Mapping*, (in press).
3. Tuch, D.S.: Q-ball imaging. *Magn. Reson. Med.* 52, 1358--1372 (2004).
4. Haroon, H.A., Morris, D.M., Embleton, K.V., Alexander, D.C., Parker, G.J.M.: Using the model-based residual bootstrap to quantify uncertainty in fiber orientations from Q-ball analysis. *IEEE Trans. Med. Imaging.* 28, 535--550 (2009).
5. Catani, M., Howard, R.J., Pajevic, S., Jones, D.K.: Virtual in vivo interactive dissection of white matter fasciculi in the human brain. *Neuroimage.* 17, 592--617 (2002)
6. Parker, G.J.M., Alexander, D.C.: Probabilistic Monte Carlo based mapping of cerebral connections utilising whole-brain crossing fibre information. *Inf. Process. Med. Imaging.* 18, 684--695 (2003).
7. Parker, G.J.M., Alexander, D.C.: Probabilistic anatomical connectivity derived from the microscopic persistent angular structure of cerebral tissue. *Philos. Trans. R. Soc. Lond. B. Biol. Sc.* 360, 893--902 (2005).
8. Smith, S.M., Jenkinson, M., Woolrich, M.W., Beckmann, C.F., Behrens, T.E.J., Johansen-Berg, H., Bannister, P.R., De Luca, M., Drobnjak, I., Flitney, D.E., Niazy, R., Saunders, J., Vickers, J., Zhang, Y., De Stefano, N., Brady, J.M., Matthews, P.M.: Advances in functional and structural MR image analysis and implementation as FSL. *NeuroImage.* 23, 208--219 (2004).
9. Shattuck, D.W., Prasad, G., Mirza, M., Narr, K.L., Toga, A.W.: Online resource for validation of brain segmentation methods. *NeuroImage.* 45, 431--439 (2009).
10. Loop, C., DeRose, T.: Generalized b-spline surfaces of arbitrary topology. *IEEE Trans. Vis. Comput. Graph.* 10, 347--356 (1990).
11. Yushkevich, P., Zhang, H., Simon, T.J., Gee, G.C.: Structure-specific statistical mapping of white matter tracts. *NeuroImage.* 41, 448--461 (2008).
12. Cornea, N., Silver, D., Yuan, X., Balasubramanian, R.: Computing Hierarchical Curve-Skeletons of 3D Objects. *The Visual Computer.* 21, 945--955 (2005).
13. Globus, A., Levit, C., Lasinski, T.: A Tool for Visualizing the Topology of Three-Dimensional Vector Fields. In: 2nd conference on Visualization, IEEE Visualization, pp. 33--40, IEEE Press, San Diego (1991).
14. Highley, J.R., Walker, M.A., Esiri, M.M., Crow, T.J., Harrison. P.J.: Asymmetry of the Uncinate Fasciculus: A Post-mortem Study of Normal Subjects and Patients with Schizophrenia. *Cerebral Cortex.* 12, 1218--1224 (2002).

A Variational, Non-Parametric Approach to the Fuzzy Segmentation of Diffusion Tensor Images

Sebastiano Barbieri¹, Miriam H.A. Bauer², Jan Klein¹, Christopher Nimsky²,
and Horst K. Hahn¹

¹ Fraunhofer MEVIS - Institute for Medical Image Computing,
Universitätsallee 29, 28359 Bremen, Germany

² Department of Neurosurgery, University of Marburg,
Baldingerstrasse, 35033 Marburg, Germany

Abstract. This paper presents a novel variational approach for the segmentation of diffusion tensor images (DTI). After a certain fiber bundle has been tracked by means of an arbitrary fiber tracking algorithm, we suggest to use the DTI segmentation algorithm to better determine the true borders of the fiber bundle. Specifically, we perform kernel density estimations of the probability density functions (PDFs) of the principal diffusion directions in the foreground - to be segmented - and the background. Thus, we choose a non-parametric approach and do not make any assumption on the distribution of the underlying data. The estimated PDFs are employed to construct a novel energy functional to be minimized. The energy functional contains a fuzzy membership function and a regularization term, to guarantee the smoothness of the resulting segmentation. A robust and efficient two-phase method is used to minimize the energy functional and simultaneously update the density functions. The algorithm is validated on both simulated DTI phantoms and real data.

Keywords: Brain, Diffusion Tensor Imaging, Fiber Tracking, Fuzzy Segmentation, Parzen Density Estimate, Non-Parametric

1 Introduction

Diffusion tensor imaging (DTI) is a magnetic resonance imaging method which allows to measure the anisotropic diffusion of water molecules in in-vivo biological tissue such as white matter (WM) in the brain [9,31,28]. An important application of DTI is fiber tractography, which assumes that the principal diffusion direction matches the orientation of the corresponding underlying fiber system and thus allows the reconstruction of the 3D architecture of WM fiber pathways [8,25,29]. In recent years, fiber tractography has become well established in the research environment with first clinical uses being reported.

A drawback of many streamline tractography algorithms is that the extent of the tracked fiber bundle is often underestimated [7]. For this reason, we suggest a variational approach to the segmentation of diffusion tensor images which may

be used as a postprocessing step for fiber tracking when it is crucial to precisely estimate the true border location of the bundle. In further detail, the voxels pierced by a tracked fiber are used to initialize the segmentation algorithm.

In [27], a fuzzy region competition algorithm for the segmentation of scalar valued images has been proposed. In this work, we illustrate how some of those ideas may be adapted to segment diffusion tensor images. Moreover, for the sake of efficiency, we suggest a simplified version of the energy functional to be minimized. The functional is composed of a fuzzy competition term and a regularization term. The competition term drives the solution toward the most likely region (the tract to be segmented or the background) based upon kernel density estimations of the PDFs of the principal diffusion directions, whereas the regularization term guarantees smooth segmentation results. A minimizer of the functional, which is robust with respect to the initialization and efficiently computed, may be obtained by using the two-phase algorithm presented in [11]. Segmentation results may be visualized in 2D as color coded likelihood maps of a voxel being part of the segmented tract, or (after thresholding) in 3D as semi-transparent hulls around the tracked fibers.

Possible applications of the algorithm include determining the exact location of the boundaries of a certain fiber bundle when planning a neurosurgical procedure or a more precise quantization of the atrophy of different white matter structures in dementia patients.

Structure of the paper. After discussing related work in Section 2, we detail the segmentation method in Section 3. In particular, we illustrate the two phases of the algorithm: the estimation of the probability density functions in Section 3.1 and the minimization of the energy functional in Section 3.2. Moreover, in Section 3.4, we suggest simple ways of making the segmentation algorithm act locally on the image. Results on modeled DTI software phantoms and on a real patient dataset are shown in Section 4 and some concluding remarks are made in Section 5.

2 Related Work

The problem of segmenting diffusion tensor data has received increasing attention in recent years. In [33], a crisp segmentation algorithm based on k -means clustering is presented with the goal of partitioning the thalamus into its different nuclei. As a distance measure, the k -means approach employs a linear combination of the Mahalanobis distance between voxel coordinates and the Frobenius norm of the difference between the two diffusion tensors at those coordinates.

The work of [34] similarly aims at segmenting thalamic nuclei from DTI, and by making use of spectral clustering and Markovian relaxation, presents the advantage of not having to explicitly define the centers of the clusters. Compared to these two approaches, in the context of tract reconstruction, fuzzy segmentation algorithms have the advantage that they can be used to determine voxels which present partial volume effects, such as the contemporary presence of different

grey matter tracts, or of different tissues such as grey matter and cerebrospinal fluid.

In [4,5,3] an interesting fuzzy and nonparametric approach to DTI segmentation is suggested. The approach makes use of the tensor representation in the Log-Euclidean framework [1] and information theory to cluster tensors belonging to a specific tract. However, from our experience, the Log-Euclidean similarity-invariant distance between tensors is very sensitive to changes in tensor eigenvalues and less sensitive with respect to changes in the principal diffusion direction, which leads to segmentation results which are able to distinguish very well between clusters of different anisotropy, but to a lesser extent between tensor clusters which differ only slightly with respect to the principal diffusion direction. For this reason, in this paper we concentrate our analysis on the distribution of the principal diffusion direction in the different tensor clusters.

In [10], a weighted graph is constructed with a number of vertexes corresponding to the number of image voxels and weights assigned to the edges based on the difference in fractional anisotropy between tensors at neighboring voxels. Binary tract extraction is obtained by means of an s - t cut of the graph. We compare the segmentation results of this min-cut based algorithm to the results of the variational approach suggested in this paper.

3 Methods

We start by computing an initial estimate of the fiber tract to be segmented by means of the streamline tractography algorithm presented in [32]. However, any other tractography algorithm may be used. Let us denote the vector-valued image containing the principal diffusion directions estimated in each voxel by I . Further, define a fuzzy membership function u over the domain Ω of I , constrained to take values in the interval $[0, 1]$. A higher value of u at voxel x corresponds to a higher likelihood for the voxel x to be part of the tract we would like to segment. Initially, we set $u = 1$ at voxels through which the tracked fibers go (the foreground of the image) and $u = 0$ elsewhere (the background of the image). Next, we apply a two-phase fuzzy region competition algorithm, described in its general form in [26]. In the version of the algorithm presented in this work, the algorithm alternates between estimating the probability density functions (PDFs) of principal diffusion directions in the foreground and background of the image and finding a fuzzy membership function u that minimizes a specific energy functional. These two steps are described in detail in the next sections.

3.1 Estimation of the Probability Density Functions

Let us denote the PDF of the principal diffusion direction at voxels belonging to the tracked bundle by p_1 and the PDF of the principal diffusion direction at voxels belonging to the background by p_2 . Because the sense of principal diffusion directions is unknown, we may restrict our computations to the upper hemisphere of the 2-sphere S^2 , which we denote by \mathcal{A} . To this end, for n approximately evenly

distributed points $\{a\}$ on \mathcal{A} we evaluate

$$p_1(a) = \frac{1}{\|u\|_1} \int_{\Omega} u(x)K(a, I(x)) dx \quad (1)$$

$$p_2(a) = \frac{1}{\|1-u\|_1} \int_{\Omega} (1-u(x))K(a, I(x)) dx \quad (2)$$

where $\|u\|_1 = \int_{\Omega} u(x) dx$ and K is a weighting function. Specifically, Equations (1) and (2) correspond to continuous versions of weighted Parzen density estimates [30]. Although possible appropriate choices for the kernel K are manifold, we use the von Mises-Fisher distribution [2,23] on S^2 with mean direction μ and concentration parameter κ

$$K(a, \mu) = C_3(\kappa) \exp(\kappa a^T \mu) \quad (3)$$

with $\kappa \geq 0$, $\|\mu\| = 1$ and C_3 a normalization constant given by

$$C_3(\kappa) = \frac{\kappa}{4\pi \sinh(\kappa)} = \frac{\kappa}{2\pi(e^{\kappa} - e^{-\kappa})} \quad (4)$$

Examples of estimated PDFs p_1 and p_2 are shown in Figure 1.

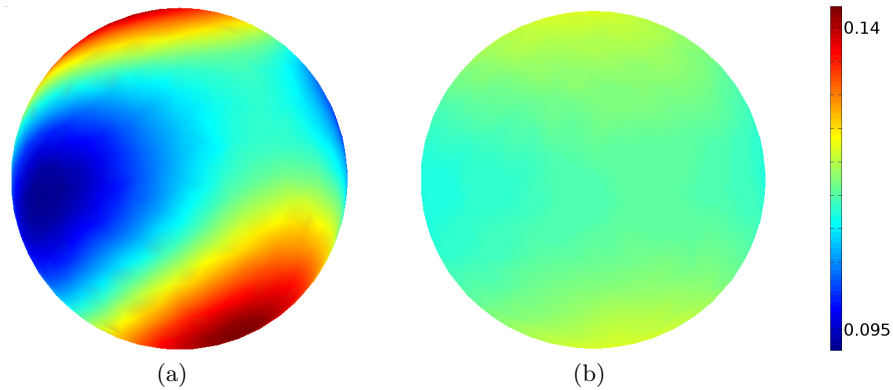


Fig. 1. Example of estimated probability density functions of the diffusion direction at voxels belonging to the tracked fiber bundle (a) and of the diffusion direction at voxels belonging to the background (b). For visualization purposes, the whole sphere is shown and not only the upper hemisphere to which we restrict our computations. Notice the strong directional preference in voxels belonging to the tracked bundle.

3.2 Fuzzy Membership Formulation

Once the PDFs p_1 and p_2 have been estimated, we suggest minimizing the following energy functional

$$F(u, p_1, p_2) = \int_{\Omega} |\nabla u(x)| dx + \lambda \int_{\Omega} \{u(x) \cdot [-p_1(I(x))] + (1-u(x)) \cdot [-p_2(I(x))]\} dx. \quad (5)$$

The first term of the energy functional is a regularization term that minimizes the total variation of u , i.e. the sum of the perimeters of its level sets, and thus guarantees the smoothness of the segmented region. The second term, weighted by a scalar $\lambda > 0$, is the fuzzy competition term which drives the membership function u towards the region of higher probability. In order to minimize F , we follow the approach described in [11] in a related context: we introduce an auxiliary variable v and minimize the approximation to F given by

$$\begin{aligned} \tilde{F}(u, v, p_1, p_2) = & \int_{\Omega} |\nabla u(x)| dx + \frac{1}{2\theta} \int_{\Omega} |u(x) - v(x)|^2 dx \\ & + \lambda \int_{\Omega} \{v(x) \cdot [-p_1(I(x))] + (1-v(x)) \cdot [-p_2(I(x))]\} dx \end{aligned} \quad (6)$$

with respect to the minimizing couple (u^*, v^*) . The scalar θ is chosen to be small, so that u^* and v^* are almost identical. The optimal v^* may be computed as [11]

$$v^*(x) = \min(\max(0, u(x) - \theta r(x)), 1) \quad (7)$$

where the error function $r(x)$ is given by $r(x) = \lambda \cdot [p_2(I(x)) - p_1(I(x))]$. For simplicity and efficiency, having already evaluated the PDFs p_1 and p_2 on n approximately evenly distributed points on \mathcal{A} , we evaluate the PDFs at $I(x)$ by using nearest-neighbor interpolation. It is easy to see that Equation (7) updates $v(x)$ to indicate a membership to the most likely region. We are now left with the minimization of the membership function u . In the form of Equation (6), only the first two terms of \tilde{F} depend on u , which are exactly the functional minimized in [12] to obtain an image of minimized total variation u from a noisy image v . Let us review the algorithm suggested in [12] to solve the total variation minimization problem and extend it to the three dimensional case. For an image q of size $N_x \times N_y \times N_z$ the gradient ∇q at (i, j, k) is defined as the vector (q_x, q_y, q_z) . For example, the partial derivative in x -direction is approximated by

$$q_x(i, j, k) = \begin{cases} q(i+1, j, k) - q(i, j, k) & \text{if } i < N_x \\ 0 & \text{if } i = N_x \end{cases} \quad (8)$$

and respectively in the other dimensions. For a vector-valued image p of size $N_x \times N_y \times N_z \times 3$, the divergence operator $\text{div } p$ is defined as

$$\begin{aligned}
(\text{div } p)(i, j, k) = & \begin{cases} p(i, j, k, 1) - p(i-1, j, k, 1) & \text{if } 1 < i < N_x \\ p(i, j, k, 1) & \text{if } i = 1 \\ -p(i-1, j, k, 1) & \text{if } i = N_x \end{cases} \\
& + \\
& \begin{cases} p(i, j, k, 2) - p(i, j-1, k, 2) & \text{if } 1 < j < N_y \\ p(i, j, k, 2) & \text{if } j = 1 \\ -p(i, j-1, k, 2) & \text{if } j = N_y \end{cases} \\
& + \\
& \begin{cases} p(i, j, k, 3) - p(i, j, k-1, 3) & \text{if } 1 < k < N_z \\ p(i, j, k, 3) & \text{if } k = 1 \\ -p(i, j, k-1, 3) & \text{if } k = N_z \end{cases} \quad (9)
\end{aligned}$$

In three dimensions, it can be shown (the proof is similar to the 2D case in [12]) that for $\tau \leq 1/12$, $p^0 = 0$ and

$$p^{n+1}(i, j, k, \cdot) = \frac{p^n(i, j, k, \cdot) + \tau(\nabla(\text{div } p^n - v/\theta))(i, j, k, \cdot)}{1 + \tau|(\nabla(\text{div } p^n - v/\theta))(i, j, k, \cdot)|} \quad (10)$$

the series

$$v - \theta \text{div } p^{n+1} \quad (11)$$

converges to the optimal solution u^* as $n \rightarrow \infty$. Similarly to the remark in the original paper that setting $\tau = 1/4$ still seems to lead to convergence for the 2D case, from our experience in 3D the algorithm appears to work well for $\tau = 1/6$ as well.

3.3 Overview of the algorithm

Summarizing, for a given tolerance $t_s \geq 0$, our algorithm works as follows:

- obtain initial guess for the segmentation of the fiber tract by means of a fiber tracking algorithm
- initialize u^0 to 1 at voxels pierced by the tracked fibers and to 0 elsewhere
- while $|u^{n+1} - u^n|_\infty > t_s$
 - estimate the PDFs p_1 and p_2 according to Equations (1) and (2)
 - set $v := u$
 - update v according to Equation (7)
 - minimize the total variation of u according to Equation (11)
- threshold u to obtain the segmented fiber tract

3.4 Local Adaptation

In order to estimate the PDFs of the principal diffusion direction not globally on the whole image but locally, we suggest applying the algorithm multiple times on subimages centered at the centerline of the tracked fibers, as schematically illustrated for a synthetic image in Figure 2(a). In our implementation we compute the centerline by simply averaging the coordinates of the tracked fibers, although more complicated skeletonization approaches such as the ones described in [14,15] may be used. Another simple option is to split the image into multiple images along one dimension, and subsequently compute a box around the tracked fibers in the remaining two dimensions.

4 Results

We test our algorithm on two synthetic datasets with varying amount of image noise and on one real image. As suggested in [16], Rician distributed noise may be simulated in a magnitude MR image by computing $|E(\mathbf{q}, \Delta) + \tilde{N}(0, \sigma^2)|$, where $E(\mathbf{q}, \Delta)$ is the attenuated MR signal and $\tilde{N}(0, \sigma^2)$ is a Gaussian distributed complex variable with mean 0 and variance σ^2 .

For both synthetic datasets, we use the parameters $\kappa = 1$, $\theta = 10$, $\lambda = 1$, $t_s = 0.1$, $t_{TV} = 0.01$. t_{TV} is the threshold parameter on the maximal difference between u^{n+1} and u^n when iteratively minimizing the total variation of u . For the real dataset we choose $\lambda = 0.5$, preferring a slightly lower competition factor because of potentially similar directions in foreground and background.

The first dataset is given by a torus-shaped DTI phantom. For details on the construction of the model, see [7]. The model presents a fiber bundle shaped as part of a torus, surrounded by highly isotropic tensors with random principal diffusion direction. The b_0 image is shown in Figure 2(a), together with the labeling of the seed ROI used for fiber tracking and the subimages along the centerline of the bundle to which our algorithm is applied. An example noisy b_0 subimage ($\sigma = 6$) is shown in Figure 2(b), and results of the variational segmentation algorithm are displayed in Figure 2(e) and 2(f). The generated segmentation results are compared to the original mask obtained by means of fiber tracking and to the min-cut based approach presented in [10], by computing the corresponding Dice’s similarity coefficient [35]. Results for the torus-shaped phantom are presented in Table 1.

Noise Standard Deviation	2.0	4.0	6.0
original mask after fiber tracking	0.844	0.771	0.654
after applying the variational segmentation algorithm	0.957	0.945	0.939
after applying the min-cut based segmentation algorithm	0.923	0.918	0.918

Table 1. Comparison of Dice’s coefficients for the torus-shaped model.

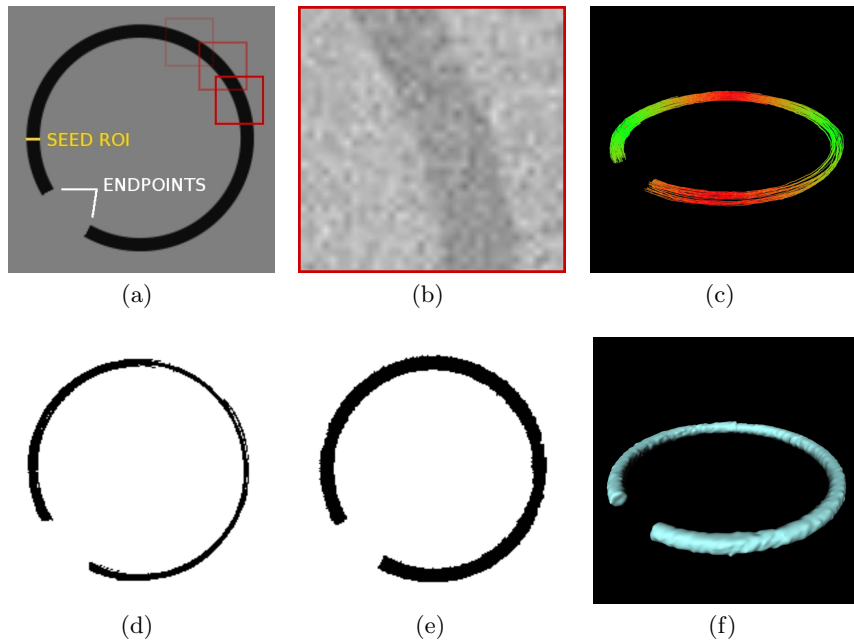


Fig. 2. (a) The b_0 image of the torus-shaped DTI phantom with labeled seed ROI used for fiber tracking and the subimages along the centerline of the bundle to which our algorithm is applied (delineated by the red boxes). (b) Example noisy b_0 subimage ($\sigma = 6$). (c) Result of fiber tracking. (d) One slice of the mask used to initialize the segmentation algorithm, given by the voxels pierced by the tracked fibers. (e) Resulting mask after applying the variational segmentation algorithm and thresholding. (f) Segmentation result displayed in 3D as iso-surface.

Next, we test our algorithm on a DTI phantom based on the BrainWeb project [13], with which we realistically modeled part of the right corticospinal tract (details on the model can be found in [6]). Both the tensors which are part of the tract and the tensors in the background have approximately the same anisotropy. Examples of tracked fibers are shown in Figure 3(a), and an example color coding of the membership function u is presented in Figure 3(b). Segmentation results for different noise levels are given in Table 2.

Noise Standard Deviation	2.0	4.0	6.0
original mask after fiber tracking	0.702	0.610	0.640
after applying the segmentation algorithm	0.888	0.868	0.862
after applying the min-cut based segmentation algorithm	0.849	0.831	0.768

Table 2. Comparison of Dice’s coefficients for the BrainWeb-based model.

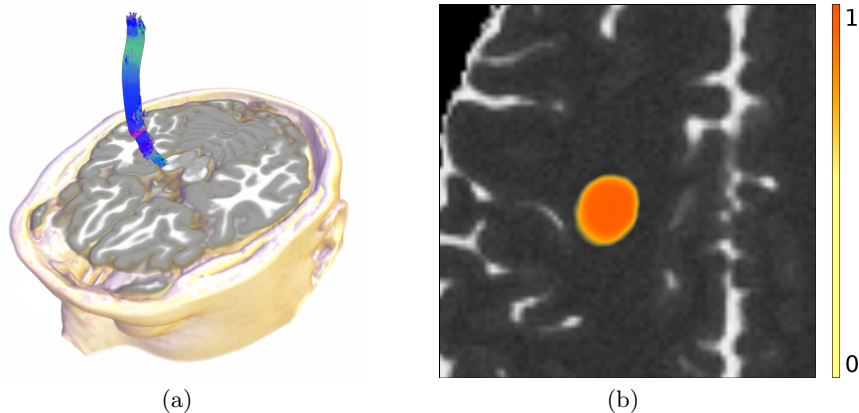


Fig. 3. (a) Example of fibers tracked on the BrainWeb-based DTI phantom, in which we modeled part of the corticospinal tract. (b) The fuzzy membership function u is color coded and overlaid on a slice of the modeled b_0 image (noise $\sigma=6$).

Finally, we test our algorithm on a real magnetic resonance dataset of a tumor patient (diffusion-weighted images with $TR/TE/FA = 10700\text{ms}/84\text{ms}/90^\circ$, voxel size is $1.80 \times 1.80 \times 1.98\text{mm}$, source: [17]) on which we track the corticospinal tract. We assume that the surgeon performing fiber tracking considers the tracked fibers to be part of the bundle he would like to segment, therefore for this dataset we do not allow for voxels to be excluded from the initial segmentation mask, but only included. The resulting segmentation is visualized in 2D by color coding the membership function u (see Figure 4(a)) and in 3D as a semi-transparent hull around the tracked fibers (see Figure 4(b)). A non-optimized Matlab [24] implementation of the algorithm on a modern PC (Intel Core2 Quad CPU) took approximately 30 minutes to segment the image.

5 Discussion

With this work, we have presented a novel variational approach to the segmentation of DTI data. The algorithm consists of two steps which are alternated in an iterative fashion: the estimation of the PDFs of the principal diffusion directions in the tract to be segmented and in the image background, followed by the minimization of an energy functional which drives voxels to the most likely region based on the principal diffusion direction in that voxel, and guarantees a smooth partition of the image by minimizing the total variation of the membership function u .

Our first tests on both synthetic data (which we could quantitatively analyze by comparing Dice's similarity coefficients) and a real dataset support the validity of the method. The Dice's coefficients are a bit lower for the BrainWeb-based phantom, which may be due to excessive smoothness imposed on the segmenta-

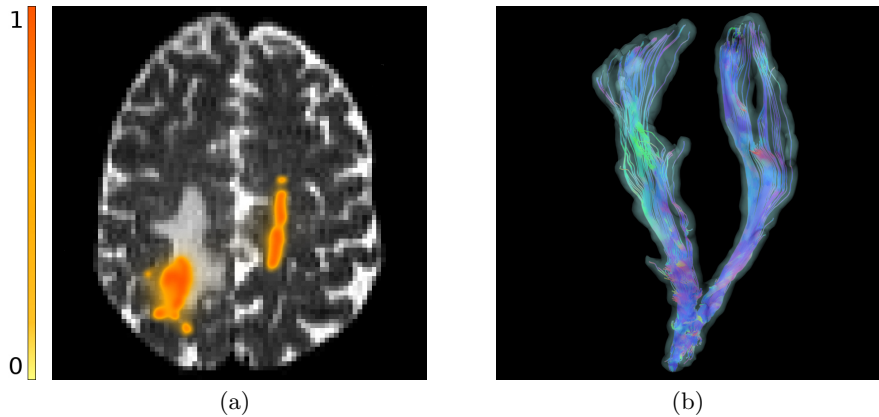


Fig. 4. The corticospinal tract of a tumor patient has been tracked and successively segmented. In (a) the fuzzy membership function u is color coded and overlaid on a slice of the original b_0 image. In (b) the segmentation result after thresholding is visualized as a semi-transparent hull around the tracked fibers.

tion result in regions near the cortex where the phantom presents an irregular border. An optimization of the parameters will be considered in future work, in addition to an in-depth analysis of the stability of the computed fuzzy membership function with respect to different initializations (i.e., different parameters used for the initial fiber tracking) and modeling of the underlying tensor data. Moreover, extensive analysis is needed in order to determine an appropriate threshold value for the likelihood function, depending on the properties (such as image noise and resolution) of the considered dataset.

Two positive indications may be inferred from the segmentation results on the synthetic test data. As a first remark, being based on an analysis of the principal diffusion directions of the tensors, the algorithm seems to perform well both when there is a large anisotropy difference between the two regions (torus-shaped model) and when the difference mainly lies in the principal diffusion direction (BrainWeb-based model). As a second remark, the algorithm seems to produce segmentation results of comparable quality when different levels of image noise are modeled. Finally, higher segmentation accuracy was obtained compared to the graph-based approach from [10].

An interesting idea for future work may be to estimate the variance-covariance matrix of the principal diffusion direction in each voxel according to the framework presented in [19,20,21] and make use of the obtained data for a pointwise kernel density estimation of the PDFs of the principal diffusion directions. This way, particularly noisy voxels could contribute less to the estimated PDFs. The algorithm should also be extended to make use of information on fractional anisotropy, or on all six tensor entries, to better deal with the case of crossing or kissing fibers.

In conclusion, we hope that after an accurate analysis of the stability of the suggested method, the algorithm may be helpful for presurgical planning and various clinical studies.

Acknowledgments

This project was funded in part by the German Research Society (DFG PE199/21-1 & DFG NI568/3-1).

References

1. Arsigny, V., Fillard, P., Pennec, X., Ayache, N.: Log-euclidean metrics for fast and simple calculus on diffusion tensors. *Magn. Reson. Med.* 56, 411–421 (2006)
2. Awate, S., H., Gee, J.: Dispersion on a sphere. In: *Proc. Roy. Soc. London Ser. A.* vol. 217, pp. 295–305 (1953)
3. Awate, S., H., Gee, J.: A fuzzy, nonparametric segmentation framework for dti and mri analysis. In: *Proc. Inf. Process Med. Imaging.* pp. 296–307 (2007)
4. Awate, S., Zhang, H., Gee, J.: Fuzzy Nonparametric DTI Segmentation for Robust Cingulum-Tract Extraction. *Lect. Notes Comput. Sci.*, Springer, Berlin, Germany (2007)
5. Awate, S., Zhang, H., Gee, J.: A fuzzy, nonparametric segmentation framework for dti and mri analysis: With applications to dti-tract extraction. *IEEE Trans. Med. Imaging* 26, 1525–1536 (2007)
6. Barbieri, S., Klein, J., Nimsy, Ch., Hahn, H.: Assessing fiber tracking accuracy via diffusion tensor software models. In: *Proc. SPIE Medical Imaging* (2010)
7. Barbieri, S., Klein, J., Nimsy, Ch., Hahn, H.: Towards image-dependent safety hulls for fiber tracking. In: *Proc. ISMRM* (2010)
8. Basser, P.: Fiber-tractography via diffusion tensor MRI (DT-MRI). In: *Proc. Int. Soc. Magn. Reson. Med.* (1998)
9. Basser, P., Mattiello, J., LeBihan, D.: MR diffusion tensor spectroscopy and imaging. *Biophys. J.* 66(1), 259–267 (1994)
10. Bauer, M., Egger, J., O’Donnell, T., Barbieri, S., Klein, J., Freisleben, B., Hahn, H., Nimsy, Ch.: A fast and robust graph-based approach for boundary estimation of fiber bundles relying on fractional anisotropy maps. In: *Proc ICPR* (2010)
11. Bresson, X., Esedoglu, S., Vandergheynst, P., Thiran, J.P., Osher, S.: Fast global minimization of the active contour/snake model. *J. Math. Imaging Vis.* 28, 151–167 (2007)
12. Chambolle, A.: An algorithm for total variation minimization and applications. *J. Math. Imaging Vis.* 20, 89–97 (2004)
13. Collins, A., Zijdenbos, A., Kollokian, V., Sled, J., Kabani, N., Holmes, C., Evans, A.: Design and construction of a realistic digital brain phantom. *IEEE Trans. Med. Imaging* 17(3), 463–468 (1998)
14. Cornea, N., Silver, D., Min, P.: Curve-skeleton properties, applications, and algorithms. *IEEE Trans. Vis. Comput. Graph.* 13, 530–548 (2007)
15. Cornea, N., Silver, D., Yuan, X., Balasubramanian, R.: Computing hierarchical curve-skeletons of 3d objects. *Visual. Comput.* 21, 945–955 (2005)
16. Hahn, H., Klein, J., Nimsy, Ch., Rexilius, J., Peitgen, H.O.: Uncertainty in diffusion tensor based fiber tracking. *Acta Neurochir. Suppl.* 98, 33–41 (2006)

17. IEEE Vis. Contest. Image Data, Case 1: <http://viscontest.sdsc.edu/2010/> (2010)
18. Jonasson, L., Bresson, X., Haggmann, P., Thiran, J., Wedeen, V.: Representing diffusion mri in 5-d simplifies regularization and segmentation of white matter tracts. *IEEE Trans. Med. Imaging* 26(11), 1547–1554 (2007)
19. Koay, C., Chang, L.C., Carew, J., Pierpaoli, C., Basser, P.: A unifying theoretical and algorithmic framework for least squares methods of estimation in diffusion tensor imaging. *J. Magn. Reson.* 182, 115–125 (2006)
20. Koay, C., Chang, L.C., Pierpaoli, C., Basser, P.: Error propagation framework for diffusion tensor imaging via diffusion tensor representations. *IEEE Trans. Med. Imaging* 26(8), 1017–1034 (2007)
21. Koay, C., Nevo, U., Chang, L.C., Pierpaoli, C., Basser, P.: The elliptical cone of uncertainty and its normalized measures in diffusion tensor imaging. *IEEE Trans. Med. Imaging* 27(6), 834–846 (2008)
22. Lenglet, C., Rousson, M., Deriche, R.: Dti segmentation by statistical surface evolution. *IEEE Trans. Med. Imaging* 25(6), 685–700 (2006)
23. Mardia, K., Jupp, P.: *Directional Statistics*. Wiley Series in Probability and Statistics, Wiley, Chichester, U.K. (1999)
24. Matlab: The MathWorks, Inc., Natick, MA
25. Mori, S., Crain, B., Chacko, V., Van Zijl, P.: Three-dimensional tracking of axonal projections in the brain by magnetic resonance imaging. *Ann. Neurol.* 45(2), 265–269 (1999)
26. Mory, B., Ardon, R.: Fuzzy region competition: A convex two-phase segmentation framework. In: *Proc. SSVM*. pp. 214–226 (2007)
27. Mory, B., Ardon, R., Thiran, J.P.: Variational segmentation using fuzzy region competition and local non-parametric probability density functions. In: *Proc. ICCV*. pp. 1–8 (2007)
28. Neil, J., Shiran, S., McKinstry, R., Schefft, G., Snyder, A., Almlie, C., Akbudak, E., Aronovitz, J., Miller, J., Lee, B., Conturo, T.: Normal brain in human newborns: apparent diffusion coefficient and diffusion anisotropy measured by using diffusion tensor MR imaging. *Radiology* 209, 57–66 (1998)
29. Parker, G., Wheeler-Kingshott, C., Barker, G.: Estimating distributed anatomical connectivity using fast marching methods and diffusion tensor imaging. *IEEE Trans. Med. Imaging* 21(5), 505–512 (2002)
30. Parzen, E.: On estimation of a probability density function and mode. *Ann. Math. Statist.* 33, 1065–1076 (1962)
31. Pierpaoli, C., Basser, P.: Toward a quantitative assessment of diffusion anisotropy. *Magn. Reson. Med.* 36, 893–906 (1996)
32. Schlüter, M., Konrad-Verse, O., Hahn, H., Stieltjes, B., Rexilius, J., Peitgen, H.O.: White matter lesion phantom for diffusion tensor data and its application to the assessment of fiber tracking. In: *Proc. SPIE Med. Imaging*. vol. 5746, pp. 835–844 (2005)
33. Wiegell, M., Tuch, D., Larson, H., Wedeen, V.: Automatic segmentation of thalamic nuclei from diffusion tensor magnetic resonance imaging. *Neuroimage* 19, 391–402 (2003)
34. Ziyang, U., Tuch, D., Westin, C.F.: Segmentation of thalamic nuclei from DTI using spectral clustering. In: *Proc. MICCAI*. pp. 807–814 (2006)
35. Zou, K., Warfield, S., Bharatha, A., Tempany, C., Kaus, M., Haker, S., Wells III, W., Jolesz, F., Kikinis, R.: Statistical validation of image segmentation quality based on a spatial overlap index. *Acad Radiol.* 11(2), 178–189 (2004)

The lateralization of structure and function in aging: A combined fMRI and DTI study.

Jeffrey T. Duda¹, Delani Gunawardena², Corey McMillan², Murray Grossman², and James C. Gee³

¹ Department of Bioengineering, University of Pennsylvania, USA,
jtduda@seas.upenn.edu,

² Department of Neurology, University of Pennsylvania, USA.

³ Department of Radiology, University of Pennsylvania, USA.

Abstract. Measures from event-related functional MRI, diffusion tensor imaging tractography and cognitive performance in a language-based task were used to test the hypothesis that lateralization of function and structure changes with age and plays a role in regulating cognitive performance. Functional activation was examined in three functionally activated regions and their opposite hemisphere homologues in healthy young adults and healthy seniors. The healthy seniors were divided into two groups, one that was cognitively matched with the young adults, and one that performed more poorly on a working memory task. The functional regions were used to identify the white matter fiber tracts that provide the biological connectivity between the activated regions and structural connectivity was measured by averaging fractional anisotropy (FA) over a geometric fiber bundle model that projects local white matter properties onto a centerline. Young adults had symmetric activation patterns. Seniors were found to have higher activation in the right posterior temporal cortex and this activation was higher for higher performing seniors than lower performing seniors. FA in the right hemisphere arcuate fasciculus was found to have higher FA in seniors, but lower FA was found in the right hemisphere short frontal fibers and the posterolateral temporal inter-hemispheric connections of seniors. Higher performing seniors also lower FA in the inferior frontal inter-hemispheric connections compared to lower performing seniors. Right hemisphere compensatory activation in older adults may be due in part to age-related changes in white matter connectivity.

1 Introduction

Lateralization, the asymmetric distribution of cognitive resources between hemispheres, is a distinctive feature of the human brain. Lateralization is particularly prominent in language resources which are primarily handled in the left hemisphere. Studies of the aging brain have suggested that older adults recruit right hemisphere resources for language processing, however the basis for the compensatory process is not known [1]. It could be due to the implementation of novel

cognitive strategies that are not used (and not needed) by younger adults except for very difficult tasks, some age-related change in the cortical anatomy, to a change in the efficiency of the connectivity between cortical regions, or some combination of the above. In this paper functional subnetworks in the brain are examined using MRI to measure both structure and function during a language processing task. A healthy young adult population is compared to healthy seniors. The seniors are grouped into higher performing and lower performing groups so that functional and structural differences may be examined.

Functional regions identified in a previous study [2] were used to examine region-averaged activation values. The functional regions were then used to identify the white matter fiber tracts that provide the communication channels between the functional regions. Atlas-based DTI tractography was used to create geometric models of fiber bundles. Deterministic tractography was used to identify the well defined association fibers that connect the functional regions of interest while a shortest-path tractography method is used to identify the inter-hemispheric connections. Structure was quantified with arc-length parameterizations of fractional anisotropy (FA) [3–6]. These structural and functional metrics were used to identify possible differences between the young adult and senior populations as well as within the high and low performing senior groups.

2 Methods

Functionally activated regions were defined using fMRI and used to examine functional activation levels in these regions as well as in homologous regions in the opposite hemisphere. The activated regions were used along with diffusion tensor MRI tractography to identify the white matter pathways that provide the biological connectivity of the network. Tract-averaged FA was measured in each fiber tract using a centerline-based method to identify structural differences related to aging. Diffusion tensor images, T1 images and fMRI were acquired for a set of ten young adults and 13 seniors. A working memory test was used to group the seniors into two sets, one that was cognitively matched with the young adults ($n=7$), and one that performed more poorly on the test ($n=6$). These groupings are used to examine the relationship between structure and function and their relationship to cognitive performance and aging.

2.1 MRI acquisition

Scans were acquired on a Siemens 3.0T Trio scanner. T1-weighted structural images were acquired using an MPRAGE protocol ($TR = 1620ms$, $TE = 3ms$, flip angle of 15° , 1 mm slice thickness, 192×256 matrix, resolution = $0.9766 \times 0.9766 \times 1.0mm$). BOLD fMRI images were acquired with fat saturation, 3 mm isotropic voxels, flip angle of 15° , $TR = 3s$, $TE_{eff} = 30ms$ and a 64×64 matrix. DT-MRI images were acquired with 4 $b = 0$ images and 30 directional diffusion weighted images (resolution = $1.875 \times 1.875 \times 2.0mm$, 112×112 matrix, $b = 1000s/mm^2$).

2.2 Analyses of fMRI

A previous study investigated the neural mechanisms that support the resolution of grammatically complex sentences [2]. Regions were identified from a contrast of the point at which an ambiguity is encountered in a “more compatible” direct object structure (e.g. “The mayor heard the election result on the radio”) minus “less-compatible” sentences (e.g. “The mayor heard the election result was fixed”) [2]. Processing of the fMRI data was performed using SPM5 [7]. For each subject, the functional data was motion-corrected, transformed into MNI space, spatially smoothed with a 8mm FWHM isotropic Gaussian kernel and interpolated to isotropic 2 mm voxels. A canonical hemodynamic response function was used to convolve the onset times of stimulus events for each condition. A general linear model approach was then used to calculate statistical parameter estimates for each subject. The previously identified cortical regions were used to determine a peak activation MNI-space coordinate which was used as the center of a spherical region of interest (ROI) with a radius of 8mm. An average t-value was calculated for each ROI, in each subject.

2.3 Analyses of DTI

Diffusion tensor tractography in individual subjects is highly subject to false-positive connections, but recent work has shown that population atlases provide an appropriate space for identifying fiber bundle geometry [8–10]. To achieve this, a multivariate atlas (DTI + T1) was created for the young and elderly subjects from larger data sets of scanner and age-matched subjects. The young and elderly atlases were then registered into a single final template space. Each subject’s high resolution T1 weighted image was registered to the corresponding age-matched template using Symmetric Normalization as implemented in Advanced Normalization Tools [11]. This was accomplished through the use of a multi-resolution, non-rigid registration algorithm to optimize a cross correlation metric under the constraints of a diffeomorphic transformation model [11]. A brain mask of the template was propagated to each subject’s T1 weighted image. These skull-stripped T1 weighted images were then registered to the FA image derived from each subject’s diffusion tensor image. The intra-subject transforms were composed with the T1 atlas transforms in order to transform the each subjects’ tensor data into the final template space using the preservation of principle technique along with log-Euclidean linear interpolation.

2.4 Fiber Tractography

The diffusion tensor component of the atlas was used to perform whole brain, deterministic fiber tractography [12]. Landmarks were manually placed in the T1 component of the atlas in order to extract well defined white matter fiber bundles [13]. The functionally activated regions were warped from MNI space into the template space and used as target regions to identify fiber bundles that connected two regions of interest. Deterministic tractography was sufficient for

identifying the association fibers that provide the intra-hemispheric connections, but was not sufficient for identifying the inter-hemispheric connections. Deterministic DTI tractography is known to have difficulty distinguishing between multiple fiber directions in a single voxel and is biased towards the most prominent fiber direction in a voxel. In the case of the corpus callosum, deterministic DTI tractography only identifies inter-hemispheric connections between superior cortical regions. To identify the most likely connective pathways between the lateral cortical regions examined here, a shortest-path methodology was employed. The total cost of a given potential pathway is determined by examining a local energy metric, $f(x)$, and summing over all points x in the path.

$$f(x) = \beta_1 d(x, x-1) + \beta_2 (1.0 - FA(x)) + \beta_3 (1.0 - \mathbf{e}(\mathbf{x})\mathbf{t}(\mathbf{x})) \quad (1)$$

where $d(x, x-1)$ is the distance between x and the previous position of x , $FA(x)$ is the fractional anisotropy of the tensor at x , $\mathbf{e}(\mathbf{x})$ is the principle direction of diffusion at x , $\mathbf{t}(\mathbf{x})$ is the tangent to the path at x , and β_1 , β_2 and β_3 are user controlled parameters (here we used $\beta_1 = 1.0$, $\beta_2 = 3.0$, and $\beta_3 = 1.0$). Dijkstra's algorithm is used to find the shortest-path between a seed point and a set of possible target points [14]. To find the fiber tracts that provide inter-hemispheric connectivity, all points in each left hemisphere region were used as seeds and the points in the homologous right hemisphere region were used as possible targets. The process was then repeated using the right hemisphere as seeds and the left hemisphere points as targets. For each pair of regions this resulted in a set of streamlines connecting the regions.

A popular approach to avoiding partial voluming bias is to incorporate a centerline or skeletonization technique in which an FA value at each point is determined by finding the maximum FA in the local neighborhood [10, 9]. Here we used a template-fiber approach where an elliptical cross-section was defined at each point along the centerline and used to identify local maxima. Each white matter tract was estimated as a set of streamlines, each of which was parametrized by arc-length to extend from 0.0 to 1.0. A BSpline was then fit to the set of all points from all streamlines in each bundle to obtain a single centerline that lies in the core of the fiber pathway of interest. For each point along the model pathway, a tangent was calculated and used to determine a perpendicular plane. The intersection of this plane with each of the streamlines in the bundle defined a set of points. The normal and binormal vectors were used to reparameterize the intersection points into 2D coordinates. Graham's scan method was used to determine the convex hull that encloses the set of intersection points [15], and least-squared method was applied to the points on the hull to define an elliptical cross-section [16]. To obtain a single FA value for the entire fiber bundle, the FA values were averaged over the length of the centerline.

3 Results

3.1 Function

The functional analyses revealed a network made up of 3 activated regions in the left hemisphere: dorsolateral prefrontal cortex (DLPFC), posterolateral temporal cortex (PLTC) and inferior frontal cortex (IFC). The region-averaged functional activation values are summarized in figure 1. To identify activation changes that potentially result from aging, a Student's t-test was used to compare the young adults to all seniors for each ROI and suggested that activation in the right posterolateral cortex is greater in seniors ($p=0.012$). This same approach was used to identify potential differences between the cognitively matched and unmatched seniors. The cognitively matched seniors were found to have greater activation in the right dorsolateral prefrontal cortex ($p=0.014$) and reduced activation in the left posterolateral cortex ($p=0.033$) compared to the unmatched seniors.

3.2 Structure

The DTI tractography identified a network of connections made up of the arcuate fasciculus (right and left hemispheres), a bundle of short frontal fibers (right and left hemispheres), and 3 subcomponents of the corpus callosum. These fiber bundles were used to generate geometric models, illustrated in figure 2. A Student's t-test was used to identify potential differences between the young adults in seniors. Reduced FA in seniors compared to young adults was found in the inter-hemispheric connection between the PLTC regions ($p=0.02889$) and in the right short frontal fibers ($p=0.00955$). Increased FA in seniors was found in the right arcuate fasciculus ($p=0.00747$). Compared to lower performing seniors, higher performing seniors had lower FA in the inter-hemispheric connections between right and left IFC.

4 Discussion

This study demonstrated the potential for using combined analysis of fMRI and DTI in examining age-related changes in function and structure in the brain and how these changes regulate behavior. A comparison of the inter-hemispheric activation patterns that occur in the high and low performing elderly adults reveals differences in the DLPFC and PLTC regions. In both cases the low performing elderly adults have higher activation in the left hemisphere compared to right, while the high performing elderly adults have higher activations in the right hemisphere compared to left. These functional differences are accompanied by structural differences in the white matter that connects these activated regions. The finding of increased FA in the right hemispheric arcuate fasciculus and decreased FA in the short frontal fibers in the right hemisphere of elderly subjects compared to young adults suggests that age-related white matter changes may facilitate the increased functional recruitment of right hemispheric resources.

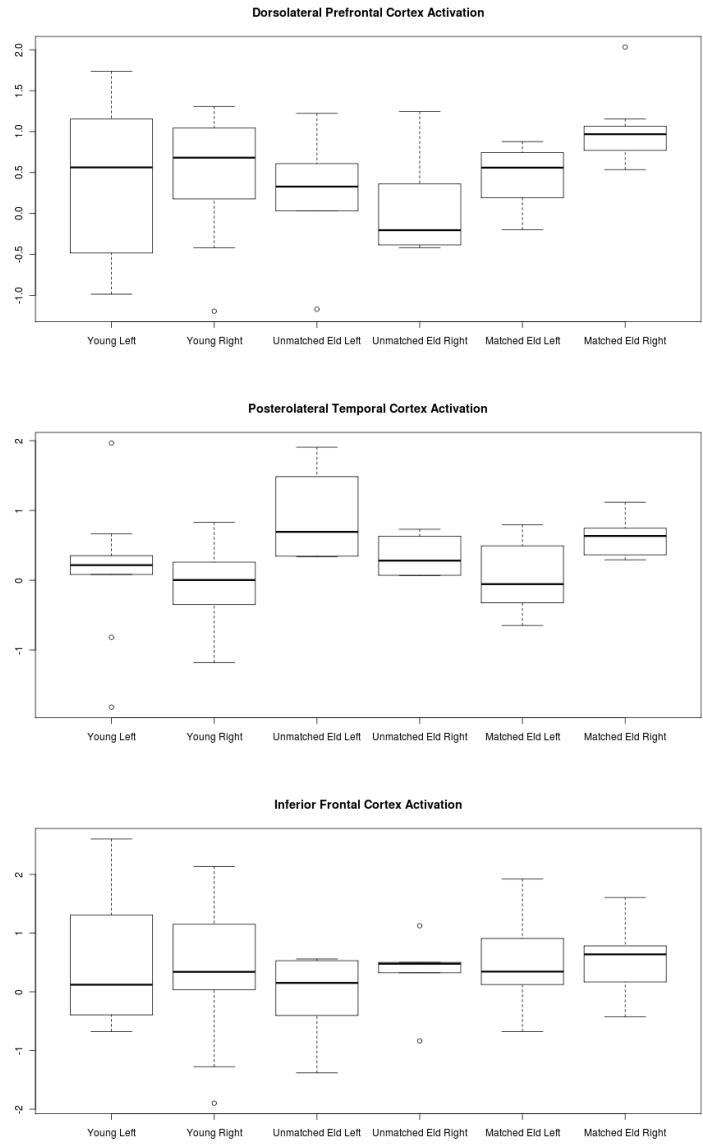


Fig. 1. Region-averaged functional activation was measured in both hemispheres in the dorsolateral prefrontal cortex (top row), posterolateral temporal cortex (middle row) and inferior frontal cortex (bottom row).

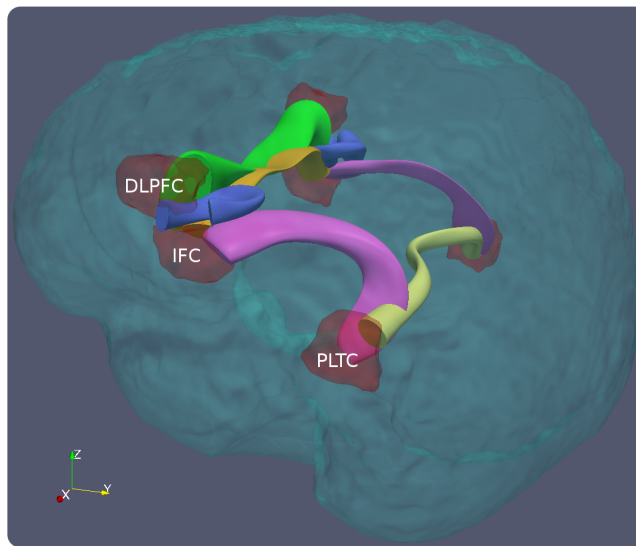


Fig. 2. A set of 3 functionally activated regions: Dorsolateral Prefrontal Cortex (DLPFC), Posterolateral Temporal Cortex (PLTC), and Inferior Frontal Cortex (IFC) were identified in the left hemisphere. These regions, along with their right hemisphere homologues were used to identify the fiber tracts that provide biological connectivity. In each hemisphere, intra-hemispheric connectivity is provided by the arcuate fasciculus (pink) and a bundle of short frontal fibers (blue). Each homologous pair of activated regions was used to identify the following subcomponents of the corpus callosum that provided inter-hemispheric connectivity: DLPFC (green), IFC (orange) and PLTC (yellow). Surface-meshes created from the the geometric models are used for visualization of the white matter tracts.

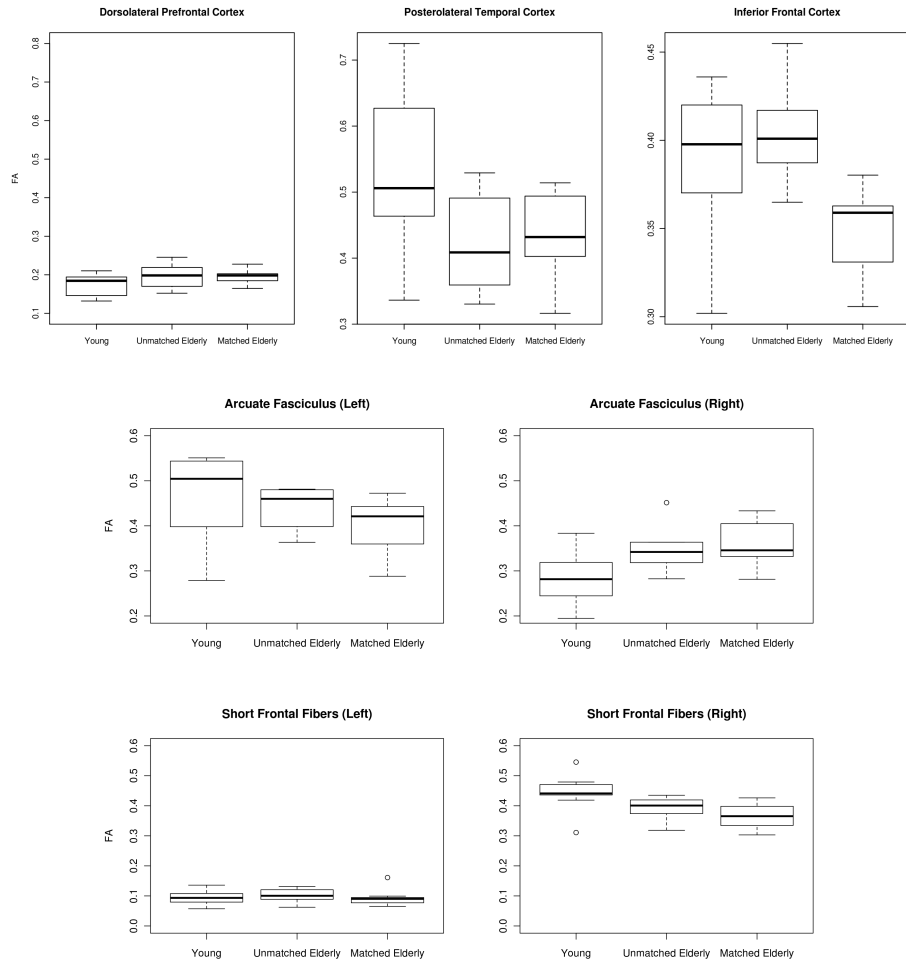


Fig. 3. Tract-averaged fractional anisotropy was measured for the portions of the corpus callosum that provide inter-hemispheric connections between the cortical regions of interest (top row), the arcuate fasciculus (middle row) and short frontal fibers (bottom row).

Age related differences in inter-hemispheric connections are also found with elderly adults exhibiting lower FA in the connection between PLTC compared to young adults. Differences between the high and low performing adults were found in the connections of the inferior frontal cortex with high performing elderly adults having lower FA than the low performing adults who had similar FA values to that of the young adults. These results suggests that age-related changes in both functional and structural lateralization have effects on cognitive performance, but due to the limited sample size and complex nature of the structures, further examination is required.

The use of template fibers with elliptical cross-sections provided an effective geometric model for examining white matter fiber bundle properties, but a great deal of opportunity exists for the development of more biologically relevant measures of structure. Here, these models were purely template-based and used to examine FA in individual subjects. Using these template-based models as a basis for fitting subject-specific models from subject-space tractography could potentially provide a more sensitive measure of structural integrity and could provide a framework that explicitly examines the geometry of white matter pathways as well as the properties of the underlying tissue. Additionally, the use of metrics that leverage the expected fiber orientation provided by the geometric model may be useful as they incorporate more widespread information about the fiber tract as opposed to the purely local measure provide by FA [17].

In summary, an atlas-based approach was used to examine age-related changes in functional and structural lateralization. Seniors were found to have higher activation in the right PLTC and this activation was greater for higher performing seniors than lower performing seniors. Age-related increases and decreases in association fiber were found with FA in the right hemisphere arcuate fasciculus being higher in seniors, but FA in the right hemisphere short frontal fibers being lower in seniors. Reduced FA was found in the the PLTC inter-hemispheric connections of all seniors. Differences were found between high and low performing seniors in the commisural connections of the IFC with low performing seniors having FA values similar to the young adults and high performing seniors having reduced FA.

References

1. Cabeza, R., Anderson, N.D., Locantore, J.K., McIntosh, A.R.: Aging gracefully: compensatory brain activity in high-performing older adults. *Neuroimage* **17**(3) (2002) 1394–1402
2. Gunawardena, D., McMillan, C., Peelle, J., Troiani, V., Grossman, M.: fMRI shows age-related changes in resolving a temporary structural ambiguity. *Proceedings of Neuroscience 2009: Society for Neuroscience’s 38th Annual Meeting, Chicago* (2009)
3. Jones, D.K., Catani, M., Pierpaoli, C., Reeves, S.J.C., Shergill, S.S., O’Sullivan, M., Golesworthy, P., McGuire, P., Horsfield, M.A., Simmons, A., Williams, S.C.R., Howard, R.J.: Age effects on diffusion tensor magnetic resonance imaging tractography measures of frontal cortex connections in schizophrenia. *Human Brain Mapping* (2005)

4. Corouge, I., Fletcher, P.T., Joshi, S., Gouttard, S., Gerig, G.: Fiber tract-oriented statistics for quantitative diffusion tensor MRI analysis. *Med Image Anal* **10**(5) (2006) 786–798
5. Maddah, M., Grimson, W.E.L., Warfield, S.K., Wells, W.M.: A unified framework for clustering and quantitative analysis of white matter fiber tracts. *Med Image Anal* **12**(2) (2008) 191–202
6. O'Donnell, L.J., Westin, C.F., Golby, A.J.: Tract-based morphometry for white matter group analysis. *Neuroimage* **45**(3) (2009) 832–844
7. Ashburner, J., Friston, K.: Unified segmentation. *NeuroImage* **26** (2005) 839851
8. Goodlett, C.B., Fletcher, P.T., Gilmore, J.H., Gerig, G.: Group analysis of DTI fiber tract statistics with application to neurodevelopment. *Neuroimage* **45**(1 Suppl) (2009) S133–S142
9. Yushkevich, P., Zhang, H., Simon, T.J., Gee, J.C.: Structure-specific statistical mapping of white matter tracts. *NeuroImage* **41** (2008) 448461
10. Smith, S.M., Jenkinson, M., Johansen-Berg, H., Rueckert, D., Nichols, T.E., Mackay, C.E., Watkins, K.E., Ciccarelli, O., Cader, M.Z., Matthews, P.M., Behrens, T.E.J.: Tract-based spatial statistics: Voxelwise analysis of multi-subject diffusion data. *NeuroImage* (2006)
11. Avants, B.B., Schoenemann, P.T., Gee, J.C.: Lagrangian frame diffeomorphic image registration: Morphometric comparison of human and chimpanzee cortex. *Medical Image Analysis* **10**(3) (2006) 397–412
12. Cook, P.A., Bai, Y., Nedjati-Gilani, S., Seunarine, K.K., Hall, M.G., Parker, G.J., Alexander, D.C.: Camino: open-source diffusion-MRI reconstruction and processing. In: *Proceedings of 14th Scientific Meeting of the International Society for Magnetic Resonance in Medicine*. (2006) 2759
13. Wakana, S., Jiang, H., Nagae-Poetscher, L.M., van Zijl, P.C.M., Mori, S.: Fiber tract-based atlas of human white matter anatomy. *Radiology* (2004)
14. Dijkstra, E.: A note on two problems in connexion with graphs. *Numerische Mathematik* **1** (1959) 269271
15. Graham, R.L.: An efficient algorithm for determining the convex hull of a finite planar set. *Information Processing Letters* **1** (1972) 344–370
16. Fitzgibbon, A. W. and Pilu, M., Fisher, R.B.: Direct least-squares fitting of ellipses. *PAMI* **21**(5) (1999) 476–480
17. Duda, J., Avants, B., Asmuth, J., Zhang, H., Grossman, M., Gee, J.: A fiber tractography based examination of neurodegeneration on language-network neuroanatomy. In: *Proc. Workshop on Computational Diffusion MRI (MICCAI'08)*, New York, NY (2008)

Determining infusion sites for Convection Enhanced Delivery using probabilistic tractography

Hubert M. Fonteijn¹, Mark Woodhouse², Ed White², Steven S. Gill, and Daniel C. Alexander¹

¹ Centre for Medical Image Computing, Department of Computer Science, University College London, UK

h.fonteijn@cs.ucl.ac.uk

² Institute of Clinical Neurosciences, Frenchay Hospital, Bristol, UK.

Abstract. Convection Enhanced Delivery is a promising tool for drug delivery that circumvents the Blood Brain Barrier. In this paper, we develop a novel algorithm that determines the optimal infusion sites, given a target site. We use probabilistic tractography maps to approximate the drug distribution for each candidate site. We show promising results for a simulated tumour site in grey matter and discuss the application of this algorithm to the planning of infusion sites.

1 Introduction

Convection Enhanced Delivery (CED) is a new and promising technique for delivering drugs to the brain that circumvents problems caused by the Blood Brain Barrier. For example, the treatment options for brain tumours have traditionally been limited to surgical removal and intravenous drug delivery. Surgical removal is problematic, because it usually leaves behind some tumour tissue, which increases the likelihood of recurrence. Intravenous drugs delivery on the other hand is severely limited by the Blood Brain Barrier [1], which prevents most of the injected drug to reach the target tissue. Moreover, intravenously delivered drugs spread throughout the whole body, which poses limits on the toxicity of the drugs. More direct delivery methods, such as CED [2], have therefore attracted great interest. In CED, one or more catheters are placed directly into the brain. The catheters then deliver the drugs into the brain tissue surrounding the catheter tip. The pressure from the infusion causes the drugs to flow to targets that can be substantial distances away from the infusion site.

A key issue in CED is how to determine the infusion sites that achieve full coverage of the target site(s). The solution to this issue involves determining what the drug distribution will be from any candidate infusion site (the forward problem) and using this knowledge to determine the most optimal combination of infusion sites given a target site (the inverse problem). So far, only the forward problem has been extensively studied. For instance, Sampson et al. [3] develop a simulation framework that determines how the drug distribution evolves over

time, using well-known techniques from the literature on computational fluid dynamics in porous media. These simulations require knowledge of the conductivity tensor at each point in the brain to determine the local flow direction. Sampson et al. derive this conductivity tensor from the local diffusion tensor, which they estimate using Diffusion Tensor Imaging (DTI). DTI is an MRI modality which sensitizes the MR signal to the direction and speed of self-diffusion of water. Sampson et al. compare the simulated drug distributions with SPECT measurements and find a volume match between simulations and SPECT measurements of 36-100 %.

In this paper, we study the inverse problem: what are the optimal infusion sites, given a target site. Potentially, infusion sites could be selected by performing an exhaustive search through all possible candidate infusion sites and their simulated drug distribution. Each flow simulation however takes hours to days, which precludes this possibility. As a result, the selection of infusion sites is currently done manually by a neurosurgeon [3]. The neurosurgeon selects a candidate infusion site, from which drug distributions are simulated. She then evaluates the resulting drug distribution and either accepts the current infusion site or proposes a new one. However, the selection of good candidate sites is complicated, because their performance depends strongly on the local microstructure of the tissue, which is invisible to the neurosurgeon. Searching for the most optimal *combination* of infusion sites in terms of their combined coverage of the target site is even more difficult to achieve by a human expert.

In this paper, we therefore propose a new algorithm which determines the optimal combination of infusion sites, given a target site and patient-specific DTI data. We hypothesize that to a first approximation the drug distribution maps of each infusion site can be replaced by their probabilistic tractography maps, which are far less time-consuming to compute. An efficient algorithm then determines the optimal combination of infusion sites given a target volume. We evaluate the algorithm on DTI data from a human subject with a simulated tumour mass and we investigate the algorithm's robustness against variations in its parameters.

This paper is organized as follows: section 2 develops the algorithm for finding the ideal catheter position based on tractography experiments. Section 3 describes the experiments and results and section 4 concludes.

2 Theory

This section introduces the algorithm with which we determine the optimal infusion sites.

2.1 Infusion site algorithm

The aim of the infusion site algorithm is to determine the optimal combination of infusion sites for a given target site. For the moment we assume that the drug distribution map for each potential infusion site is available. The algorithm

proceeds by searching for the combination of infusion sites that maximizes the concentration of drugs in the target site. Exhaustive search is possible for up to two infusion sites, but becomes computationally infeasible for a larger number of infusion sites, because the number of possible combinations increases exponentially. We therefore implement a standard genetic algorithm for combinatorial search [4], using a population size of 100 x number of infusion sites, 1000 generations, a cross-over probability of 0.8 and a mutation probability of 0.1 and elitist selection. We find that the algorithm always converges to the most optimal solution within 100 generations.

Fluid flow simulations of drug distributions are too slow to run for all potential infusion sites. Here we approximate the drug distribution maps by probabilistic tractography maps. Probabilistic tractography provides an index of connectivity between two regions, which is based on a local probability distribution for the fibre direction. Generally, probabilistic tractography results in high connectivity values along the major pathways and lower values away from these pathways, a structural feature which probabilistic tractography shares with drug distribution maps. We use the PICO algorithm [5] which uses a calibration method that maps the anisotropy of the diffusion tensor to the uncertainty around its first eigenvector. This means that the probability is very narrowly distributed in voxels with a very anisotropic diffusion tensor, while voxels with an isotropic Diffusion Tensor have a very diffuse probability distribution function. The local probability distributions become therefore analogous to the conductivity tensors in fluid flow simulations: conductivity tensors with low anisotropy will locally disperse the fluid flow. The abovementioned similarities have led us to use probabilistic tractography maps as a fast approximation of fluid flow simulations.

We focus on tumour sites in grey matter. Probabilistic tractography is to a large extent uninformative in grey matter, because in grey matter, diffusion tensors are isotropic. We therefore define the boundary of the tumour with white matter as the target and determine the infusion voxels which maximize the coverage of this boundary. We assume that most of the tumour mass will be removed surgically and that the main aim of the drug infusions is to terminate any remaining tumour cells. This further motivates targeting the surrounding white matter because tumour cells spread preferentially along white matter pathways.

We narrow the set of potential infusion sites down by starting tractography in all of the voxels in the tumour’s white matter boundary. We create a mask of candidate voxels by selecting voxels that exceed a PICO threshold (0.05). We then start a new tractography experiment from each of the candidate voxels separately. We assume that an infusion is not a point process but that the voxels in an area around the infusion voxel act as a source as well. Therefore we determine for each voxel which other voxels are within a sphere of influence of radius r_{soi} . For each candidate infusion voxel, we now calculate its PICO value to each tumour boundary voxel, by taking the maximum PICO value over all voxels in the infusion voxel’s sphere of influence. If a voxel in the tumour’s boundary has a PICO value that exceeds the threshold value $\lambda_{threshold}$ we set its coverage

value for that candidate infusion voxel to one. We thus create a binary coverage matrix of *number of candidate voxels* x *number of voxels in tumour boundary*.

The algorithm has two free parameters: r_{soi} and $\lambda_{threshold}$. We aim to determine infusion sites that do not critically depend on these parameters. We therefore repeat the experiment for a range of different parameter combinations and run the genetic algorithm using the average of the coverage matrices for all different parameter settings as an input.

3 Experiments and Results

We perform four experiments to demonstrate the infusion site algorithm and to investigate the dependence of the infusion sites on the algorithm’s free parameters. We perform these experiments using DTI data from a 28 year old female. After informed consent has been given, we acquire diffusion-weighted MR images using a 3 T Siemens Trio scanner with maximum gradient strength 40 mT/m. We use a twice-refocused PGSE sequence to acquire diffusion-weighted scans in 64 non-collinear directions and 1 scan with no diffusion weighting. The diffusion-weighting and image sequence parameters are as follows: $b = 1000ms^{-2}$, TE = 88 ms, TR = 8 s, 70 slices with no gap, matrix size 96 x 96, resolution 2 x 2 x 2 mm. Preprocessing consists of aligning all volumes to the first volume using rigid-body transformations and Mutual Information as a similarity measure. Diffusion tensors are then fitted to the data by linear regression on the log-measurements. The eigenvectors and eigenvalues of the Diffusion Tensors are calculated and Fractional Anisotropy (FA) maps are created for visualization purposes. All DTI processing and tractography is performed in Camino [6].

We simulate a tumour mass in the subject’s temporal lobe by drawing a Region of Interest on the subject’s FA map (see figure 1). We use this tumour mass as a target site for the following experiments:

In the first experiment, we demonstrate that candidate infusion sites that are relatively nearby to each other can have a markedly different coverage of the tumour site. In figure 2 we show the PICo maps and tumour coverage using $r_{soi} = 9$ mm and $\lambda_{threshold} = 0.05$. Clear differences can be seen in both maps, with more limited PICo maps for the infusion site in the lower row.

In the second experiment, we investigate the dependence of the PICo maps on the algorithm’s parameters, using the following parameter settings: $r_{soi} = [3, 6, 9]$ mm and $\lambda_{threshold} = [0.05, 0.1, 0.2]$. Figure 3 shows the results for the same infusion sites as in figure 2. The PICo maps show the strongest dependence on r_{soi} while showing minimal dependence on $\lambda_{threshold}$.

In the third experiment, we study the influence of the algorithm’s parameters on the optimal infusion sites. We use the infusion site algorithm to determine one optimal infusion site, using the same parameters as in the second experiment. Figure 4 shows that in all different parameter settings a very similar optimal infusion site is found. This demonstrates the robustness of our procedure against variations in its parameters.

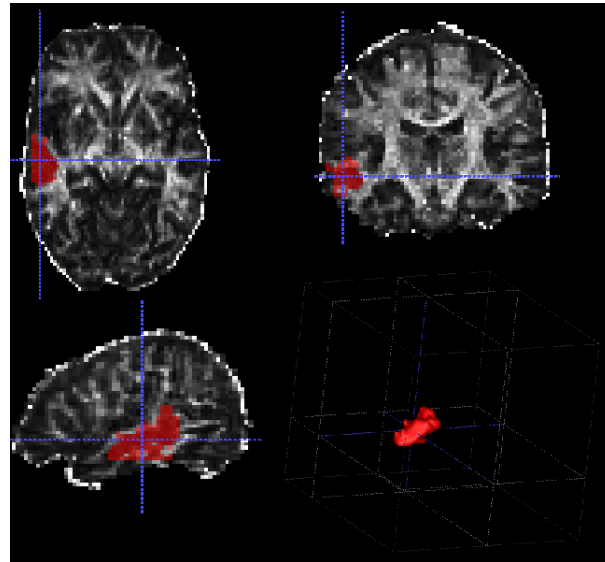


Fig. 1. shows the simulated tumour. The background image in this and all subsequent figures is the subject's FA image.

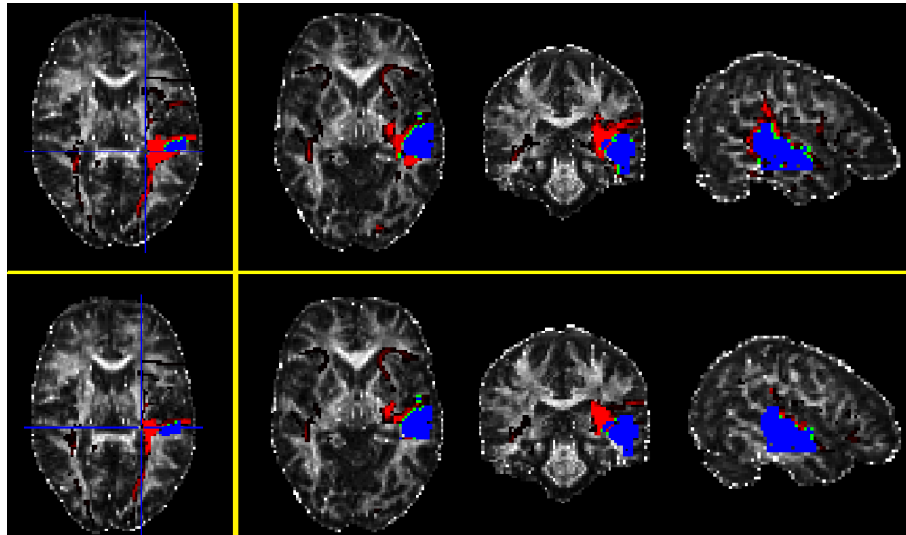


Fig. 2. shows tractography and coverage results of two neighboring infusion sites. Rows correspond to the different infusion sites. The cross hairs in the first column indicate the infusion sites. Blue indicates the tumour site. Red indicates the tractography results and green indicates the voxels in the tumour that are covered by the infusions site.

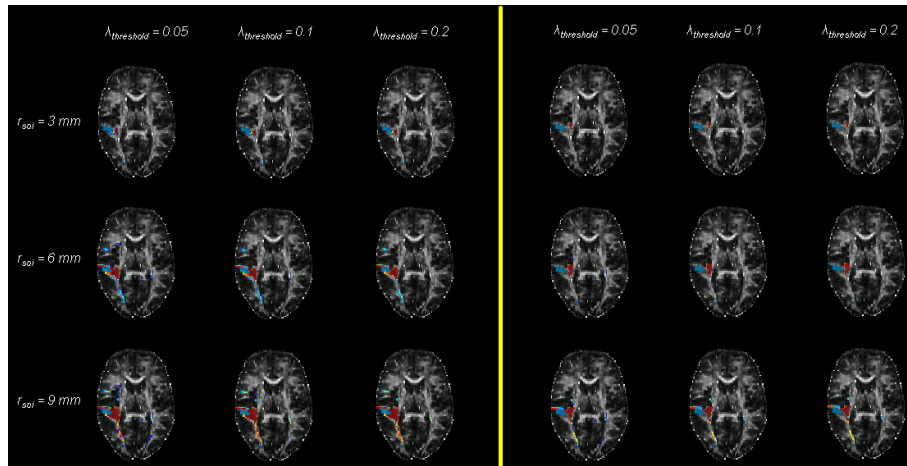


Fig. 3. shows thresholded tractography maps using the infusion sites in figure 2 for all different parameter combinations of the infusion site algorithm.

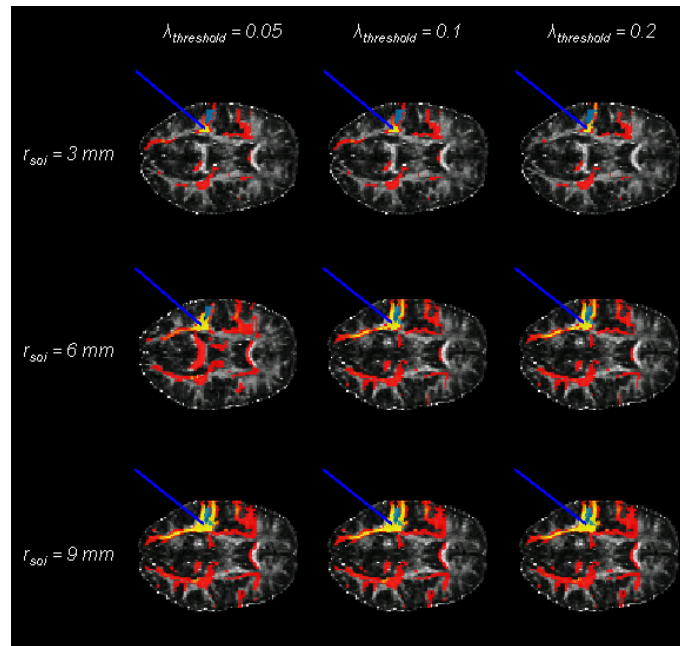


Fig. 4. shows the optimal infusion site when the maximum number of infusion sites is one. Results are shown for all different parameter combinations of the infusion site algorithm. The blue lines indicate the infusion site. Red indicates the resulting tractography map and blue indicates the tumour site.

In the fourth and last experiment we determine the optimal infusion site for up to four infusions. We now use a coverage matrix that is averaged over all different parameter settings. Figure 5 shows that the most optimal set of infusion sites for $N - 1$ infusions generally reoccurs in the set of optimal infusion sites for N infusions. The coverage is generally small, but is likely to be decreased by coverage contributions from low r_{soi} and high $\lambda_{threshold}$.

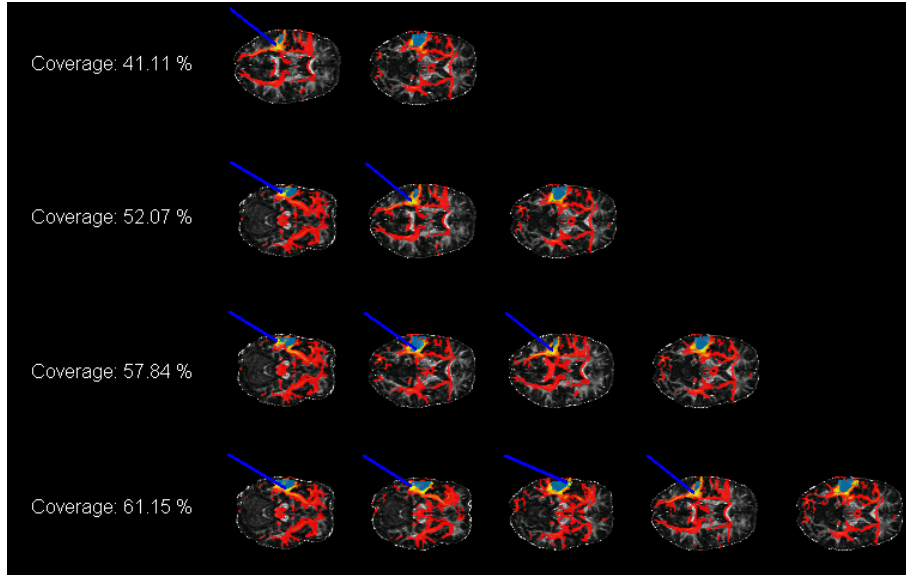


Fig. 5. shows the optimal infusion sites for a maximum number of infusion sites of 1 - 4. The blue lines indicate the infusion site. Red indicates the resulting tractography map and light blue indicates the tumour site.

4 Discussion

In this paper, we develop an algorithm to determine the most optimal infusion sites for CED, given a target site and a maximum number of infusion sites. We use probabilistic tractography maps as an approximation for drug distribution maps for each infusion site and show that good coverage can be achieved with a few strategically placed infusion sites.

The ideal input for the algorithm would be accurate fluid flow simulations. However, beside the fact that fluid flow simulations generally are too time consuming to use in exhaustive searches, there is also great uncertainty around the parameter settings that should be used in fluid flow simulations in the human brain. For instance, the eigenvectors of the conductivity tensor can be inferred

from the eigenvectors of the local Diffusion Tensor, but such equivalence relationship does not exist for the eigenvalues of the conductivity tensor and the diffusion tensor. Other parameters that need to be specified are the intracellular volume fraction (or porosity) and the initial pressure drop at the infusion site. We speculate however that the main effect of these parameters is on the spread of drug distributions away from the white matter fibre tract. This means that only in extreme cases the end distribution of the drugs will not include the grey matter site at which the targeted white matter tracts end. This makes fibre tractography a conservative estimate of CED drugs distributions, which in the face of abovementioned uncertainty around simulation parameters, is a useful starting point for finding optimal infusion sites. We show moreover that finding optimal infusion sites does not critically depend on the exact settings of our algorithm. In future experiments we will investigate whether this also applies when using simulated drug distributions, using a range of fluid flow simulation parameters.

By using probabilistic tractography maps instead of fluid flow simulations, we loose all information about the temporal evolution of the drug distribution. This information is critical in planning the duration of the infusion procedure. However, we argue again that because of the number of unknown parameters in fluid flow simulations, it is currently impossible to provide accurate temporal information using these simulations. The only way to improve this situation is offered by experiments in which fluid flow simulations are calibrated against experimentally measured infusion distributions.

We observe that the fibre tracts do not only reach the target site but also more distant grey matter sites. If the toxicity of the infusate is high, this will lead to serious side effects. However, the target site is always much closer to the infusion sites than the other grey matter sites that are reached. Therefore, carefully controlling the infusion time should prevent the drugs from reaching more distant targets. This however again requires knowledge about the temporal evolution of the drug distribution.

The algorithm can be trivially extended to two or more tumour sites. In these situations, placing catheters into the brain's white matter (instead of grey matter) is even more appealing, because tumour cells are hypothesized to spread along white matter tracts. It is therefore conceivable that an effective treatment would consist of placing a catheter in the middle of the white matter bundle that connects the primary tumour site with the secondary tumour site. Longer distances however increase the need for longer infusion times. This will also increase the uncertainty around the spread of the drugs into unwanted targets.

References

1. Groothuis, D.: The blood-brain and blood-tumor barriers: a review of strategies for increasing drug delivery. *Neuro-oncology* **2**(1) (2000) 45
2. Bobo, R., Laske, D., Akbasak, A., Morrison, P., Dedrick, R., Oldfield, E.: Convection-enhanced delivery of macromolecules in the brain. *Proceedings of the National Academy of Sciences* **91**(6) (1994) 2076

3. Sampson, H., Raghavan, R., Brady, M., Provenzale, M., Herndon, E., Croteau, D., Friedman, A., Reardon, D., Coleman, R., Wong, T., et al.: Clinical utility of a patient-specific algorithm for simulating intracerebral drug infusions. *Neuro-oncology* **9**(3) (2007) 343
4. Mitchell, M.: *An introduction to genetic algorithms*. The MIT press (1998)
5. Parker, G., Haroon, H., Wheeler-Kingshott, C.: A framework for a streamline-based probabilistic index of connectivity (PICO) using a structural interpretation of MRI diffusion measurements. *Journal of Magnetic Resonance Imaging* **18**(2) (2003) 242–254
6. Cook, P., Bai, Y., Nedjati-Gilani, S., Seunarine, K., Hall, M., Parker, G., Alexander, D.: Camino: open-source diffusion-MRI reconstruction and processing. In: *14th Scientific Meeting of the International Society for Magnetic Resonance in Medicine*. (2006) 2759

A spatial variation model of white matter microstructure

Gemma L. Morgan¹, Hui Zhang¹, Brandon Whitcher², and Daniel C. Alexander¹

¹ Centre for Medical Image Computing, University College London, London, UK
g.morgan@cs.ucl.ac.uk

² Clinical Imaging Centre, GlaxoSmithKline, London, UK

Abstract. In this study, we introduce a new technique to model the variation of microstructural parameters across specific brain regions. We use a simple model of diffusion in each voxel, but model the variation of parameters across the region using penalised splines. We fit the whole region model directly to the diffusion-weighted signals. We test the technique on the mid-sagittal section of the corpus callosum (CC) using a diffusion MRI data set with distinct age groups. The method detects differences and separates the groups.

1 Introduction

Diffusion MRI is a powerful, non-invasive imaging tool which measures the displacement of water molecules *in vivo*. Because the paths of water molecules are heavily influenced by the shape and structure of the environment in which they move, diffusion MRI is a sensitive probe for measuring tissue microstructure. It has been used extensively to study white matter in the brain. From a clinical perspective, this is an invaluable technique as we can use diffusion MRI to infer microstructural tissue changes due to pathology, potentially improving our understanding and treatment of neurological diseases. However, to do this we need a biomarker that is both sensitive and specific to underlying microstructure changes. The most commonly used white matter biomarkers are Fractional Anisotropy (FA) and Mean Diffusivity (MD), but they are difficult to relate to specific tissue features. More complex models exist with parameters that correspond to specific microstructure changes [4–6] but as model complexity increases accurate parameter estimation is more susceptible to noise.

In this study, we present a new technique which uses a spatial model within an ROI or tract to describe the variation of tissue diffusion properties. The method fits a spatial model directly to the diffusion-weighted signals, which should reduce the effect of noise on parameter estimation and better capture the underlying variation of parameters. The method combines with diffusion models of varying complexity, allowing a variety of biomarkers to be studied. Because the model is fit within a shaped-based normalisation framework, this technique could be used in group comparison studies. The spatial model can be compared between populations, providing localised information about tissue changes.

The paper is organised as follows. In Section 2 we discuss diffusion models and review previously proposed group study techniques. In Section 3 we introduce our Spatial Variation framework and in Section 4 we apply it to diffusion MRI data with distinct age groups. We discuss our results and conclude in Section 5.

2 Background

In this section we describe some of the most commonly used models of water diffusion in tissue and provide an overview of current methods used to perform group studies. We also introduce the concept of continuous medial representation which we make use of in our Spatial Variation model in Section 3.

2.1 Diffusion Models

To date, most diffusion MRI group studies use the diffusion tensor (DT) [1] to relate diffusion-weighted signals to the diffusion properties of tissue. The DT model assumes that the displacement of water particles is Gaussian and fits a tensor to the diffusion-weighted signals that represents the amount of diffusion along different directions. Scalar indices such as FA and MD can be derived from the elements of the DT [2] and used as biomarkers in group studies. However, water diffusion in the brain is not Gaussian (particularly in white matter where water is restricted by myelinated axons) and FA and MD cannot be directly related to the underlying tissue microstructure. Recently, Panagiotaki et al [3] showed that simple two-compartment models of diffusion, such as a ball and stick [4] or tensor and stick, provide a better fit to diffusion MR data than the DT model. These models mimic the structure of white matter more closely than the DT and the model parameters are potentially more physiologically relevant.

2.2 Group Studies

Group studies can be broadly divided into three categories - region of interest (ROI), voxel or tract based. In ROI studies, the anatomical feature is segmented in each subject and the parameter of interest (usually FA or MD) is averaged over the ROI to provide one value for each subject. However, the effect of averaging could mask small but potentially significant differences in spatial variation between subjects. Unless the ROIs are small, it is not possible to localise the tissue changes. Voxel-based approaches such as Voxel Based Morphometry (VBM) [7] take a very different approach and compare all voxels in the brain between subjects. To do this effectively, the data must be very carefully registered as misalignment and excessive data smoothing can both introduce false positives. Tract-based spatial statistics (TBSS) [8] has been proposed to circumvent some of these problems by projecting each data set onto a template skeleton and performing statistics only on the skeleton. Whilst it does avoid the need for smoothing and perfect alignment, reducing the data down to a skeleton could reduce the statistical significance of the results. Finally, tract based methods use

fibre tractography algorithms to segment and study individual tracts of interest. Tracts are analysed either by averaging parameter values along the whole tract or, more recently, sampling parameter values along the arc length of the tract to create a function [9, 10]. These functions can be analysed either by using point-wise [9] or functional analysis [10]. Like TBSS, these techniques consider only peak parameter values from the centre of the tract, again discarding potentially useful information. These techniques work well for tract with tubular geometries; however it is also possible to derive skeletons for tracts with sheet-like structure using techniques such as tract-specific analysis (TSA) [11, 14].

2.3 Continuous medial representation

Continuous medial representation (cm-rep) is a shape analysis technique which has been shown to be suitable for analysing white matter tracts using medial axes for two-dimensional structures such as the mid-sagittal cross-section of the CC [13] and medial surfaces for three-dimensional sheet-like tracts such as the corticospinal tract [11, 14]. It allows for comparison between populations using shape-based normalisation which aligns objects based on global shape and is particularly appropriate for white matter tracts which have homogeneous interiors.

3 Methods

In this Section we introduce the Spatial Variation framework and describe a simple implementation. We discuss some statistical techniques which can be used to assess differences in spatial models between groups.

3.1 Spatial Variation framework

The Spatial Variation framework estimates microstructure parameters across a whole tract using prior spatial information to constrain the fitting. Rather than fitting in each voxel individually, it uses a forward model that predicts the diffusion MR signals within the whole tract using a set of spatial functions, the spatial model, that control the regional variation of microstructure parameters across the tract. The key components of the method are the spatial model, which predicts the diffusion model parameters in every voxel, and the local diffusion model, which calculates the diffusion MR signals in every voxel from the diffusion model parameters. The optimal spatial model, which should be fully described by a small set of parameters, is found by minimising an objective function based on differences between predicted and measured diffusion MR signals. This process is illustrated in Figure 1, which gives an overview of the pipeline.

The framework itself is independent of the choice of spatial model, diffusion model and objective function. In the next sections, we describe one possible implementation using simple spatial and diffusion models, and show how the cm-rep of tracts can be used to bridge the gap between global and local parameters.

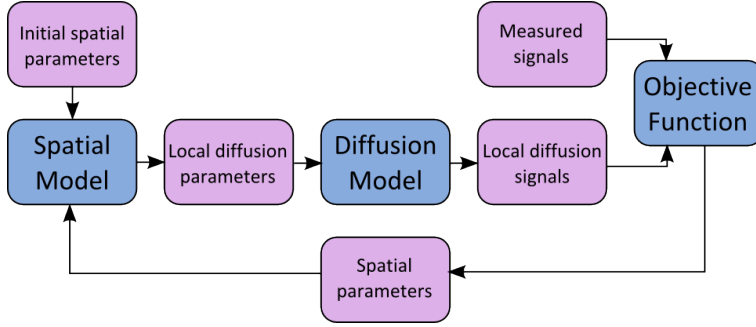


Fig. 1: The shape model comprises a set of curves describing the variation of diffusion model parameters across the tract medial axis. These curves predict local diffusion parameters in every voxel of the tract. The diffusion model predicts the MR signals, given the predicted diffusion parameters. The shape model is controlled by a small set of parameters, and its goodness of fit can be calculated using an objective function based on predicted and measured MR signals. The spatial model is optimised by iteratively minimising the objective function.

Spatial Model We choose to model the variation of the diffusion model parameters using B -splines, a natural choice of basis functions since they effectively capture local features of non-periodic data. Specifically, we follow the penalised B -spline (P -spline) approach of Eilers and Marx [16] which uses a large number N of equally spaced knots to specify the m^{th} order basis functions B . The basis functions are penalised during optimisation to reduce excessive local variation. Each diffusion model parameter $\mathbf{p}=(p_1, p_2, \dots p_k)$ is written as a function of position along the medial axis s using these basis functions as

$$p_k(s, \mathbf{a}) = \sum_{n=1}^{N-m} a_{k,n} B_n(s), \quad (1)$$

where \mathbf{a} are the relative weights of the basis functions. We optimise \mathbf{a} so the set of functions \mathbf{p} best reflect the true variation of the diffusion parameters across the tract. This requires us to compare the observed MR signals, measured in voxels with discrete spatial positions, with MR signals predicted from our continuous model. The cm-rep provides a convenient way to convert our predictions from continuous to discrete as it outputs a list of points lying on the medial axis. We use a simple nearest neighbour approach to assign a distance along the medial axis to all voxels of interest. Once we know the positions of all voxels along the medial axis, we can predict the diffusion parameters, and thus the MR signals, at these locations only.

Diffusion Model A modified ball and stick model is used to describe water diffusion in tissue. The standard ball and stick model [4] is a simple two-compartment model that models the total diffusion MR signal as a mixture of

signals due to the restricted intra-axonal water (the stick) with volume fraction f and orientation \mathbf{e} defined by angles θ and ϕ and the hindered extra-axonal water (the ball). Both compartments have diffusivity d . Our modification involves a third compartment to account for cerebrospinal fluid (CSF) contamination with volume fraction g and diffusivity d_{CSF} .

The spatial model outlined in Section 3.1 assumes that the white matter microstructure parameters $\mathbf{p}=(f, d, \theta, \phi)$, may be written as smoothly varying functions parameterised by coefficients $\mathbf{a}=(\mathbf{a}_f, \mathbf{a}_d, \mathbf{a}_\theta, \mathbf{a}_\phi)$ as shown in Equation 1; however we cannot assume the same thing of the partial volume parameters, g and d_{CSF} . Prior to fitting the spatial model, we estimate g in all voxels of interest from the $b=0$ images. We write the total signal S in the $b=0$ image as a mixture of white matter signal S_{WM} and CSF signal S_{CSF}

$$S = gS_{CSF} + (1 - g)S_{WM}. \quad (2)$$

We estimate average values for S_{CSF} and S_{WM} from voxels that are manually segmented as ‘pure’ CSF or white matter voxels in the $b=0$ image and solve for g . We set d_{CSF} to $3.0 \times 10^{-9} \text{ m}^2\text{s}^{-1}$, a typical value for CSF.

The model for the i^{th} diffusion MR signal in the j^{th} voxel may be written as

$$\tilde{A}_{ij}(\mathbf{p}_j(\mathbf{a}); g_j, b, \hat{\mathbf{G}}_i) = g_j e^{-bd_{CSF}} + (1 - g_j) \left(f_j e^{-bd_j (\mathbf{e}(\theta_j, \phi_j) \cdot \hat{\mathbf{G}}_i)^2} + (1 - f_j) e^{-bd_j} \right) \quad (3)$$

where b is the diffusion-weighting factor and $\hat{\mathbf{G}}_i$ is the gradient direction.

Optimisation We estimate the spatial model coefficients \mathbf{a} that best describe the variation of the model parameters \mathbf{p} across the whole region. We do this by minimising the sum of squared differences between \tilde{A}_{ij} predicted from Equation 3 and the observed signals A_{ij} in all J voxels, subject to regularisation. Our objective function is

$$\arg \min \left(\sum_{i=1}^I \sum_{j=1}^J (A_{ij} - \tilde{A}_{ij}(\mathbf{p}_j(\mathbf{a}); g_j, b, \mathbf{G}_i))^2 + \sum_{k \in (f, d, \theta, \phi)} \lambda_k \sum_{n=1}^{N-m} (\Delta^2 a_{k,n})^2 \right). \quad (4)$$

For the regularisation term, we use a second order difference penalty on \mathbf{a}_k , which enforces the smoothness of our solutions [16]. We minimise the objective function iteratively using a Levenberg-Marquardt algorithm.

3.2 Statistical analysis

After fitting the spatial model for each subject, we can test for group differences using functional data analysis [15]. The mean curve for each parameter $\bar{p}_k(s)$ for each group can be written as

$$\bar{p}_k(s) = \sum_{q=1}^Q p_{k,q}(s) \quad (5)$$

where $p_{k,i}(s)$ are the individual curves for the Q subjects. We test for group differences in these mean parameter curves at l points sampled along the medial axis using Student’s t test. To correct for multiple comparisons we use a Westfall-Young randomisation method proposed by Cox and Lee [17], specifically designed for functional data. Unlike traditional multiple comparison corrections, which lose significance as l increases, p-values obtained using Westfall-Young randomisation converge to the continuum limit as $l \rightarrow \infty$.

4 Experiments and Results

We demonstrate this method on the mid-sagittal section of the CC. We choose this region as the relatively constant fibre orientation reduces the number of parameters to estimate. Histology studies [18] have also shown that underlying microstructural indices such as axon radius and density vary smoothly over the anterior-posterior direction of the CC, which we hypothesise will manifest as smooth variation in parameters such as f and d .

4.1 Data acquisition and pre-processing

In this study, our diffusion MRI data sets are drawn from the large IXI database (freely available at: www.brain-development.org). We use data from 30 subjects who divide into two distinct groups: 20-29 years old (9 female, 6 male) and 60-69 years old (9 female, 6 male). All data were acquired on a 3T scanner using 15 gradient directions ($b=1000 \text{ s mm}^{-2}$) and 1 $b=0 \text{ s mm}^{-2}$ measurement.

The key pre-processing steps required are to identify the mid-sagittal slice of the CC and to extract the medial axis. First the brain is extracted using FSL’s BET tool [19] and FA maps are calculated. From these FA maps we identify the mid-sagittal slice [20]. Thresholding (FA >0.35) and connected component analysis isolate the CC on this slice. ITK-SNAP [21] is used to make minor manual adjustments to the segmentation, for example in cases where the fornix is misclassified as part of the CC. The medial axis of the CC can then be extracted using `cm-rep` [13].

4.2 Spline fitting

Due to the coherent orientation of fibres within the CC, we fit constants for θ and ϕ across the whole ROI. The splines modelling the variation of f and d across the CC are fit by dividing the normalized medial axis length into 20 intervals described by 21 cubic B -splines. In total, we fit 44 parameters for each data set. Using Generalised Cross Validation (GCV) across all data sets, we set the regularisation parameters for f and d to be $\lambda_d=\lambda_f=10$.

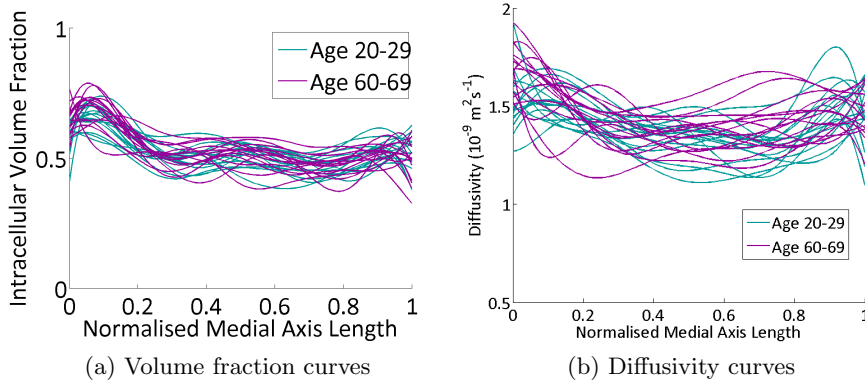


Fig. 2: The fitted curves for (a) volume fraction and (b) diffusivity are shown for all subjects. Volume fraction is consistent amongst all subjects, but we see bigger group differences in diffusivity.

4.3 Results

Figure 2 shows the volume fraction and diffusivity curves for all subjects. The volume fraction curves have consistent shapes for all subjects, whereas the diffusivity curves show greater differences between the groups.

Figure 3 shows the mean volume fraction and diffusivity curves calculated using Equation 5. Again, this highlights the similarities in volume fraction between the groups and the increases in diffusivity in the anterior genu and anterior splenium in the older group.

Using the statistical techniques discussed in Section 3.2, we calculate p-values for the mean group differences in both volume fraction and diffusivity at 100 positions along the medial axis length (Figure 4). After correcting for multiple comparisons, we see that at the tip of the genu ($s=0-0.4$), there is significantly higher diffusivity in the older group than the younger, as well as a trend towards decreased volume fraction ($s=0.02$). Additionally, there is a trend towards higher diffusivity in the older group in the anterior splenium ($s=0.71-0.76$), although this is not accompanied by a corresponding change in volume fraction.

5 Discussion

We have presented a new technique that models the variation of microstructure parameters across white matter tracts. We have shown that it can identify and localise group differences due to age in the mid-sagittal section of the CC. Specifically, we have found a significant increase in diffusivity in the anterior genu with age combined with a trend towards reduced volume fraction. We also observe a trend towards increased diffusivity with age in the anterior splenium. Although it is commonly known that ventricle size increases with age [22], we

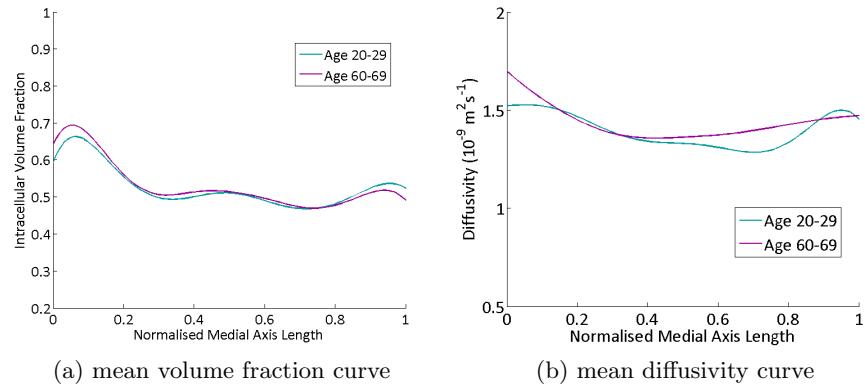


Fig. 3: The mean curves for (a) volume fraction and (b) diffusivity are shown for all subjects.

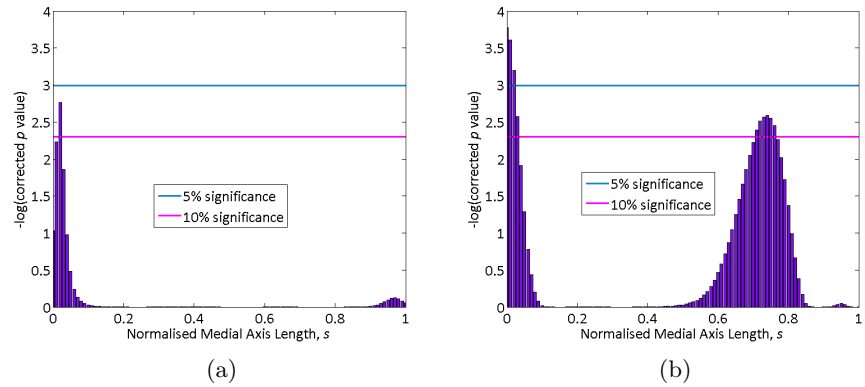


Fig. 4: Plots of p-values as a function of the medial axis position showing group differences in (a) volume fraction and (b) diffusivity. There is a significant increase in diffusivity and trend towards decreased volume fraction in the anterior genu in the older group. We also see a trend towards increased diffusivity with age in the anterior splenium.

think it is unlikely that the change in diffusivity in the genu is due to this effect as our diffusion model explicitly accounts for partial volumes. Previous studies [23] have shown significant changes due to age in the genu, which supports our results. Even though we have been able to localise tissue differences due to age, we cannot specify what causes these changes, e.g. larger axon diameters or lower axon densities, due to the simplicity of our diffusion model.

Future work will use this method to measure small but significant changes in tissue microstructure due to pathology that other standard techniques might miss. This is because data is pooled across the whole ROI or tract to reduce the effect of noise on parameter estimation. However several improvements need to be made. First, we will extend the method to three dimensions so that we can model microstructure variation across whole tracts rather than single slices. We will also exploit the analytical form of the spline curves further to see if the spline derivatives can be used to identify microstructural group differences. Finally, we will replace our simple model of diffusion with more complex models in order to investigate more physiologically relevant microstructure parameters such as axon radius and density. When using these complex models with parameters that are difficult to estimate, the real power of this method to pool data and reduce the effect of noise will be apparent.

6 Acknowledgements

We would like to thank Dr Hui Sun and Prof Paul Yushkevich, University of Pennsylvania, for invaluable assistance with the continuous-medial representation code. This work is funded by GlaxoSmithKline and EPSRC.

References

1. Basser, P.J., Mattiello, J., Le Bihan, D.: MR diffusion tensor spectroscopy and imaging. *Biophysical Journal*, 259–267 (1994)
2. Basser, P.J., and Pierpaoli, C.: Microstructural and Physiological Features of Tissues Elucidated by Quantitative-Diffusion-Tensor MRI. *Journal of Magnetic Resonance, Series B*, 111, 209–219 (1996)
3. Panagiotaki, E., Fonteijn, H., Siow, B., Hall, M.G., Price, A., Lythgoe, M.F., Alexander, D.C.: Two-compartment models of the diffusion MR signal in brain white matter. *Medical Image Computing and Computer Assisted Intervention (MICCAI)* London:Springer, 1, 329–336 (2009)
4. Behrens, T.E.J., et al. Characterization and Propagation of Uncertainty in Diffusion Weighted MR Imaging. *Magnetic Resonance in Medicine*, 50, 1077–1088 (2003)
5. Assaf, Y. et al.: New Modeling and Experimental Framework to Characterize Hindered and Restricted Water Diffusion in Brain White Matter. *Magnetic Resonance in Medicine*, 52, 965–978 (2004)
6. Alexander, D.C.: A general framework for experiment design in diffusion MRI and its application in measuring direct tissue-microstructure features. *Magnetic Resonance in Medicine*, 60, 439–448 (2008)

7. Ashburner, J., and Friston, K.J.: Voxel-Based Morphometry - The Methods. *NeuroImage*, 11, 805–821 (2000)
8. Smith, S., Jenkinson, M., Johansen-Berg, H., Rueckert, D., Nichols, T.E., Mackay, C.E., Watkins, K.E., Ciccarelli, O., Cader, M.Z., Matthews, P.M., and Behrens, T.E.J.: Tract-based spatial statistics: Voxelwise analysis of multi-subject diffusion data. *NeuroImage*, 31, 1487–1505 (2006)
9. Maddah, M., et al Findings in Schizophrenia by Tract-Oriented DT-MRI Analysis. *Medical Image Computing and Computer Assisted Intervention (MICCAI)*, Springer, 1, 917–924 (2008)
10. Goodlett, C.B., Fletcher, P.T., Gilmore, J.H., and Gerig, G.: Group analysis of DTI fiber tract statistics with application to neurodevelopment. *NeuroImage*, 45, S133–S142 (2009)
11. Yushkevich, P.A., Zhang, H., Simon, T.J., and Gee, J.C.: Structure-specific statistical mapping of white matter tracts. *NeuroImage*, 41, 448–461 (2008)
12. Yushkevich, P.A., Zhang, H., Gee, J.C.: Continuous medial representation for anatomical objects. *IEEE Trans Med Imaging*, 25, 1547–1564 (2006)
13. Sun, H., Yushkevich, P.A., Zhang, H., Cook, P.A., Duda, J.T., Simon, T.J., Gee, J.C.: Shape-Based Normalization of the Corpus Callosum for DTI Connectivity Analysis. *IEEE Transactions on Medical Imaging*, 26, 1166–1178 (2007)
14. Zhang, H., Awate, S.P., Das, S.R., Woo, J.H., Melhem, E.R., Gee, J.C. and Yushkevich, P.A.: A tract-specific framework for white matter morphometry combining macroscopic and microscopic tract features. *Medical Image Analysis*, In press (2010)
15. Ramsay, J.O. and Silverman, B.W.: *Functional Data Analysis*. Springer (2005)
16. Eilers, P.H.C. and Marx, B.D.: Flexible smoothing with B-splines and penalties. *Statistical Science*, 11, 89–121 (1996)
17. Cox, D.D. and Lee, J.S.: Pointwise testing with functional data using the Westfall-Young randomization method. *Biometrika*, 95, 621–634 (2008)
18. Aboitiz, F., Scheibel, A.B., Fisher, R.S. and Zaidel, E.: Fiber composition of the human corpus callosum. *Brain Research*, 598, 143–153 (1992)
19. Smith, S.M.: Fast robust automated brain extraction. *Human Brain Mapping*, 17, 143–155 (2002)
20. Ardekani, B.A., Kershaw, J., Braun, M. and Kanno, I.: Automatic detection of the mid-sagittal plane in 3-d brain images. *IEEE Trans. Med. Imaging*, 16, 947–952 (1997)
21. Yushkevich, P.A., Piven, J., Hazlett, H.C., Smith, R.G., Ho, S., Gee, J.C., and Gerig, G.: User-guided 3D active contour segmentation of anatomical structures: Significantly improved efficiency and reliability. *NeuroImage*, 31, 1116–1128 (2006)
22. Haug, G.: Age and sex dependence of the size of normal ventricles on computed tomography. *Neuroradiology*, 14, 201–204 (1977)
23. Otaa, M., Obataa, T., Akinea, Y., Itoa, H., Ikehirac, H., Asadad, T., and Suharaa, T.: Age-related degeneration of corpus callosum measured with diffusion tensor imaging. *NeuroImage*, 31, 1445–1452 (2006)

A Multivariate Group-wise Genetic Analysis of White Matter Integrity using Orientation Distribution Functions

Natasha Leporé^{*1}, Caroline Brun^{*2}, Maxime Descoteaux³, Yi-Yu Chou⁶, Greig de Zubicaray⁴, Katie McMahon⁴, Margaret J. Wright⁵, Nicholas G. Martin⁵, James C. Gee², Paul M. Thompson⁶ [* equal contribution]

¹ University of Southern California and Children’s Hospital Los Angeles, Los Angeles, CA 90034, USA

² Penn Image Computing and Science Laboratory, University of Pennsylvania, Philadelphia, PA, 19104, USA

³ Université de Sherbrooke, Faculté des Sciences, Sherbrooke, QC, J1K 2R1, Canada

⁴ University of Queensland, Brisbane, Australia

⁵ Genetic Epidemiology Lab, QIMR, Brisbane, Australia

⁶ Laboratory of Neuro Imaging, UCLA, Los Angeles, CA 90095, USA

Abstract. Diffusion magnetic resonance imaging has become an important tool for comparing brain white matter fiber structure between groups of subjects. While voxel-wise statistical comparison are typically performed on scalar values derived from the diffusion tensors (*DT*), several authors have advocated applying multivariate statistics to better exploit the information contained in the tensors, as they show significant improvements over their univariate counterparts. The *DT*s are good approximations to the fiber orientation in regions with no fiber crossings or partial volumed voxels; however, fiber crossings are ubiquitous in the brain, and the tensor approximation fails throughout a significant portion of the image. Consequently, here we treat this issue by analyzing the raw diffusion data directly and by building orientation distribution functions (*ODFs*), using the modified spherical harmonic decomposition from [7]. More precisely, we first perform linear and nonlinear registrations to transform these diffusion-weighted images to a common space, and a subsequent local rotation to reorient the diffusion signal and thus align it to the anatomy. We then build the *ODFs*. Our dataset consists of 25 identical and 25 fraternal twin pairs (100 healthy adult twins, age: 24.6 ± 1.8 SD years), for whom we aimed to study the genetic contribution to white matter integrity. A multivariate intraclass correlation value (*ICC*) is obtained from the coefficients of the spherical harmonics at each voxel, resulting in a map that represents similarity within twin pairs in each of the twin groups. From there, the heritability can be computed. These statistics obtained from the multivariate *ICC* are compared to those from a more commonly used scalar measure: the generalized fractional anisotropy (*GFA*). As shown here, accounting for directionality increases the signal detection.

1 Introduction

Voxel-wise analyses of brain MR data have yielded considerable knowledge about changes in brain shape and volume in health and disease. Among these methods, tensor based morphometry (TBM) uses a nonlinear warping to align all images in a data set to a common space. A statistical analysis is then performed, typically on the determinants of the Jacobian matrices J of the deformation in the case of structural images, e.g. [25], on the fractional anisotropy (FA) in case of diffusion tensor images [20], or on other sets of shape change descriptors specific to fiber bundles [34].

While in the past most of these analyses compared a single type of information per voxel, new models have increasingly been focused on making a more full use of multivariate data. In particular, in [24], the authors extended TBM by performing statistics on a symmetric function of the Jacobian matrix, i.e., the 6-parameters deformation tensors $\sqrt{J^t J}$, in place of its determinant. This method outperformed the univariate statistical analysis of $\det J$ for mapping brain changes in HIV/AIDS in that groupwise differences were detected that were not statistically significant with $\det J$. In [20], the authors drew the same conclusion while using a TBM-like multivariate analysis on the full diffusion tensor. Because DT and $\sqrt{J^t J}$ do not form a vector space under the standard operations of matrix addition and scalar multiplication, the log-Euclidean framework was used [2]. Zhang et al. [34] combined both sets of information -the diffusion tensors and the Jacobian matrices- to compute shape and orientation changes in white matter fiber bundles. In [33], the authors used isomap manifold learning and similarly found that retaining the full diffusion tensor information yielded greater effect sizes in group studies. [4] focused on a different method as they decomposed the diffusion tensor into FA , mean diffusivity (MD) and different modes computed from the DT . These scalar values were gathered to form their multivariate basis. Bilateral temporal changes were found in young professional boxers compared to controls with all measures, but the sensitivity was greatly improved with both the linear discriminant multivariate analysis and the more traditional Hotelling T^2 compared to the scalar measures.

However, using DT 's and their derived quantity ignore key information in the image. When only one fiber is present at a given voxel, the diffusion tensor is a satisfying representation of the white matter structure: the DT can be viewed as an ellipse with the eigenvector associated with its largest eigenvalue pointing in the approximate direction of the fiber. A problem arises though when fiber crossings are present within the voxel. In this case, more appropriate descriptions have been developed to approximate the diffusion partial differential equation that represents the HARDI signal, such as the fiber orientation distribution [1], the diffusion orientation transform [28] or the orientation distribution function advocated in [32] and [8]. All these methods account for more than one main direction, and one of them was even used to examine the difference between curving and fanning fiber tract configurations [29].

In [13], the author focused on using the full ODF geometry for enhancement or segmentation of data from single subjects. Other authors used fields of ODF s

[26] or region-based statistical surface evolution [10] to segment fiber bundles. However, to our knowledge, only very few studies have performed group statistical analyses of *ODF* fields in human populations. The works that exist used univariate statistics on *ODFs*, for example the generalized fractional anisotropy (*GFA*), the equivalent of *FA* for *ODFs*, or the Jensen-Shannon divergence that measures the complexity of the diffusion [6], [5].

Here we aim to take better advantage of the multi-dimensionality of *ODFs*, written in a modified spherical harmonics expansion as in [8]. The *GFA* reduces all the coefficients of the spherical harmonics to a single scalar value, so much of the information is then lost. Instead, we compute statistics using the multivariate information contained in the spherical harmonics coefficients and compare the results to its scalar corresponding value, i.e., *GFA*.

All our analyses are performed on a healthy twins data set (100 subjects, 22 – 27; mean age: 24.6 ± 1.8 SD year). Twin studies can reveal whether specific neuroanatomical measures are predominantly influenced by genetics or shared or individual environments, by comparing twin pairs with different degrees of genetic affinity. Identical (or monozygotic, *MZ*) twins share the same genetic material, whereas fraternal (or dizygotic, *DZ*) twins share, on average, only half of their genetic polymorphisms (random DNA sequence variations that occur among normal individuals). *DZ* twins are commonly studied in lieu of other siblings because they are the same age, preventing any age-related confounds. Identical and fraternal twin pairs are compared to ensure, to the greatest possible extent, comparable upbringings and family environments despite varying degrees of genetic resemblance.

The statistic we use is the intraclass correlation (ICC), a measure of similarity within twin pairs that will be computed in each of the two (*MZ* and *DZ*) groups. For the multivariate case, we adapt the ICC formula derived in [21,22] for the multivariate diffusion tensor in twins to our *ODF* framework. and we compare it to the univariate one on *GFA*. The results found here show that using more of the information in the *ODFs* increases the detection power to find genetic influence on local white matter structures when compared to using the *GFA* only.

2 Method

2.1 Subjects

105-gradient high angular resolution diffusion imaging (HARDI) data were acquired from 25 pairs of healthy young adult monozygotic twins (*MZ*; 10 men/15 women) and 25 same-sex pairs of dizygotic twins (*DZ*; 9 men/ 16 women) on a 4 Tesla Bruker Medspec MRI scanner using an optimized diffusion imaging sequence [17]. The age range for the subjects was 22 – 27 (mean age: 24.6 ± 1.8 SD year). 105 images were acquired: 11 baseline (b_0) images with no diffusion sensitization (i.e., *T2*-weighted images) and 94 diffusion-weighted images (b-value 1159 s/mm^2) for which gradient directions were evenly distributed on the hemisphere. Imaging parameters were: TR/TE 92.3/8250 ms, 55 x 2mm contiguous

slices, FOV = 23 cm. The reconstruction matrix was 128x128, yielding a 1.8x1.8 mm² in-plane resolution. Total scan time was 14.5 minutes.

Corresponding 3D T1-weighted images of the same subjects were also acquired with an inversion recovery rapid gradient echo sequence using the same 4T Bruker Medspec MRI scanner. Acquisition parameters were: TI/TR/TE=1500/2500/3.83 msec; flip angle=15 degrees; slice thickness = 0.9 mm, with an acquisition matrix of 256x256x256.

All subjects were screened via physical and psychological tests and excluded cases of pathology known to affect brain structure. No twin subjects reported a history of significant head injury, a neurological or psychiatric illness, substance abuse or had a first-degree relative with a psychiatric disorder. The study was approved by the Research Ethics Committees at QIMR and UQ and the Institutional Review Board at UCLA.

2.2 Pre-processing

Extracerebral tissues were removed from the 3D structural MRI scans using the Brain Surface Extraction software (BSE) [31] followed by manual editing. Edited T1 scans were linearly registered to a high-resolution single-subject brain template image, the Colin27 template [14], using the *FLIRT* software [16]. A Minimal Deformation Target (MDT) was generated from the 100 subjects' images (using the method in [18]) and each of these 3D structural image was warped to the *MDT* using a 3D fluid registration algorithm that allows large deformations while guaranteeing diffeomorphisms ([23], [3]). Jacobian matrices, representing local volume expansions or contractions relative to the template image, were calculated from the deformation fields for each subject.

From the diffusion weighted images, voxel-wise diffusion tensors were generated with the *MedINRIA software*. Log-Euclidean tensor de-noising was used to eliminate singular, negative definite, or rank-deficient tensors. A diagonal component image (D_{xx}) was masked and used as a template to eliminate extracerebral tissues from all the DW images. Echo Planar Imaging distortion corrections were performed both by linearly and nonlinearly aligning each of DWI images to its corresponding sMRI image, using the *FLIRT* software [16] and the above mentioned nonlinear registration algorithm [3].

We applied the deformation fields - that point from the nonlinear registration of T1-weighted images to the *MDT*- to each of the gradient images to warp them to a common space. However, since the diffusion signal is not correctly aligned to the anatomy after the transformation, we rotate the gradients in the registered diffusion weighted images using the method described in [15]. In this paper, the authors presented a method for reorienting the *ODFs*. Here we use the same concept that we apply to the Gradient diffusion images. As such, the diffusion signal reorientation procedure is as follow: the diffusion signal is represented by a set of gradient vectors distributed over a sphere, which is common to all subjects. At each voxel, for each subject, the jacobian matrix is applied to each of these vectors, which are then re-adjusted to the proper length. This gives a diffusion value for each newly oriented vector. For more simplicity, because we

work on group comparison, finding values corresponding to the original vectors are more convenient. In order to do so, the value of the signal at each of the original gradient directions is interpolated from the rotated data.

Once the reorientation is done in this normalized space, we build a voxel-wise map of ODF and derived-GFA values for each subject, which will serve as a basis for our statistical analysis, i.e., the computation of univariate(ICC_u), multivariate Intraclass Correlation (ICC_m) for both the MZ and DZ groups and the heritability corresponding to the two types of ICC .

2.3 GFA vs ODFs

We are looking to compare the results obtained with the computation of the ICC_u (from the standard GFA) to the ICC_m (from the multivariate ODFs). The GFA is a generalization of the fractional anisotropy, and is defined for the ODF Ψ as

$$GFA = \sqrt{\frac{n \sum_{I=1}^n (\Psi(u_i) - \langle \Psi \rangle)^2}{(n-1) \sum_{I=1}^n (\Psi(u_i))^2}}, \quad (1)$$

where the u_i are gradient directions, $i = 1, \dots, n$ and $\langle \Psi \rangle$ is the mean ODF with respect to the spherical angle.

The multivariate intraclass correlation, however, is computed from the coefficients of the modified spherical harmonics expansion. The modified basis is indexed by a pair of infinite sequences of parameters $l = 0, 2, 4, \dots$, and $m = -l, \dots, 0, \dots, l$ [7]:

$$Y_i = \begin{cases} \sqrt{2} \operatorname{Re}(Y_l^{|m|}) & \text{if } m < 0 \\ Y_l^m & \text{if } m = 0 \\ \sqrt{2}(-1)^{m+1} \operatorname{Im}(Y_l^m) & \text{if } m > 0 \end{cases}$$

(so $l = 0$ for Y_1 , $l = 2$ for $Y_{2, \dots, 6}$, and $l = 4$ for $Y_{7, \dots, 15}$). Here, we truncate the series at $l = 4$. If c_i is the coefficient of Y_i , then we compute the multivariate statistics on

$$(|c_1|, \sqrt{|c_2|^2 + \dots + |c_6|^2}, \sqrt{|c_7|^2 + \dots + |c_{15}|^2}) \quad (2)$$

Hence the definition of the GFA, which is written as follows:

$$GFA = \sqrt{1 - \frac{c_1^2}{\sum_{i=1}^{15} c_i^2}} \quad (3)$$

2.4 Statistical Analysis in Twins

Univariate Intraclass Correlation To measure the resemblance between twin pairs for diffusion-derived measures, we compute the intraclass correlation coefficient (ICC) for both the MZ and the DZ groups, according to the formula

[30]

$$ICC_u = \sigma_b^2 / (\sigma_b^2 + \sigma_w^2). \quad (4)$$

Here, σ_b^2 is the pooled variance between pairs and σ_w^2 is the variance within pairs.

In quantitative genetics, heritability is defined as the proportion of the observed variation in a measurement that is attributable to genetic factors. We computed Falconer's heritability statistic, h^2 , defined as twice the difference in correlation between *MZ* and *DZ* pairs

$$h^2 = 2(rMZ - rDZ) \quad (5)$$

where rMZ and rDZ are the *ICC* measures for the *MZ* and *DZ* groups, respectively.

Multivariate Intraclass Correlation For non-scalar data, equation 4 does not apply. Instead, we use a multivariate measure of intraclass correlation based on [19], as detailed in [22]. Consider each of the N independent variables as belonging to a N -component vector, and denote by x_{1i} and x_{2i} the respective vectorized variables for both members of the i -th twin pair. Define the intrapair means by $\bar{x} = (x_{1i} + x_{2i})/2$, where $i = 1, \dots, Np$, and Np is the number of twin pairs. Then the multivariate intraclass correlation is given by

$$r_m = sv_{max}[(MS_b^m + MS_w^m)^{-1/2}(MS_b^m - MS_w^m)(MS_b^m + MS_w^m)^{-1/2}] \quad (6)$$

where sv_{max} denotes the largest singular value of the matrix in brackets, and m, b and w stand for multivariate, between and within, respectively.

$$MS_b^m = \frac{1}{N_p - 1} \sum_{i=1}^{N_p} (\bar{x}_i - \frac{1}{N_p} \sum_{k=1}^{N_p} \bar{x}_k) (\bar{x}_i - \frac{1}{N_p} \sum_{k=1}^{N_p} \bar{x}_k)^T$$

$$MS_w^m = \frac{1}{2N_p} \sum_{i=1}^{N_p} \sum_{j=1}^2 (x_{ji} - \bar{x}_i) (x_{ji} - \bar{x}_i)^T$$

It is noteworthy to point that the *ICC* equations are fed with Jacobian determinants computed from the registration of a group of subjects to a common template (in the case of a structural MRI group analysis) or with reoriented ODFs computed in a normalized space. Consequently, two images from a given twin pair are not directly compared. Only the entities that relate each of the twin from a twin pair to the template are compared.

Correction for the non-normal distribution Because the data was normally distributed, we computed p values at each voxel with a voxelwise permutation test, where all subjects' labels were permuted, to establish a null distribution for the *ICC* statistics at each voxel [27]. The null hypothesis for the intraclass

correlation was $ICC = 0$ (no correlation). To control the standard error of p , we performed 5000 permutations at each voxel [11]. To control for multiple spatial comparisons implicit in computing maps of statistics, we computed the omnibus probability (i.e., probability corrected for multiple comparisons), $p_{corrected}$, using the suprathreshold volume, for maps thresholded at $p = 0.05$. This value assesses the overall significance of the observed pattern of effects in the statistical maps [27].

3 Results

Figures 1 and 2 present the univariate and multivariate statistical analyses, respectively. Intraclass correlation maps are shown in both figures for the *MZ* and *DZ* groups along with their corresponding p -values. The heritability is also displayed for both measures. Blue colors represent a very small correlation (or heritability) whereas red color regions are highly correlated (or heritable). In the statistical maps, red area represent regions where the ICC is significant ($p < 0.05$), while there is no significance in the blue regions. Results are overall consistent for the two groups, with regions of high heritability including the white matter surrounding the corona radiata, the corticospinal tract and the corpus callosum. Figure 2, while noisier than Figure 1, shows much higher detection power in all regions, and more widespread changes. In particular, the occipital and frontal regions and short association fibers are heritable with the multivariate measure, but not with the GFA.

4 Conclusion

Here we described a method to perform quantitative genetic computations on the orientation distribution functions, combining novel methods from multivariate statistics, spectral representation of the angular diffusion signal, and the classical twin design to understand the causes of variations in fiber architecture in human populations. In recent years, several authors have shown that tensor statistics can outperform scalar measures derived from the diffusion tensor. In this paper, we extended this work to the orientation distribution function, which better approximates the underlying fiber architecture than the single tensor model, when multiple dominant directions or tissue types are found in a voxel. All data was nonlinearly aligned to a common template, using a local polar decomposition of the registration field to apply the rotation term to the gradient data, before fitting an ODF. We then transformed the full diffusion gradient data in a spherical harmonic basis, and we compute $\sqrt{\sum c_i^2}$ at each order, to obtain a 3-component vector at each voxel. And finally, after this projection onto a countable basis, we adapted the definition of the intraclass correlation to sequences in Hilbert space, using a maximal eigenvalue approach similar to that used in canonical correlation analysis.

We are in the process of testing potential improvements to this methods. Here we decompose the spherical harmonic up to the fourth order, but gains

in power may be achieved from increasing the order of the decomposition. On the other hand, adding extra components may add extra noise, hence reducing signal detection. Alternatively, it may be that we could dispense with the ODF altogether, and perform the statistics directly on the diffusion signal itself.

The resulting resemblance and heritability estimates detected all regions found with the more commonly used scalar measures, but also additional ones such as the occipital and frontal regions and the short association fibers. This approach is applicable to studies of group differences in HARDI, but is of special relevance in genetic studies. In genetic studies in particular, vast numbers of subjects must typically be scanned to discover specific genes that are associated with fiber integrity. This is because genetic effects are weak and many single nucleotide polymorphisms are thought to contribute to the observed variance in fiber architecture in human populations. With this in mind, it seems wise to retain the full diffusion propagator in the genetic analysis, to empower the search for genetic variations that affect human brain integrity and connectivity. The first step in this quest is to establish that the ODF fields themselves contain heritable information. In future work, we will use this multivariate method to empower the search for quantitative trait loci on the human genome that contribute to the integrity and connectivity of the human brain.

References

1. Alexander, D. *Multiple-fiber reconstruction algorithms for diffusion MRI*, Annals of the New York Academy of Sciences, 113–133, (2005)
2. Arsigny, V., Fillard, P., Pennec, X., Ayache, N., *Log-Euclidean metrics for fast and simple calculus on diffusion tensors*, Magnetic Resonance in Medicine, **56**(2), 411–421, (2006).
3. Brun, C., Lepore, N., Pennec, X., Chou, Y.-Y., Lee, A.D., de Zubicaray, G.I., McMahon, K., Wright, Barysheva, M., M., Toga, A.W., Thompson, P.M., *A new registration method based on Log-Euclidean tensor metrics and its application to genetic studies*, ISBI, Paris, France (2008).
4. Chappell, M.H., Brown, J.A., Dalrymple-Alford, J.C., Uluğ, A.M., Watts, R., *Multivariate analysis of diffusion tensor imaging data improves the detection of microstructural damage in young professional boxers*, Magnetic Resonance Imaging, **26**(10), 1398–1405, (2008).
5. Chiang, M.C., Klunder, A.D., McMahon, K., de Zubicaray, G.I., Wright, M., Toga, A.W., Thompson, P.M., *Information-Theoretic Analysis of Brain White Matter Fiber Orientation Distribution Functions*, Information Processing in Medical Imaging, (2007).
6. Chiang, M.C., Barysheva, M., Lee, A.D., Madsen, S.K., Klunder, A.D., Toga, A.W., McMahon, K.L., de Zubicaray, G.I., Meredith, M., Wright, M.J., Srivastava, A., Balov, N., Thompson, P.M., *Brain Fiber Architecture, Genetics, and Intelligence: A High Angular Resolution Diffusion Imaging (HARDI) Study*, Medical Image Computing and Computer Assisted Intervention, New York, NY, USA, 1060–1067, (2008).
7. Descoteaux, M., Angelino, E., Fitzgibbons, S., Deriche, R., *Regularized, Fast and Robust Analytical Q-Ball Imaging*, Magnetic Resonance in Medicine, **58**(3), 497–510, (2007).

8. Descoteaux, M., *High Angular Resolution Diffusion MRI: From Local Estimation to Segmentation and Tractography*, PhD Thesis, Université de Nice - Sophia Antipolis, (2008).
9. Descoteaux, M., Deriche, R., Knoesche, T., Anwander, A., *Deterministic and Probabilistic Tractography Based on Complex Fiber Orientation Distributions*, IEEE Transactions in Medical Imaging, **28**(2), 269–286, (2008).
10. Descoteaux M., Deriche, R., *High Angular Resolution Diffusion MRI Segmentation Using Region-Based Statistical Surface Evolution*, Journal of Mathematical Imaging in Vision, special issue on Mathematics in Image Analysis , **33**(2), 239–252 (2009).
11. Edgington, E.S., *Randomization Tests*, 3rd Edition Marcel Dekker, (1995).
12. Fletcher, P.T., Joshi, S. *Principal geodesic analysis on symmetric spaces: Statistics of diffusion tensors*, ECCV Workshops on Computer Vision Approaches to Medical Image Analysis (CVAMIA), 87–98, (2004)
13. Goh, A., Lenglet, C., Thompson, P.M., Vidal, R. *Estimating Orientation Distributions with Probability Density Constraints and Spatial Regularity*, Medical Image Computing and Computer Assisted Intervention, London, UK, (2009).
14. Holmes, C.J., Hoge, R., Collins, L., Woods, R., Toga, A.W., Evans, A.C., *Enhancement of MR images using registration for signal averaging*, J Comput Assist Tomogr, **22**(2) , 324–333, (1998).
15. Hong, X., Arlinghaus, L.R., Anderson, A.W., *Spatial normalization of the fiber orientation distribution based on high angular resolution diffusion imaging data*, Magn Reson Med **61**(6), 1520–1527, (2009).
16. Jenkinson, M., Smith, S., *A global optimization method for robust affine registration of brain images*, Med Image Anal 5(2), 143–56, (2001).
17. Jones, D.K., Horsfield, M.A., Simmons, A., *Optimal strategie for measuring diffusion in anisotropic systems by magnetic resonance imaging*, Magn Reson Med, **42**(3), 515–25, (1999).
18. Kochunov, P., Lancaster, J., Thompson, P.M., Woods, R.P., Hardies, J., Fox, P.T., *Regional spatial normalization: towards an optimal target*, J Comput Assist Tomogr 25(5), 805816, (2001).
19. Konishi, S., Khatri, C.G., Rao, C.R. *Inferences on multivariate measures of interclass and intraclass correlations in familial data*, J R Statist Soc **53**(3), 649–659, (1991).
20. Lee, A.D., Lepore, N., Lepore, F., Alary, F., Voss, P., Brun, C., Chou, Y-Y., Barysheva, M., Toga, A.W., Thompson, P.M., *Brain differences visualized in the blind using tensor manifold statistics and diffusion tensor imaging*, Frontiers in the Convergence of Bioscience and Information Technologies, 470–477, (2007).
21. Lee, A.D., Lepore, N., Barysheva, M., Chou, Y.-Y., Schwartzman, A., Brun, C.C., Madsen, S.K., de Zubicaray, G.I., McMahon, K., Wright, M., Toga, A.W., Thompson, P.M., *A multivariate analysis of the effect of genes and environment on brain fiber architecture*, submitted to Neuroimage (2010).
22. Lee, A.D., Lepore, N., de Leeuw, J., Brun, C.C., Barysheva, M., McMahon, K.L., de Zubicaray, G.I., Martin, N.G., Wright, M.J., Thompson, P.M., *Multivariate Variance-Components Analysis in DTI*, International Symposium on Biomedical Imaging, Rotterdam, The Netherlands, (2010).
23. Lepore, N., Chou, Y-Y., Lopez, O.L., Aizenstein, H.J., Becker, J.T., Toga, A.W., Thompson, P.M., *Fast 3D fluid registration of brain magnetic resonance images*, SPIE conference on Physiology, Function and Structure from Medical Images, San Diego, CA, USA, (2008).

24. Lepore, N., Brun, C., Chou, Y.-Y., Chiang, M.-C., Dutton, R.A., Hayashi, K.M., Lueders, E., Lopez, O.L., Aizenstein, H.K., Toga, A.W., Becker, J.T., Thompson, P.M., *Generalized Tensor-Based Morphometry of HIV/AIDS using multivariate statistics on deformation tensors*, IEEE Transactions on Medical Imaging, 27(1), 129–14, (2008a).
25. Leporé N., Voss P., Chou, Y.-Y., Fortin, M., Gougoux, F., Leporé F., Lee, A.D., Brun, C.C., Lassonde, M., Madsen, S.K., Toga, A.W., Thompson, P.M., *Brain Structure Changes Visualized in Early- and Late-Onset Blind Subjects*, NeuroImage, 49(1), 134–40, (2010)
26. McGraw T., Vemuri B., Yezierski R., Mareci T., *Segmentation of High Angular Resolution Diffusion MRI Modeled as a Field of von Mises-Fisher Mixtures*, European Conference on Computer Vision (ECCV), 3953, 463–475, (2006)
27. Nichols, T.E., Holmes, A.P., *Non parametric permutation tests for functional neuroimaging: a primer with examples*, Hum Brain Map 15(1), 1–25, (2002). ,
28. Ozarslan, E., Mareci, T.H., *Generalized diffusion tensor imaging and analytical relationships between diffusion tensor imaging and high angular resolution diffusion imaging*, Magn Reson Med, 50(5), 955–965, (2003)
29. Savadjiev, P., Campbell, J.S., Descoteaux, M., Deriche, R., Pike, G.B., Siddiqi, K., *Labeling of ambiguous subvoxel fibre bundle configurations in high angular resolution diffusion MRI*, Neuroimage, 41(1), 58–68, (2008)
30. Scout, P.E., Fleiss, J.L., *Intraclass correlations: Uses in assessing rater reliability*, Psychol Bull, 86(2), 420–428 (1979).
31. Shattuck, D.W., Leahy, R.M., *BrainSuite: an automated cortical surface identification tool*, Med Image Anal, 6(2), 129–42 (2002).
32. Tuch, D., *Q-Ball Imaging*, Magnetic Resonance in Medicine 52(6), 1358–1372, (2004).
33. Verma, R., Khurd, P., Davatzikos, C., *On Analyzing Diffusion Tensor Images by Identifying Manifold Structures Using Isomaps*, IEEE Transactions in Medical Imaging, 26(6), 772–778, (2007).
34. Zhang, H., Yushkevich, P.A., Rueckert, D., Gee, J.C., *Tensor-Based Morphometry of Fibrous Structures with Application to Human Brain White Matter*, Medical Image Computing and Computer-Assisted Intervention, London, United Kingdom, 466–473, (2009).
35. Zöllei, L., Stevens, A., Huber, K., Kakunoori, S., Fischl, B., *Improved tractography alignment using combined volumetric and surface registration*, NeuroImage, 51(1), 206–213 (2010).

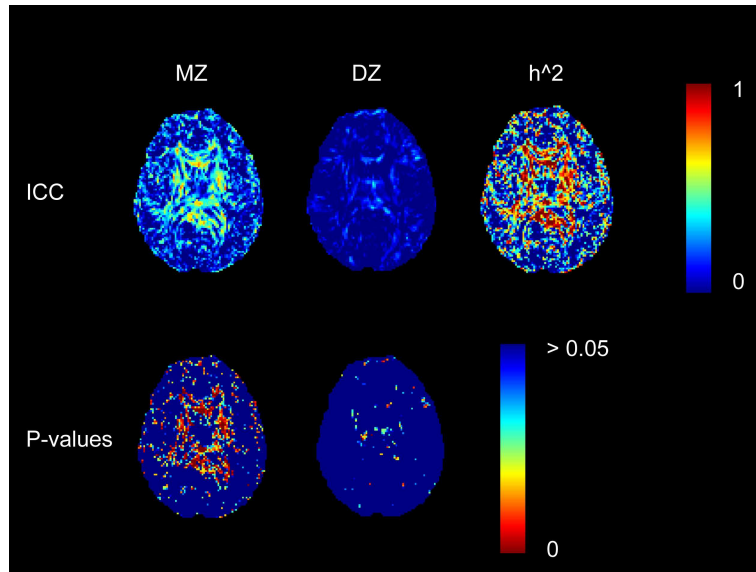


Fig. 1. *Top and Bottom Left:* Univariate Intraclass correlation (Generalized Fractional Anisotropy) for the *MZ* and *DZ* and their corresponding *p*-values. *Right:* Heritability computed from the univariate *ICC*

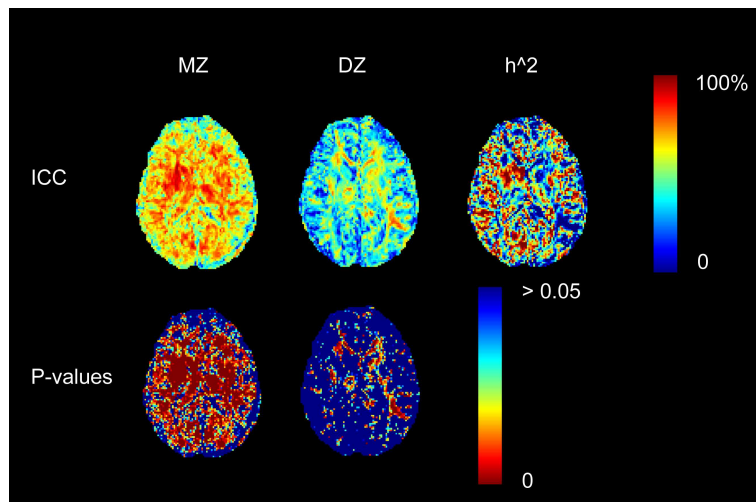


Fig. 2. *Top and Bottom Left:* Multivariate Intraclass correlation (Orientation Distribution Functions) for the *MZ* and *DZ* and their corresponding *p*-values. *Right:* Heritability computed from the multivariate *ICC*

Robust model-based transformation and averaging of diffusion weighted images – applied to diffusion weighted atlas construction

Marc Niethammer, Yundi Shi, Sami Benzaid, Mar Sanchez, Martin Styner

UNC Chapel Hill

Abstract. This paper describes a method for model-based averaging of sets of diffusion weighted magnetic resonance images (DW-MRI) under space transformations (resulting for example from registration methods). A robust weighted least squares method is developed. Synthetic validation experiments show the improvement of the proposed estimation method in comparison to standard least squares estimation. The developed method is applied to construct an atlas of *diffusion weighted images* for a set of macaques, allowing for a more flexible representation of average diffusion information compared to standard diffusion tensor atlases.

1 Introduction

Diffusion weighted magnetic resonance imaging (DW-MRI) has become an indispensable tool for in-vivo analysis of tissue properties, in particular for brain imaging. Data analysis is typically not performed on the DW-MRIs directly, but based on diffusion tensors or derived measures. Recently, attention has shifted to more flexible representations, such as orientation distribution functions or even full directional displacement probability distributions. To analyze data in-between or across subjects the use of atlas-based methods has been tremendously successful. While atlases for structural MRI data and diffusion tensors exist, methods to construct atlases for more general descriptions of diffusion information have not been thoroughly explored, but would be of high value to allow for comprehensive data analysis. Challenges for the estimation of such atlases are: (1) the signal to noise ratio (SNR), (2) the chosen signal representation, (3) the need to account for orientation changes for orientation-dependent quantities such as diffusion tensors or the DWIs themselves, and (4) the choice of a proper registration method to compute the transformations from subject to atlas space.

While high SNR DW-MRIs can be obtained with sophisticated imaging protocols and long acquisition times, for many studies increased acquisition times are not realistic (for example when anesthesia is used and cannot be applied for an unlimited duration) and the available images are consequentially noisy. Therefore, a vast number of methods has been developed to increase signal to noise ratios. These range from simple voxel-wise averaging to technically sophisticated averaging procedures for diffusion tensors. To perform optimal averaging (from a statistical point of view), the non-Gaussian noise characteristic of DW-MRI signals should be considered. Further, the use of statistically robust estimation

methods is advisable to allow for the rejection or down-weighting of potential outliers.

Such statistically robust estimation methods have been studied for tensor estimation in [1,2,3]. This paper explores statistically robust estimation methods in the context of general parametric models taking into account an approximation to the Rician noise model. In particular, a robust variant of weighted-least-squares is investigated and applied to construct an atlas of DWIs based on a spherical harmonics expansion, which has not been investigated previously.

Diffusion information is orientation dependent, which needs to be accounted for within the atlas-building process. In the simplest case this can be accomplished by using a tensor model and reorienting the tensors according to the local deformation given by the mapping from subject to atlas space [4,5,6]. Atlas-building based on a 4th order tensor model has been proposed in [7]. In both cases, the challenge is to incorporate appropriate spatial transformations within the image-match term of the registration formulation. Instead of using the transformation of a diffusion model directly it can also be used to reconstruct DWIs for any given gradient direction. Based on this idea Tao and Miller [8] developed an image-to-image registration method by interpolating diffusion information on the sphere using a weighted average based on geodesic distances on the sphere. Yu [1] uses a robust tensor model to generate DW signals driving a registration process and Melbourne [9] addresses contrast changes for image-to-image registration by principal component modeling.

For this paper the computation of the maps from subject to atlas space (the registration) is not the focus (for the experimental section, this is accomplished through a fluid flow registration on fractional anisotropy images). Instead, it is concerned with robustly computing average DWI images from a set of images in atlas space, thereby constructing a DWI atlas. Note however, that the methods by [7,8,1,9] could easily be adapted to function as component algorithms to compute the maps to atlas space, to achieve improved alignment in particular in the areas of crossing fibers.

Sec. 2 discusses DWI noise models. Sec. 3 introduces the general robust M-estimation framework for DW measurements. Secs. 3.1 and 3.2 discuss the estimation of individual signals and parametric signal profiles respectively. Sec. 4 highlights applications to registration and atlas-building. Results for the construction of a diffusion-weighted atlas are shown in Sec. 5.

2 Noise Modeling

Measured diffusion weighted images are assumed to follow a Rician noise distribution with probability density function [10]

$$p(S_i) = \frac{S_i}{\sigma_i^2} e^{-\frac{S_i^2 + (S_i^n)^2}{2\sigma_i^2}} I_0 \left(\frac{S_i S_i^n}{\sigma_i^2} \right), \quad (1)$$

where S_i is the measured (noisy) signal, S_i^n is the true signal, σ_i^2 is the noise variance, and I_0 the modified Bessel function of order 0. Given a set of measure-

ments $\{S_i\}$ and a signal model (tensor, spherical harmonics expansion, etc.), the maximum likelihood (ML) estimators can be formulated and solved numerically.

The log-transformed random variables S_i can be approximated as Gaussian distributed random variables with a signal-dependent variance [10], i.e.,

$$\log(S_i) \approx \log(S_i^n) + \epsilon_i, \quad \epsilon_i \sim N\left(0, \frac{\sigma_i^2}{(S_i^n)^2}\right), \quad (2)$$

where $N(\mu, \sigma^2)$ denotes a normal distribution with mean μ and variance σ^2 . This is an excellent approximation for reasonably high signal to noise ratios; see [10] and Fig. 1. This relation can be exploited for the estimation of any parametric model. Typically, σ_i is assumed constant, since noise in the DWIs is expected to be constant. However (see Sec. 5), this assumption is problematic for robust estimators and bias field correction should be applied to DWIs to equalize noise levels.

3 Robust estimation of diffusion weighted signals

Least squares (LS) estimation for signals derived from log-transformed DWIs is simple, approximates the Rician noise model well for moderate and large signal amplitudes (when using weighted least squares) and is still predominantly used in practice. Due to the Gaussian noise model in the log-domain, it is easy to make use of robust M-estimation methods, where a model residual is penalized by a non-quadratic loss function. The benefits of such an approach have been demonstrated for tensor estimation [2,3]. This paper investigates robust signal estimation for general parametric models from sets of DWIs. This includes simple signal averages (for repeated measurements) as well as the coefficient estimation for series expansions of diffusion profiles (e.g., spherical harmonics expansion), where statistically robust methods have so far not been applied. (Note that methods have been developed [11,12] which impose a certain level of smoothness and therefore show decreased sensitivity to noise and improved reconstruction quality. However, the notion of robustness in [11,12] is different from the one used in this paper, which addresses outliers and can be combined with a smoothness assumption as a prior on the parametric model.)

To avoid explicitly identifying (and rejecting) outliers, outliers can be down-weighted by an appropriate choice of loss function $\rho(u)$. In general, given a model parametrized by coefficients \mathbf{c} , M-estimation [13,14] amounts to minimizing

$$E(\mathbf{c}) = \sum_{i=1}^N \rho\left(\frac{r_{i,\mathbf{c}}}{v_i}\right), \quad (3)$$

where $r_{i,\mathbf{c}}$ is the residual measuring the difference between the i -th measurement and the chosen model, and v_i is a possibly signal-dependent scale factor. The loss function $\rho(u) = \frac{1}{2}u^2$ recovers LS optimization. The optimality condition is

$$\frac{dE(\mathbf{c})}{d\mathbf{c}} = \sum_{i=1}^N w\left(\frac{r_{i,\mathbf{c}}}{v_i}\right) \frac{1}{v_i^2} \frac{dr_{i,\mathbf{c}}}{d\mathbf{c}} r_{i,\mathbf{c}} = 0, \quad (4)$$

where $w(u) = \frac{1}{u} \frac{d\rho(u)}{du}$ is called the weight function. For the special case of the quadratic loss function, $w(u) = 1$; choosing $\frac{1}{v_i^2} = \frac{(S_i^n)^2}{\sigma^2}$ results in the weighted least squares problem for diffusion weighted images, where σ is the noise variance in the diffusion weighted signals (assumed constant) and a parameter of the Rician distribution. For the experiments in this paper this parameter is estimated from a baseline image [15]. Thus, robust M-estimation for DWIs can be written in general as

$$E(\mathbf{c}) = \sum_{i=1}^N \rho \left(\frac{S_i^n r_{i,\mathbf{c}}}{\sigma} \right). \quad (5)$$

Operating on log-transformed signals is essential for the weighted LS approximation to the Rician noise model and fits nicely into the M-estimation framework.

Choosing $r_{i,\log S^n} = \log S_i - \log S_i^n$ (where $S_i^n = S^n$ is a constant) and $r_{i,\{\log S_0^n, D\}} = \log S_i - \log S_0^n + \frac{1}{b} g_i^T D g_i$ (with $\log S_i^n = \log S_0^n - \frac{1}{b} g_i^T D g_i$) results in estimators for a single signal S^n and for the baseline image S_0^n and the diffusion tensor D respectively. (Note that in the absence of the nominal value S_i^n , its value is chosen according to the parametric model.) Other parametric models may be chosen, e.g.,

$$r_{i,\mathbf{c}} = \log S_i - \sum_{j=1}^R c_j Y_j(\theta_i, \phi_i) \quad (6)$$

where $\{Y_j(\theta, \phi)\}$ define a model-basis on the sphere. Any spherical basis – not necessarily restricted to a spherical shell – fits into this estimation framework.

In what follows, measurements are assumed to be either baseline images (with no diffusion weighting) or have gradients distributed on a spherical shell (i.e., for a fixed b value). While a multitude of robust loss functions have been proposed, the remainder of the paper focuses on the Huber function

$$\rho(u) = \begin{cases} \frac{1}{2}u^2, & |u| \leq \theta, \\ \frac{1}{2}\theta(2|u| - \theta), & |u| > \theta, \end{cases}, \quad w(u) = \begin{cases} 1, & |u| \leq \theta \\ \frac{\theta}{|u|}, & |u| > \theta \end{cases} \quad (7)$$

since it is quadratic for $u \leq \theta$. Therefore the minimizer to Eq. 5 recovers the optimal weighted least-squares solution for small residuals and down-weights potential outliers with larger residuals. In Eq. 7, θ is a design parameter. Since the scale parameter standardizes the residuals with $\frac{S_i^n}{\sigma}$ (according to the weighted least squares approximation for the Rician noise model), fixing θ specifies the transitioning point between a quadratic and a absolute difference penalizer at θ times the expected standard deviation of the residuals. (For all experiments in this paper: $\theta = 2$). Such a down-weighting of a residual's influence with residual magnitude is a fundamental property of robust M-estimators to diminish the effect of potential outliers (for example: using a quadratic loss function to estimate a central element for a set of real numbers recovers the mean, while using the magnitude function recovers the median). In fact, loss-functions such as the truncated quadratic function can also be used which disregard values above a certain residual threshold in the estimation process (where the weighting function w becomes zero).

3.1 Averaging of corresponding diffusion weighted images

The signal underlying a set of corresponding diffusion weighted images $\{S_i\}$ (which correspond to the same gradient direction and are expected to be drawn from the same distribution) can be reconstructed, assuming the Gaussian model with mean-dependent variance, by minimizing Eq. 5 with $r_{,\log S^n} = \log S_i - \log S^n$. This is useful for the averaging of sets of baseline images which do not change contrast under space transformations. Assuming a given, identical variance for all measurements, the solution to the optimization problem is

$$S^n = e^{\frac{1}{n} \sum_{i=1}^n \log S_i} = \prod_{i=1}^n (S_i)^{\frac{1}{n}},$$

which is the geometric mean of the measured values. The robust version using the Huber function can be solved by iterating

$$(S^n) \leftarrow \prod_{i=1}^n (S_i)^{\frac{w_i}{W}}, \quad W = \sum_{i=1}^n w_i, \quad w_i = w \left(\frac{S^n (\log S_i - \log S^n)}{\sigma} \right) \left(\frac{S^n}{\sigma} \right)^2$$

to convergence. Note that this is not an ML estimate under the assumed noise model, but rather a pseudo ML estimate [16], where the signal variance is estimated or known. It is easy to compute and results in significantly improved signal estimation quality over arithmetic averaging as demonstrated in Figs. 1 and 2. Estimation quality is comparable to the one for the maximum-likelihood estimator using the Rician noise model for large and moderately large signal values. Further, the robust estimator outperforms the non-robust variants when outliers are present. This motivates using the robust weighted approach for the estimation of more general diffusion profiles.

3.2 Estimation of diffusion profiles

Given a basis for signal representation on the sphere with the residual defined as in Eq. 6 (for example spherical harmonics) the same iterative reweighting process as for the estimation of corresponding DWIs of Sec. 3.1 can be applied for the estimation of the series coefficients, \mathbf{c} . The robust estimation model is given in Eq. 5. Working in the log-transformed domain also has the benefit that the overall estimated signal (obtained by exponentiation) is assured to be positive, which is physically meaningful. Arguably, the fitting domain should be irrelevant if the correct noise model for the respective signal representation is used. Regularized solutions are obtained by penalizing basis coefficients

$$E(\mathbf{c}) = \mathbf{c}^T L \mathbf{c} + \sum_{i=1}^N \rho \left(\frac{S_i^n r_{i,\mathbf{c}}}{\sigma} \right). \quad (8)$$

For spherical harmonics the regularization matrix L can be chosen such that it results in smoothing of the reconstructed signal on the spherical shell (according

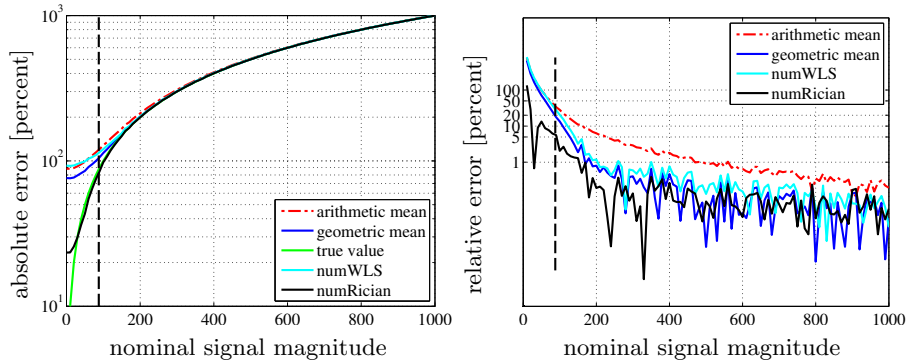


Fig. 1. Absolute (left) and relative error (in percent; right) for estimating a nominal diffusion weighted signal at various signal intensity levels for a noise level $\sigma = 70$. Estimations were obtained using the arithmetic mean, the geometric mean (pseudo-maximum-likelihood), the weighted least squares maximum-likelihood (ML) estimator (WLS) and through estimation by the Rician ML estimator. Each value represents the average of the estimation errors for 1,000 runs using ten independent measurements corrupted with Rician noise. The vertical dashed line indicates the mean for Rayleigh noise $\mu = \sqrt{\frac{\pi}{2}}\sigma$, ie., what the expected intensity value would be in the presence of a zero signal. The Rician ML estimator is superior to all other estimator for very low signal values. However, the simple geometric mean performs well for moderate to high signal values. The arithmetic mean shows the worst performance.

to the Laplace-Beltrami smoothing operator) as described in Descoteaux [11]. Note that the energy balance between prior and data likelihood changes for large numbers of measurements. Therefore, for a fixed model order the influence of the prior decreases with an increase in measurements and the estimator converges to the ML estimator in the limit. This is a standard property of the MAP estimator and highly useful for example for DWI atlas building (see Sec. 4), where large numbers of images are averaged and a prior is no longer urgently needed.

The performance of the robust estimation method for a real, symmetric spherical harmonics basis is demonstrated for two example diffusion profiles (crossing and non-crossing) in comparison to fitting the signal through LS in the original domain and in the log-transformed domain respectively (see Tables 1 and 2). The robust weighted approach outperforms the two other methods, in particular when the number of measurements is large in comparison to the model order.

4 Application to registration and DW atlas-building

While methods for diffusion tensor (DT) [6] and higher-order tensor [7] atlas-building have been developed, methods for the computation of DW atlases have not been explored. This paper is not concerned with developing a new way of computing the space transformations from subject to atlas space, but instead

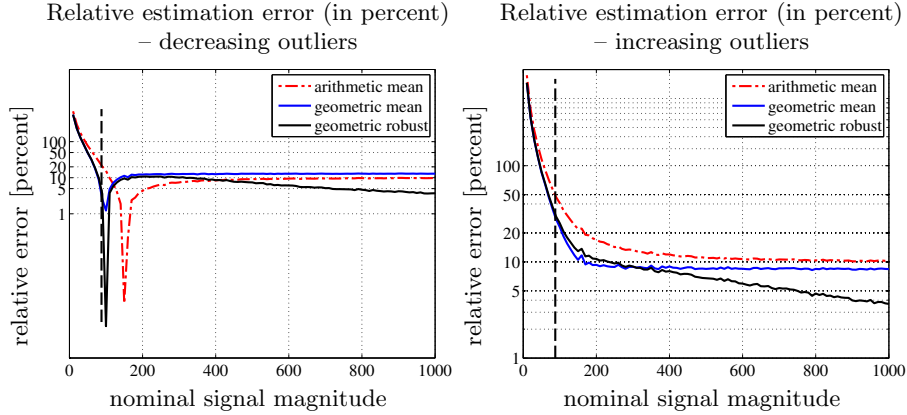


Fig. 2. Relative estimation error for the robust estimation method using the Huber function with $\theta = 2$. Each value represents the average of the estimation errors for 1,000 runs using ten independent measurements corrupted with Rician noise. For each set of ten measurements two were randomly chosen and their value was decreased by 50% (left) or increased by 50% (a similar outlier-creation strategy as in [2]). The robust geometric mean shows greatly improved performance for increasing outliers. It performs better than the geometric mean for decreasing outliers and also shows improved performance for larger values in comparison to the arithmetic mean. Presumably this can be explained by the large expected signal variations for low signal values, which makes outlier rejection more difficult in these cases. Further the estimation error shows dips only for the case of outliers decreasing signal magnitude. Presumably this is due to the fact that the estimators in general tend to overestimate signal magnitude and therefore at certain values the outliers can have a seemingly beneficial effect. (In fact the dips shift to the left with stronger signal drops – not shown in this figure.)

makes use of the transformations to compute a new average set of DWIs for a canonical set of gradient directions. The atlas-building strategy used for the experimental results in Sec. 5 is due to Joshi et al. [17]. Here, a greedy approach is used to obtain the set of space transformations, $\{\Phi^i\}$ and the average atlas image I^T approximately minimizing the energy

$$E(I^T, I^i) = \sum_{i=1}^N \left(\int_0^1 \|v^i\|_L^2 dt + \|I^T - I^i(1)\|_{L_2}^2 \right),$$

such that $(I^i)_t + \nabla I^i \cdot v^i = 0, \quad I^i(0) = I_0^i,$

where I^T denotes the atlas image, $I^i(t)$ the subject image transformed for time t through the velocity field v^i and L is a differential operator to ensure smoothness of the transformations. The maps from subject to atlas space can be computed for each subject i by solving $\Phi_t^i + D\Phi^i v^i = 0; \Phi^i(0) = id$, where id denotes the identity map and D the Jacobian. For the experiments in this paper, $\{I^i\}$

		Gradient scheme and estimation method					
		46 dir			181 dir		
		SHO-2	SHO-4	SHO-8	SHO-2	SHO-4	SHO-8
rel. error [percent]	0	6.2/14.2/ 4.7	7.8/11.5/ 6.2	10.0/12.5/ 8.9	3.3/13.6/ 2.5	4.0/9.4/ 3.2	5.3/8.8/ 4.5
	10↑	9.7/13.7/ 8.4	10.2/13.7/ 9.0	11.7/14.6/ 10.7	5.3/10.5/ 4.4	5.6/10.2/ 4.7	6.5/10.5/ 5.5
	20↑	11.6/15.4/ 10.5	12.0/15.6/ 11.0	13.2/16.4/ 12.3	6.8/11.7/ 5.7	7.2/11.9/ 6.1	7.9/12.4/ 6.9
	30↑	13.4/17.2/ 12.4	13.8/17.6/ 13.0	14.9/18.4/ 14.2	8.5/13.4/ 7.3	9.0/13.9/ 7.8	9.6/14.4/ 8.6
	10↓	10.0/13.0/ 8.5	10.7/12.9/ 9.0	12.0/13.8/ 10.8	5.8/9.9/ 4.5	6.3/9.3/ 4.7	7.2/9.5/ 5.5
	20↓	12.2/14.0/ 10.7	12.8/14.2/ 11.3	13.8/15.0/ 12.4	7.8/10.1/ 5.9	8.6/10.2/ 6.4	9.4/10.5/ 7.2
	30↓	14.3/15.3/ 12.9	14.9/15.7/ 13.5	15.8/16.4/ 14.5	10.3/11.1/ 7.9	11.0/11.4/ 8.5	11.8/11.9/ 9.3

Table 1. Estimation results for a diffusion model of the form $S_k = S_0(0.2e^{-bd} + 0.8e^{-bdg_k^T Ag_k})$, with $S_0 = 1000$, $b = 1000$, $d = 0.002$, $A = e_1 e_1^T$, where $e_1 = (1, 0, 0)^T$. Gradient directions were obtained by constructing icosadelta-hedra with 92 and 362 vertices through the electric repulsion model, with antipodal pairs removed to result in gradient schemes with 46 and 181 directions respectively. Results are tabulated for different orders of the spherical harmonics expansion (2, 4, 8) and for different percentages of outliers (0, 10, 20, 30), where outliers were generated by increasing ↑ or decreasing ↓ their value by 50%. Rician noise of $\sigma = 70$ was added to all measurements. Results are tabulated as a/b/c, where: a=LS in log-transformed domain; b=LS in original signal domain; c=robust weighted LS in log-domain. Results represent the mean relative errors for all gradient directions averaged over 1,000 random experiments in percent. The robust WLS method (described in this paper) outperforms the two other methods.

		Gradient scheme and estimation method					
		46 dir			181 dir		
		SHO-2	SHO-4	SHO-8	SHO-2	SHO-4	SHO-8
rel. error [percent]	0	8.0/8.1/ 7.9	7.6/7.5/ 7.3	8.9/9.0/ 8.8	7.0 /7.3/7.1	5.3/5.5/ 5.2	5.6/5.7/ 5.5
	10↑	9.2/9.5/ 9.0	9.4/9.9/ 9.2	10.5/10.9/ 10.4	6.3/6.6/ 6.1	6.2/6.8/ 5.9	6.6/7.3/ 6.3
	20↑	10.8/11.4/ 10.5	11.0/11.9/ 10.9	12.0/12.7/ 11.8	7.2/8.1/ 6.8	7.5/8.6/ 7.0	8.0/9.2/ 7.5
	30↑	12.4/13.4/ 12.2	12.8/13.9/ 12.7	13.7/14.8/ 13.6	8.6/10.0/ 8.1	9.0/10.6/ 8.5	9.6/11.2/ 9.1
	10↓	9.5/9.1/ 8.9	10.0/9.3/ 9.1	11.0/10.4/ 10.2	6.4/6.2/ 5.9	6.7/6.1/ 5.8	7.3/6.6/ 6.3
	20↓	11.5/10.6/ 10.4	12.0/10.9/ 10.8	12.8/11.9/ 11.8	8.2/7.1/ 6.7	8.8/7.4/ 7.0	9.4/8.0/ 7.6
	30↓	13.5/ 12.2 / 12.2	14.1/ 12.7 /12.8	14.9/ 13.6 /13.7	10.3/8.6/ 8.3	11.1/9.1/ 8.8	11.8/ 9.6 / 9.6

Table 2. Estimation results for a two-tensor diffusion model of the form $S_k = S_0(0.2e^{-bd} + 0.4e^{-bdg_k^T Ag_k} + 0.4e^{-bdg_k^T Bg_k})$, with $b = 1000$, $S_0 = 1000$, $d = 0.002$. A and B where constructed as the outer product of two vectors at an angle of 70 degrees. Table information is organized in the same way as in Table 1. The robust method performs best in almost all cases.

denotes the set of FA images for the subjects. Note that any other atlas-building strategy for diffusion weighted images can be used to obtain the set of space transformations from subject to atlas space. In particular, registration strategies using orientation information within the image similarity measure could be useful [7,8,1,9,18,19] as components for the atlas building.

As in DT atlas building, DW atlas-building requires signal transformation and signal averaging. This can either be done by model fitting in the original image domain followed by transformation and averaging of the model coefficients

or by adjusting the B-matrix according to the space transformation as discussed in [5]. Based on the model fitting and averaging method outlined in the previous section, this paper follows the latter approach.

While for affine transformations the measurement frame can be adjusted globally, doing so in the context of non-rigid registration would require local adjustments of measurement frames and prohibitive storage space for large numbers of images. Therefore, an estimation of the DWIs in the transformed space for a given set of gradient directions is useful. This can be accomplished by locally reorienting the gradient directions $\{g_i\}^j$ for all j original images in atlas space, based on the space transformations [4]. The associated signal intensities $\{S_i\}^j$ are kept fixed. Given the set of associated rotations $\{R^j\}$, the new compound signal is

$$\cup_j \{R^j g_i\}^j, \quad \text{with signals} \quad \cup_j \{S_i\}^j.$$

Computing the series coefficients for a robust approximation of the compound signal results in a continuous parametric function which can be evaluated for any desired gradient direction. This allows resampling for a set of canonical gradient directions and can be used for atlas-building with any chosen parametric model. Fig. 3 illustrates this principle as used in Sec. 5 to build a diffusion weighted atlas.

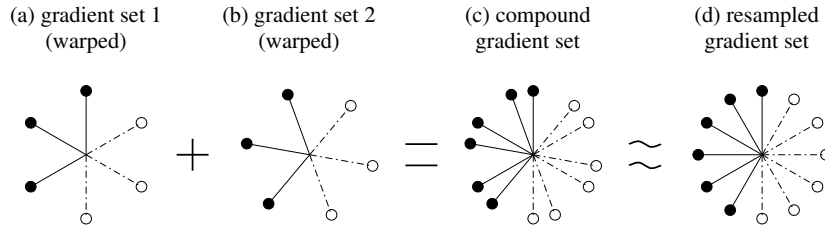


Fig. 3. Principle of gradient warp to obtain resampled DWIs illustrated by two exemplary sets of gradient directions. Solid and dashed lines denote antipodal pairs for gradient directions. Gradient directions are typically identical before transformation to atlas space. Given space transformations to atlas space the gradient directions are locally rotated consistent with the local spatial rotation induced by the transformation maps (a,b). The DWI values stay fixed, but the full set of measurements is attributed to a new compound set of gradients (c). Since nonlinear space transformations are to be supported the profile of DWI values are resampled (in the ADC domain) based on a robust model fit using spherical harmonics to yield a set of DWIs with a chosen, canonical set of gradient directions valid for the full atlas space (d).

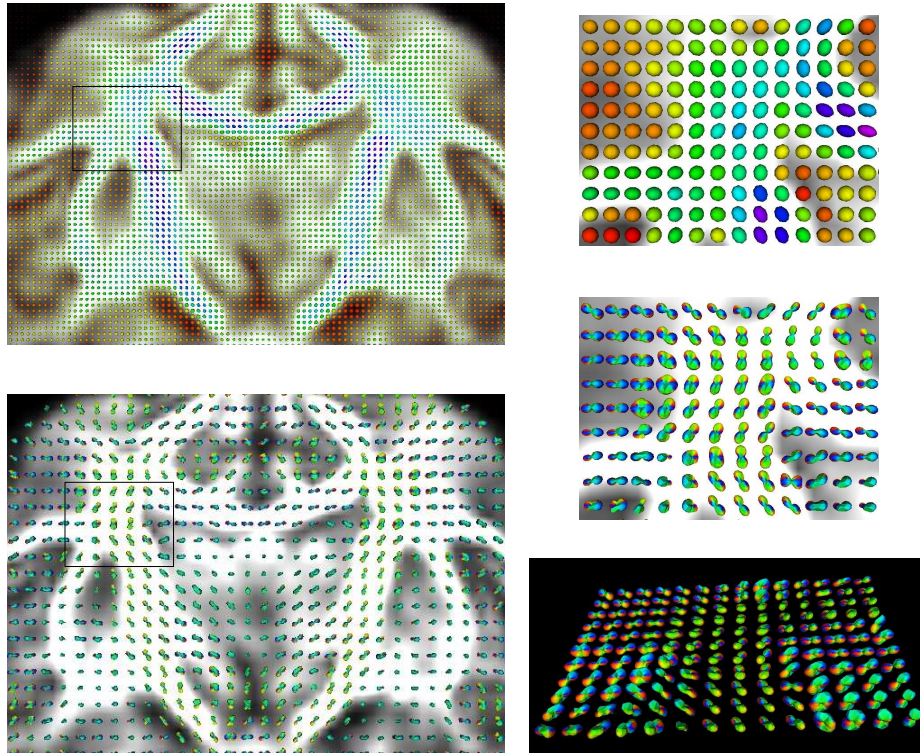
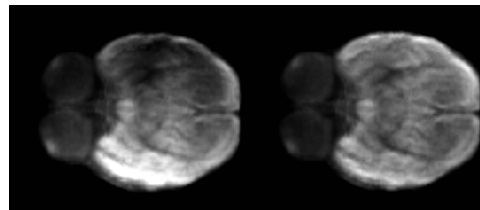


Fig. 4. Coronal brain slice with ODF and tensor ellipsoids overlaid on an FA image. The ROI where the fibers from internal capsule and corpus callosum are expected to cross is marked. Right: tensor ellipsoids (top) and ODF (middle and bottom, with two different viewing angles) shown for this ROI. ODFs reconstructed from the DWI atlas demonstrate complex fiber structure while tensor ellipsoids from the tensor atlas show very limited information.

Fig. 5. Effect of bias field on residuals. Signal intensity increases with the number of residuals above the Huber threshold $\theta = 2$. Without bias-field correction (left) and with bias-field correction (right). Bias-field correction removes most of the asymmetry.



5 Diffusion Weighted Atlas-building Results

Ten rhesus monkeys of age 6 months were scanned on a 3T Siemens Trio scanner with 8-channel phase array trans-receiving volume coil. DWIs were acquired with: voxel size: $1.3 \times 1.3 \times 1.3 \text{mm}^3$ with zero gap, 60 directions, TR/TE=5000/86

ms, 40 slices, FOV: 83 mm, b:0, 1000 s/mm^2 , 12 averages. DWIs were up-interpolated to 0.65 mm^3 isotropic using windowed sinc interpolation. Tensors were calculated using WLS. Fractional anisotropy (FA) maps were used to construct an unbiased deformable atlas [17]. The diffeomorphic map for each individual FA to the atlas was used to warp the tensors [4] and to transform the DWIs for each subject. Warped tensor fields were averaged in the log-Euclidean space to generate the tensor atlas. The DWI atlas was computed using the robust WLS method using an 8th order symmetric spherical harmonics (SH) basis for the gradient directions and independently the robust WLS method for the baseline image.

To robustly fit the compound model of Sec. 4, requires fixing a scale parameter. For the Huber function model, the noise variance σ and the cut-off value θ need to be determined. To assure that σ is constant across the images DWIs should be bias corrected. Otherwise the outlier detection may produce inconsistent results (see Fig. 4). Note that for standard LS fitting bias field correction is typically not necessary for DWIs, because the quantities of interest are either ratios (as in DTI) or the weight function is scale-independent.

Orientation distribution functions (ODFs) were computed from the DWI atlas using 8th order SHs [11]. Fig. 4 shows the comparison between tensor ellipsoids and ODFs in a region where fibers running along the corpus callosum meet the internal capsule and the corticospinal tracts. ODFs show complex fiber structure possibly due to fiber crossing and branching, which is consistent with previous studies [11]. This information is not preserved with the tensor approach. In particular, Fig. 4 also shows that the DWI atlas successfully preserves directional information.

6 Conclusions

This paper proposed robust estimation methods for parametric models based on DWIs. Estimation is performed in the log-transformed space to exploit the approximation of the Rician noise model by a Gaussian with signal-dependent variance. By applying the estimation method to registered DWIs a DW-atlas was constructed. This allows for the representation of average diffusion information with more flexible diffusion models than the diffusion tensor. While the method was demonstrated for a one shell acquisition scheme, it could be extended to atlas-building for multi-shell acquisitions. Future work (1) will explore the effects of different basis functions on the representation of diffusion measures under the resampling step, (2) will perform atlas-building for larger numbers of subjects and for acquisitions with higher b-values to investigate the preservation of crossings for DWI atlases, and (3) will use advanced atlas-building methods which incorporate directional information with a statistically robust image similarity term to possibly improve alignment results. The software will be available in open source form.

References

1. Yu, B.: Correcting for Motion between Acquisitions in Diffusion MR. PhD thesis, University College London (2009)
2. Chang, L.C., Jones, D.K., Pierpaoli, C.: RESTORE: Robust estimations of tensors by outlier rejection. *Magnetic Resonance in Medicine* **53** (2005) 1088–1095
3. Mangin, J., Poupon, C., Clark, C., Le Bihan, D., Bloch, I.: Distortion correction and robust tensor estimation for MR diffusion imaging. *Medical Image Analysis* **6**(3) (2002) 191–198
4. Alexander, D., Pierpaoli, C., Basser, P., Gee, J.: Spatial transformations of diffusion tensor magnetic resonance images. *IEEE Transactions on Medical Imaging* **20**(11) (2001) 1131–1139
5. Leemans, A., Jones, D.: The B-matrix must be rotated when correcting for subject motion in DTI data. *Magnetic Resonance in Medicine* (2009)
6. Goodlett, C., Davis, B., Jean, R., Gilmore, J., Gerig, G.: Improved correspondence for DTI population studies via unbiased atlas building. *Lecture Notes in Computer Science* **4191** (2006) 260–267
7. Barmpoutis, A., Vemuri, B.C.: Groupwise registration and atlas construction of 4th-order tensor fields using the R+ Riemannian metric. In: *Proceedings of MIC-CAI*. (2009) 640–647
8. Tao, X., Miller, J.: A method for registering diffusion weighted magnetic resonance images. *Lecture Notes in Computer Science* **4191** (2006) 594
9. Melbourne, A.: Alignment of Contrast Enhanced Medical Images. PhD thesis, University College London (2009)
10. Salvador, R., Pena, A., Menon, D.K., Carpenter, T.A., Pickard, J.D., Bullmore, E.T.: Formal characterization and extension of the linearized diffusion tensor model. *Human Brain Mapping* **24** (2005) 144–155
11. Descoteaux, M., Angelino, E., Fitzgibbons, S., Deriche, R.: Regularized, fast, and robust analytical q-ball imaging. *Magnetic Resonance in Medicine* **58** (2007) 497–510
12. Clarke, R.A., Scifo, P., Rizzo, G., Dell’Acqua, F., Scotti, G., Fazio, F.: Noise Correction on Rician Distributed Data for Fibre Orientation Estimators. *IEEE Transactions on Medical Imaging* **27**(9) (2008) 1242–1251
13. Stewart, C.V.: Robust parameter estimation in computer vision. *SIAM Review* **41**(3) (1999) 513–537
14. Rousseeuw, P.J., Leroy, A.M.: Robust regression and outlier detection. Wiley (1987)
15. Aja-Fernández, S., Niethammer, M., Kubicki, M., Shenton, M., Westin, C.: Restoration of DWI data using a Rician LMMSE estimator. *IEEE transactions on Medical Imaging* **27**(10) (2008) 1389–1403
16. Carroll, R.J., Wu, C.F.J., Ruppert, D.: The effect of estimating weights in weighted least squares. *Journal of the American Statistical Association* **83**(404) (1988) 1045–1054
17. Joshi, S., Davis, B., Jomier, M., Gerig, G.: Unbiased diffeomorphic atlas construction for computational anatomy. *NeuroImage* **23**(Supplement 1) (2004) S151 – S160 *Mathematics in Brain Imaging*.
18. Alexander, D.C., Gee, J.C.: Elastic matching of diffusion tensor images. *Computer Vision and Image Understanding* **77**(9) (2000) 233–250
19. Ruiz-Alzola, J., Westin, C.F., Warfield, S.K., Alberola, C., Maier, S.E., Kikinis, R.: Nonrigid registration of 3d tensor medical data. *Medical Image Analysis* **6**(2) (2002) 143–161

A Log-Euclidean Statistical Analysis of DTI Brain Deformations

Andrew Sweet¹ and Xavier Pennec¹

Asclepios, INRIA Sophia-Antipolis, France
andrew.sweet@sophia.inria.fr

Abstract. Diffusion tensor images (DTIs) provide information about deep white matter anatomy that structural magnetic resonance images typically fail to resolve. Non-linear registration of DTIs provides a way to capture the deformations of these structures that would otherwise go unobserved. Here we use an existing method that fully incorporates a useful vector space parameterization of diffeomorphisms, thereby allowing simple and well defined calculation of deformation statistics. An initial analysis of the statistics produced by registration of a group of 37 HIV/AIDS patients illustrates principal modes of deformation that are anatomically meaningful and that corroborate with previous findings. The registration method is developed by incorporating these modes into a statistical regularization criterion. Even though initial results suggest this new criterion over-constrains the registration method, we discuss plausible ways to address this.

1 Introduction and Motivation

Computational anatomy aims to use transformations, produced by non-linear registration, to compute deformation statistics of anatomical structures that can account for biological variability within a population [1]. A first requirement of the registration method is that the result should be easily usable in subsequent statistical analyses. A second requirement is that the images the method can register should contain information that is rich enough to correctly describe anatomically meaningful deformations. In this work, we specifically consider DTIs, which represent the diffusion of water in the brain using a second order symmetric tensor at each voxel [2]. DTI registration is of particular interest because it provides unique information about major deep white matter structures, the deformations of which we propose may be more significant than changes observed from scalar image registration. This is likely to be especially true in HIV/AIDS patients, where significant white matter changes have previously been reported [3,4].

Both these requirements are met by the log-domain diffeomorphic demons algorithm [5], which directly estimates a vector space parameterization of a diffeomorphism, and has been adapted for use on DTIs [6] as described in Sec. 2. We then explain how, in Sec. 3, first and second order statistics can be computed for inter-subject registration of a group subjects. Further developments to the

registration method are proposed in the same section, by describing how these statistics can be reintegrated into a regularization criterion. An initial analysis demonstrates, in Sec. 4, that the statistics describe anatomically meaningful modes of deformation. However, experiments detailed in this section show that the statistical regularization criterion over-constrains the registration in some areas of the brain. We conclude by discussing, in Sec. 5, how these current problems might be overcome and propose ways in which the statistics could be used to constrain registration of other modalities.

2 Log-domain Diffeomorphic Registration of DTIs

2.1 A Log-Euclidean Parameterization of Diffeomorphisms

Throughout this work, it is assumed there is a non-parametric spatial transformation s from a moving image, M , to a fixed image, F . When the images are of different subjects, it is desirable that s should be a *diffeomorphism* which respects an *inverse consistency* constraint [7]. The log-domain diffeomorphic demons method [5] provides an approach to find an s that respects these constraints by exploiting the log-Euclidean framework for diffeomorphisms [8]. This framework considers the space of diffeomorphisms that can be identified by tangent vectors at the identity transformation. Each tangent vector defines a smooth stationary velocity field \mathbf{v} , which is related to a diffeomorphism through the exponential map $s = \exp(\mathbf{v})$. The main advantage of this parameterization is that \mathbf{v} lies in a vector space, so that proper arithmetic and statistical analysis can be easily performed. Additionally, the negated velocity field provides simple access to the inverse transformation $s^{-1} = \exp(-\mathbf{v})$.

2.2 Log-Domain Diffeomorphic Demons Registration

The log-domain diffeomorphic demons registration method [5] works by attempting to iteratively minimize an energy

$$E(F, M, \mathbf{v}, \mathbf{w}) = \text{Sim}(F, M \circ \exp(\mathbf{w})) + \text{Dist}(\mathbf{v}, \mathbf{w}) + \text{Reg}(\mathbf{v}) \quad (1)$$

where $c = \exp(\mathbf{w})$ is a non-parametric spatial transformation that attempts to achieve point correspondences between F and M . The introduction of the hidden variable, \mathbf{w} , allows the energy to be split into two forms, each of which can be optimized alternately in the following scheme [9].

1. **Correspondence:** given the current \mathbf{v} , find the \mathbf{w} that minimizes

$$E_{\text{corr}}(F, M, \mathbf{v}, \mathbf{w}) = \text{Sim}(F, M, \exp(\mathbf{w})) + \text{Dist}(\mathbf{v}, \mathbf{w}). \quad (2)$$

2. **Regularization:** given the \mathbf{w} found from step 1, find the \mathbf{v} that minimizes

$$E_{\text{reg}}(\mathbf{v}, \mathbf{w}) = \text{Dist}(\mathbf{v}, \mathbf{w}) + \text{Reg}(\mathbf{v}). \quad (3)$$

Solving (2) is equivalent to finding a small update transformation $u = \exp(\mathbf{u})$ to compose with the current one such that $c = s \circ u$. One usually defines the similarity and distance criteria as $\text{Sim}(F, M, \exp(\mathbf{w})) = \sigma_i^{-2} \|F - M \circ \exp(\mathbf{w})\|^2$ and $\text{Dist}(s, c) = \sigma_d^{-2} \|\mathbf{v} - \mathbf{w}\|^2$ respectively, where σ_i weights the uncertainty of the images and is typically defined as $\|F - M \circ \exp(\mathbf{w})\|$, whereas σ_d weights the spatial uncertainty between \mathbf{v} and \mathbf{w} and therefore controls the size of the update \mathbf{u} . The inverse consistency constraint, which we use throughout this work, can be imposed by defining a similarity criterion that is independent of the image order $\text{Sim}(F, M, \exp(\mathbf{w})) = \sigma_i^{-2} (\|F - M \circ \exp(\mathbf{w})\|^2 + \|M - \exp(-\mathbf{w}) \circ F\|^2)$. These choices have the advantage that (2) has an approximate closed form solution that can be found independently at each point of an image.

In the absence of prior knowledge, a sensible choice for the regularization criterion would be one that penalizes the harmonic energy of the velocity field $\sigma_r^{-2} \|\nabla \mathbf{v}\|^2$, where σ_r^{-2} weights the spatial uncertainty of s alone. Instead, the demons method smooths the correspondence field to give the transformation velocity field $\mathbf{v} = \mathcal{G}[0, \sigma_d^{-2} \sigma_r^2 I] * \mathbf{w}$, which can be shown [10] to be the Tikhonov regularized solution of (3). This means that a harmonic energy criterion $\text{Reg}(\mathbf{v}) = \sigma_r^{-2} \|\nabla \mathbf{v}\|_K^2$ is only definable with respect to a Hilbert space K .

2.3 How to Account for Registration of DTIs

Like diffeomorphisms, symmetric second order tensors lie on a manifold, which makes properly defining the similarity criterion between two DTIs problematic. A definition can be made by exploiting the log-Euclidean framework for tensors [11], which achieves a good approximation of the Riemannian metric. In this case, a log-tensor, \mathbf{T} , which exists in the tangent space at the identity matrix, parameterizes a tensor T through the exponential map $T = \exp(\mathbf{T})$. This parameterization also allows proper linear interpolation of tensors images, which is required when resampling at the same regular points in both images after a discrete transformation has been applied to M .

A further difficulty of non-linear DTI registration is that non-rigid transformation of tensors causes their local orientation to be lost. There are two major reorientation schemes that attempt to correct for this: preservation of principal directions; and finite strain [12]. Here we only consider the finite strain approach because an analytic gradient of its effect can be used in the demons optimization and improves registration performance compared to a scheme where orientation is simply corrected after each standard update [13]. Furthermore, this method can be easily adapted to use the log-domain parameterization with little affect on registration performance [6].

3 Computation and Reuse of Deformation Statistics

3.1 Defining a Distribution of Group-Wise Deformations

While the log-domain parameterization allows desirable constraints to be respected, its most important benefit is that we can properly compute deformation

statistics by calculating vector statistics of the velocity fields. Imagine that we have a group of m subjects $\{S_1, \dots, S_m\}$ and want to find the set of $n = m(m-1)$ velocity fields $\mathbf{v}_{i,j}$ that represent the transformations from S_i to S_j . As the inverse consistency constraint is respected, only $n/2$ registrations need to be performed because each one gives access to the forwards and inverse transformations represented by \mathbf{v} and $-\mathbf{v}$ respectively. As this implies that the mean velocity field is guaranteed to be the zero field, the immediate topic of interest is how the n fields vary.

Consider that the number of variables in a field, p , is three times the number of voxels in an image. Ignoring background voxels means that $p \approx 10^6$ for a typical DTI with an isotropic spatial resolution of 2mm. We can usually expect DTI datasets to contain images from around $m \approx 10^2$ subjects, implying that $n \approx 10^4$. This suggests that estimating the $p(p+1)/2$ values of the covariance matrix $\Sigma_{\mathbf{v}}$ will be highly underdetermined. However, in the demons framework, the regularization criterion effectively imposes the velocity field to be drawn from $\mathcal{G}[0, \sigma_d^{-2} \sigma_r^2 I]$ subject to the constraints from the data. When $\sigma_d^{-2} \sigma_r^2$ is large enough, there should be a significant amount of spatial correlation in the field due to the locally imposed smoothness. This means that the effective number of variables, which we denote as p' , should be far less than p .

Even so, estimating the $p'(p'+1)/2$ values of $\Sigma_{\mathbf{v}}$ is still likely to be underdetermined and presents practical computation problems as well. In order to tackle both these difficulties, we perform principal components analysis (PCA) on the velocity fields to define a rank-reduced covariance matrix $\Sigma_{\mathbf{v}}^{(k)} = \mathbf{Y}^{(k)} \mathbf{\Lambda}^{(k)} \mathbf{Y}^{(k)\top}$, where the columns of $\mathbf{Y}^{(k)}$ are the k principal eigenvectors of $\Sigma_{\mathbf{v}}$, $\{\mathbf{y}_1, \dots, \mathbf{y}_k\}$, and the diagonal of $\mathbf{\Lambda}^{(k)}$ contains its k principal eigenvalues $\{\lambda_1, \dots, \lambda_k\}$. In this model, we can consider the projection of a velocity field \mathbf{v} onto the k major eigenvectors, which gives $\mathbf{v}^{(k)} = \sum_{i=1}^k (\mathbf{v}^\top \mathbf{y}_i) \mathbf{y}_i = \sum_{i=1}^k \alpha_i \mathbf{y}_i$. This assumes a Gaussian distribution on the fields where $P(\alpha_i) = \mathcal{G}[0, \lambda_i]$ and $P(\mathbf{v}^{(k)}) = \prod_{i=1}^k \mathcal{G}[0, \lambda_i]$.

Under the Baker-Campbell-Hausdorff (BCH) assumptions [5], the composition of two diffeomorphisms $\exp(\mathbf{a})$ and $\exp(\mathbf{b})$ can be approximated by the exponential of their addition $\exp(\mathbf{a}) \circ \exp(\mathbf{b}) \approx \exp(\mathbf{a} + \mathbf{b})$. Technically, this should only hold when \mathbf{b} has a small magnitude, but here, we investigate what happens empirically when this constraint is loosened. We do so because this means that the fields generated by registration from one particular subject to all $m-1$ others are approximate basis vectors for the space of all n fields (Fig. 1). Of course, if we choose a different reference subject, we will find a different set of approximate basis vectors. In this sense, performing PCA corresponds to defining an orthogonal basis that should not be biased towards any particular subject and that should reduce the effects of the BCH approximations in our model.

3.2 A Statistically Regularized Demons Method

Minimizing the regularization energy (3) in the demons framework can be seen as the equivalent of maximizing the posterior probability of \mathbf{v} given \mathbf{w} from

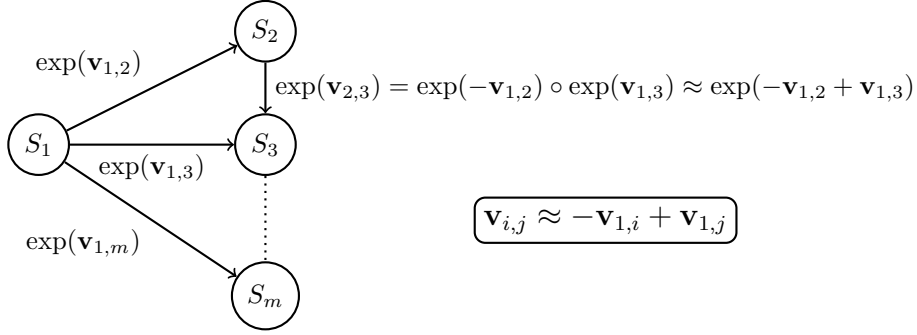


Fig. 1: Under our Baker-Campbell-Hausdorff approximations, the velocity fields that represent the transformations from one subject, here S_1 , to all other subjects, S_2, \dots, S_m , are basis vectors for the space of velocity fields that represent transformations between any two subjects.

the correspondence step. In this sense, the distance criterion is related to the likelihood, in that $\text{Dist}(\mathbf{w}, \mathbf{v}) \propto -\log(P(\mathbf{w}|\mathbf{v}))$, and the regularization criterion acts as a prior assumption on the distribution of \mathbf{v} , in that $\text{Reg}(\mathbf{v}) \propto -\log(P(\mathbf{v}))$. Under the usual assumptions, we have $P(\mathbf{w}|\mathbf{v}) = -\log(\mathcal{G}[\mathbf{v}, \sigma_d^2 \mathbf{I}])$ and $P(\mathbf{v}) = \mathcal{G}[\mathbf{0}, \sigma_r^2 (\nabla^* \nabla)^{-1}]_K$, the latter of which assumes no prior knowledge on where the field should be smooth or where there should be covariation.

Given our reduced-rank definition of $\Sigma_{\mathbf{v}}$, we can introduce such knowledge by replacing the usual prior on \mathbf{v} with a prior on the projection $P(\mathbf{v}^{(k)}) = \mathcal{G}[\mathbf{0}, \Sigma_{\mathbf{v}}^{(k)}]$. This yields a MAP estimate of

$$\mathbf{v}^{(k)} = \underset{\mathbf{v}^{(k)}}{\text{argmax}}[P(\mathbf{v}^{(k)}|\mathbf{w})] = \underset{\mathbf{v}^{(k)}}{\text{argmin}}[E_{\text{reg}}^{(k)}(\mathbf{v}^{(k)}, \mathbf{w})] \quad (4)$$

where

$$\begin{aligned} E_{\text{reg}}^{(k)}(\mathbf{v}^{(k)}, \mathbf{w}) &= -\log(\mathcal{G}[\mathbf{v}^{(k)}, \sigma_d^2 \mathbf{I}]) - \log\left(\prod_{i=1}^k \mathcal{G}[0, \lambda_i]\right) \\ &= \frac{1}{2} \sum_{i=1}^k \left(\sigma_d^{-2} (\alpha_i^2 - 2\alpha_i \beta_i) + \frac{\alpha_i^2}{\lambda_i} \right). \end{aligned} \quad (5)$$

Here $\beta_i = \mathbf{w}^T \mathbf{y}_i$ is the coordinate of the correspondence velocity field projected on the i^{th} eigenvector. The minimization of (5) can be performed independently on each projected coordinate to give $\alpha_i = (1 + \sigma_d^2 \lambda_i^{-1})^{-1} \beta_i$. Empirical results given in Sec. 4 show that when using a suitable value of k , it is the case that $\lambda_i \gg \sigma_d^2$, which means $\alpha_i \approx \beta_i$. Therefore, we approximately minimize (5) by simply projecting \mathbf{w} onto the eigenvectors of $\Sigma_{\mathbf{v}}$ to give $\mathbf{v}^{(k)}$.

4 Experiments and Results

4.1 Data, Pre-Processing and Registration Details

Diffusion weighted imaging data of a set of 37 HIV/AIDS patients are provided by the Neuradapt study group and the authors would like to acknowledge M. Vassallo, C. Lebrun and S. Chanalet for making these available. We use 30 subjects, denoted as group A, for statistical estimation, and reserve the other 7, denoted as group B, for validation. For each subject, a single unweighted ($b = 0$) image was acquired along with 23 gradient weighted ($b = 700 \text{ s/mm}^2$) images with spatial dimensions of $0.9375 \text{ mm} \times 0.9375 \text{ mm} \times 5.5 \text{ mm}$. Correction for subject motion and eddy currents is achieved by affinely registering the diffusion weighted images of each subject to their $b = 0$ image using FSL [14].

DTIs are reconstructed using a log-Gaussian noise model and non-positive tensors are replaced with a local mean [15]. The affine registration method described in [16] is used to register each subject's $b = 0$ image to that of the 2mm ICBM-DTI-81 template [17]. The affine transformations produced are applied to their corresponding DTIs, using finite strain reorientation, so that the DTIs lie in a common global coordinate system. Finally, the brain extraction toolkit [18] is used to generate a brain foreground mask from each affinely registered $b = 0$ image, which is applied to the affinely registered DTI to remove any tensors outside of the brain.

After pre-processing, non-linear registration is performed between each unique pair of subjects in groups A and B. All registrations use $\sigma_d = 1$ and are allowed to iterate ten times, which is enough to ensure reasonable convergence of the solutions. In order to generate results over a range of transformation regularities, registration is repeated using $\sigma_r = \{0.8, 1.2, \dots, 2\}$.

4.2 What Are the Major Modes of Deformation?

Eigenvectors and eigenvalues are estimated from the velocity fields generated in group A and we compute the i^{th} mode of deformation as $\exp(\sqrt{\lambda_i} \mathbf{y}_i)$. Figure 2 demonstrates that the first four major modes are anatomically meaningful in the sense that areas of significant displacement are concentrated in and around identifiable anatomical structures. We find that these modes are relatively consistent across the range of regularization parameters used. One unsurprising difference is that larger regularization produces smoother modes that are more spatially sparse. This suppression of probably noisy deformations swaps the order of the third and fourth modes at the extreme values of σ_r used.

The first mode exhibits large displacement in the area under the corpus callosum, which actually corresponds to an expansion in the ventricles, and correlates with a rotation around the cerebellum. The second mode represents an expansion in the cerebellum that causes a displacement of the brain stem, which both correlate with expansion in the cortical areas. The third mode, for $\sigma = 2$, exhibits fairly complicated deformation that is localized around the cerebellum and brain stem. The fourth, again for $\sigma = 2$, mostly accounts for an expansion of

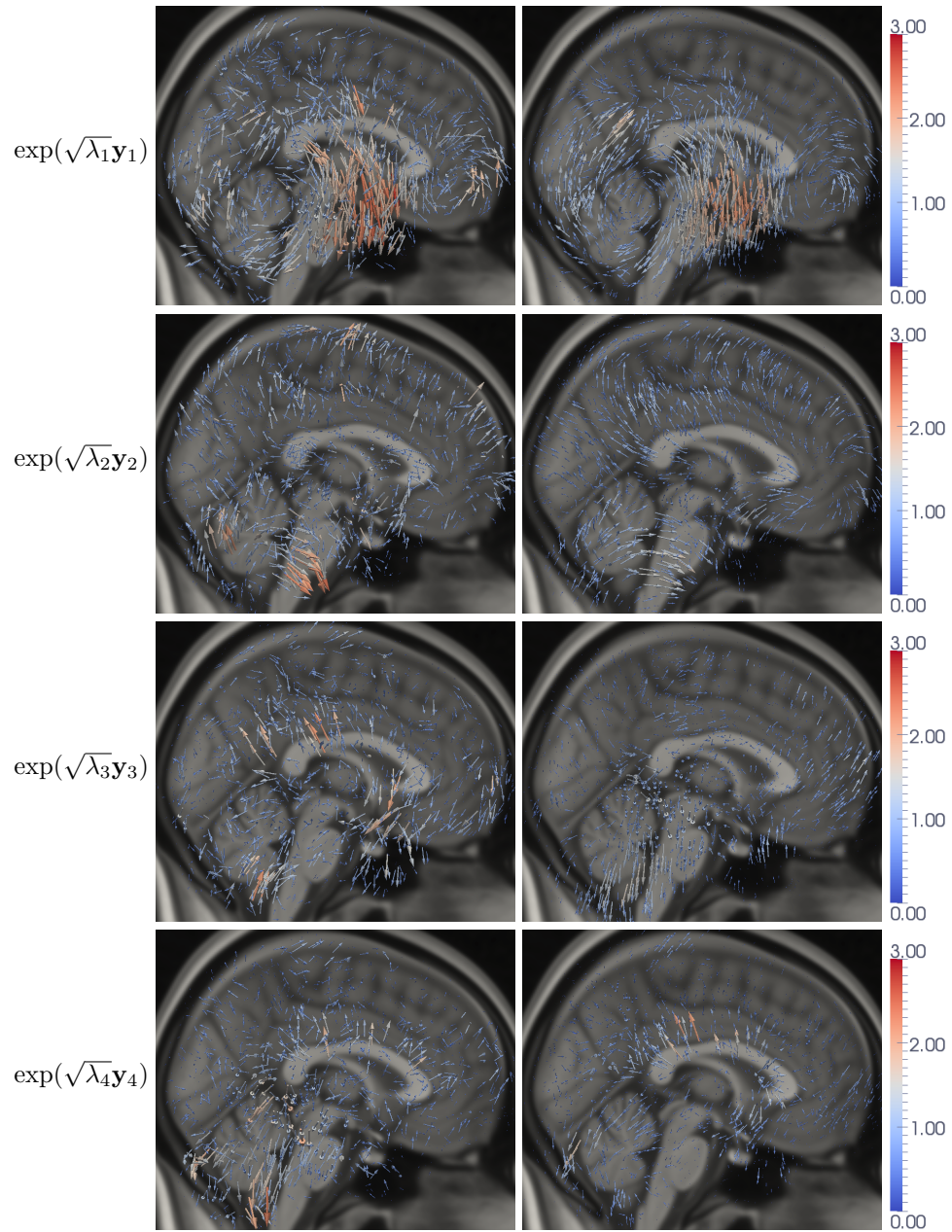


Fig. 2: A mid-sagittal view of the 4 major modes of displacement found from inter-subject DTI registration of group A using low (left) and high (right) values of $\sigma_r = 0.8, 2.0$. Arrows indicate displacement direction and color corresponds to displacement size in mm. The background is the T1 1mm MNI-152 template.

the ventricles that causes displacement above the corpus callosum, particularly close to the genu. It is of interest that there is large amount of deformation in and around the cerebellum because this is compatible with cerebellar changes previously found in HIV/AIDS [19].

Less regularization obviously produces more variance in the velocity fields, which causes larger eigenvalues (Fig. 3). Here, we see that the distribution of the first $m - 1$ eigenvalues is roughly exponential, but, as expected from our discussion in Sec. 3.1, the eigenvalues drop off sharply from here because the space of velocity fields is approximately $m - 1$ dimensional. The other $n - m + 1$ eigenvalues are roughly constant at all values of σ_r and are likely to be either noise or modes of deformation that are very specific to certain pairs of subjects. As σ_r is increased, we are better posing the problem of estimating the eigendecomposition given the number of data available. The small difference between distributions at $\sigma_r = 1.6$ and 2 suggests that using a value of around $\sigma_r = 1.6$ is suitable. However, even in this case, only around 80% of the variance in the data is accounted for by the first $m - 1$ eigenvalues. This may be due to the BCH approximations in our model or a non-Gaussian distribution of the velocity fields.

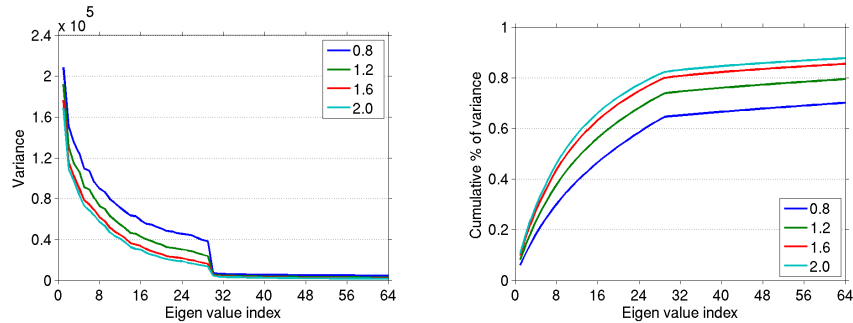


Fig. 3: The eigenvalues (left) and the cumulative percentage of variance they account for (right) from PCA performed on the 435 velocity fields found by inter-subject DTI registration of group A using $\sigma_r = \{0.8, 1.2, \dots, 2\}$.

In order to test whether or not the eigenvectors generalize well to other subjects, we calculate the mean square error between the velocity fields found from inter-subject registration of group B and the projections of these onto the eigenvectors $\frac{1}{n} \sum_{i=1}^n \mathbf{v}_i - \sum_{j=1}^k \alpha_j \mathbf{y}_j$. We see that as the number of eigenvectors is increased, this error approximately decreases linearly across all values of σ_r , which suggests that generalization is only reasonable (Fig. 4). Again, there is little difference between $\sigma_r = 1.6$ and 2. The localization of the errors for $\sigma_r = 1.6$ and $k = 29$, which is representative for all values of σ_r , is mostly in cortical regions rather than in major white matter structures. This suggests that the eigenvectors generalize well for deformations in deep central areas of the brain, but that deformations in outer areas are likely to be more subject specific.

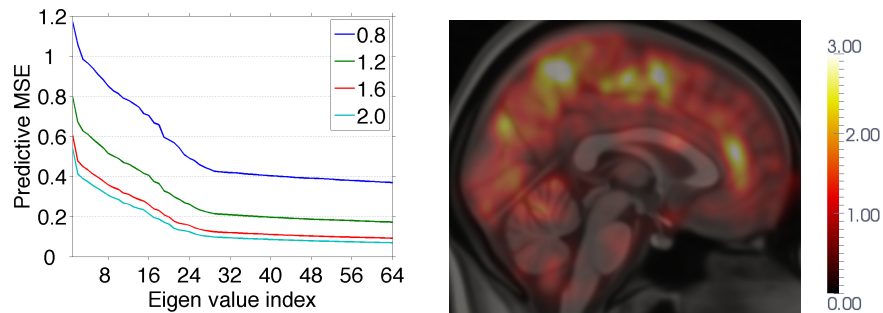


Fig. 4: The mean square error between the velocity fields in group B and the projections of these onto the eigenvectors estimated from group A using $\sigma_r = \{0.8, 1.2, \dots, 2\}$ (left). Also shown (right) is a mid-sagittal slice of the mean square error for $k = 29$ and $\sigma_r = 1.6$ overlaid on the T1 1mm MNI-152 template.

Using this approach, the error may be higher in cortical regions simply because the velocity is higher in these areas. To compensate for this potential bias, we consider the relative mean square error, where each error vector of each field is normalized by the square norm of the local velocity vector (Fig. 5). Although we observe some differences in how this error is distributed across σ_r , the localization of the error for $k = 29$ and $\sigma_r = 1.6$ is similar, in that high errors are mostly found close to the cortices and outside of major white matter structures.

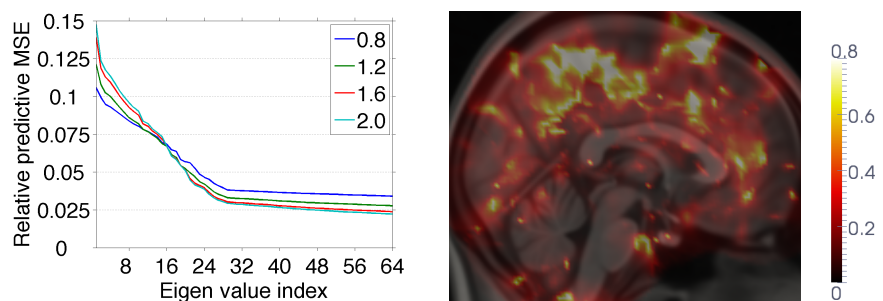


Fig. 5: The relative mean square error between the velocity fields in group B and the projections of these onto the eigenvectors estimated from group A using $\sigma_r = \{0.8, 1.2, \dots, 2\}$ (left). Also shown (right) is a mid-sagittal slice of the relative mean square error for $k = 29$ and $\sigma_r = 1.6$ overlaid on the T1 1mm MNI-152 template.

4.3 How Does Statistical Regularization Affect DTI Registration?

Registration is also performed on group B using the statistically regularized method with $k = \{4, 8, \dots, 48\}$ and the eigenvectors found from group A with $\sigma_r = 1.6$. Figure 6 shows that the mean square error between the registered DTIs using statistical regularization for all values of k is significantly higher than that using the original method, which suggests that the statistical prior knowledge is over-constraining the registration. The localization of this error (Fig. 7) shows that the statistically regularized method behaves similarly to the original method in some deep internal areas of the brain, such as the mid-body of the corpus callosum and the ventricles, but fails to account for the error in other areas, such as the genu, splenium and parts of the brain stem.

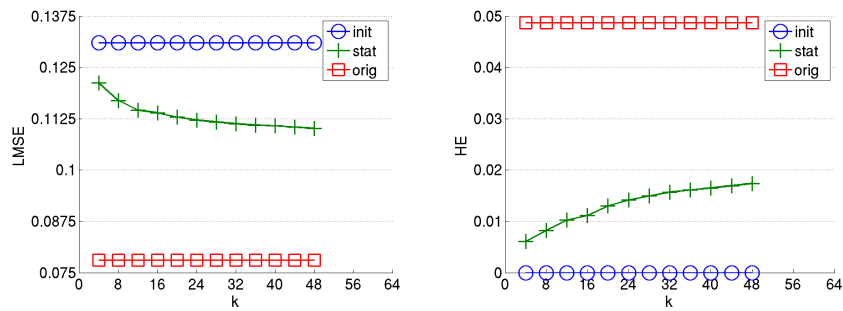


Fig. 6: The mean square error (left) between the registered DTIs and the harmonic energy of the transformation (right) using the statistically regularized method with $k = 4, 8, \dots, 48$ eigenvectors at $\sigma_r = 1.6$. For comparison the initial error and the final error for the original method at $\sigma_r = 1.6$ are also shown.

However, note that the harmonic energy of the statistically regularized transformation is considerably lower for all values of k (Fig. 6). It is possible that when compared at similar harmonic energies, the statistically regularized method may produce lower errors than the original method, although the current results cannot show this.

5 Conclusions and Further Work

Here, we present an investigation of the deformations between DTIs of a reasonably sized group of HIV/AIDS patients using log-domain diffeomorphic demons registration. The major principal components of the underlying transformations describe anatomically meaningful modes of deformation between deep structures in the brain, which generalize well to other patients. These encouraging initial results are not only interesting in their own right, but also help to validate the development of log-domain methods that directly parameterize diffeomorphic

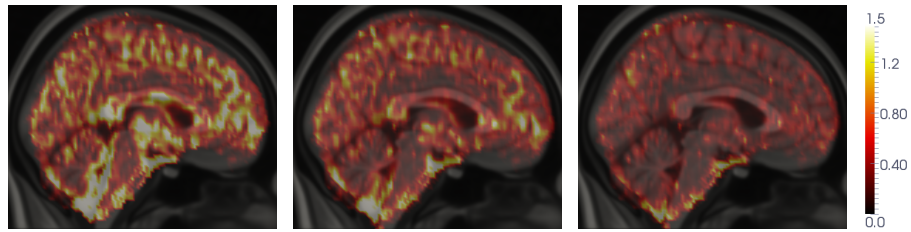


Fig. 7: The mean square error between the registered DTIs using the statistically regularized method with $k = 28$ eigenvectors at $\sigma_r = 1.6$ (middle) and the original method using $\sigma_r = 1.6$ (right). For comparison, the initial error is also shown (left). All errors are overlaid on T1 1mm MNI-152 template.

transformations. Although the incorporation of these modes into the statistical regularization criterion is perhaps less successful, we do observe that they reliably capture deformation in deep areas of the brain. As the formulation of the statistically regularized method is independent of the image modality, we could use DTI deformation statistics to better constrain T1 registration, which can prove difficult in these deep areas due to the lack of signal and contrast.

From a methodological point of view, performing PCA on the velocity fields amounts to computing the eigensystem from the sample covariance matrix, which is known to be unstable in high dimensions. This instability may explain why the statistical regularization method proposed here is overly restrictive, implying that alternatives to PCA should be considered. Alternatively, rather than project the correspondence field at each iteration of the demons algorithm, it may make more sense to directly optimize the coordinates of the velocity field $\{\alpha_1, \dots, \alpha_k\}$ on the eigenvectors. It could also be the case that the methodology is well defined, but that the registration cannot reliably capture deformations from DTIs in some areas of brain, such as the cortices. Further investigation should focus on exploring how stable the eigendecomposition as the size of the subject group is increased, although this may present problems in terms of computation time.

References

1. Pennec, X.: Statistical computing on manifolds: from riemannian geometry to computational anatomy. In Nielsen, F., ed.: *Emerging Trends in Visual Computing*. Volume 5416 of LNCS. (2008) 347–386
2. Basser, P.J., Mattiello, J., LeBihan, D.: MR diffusion tensor spectroscopy and imaging. *Biophysical journal* **66**(1) (1994) 259–267
3. Sullivan, E.V., Pfefferbaum, A.: Diffusion tensor imaging in normal aging and neuropsychiatric disorders. *European Journal of Radiology* **45**(3) (2003) 244–255
4. Leporé, N., Brun, C., Chou, Y.Y., Chiang, M.C., Dutton, R.A., Hayashi, K.M., Luders, E., Lopez, O.L., Aizenstein, H.J., Toga, A.W., Becker, J.T., Thompson, P.M.: Generalized tensor-based morphometry of HIV/AIDS using multivariate statistics on deformation tensors. *IEEE Transactions on Medical Imaging* **27**(1) (2008) 129–141

5. Vercauteren, T., Pennec, X., Perchant, A., Ayache, N.: Symmetric log-domain diffeomorphic registration: A demons-based approach. In Metaxas, D., Axel, L., Fichtinger, G., Székely, G., eds.: Proc. MICCAI 2008. Volume 5241 of LNCS. (2008) 754–761
6. Sweet, A., Pennec, X.: Log-domain diffeomorphic registration of diffusion tensor images. In: Proc. of Workshop on Biomedical Image Registration 2010. Volume 6204 of LNCS., Lübeck, Germany (July 2010) 198–209
7. Klein, A., Andersson, J., Ardekani, B.A., Ashburner, J., Avants, B., Chiang, M.C., Christensen, G.E., Collins, L.D., Gee, J., Hellier, P.: Evaluation of 14 nonlinear deformation algorithms applied to human brain MRI registration. *NeuroImage* **46**(3) (2009) 786–802
8. Arsigny, V., Commowick, O., Pennec, X., Ayache, N.: A log-Euclidean framework for statistics on diffeomorphisms. In Larsen, R., Nielsen, M., Sporring, J., eds.: Proc. MICCAI 2006. Volume 4190 of LNCS. (2006) 924–931
9. Cachier, P., Ayache, N.: Isotropic energies, filters and splines for vectorial regularization. *Journal of Mathematical Imaging and Vision* **20**(3) (2004) 251–265
10. Nielsen, M., Florack, L., Deriche, R.: Regularization, scale-space, and edge detection filters. *Journal of Mathematical Imaging and Vision* (1997)
11. Arsigny, V., Fillard, P., Pennec, X., Ayache, N.: Log-Euclidean metrics for fast and simple calculus on diffusion tensors. *Magnetic Resonance in Medicine* **56**(2) (2006) 411–421
12. Alexander, D.C., Pierpaoli, C., Basser, P.J., Gee, J.C.: Spatial transformations of diffusion tensor magnetic resonance images. *IEEE Transactions on Medical Imaging* **20**(11) (2001) 1131–1139
13. Yeo, B.T.T., Vercauteren, T., Fillard, P., Peyrat, J.M., Pennec, X., Golland, P., Ayache, N., Clatz, O.: DT-REFinD: Diffusion tensor registration with exact finite-strain differential. *IEEE Transactions on Medical Imaging* **28**(12) (2009) 1914–1928
14. Smith, S.M., Jenkinson, M., Woolrich, M.W., Beckmann, C.F., Behrens, T.E., Johansen-Berg, H., Bannister, P.R., Luca, M.D., Drobnjak, I., Flitney, D.E., Niazy, R.K., Saunders, J., Vickers, J., Zhang, Y., Stefano, N.D., Brady, J.M., Matthews, P.M.: Advances in functional and structural MR image analysis and implementation as FSL. *NeuroImage* **23**(Supplement 1) (2004) S208 – S219 Mathematics in Brain Imaging.
15. Fillard, P., Pennec, X., Arsigny, V., Ayache, N.: Clinical DT-MRI estimation, smoothing and fiber tracking with log-Euclidean metrics. *IEEE Transactions on Medical Imaging* **26**(11) (2007) 1472–1482
16. Ourselin, S., Roche, A., Prima, S., Ayache, N.: Block matching: A general framework to improve robustness of rigid registration of medical images. In DiGioia, A.M., Delp, S., eds.: Proc. MICCAI 2000. Volume 1935 of LNCS. (2000) 557–566
17. Mori, S., Oishi, K., Jiang, H., Jiang, L., Li, X., Akhter, K., Hua, K., Faria, A.V., Mahmood, A., Woods, R., Toga, A.W., Pike, G.B., Neto, P.R., Evans, A., Zhang, J., Huang, H., Miller, M.I., van Zijl, P., Mazziotta, J.: Stereotaxic white matter atlas based on diffusion tensor imaging in an ICBM template. *NeuroImage* **40**(2) (2008) 570–582
18. Smith, S.M.: Fast robust automated brain extraction. *Human Brain Mapping* **17**(3) (2002) 143–155
19. Klunder, A.D., Chiang, M.C., Dutton, R.A., Lee, S.E., Toga, A.W., Lopez, O.L., Aizenstein, H.J., Becker, J.T., Thompson, P.M.: Mapping cerebellar degeneration in HIV/AIDS. *Neuroreport* **19**(17) (2008) 1655–1659

Combinatorial Streamline Tractography using constrained two-tensor model

Tong Tong¹, Wei Liu¹, Yufeng Huang¹, Huanqing Feng¹, and chuanfu Li^{1,2}

¹Biomedical Engineering Center, University of Science and Technology of China, Hefei, China

²Medical Image Center, First Affiliated Hospital of Anhui Traditional Medicine College, Hefei, Anhui, China

Abstract. Diffusion tensor imaging (DTI) provides a unique tool for tracing and visualizing nerve fiber tracts in vivo. Many fiber tracking techniques have been proposed to evaluate intactness of white matter pathways over recent years. However, traditional deterministic tractography fails to reveal structure in regions where multiple fiber bundles intersect since the single-tensor model cannot describe this complexity. Probabilistic tracking methods may provide an alternative technique to address this problem, but it is a time-consuming process to implement a probabilistic algorithm and the result is a connectivity map, which may be difficult to interpret. In this paper we proposed a Combinatorial Streamline Tractography (CST) which combines the advantages of both deterministic methods and constrained two-tensor model, considering deterministic methods are fast with generating recognizable geometric pathways while two-tensor are robust and able to trace the two tracts in the crossing region without dispersing or terminating early. We evaluate the performance of this method on a synthetic dataset and an real brain diffusion MRI dataset. The results demonstrate that this approach not only successfully reveals structure in crossing regions over a broad range of crossing angles and curvatures, but also it is efficient and robust for clinical use.

1 Introduction

Diffusion tensor imaging (DTI) has provided a unique non-invasive method for investigating the structure of human brain in vivo. Since the advent of this new imaging modality, neuroscientists has used DTI to reconstruct fiber pathways in human brain for investigating how neurons connect from one region to other regions, or how anatomical neuronal network underlies the structural organization of the whole brain [1,2]. However, such research relies heavily on the chosen algorithm of reconstructing fiber bundles – a process called tractography, which is an important application of diffusion tensor imaging. Assuming the diffusion tensor’s largest eigenvectors representing the main direction of fibers within a voxel, common tractography algorithms are usually carried out by following the direction to reconstruct a fiber from a seed region of interest (ROI). Such traditional streamline tracking methods have several problems. First, due to limited resolution of MRI, some voxels may contain two or more fiber orientations and fiber tractography is inaccurate in regions

where fibers cross or twist within the voxel. Second, the quality of streamline tracking results can be easily influenced by the partial volume effects and local noise, which may accumulate errors over a long-distance propagation. Third, the selection of ROI has a tremendous impact on the tracking results and it lacks ground truth for making comparison between different tracking algorithms.

Probabilistic tracking appeared to overcome some limitations of classical tractography and has received considerable interest in recent years [3,4,5,6]. These methods have two steps [5]. Firstly a probability density function (PDF) is used to model the uncertainty for local fiber orientations in DTI measurements at each voxel. Then a streamline propagation process is repeated several thousands of times by randomly sampling each direction from the PDF. Although probabilistic tracking can trace more accurately in regions of crossing fibers and be less noise-sensitive compared to traditional streamline tracking methods, it still has some drawbacks. First, since probabilistic methods return a connectivity map which shows the probability of each voxel connected to the seed, it is difficult to calculate some morphological descriptions such as length, curvature of fibers. Second, the visualization of a 3D volume connectivity map may be harder to interpret, whereas the visualization of discrete geometric fibers is easily recognizable. Third, it may take hours even days to implement a probabilistic algorithm [7], which is very slow and can't be used interactively.

Another approach to resolve crossing fibers is to apply multiple tensors model to tractography. A tractography algorithm based on mixtures of two Gaussian densities is proposed in [8] to track complex fiber crossing regions where single Gaussian model is inadequate, but this approach needs a high number of parameters to fit. A constrained bi-Gaussian model is also introduced in [9] for analysis of crossing fibers with fewer model parameters. This two-tensor method utilizes the information present in the single tensor, constraining two tracts within a voxel in the plane spanned by the two largest eigenvectors of the single tensor fit. This method is robust and practical especially when gradient directions are acquired with a small number.

As deterministic methods are fast and two-tensor are able to trace the two tracts in the crossing region, we proposed a Combinatorial Streamline Tractography (CST) which combines the advantages of both deterministic methods and constrained two-tensor model. The performance of CST is verified by comparing the results to other three single-tensor tractography on both synthetic datasets and real human brain dataset.

2 Approach

Section 2.1 introduces single tensor model and three types of fiber tracking methods based on this model. Tractography based on the new constrained two-tensor model is described in Section 2.2 and Section 2.3 introduces how the proposed method CST is implemented with the constrained two-tensor model.

2.1 Single Tensor Model

The diffusion tensor is a set of symmetric positive-definite tensor describing the random motion of water molecules. The relationship between one diffusion tensor D and the acquired MRI signal S_i at a given point can be described by the following equation [10]:

$$S_i = S_0 W e^{-b \mathbf{g}^T D \mathbf{g}} \quad (1)$$

where b is a factor describing the gradient timing and strength, \mathbf{g} is a unit vector representing the direction of a diffusion gradient, S_0 is the signal intensity acquired when b value is 0, and D is the apparent diffusion tensor. After having acquired a Diffusion-Weighted MRI (DWI) dataset, the diffusion tensors D coefficients can be estimated by several ways and is usually solved by the linear least squares method.

From the fitted tensor in each voxel, the principal direction of diffusion is supposed to be the largest eigenvector of D . A nerve fiber can be traced as a streamline from an initial seed point, and the fiber described as a 3D space curve can be computed by the following equation:

$$\frac{d\mathbf{r}(s)}{ds} = \mathbf{t}(s) \quad (2)$$

Where $\mathbf{t}(s)$ is the unit tangent vector of local path and $\mathbf{r}(s)$ is the fiber path position. We solve this equation using 4th Runge-Kutta integration method.

The streamline tracking method (FACT) computes fibers by following the major eigenvector. For each step the new fiber direction $\mathbf{v}_{new} = \mathbf{e}_1$, where \mathbf{e}_1 represent the largest eigenvector of current point. The tensor deflection (TEND) algorithm uses the entire diffusion tensor field to deflect the current fiber direction \mathbf{v}_{in} . For each step the new fiber direction $\mathbf{v}_{out} = D\mathbf{v}_{in}$. The tensorline tracking technique combine the FACT method and the TEND method. For each step the new fiber direction $\mathbf{v}_{new} = c_l \mathbf{e}_1 + (1 - c_l)((1 - w)\mathbf{v}_{in} + w\mathbf{v}_{out})$, where \mathbf{v}_{out} is the direction computed from TEND, $c_l = (\lambda_1 - \lambda_2) / (\lambda_1 + \lambda_2 + \lambda_3)$ is the linear anisotropy coefficient and w is a user-defined weighting.

2.2 Constrained Two-tensor Model

For voxels containing a mixed diffusion pattern, a general two-tensor model can be expressed by a weighted sum of two Gaussian functions:

$$S = S_0 W_1 e^{-b \mathbf{g}^T D_1 \mathbf{g}} + S_0 W_2 e^{-b \mathbf{g}^T D_2 \mathbf{g}} \quad (3)$$

Where w_1 , w_2 are convex weights and $w_1 + w_2 = 1$, s_0 is the original signal without diffusion weighting.

This general two-tensor model described in Eq.(3) has 14 parameters to fit (7 parameters for each tensor). The high number of parameter results in a high level of instability in estimating the two tensors. In our work, we use the constrained two-tensor model proposed in [9], which has only 4 free parameters to fit. The model has two additional physical reasonable constraints: it assumes two cylindrically symmetric tensors and the two fiber tracts are constrained in the plane spanned by the first two principal eigenvectors, which are computed from the single tensor model. A further assumption is that both the fiber has the same parallel and perpendicular apparent diffusion constants (ADC) λ_1 , λ_3 . Base on this two constraints, two tensors are defined as follows:

$$\mathbf{D}_1 = \begin{bmatrix} d_{x1} & d_{x3} & 0 \\ d_{x3} & d_{x2} & 0 \\ 0 & 0 & \lambda_3 \end{bmatrix}, \quad \mathbf{D}_2 = \begin{bmatrix} d_{y1} & d_{y3} & 0 \\ d_{y3} & d_{y2} & 0 \\ 0 & 0 & \lambda_3 \end{bmatrix} \quad (4)$$

Where,

$$\begin{aligned} d_{q1} &= \cos^2 \varphi_p \Delta\lambda + \lambda_3 \\ d_{q2} &= \sin^2 \varphi_p \Delta\lambda + \lambda_3 \\ d_{q3} &= \frac{\sin 2\varphi_p}{2} \Delta\lambda \\ \Delta\lambda &= \lambda_1 - \lambda_3, p \in \{x, y\} \end{aligned}$$

This model has 7 free parameters to fit. 3 of them (eigenvalue λ_3 and eigenvector \mathbf{e}_3) are calculated from the single-tensor fit, so the remaining 4 parameters are:

- w_1 : fraction of the first tract
- φ_x and φ_y : the angles subtended by the principal diffusion directions of the two diffusion tensor in the plane
- λ_1 : the principal eigenvalue which is assumed to be the same in both fiber tracts.

Transforming the gradient vectors into the new orthonormal coordinate system define by $[\mathbf{e}_1, \mathbf{e}_2, \mathbf{e}_3]$: $\mathbf{g} \rightarrow \mathbf{G}$, the signal attenuation equation is then given as follow:

$$\mathcal{S} = s_0 w_1 e^{-b \mathbf{G}' \mathbf{D}_1 \mathbf{G}} + s_0 (1 - w_1) e^{-b \mathbf{G}' \mathbf{D}_2 \mathbf{G}} \quad (5)$$

Eq. (5) can be solved by using nonlinear least-squares methods. In our work, we solve this equation using Levenberg-Marquardt non-linear optimization.

2.3 Combinatorial Streamline Tractography (CST)

From a geometrical viewpoint, the diffusion tensor in each voxel can be divided into three types – linear, planar and spherical. The two-tensor model are supposed to apply in the crossing area, where the voxels are characterized as “planar”. As in the non-crossing area, the single-tensor model can fully be fitted to every voxel. If the constrained two-tensor model was fitted to the non-planar area, it may lead to a poor estimate of the underlying fiber orientation. Voxels can be characterized as planar when there are more than two non-parallel fibers running through and the planar anisotropy index $c_p = (\lambda_1 - \lambda_3) / (\lambda_1 + \lambda_2 + \lambda_3)$ is above a user defined threshold. In the linear area we apply TEND algorithm described in Section 2.1.

The fiber tracking starts from a given position p_0 and we compute planar anisotropy index c_p of p_0 . If c_p is above the threshold, then p_0 is in the non-crossing area and the new fiber orientation is $v_{out} = Dv_{in}$. when the fiber run through the crossing area, we use the two-tensor model to compute two new fiber orientation and one of them is chosen when the eigenvector has the smaller angular difference with the principal eigenvector of the previous position. The new fiber orientation is $v_{out} = D^{selected}v_{in}$. if p_0 is in the crossing area, we propagate the fiber along the two principal eigenvector of the two tensors. Therefore the output consists of two paths under this circumstance. Also the initial tracking step proceed along both the positive and negative of these direction in order to obtain the whole fibers.

In order to compute tensor at an arbitrary position, we use single tensor trilinear interpolation when the position is in the non-crossing area. In the case of two-tensor estimation the correspondence becomes complex with 64 neighborhood for tricubic interpolation. Because of this problem we compute the signal S_i by interpolating the diffusion eighted images and the two tensors are estimated from the interpolated signal by fitting Eq. (5). In our work, trajectories are terminated when fractional anisotropy FA falls below a level (typically 0.1-0.2), when angular difference is above threshold, when the curvature becomes too small or when the fiber reaches the largest steps (typically 1000).

3 Experiments

We evaluate our CST algorithm on both synthetic datasets and an in-vivo dataset. For each dataset, we compare our method against three traditional single-tensor tractography algorithms. Synthetic dataset representing crossing fibers over a broad range of angles is first tested for evaluating the performance of the proposed algorithm and we also generate synthetic datasets with different noise levels to verify the robustness of the algorithm. Then a real brain dataset is examined to demonstrate how the proposed algorithm performs against other single-tensor streamline tractography.

3.1 Synthetic dataset

In order to evaluate the performance of CST algorithm in the fiber crossing area, we first construct a synthetic ground truth MR signals based on Eq. (5) at $b=1000$ with 13 gradient directions. The dataset has $32 \times 32 \times 32$ voxels with an resolution of $2 \times 2 \times 2 \text{ mm}^3$, containing two curved fiber bundles running across each other. Thus in the crossing region we get a broad range of different crossing angles and also the curvatures of fibers vary at different location.

In Fig. 1, we have compared the performance of the proposed method with that of three alternative methods. All the algorithms are implemented under the same termination criteria (with fa threshold = 0.2, angular threshold = 45, planar anisotropy threshold = 0.2, the length of each fiber constraints in [10 mm 300mm]). Fig. 1 (a) shows the tensor field of the synthetic signals. Starting from a same seed region of interest (the red region in Fig. 1), the results of traditional deterministic tractography – FACT, TEND and TENSLINE are presented in Fig. 1(b), Fig. 1(c) and Fig. 1(d) respectively. Obviously none of the three algorithm is able to recover the crossing curved fibers correctly, since tensors are unable to model the two fiber orientation in the crossing area. CST, however, is able to detect the curved fiber bundle by using the constrained two-tensor model described in Section 2.2 (Fig. 1 (d)). The other curved fiber bundle can also be tracked correctly by defining another seed ROI (Fig. 1 (e)). If the seed ROI is in the crossing area, two different curved fiber bundles are obtained since each seed in ROI has two different principal diffusion vectors (Fig. 1 (e)).

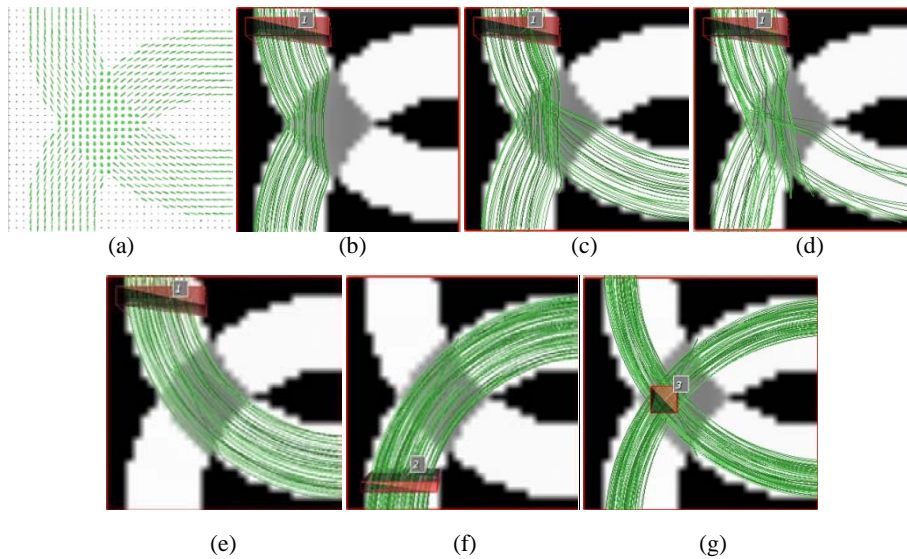


Fig. 1. Fiber tracking results of different algorithms on synthetic dataset. (a) 2D tensor field of the synthetic dataset. (b) FACT tracking results from seed ROI 1 (red). (c) TEND tracking results from ROI 1. (d) TENSLINE tracking results from ROI 1. (e) CST tracking results from ROI 1. (f) CST tracking results from ROI 2. (g) CST tracking results from seed ROI 3 (in the crossing area).

We also examine the robustness of the algorithm by adding different levels of Rician noise to the synthetic dataset. The tracking results of our method are presented in Fig. 2 under different SNRs of 33.3, 25, 20 and 16.7. Tracking results show that our method is able to trace all the fiber bundle correctly when SNR is above 33.3. The higher level of noise added to the dataset, the less fibers we obtain since some fibers may terminate early due to noise. However, few of fake fibers are found in all the results even though the level of noise is very high.

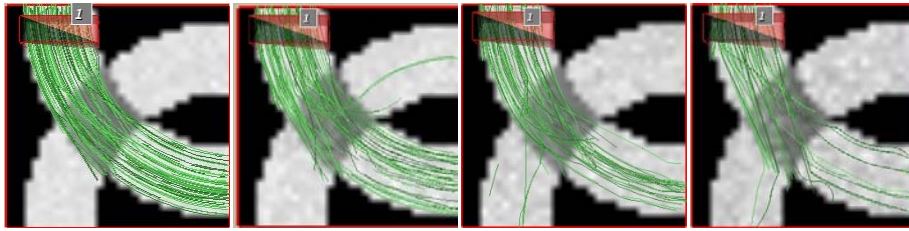


Fig. 2. Fiber tracking results of the proposed method under different level of noise. From left to right, SNR is 33.3, 25, 20 and 16.7 respectively.

3.2 Diffusion MRI dataset

The brain dataset was acquired from a healthy adult volunteer for two b-values, $b = 0$ and $b = 800 \text{ s/mm}^2$ along 12 different diffusion directions. We used a 1.5T SIEMENS SYMPHONY scanner and image size is $128 \times 128 \times 30$, resolution is $1.797 \times 1.797 \times 3.9 \text{ mm}$.

Fig. 3 shows the tracking results of different algorithms from seed region in a sagittal slice of the corpus callosum. The result of FACT tracking (Fig. 3 a) shows that this method traces out the dominant pathways especially in the high fractional anisotropy area, but all the fibers are not very long since this method may terminate early in high curvature area. The tracking result of TEND (Fig. 3 b) is better than FACT, as it can trace out some long fibers and make fibers more smooth. This is because TEND algorithm uses the entire diffusion tensor field to deflect the current fiber direction. The TENSILINE method performs slightly better than FACT but worse than TEND since it is a mixture of these two techniques (Fig. 3 c). In contrast, our proposed method is able to pick up many long pathways consistent with the apparent anatomy (Fig. 3 d). It traces out more smooth tracts in comparison with other three single-tensor streamline tractography. From these experiments, we confirm that our proposed CST algorithm is able to trace the underlying pathways which the traditional tractography fails to pick up.

We made a statistics of the whole brain fiber tracts showed in Table 1. In terms of number and average length of all the fiber tracts, it demonstrates that CST gets the largest amount of fiber tracts and longest average length among these algorithms. Also fibers of CST and TEND are more smooth than those of other two algorithms according to the average curvature. Although CST consumes a little more time than other algorithms, it is still acceptable for clinical use.

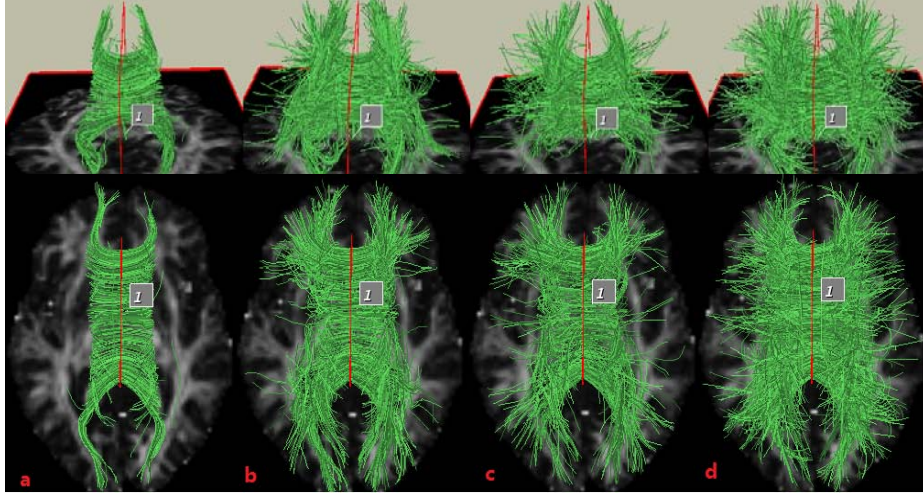


Fig. 3. Comparison of four fiber tracking algorithm on real brain dataset originating from the center of the entire corpus callosum (CC) viewed from above. From left to right, figures are the results of STT, TEND, TENSLINE, CST respectively. The top column and the bottom column are the same results from different views. Seed region indicated in red.

Table 1. Statistics of whole brain fiber tracts.

	STT	TEND	TENSLINE	CST
Number of fiber tracts	6453	7485	7241	8577
Average length/mm	32.5109	37.4077	32.6059	38.5897
Average curvature	0.1734	0.1054	0.0711	0.1154
Time/s	38.547	42.938	43.079	60.844

4 Conclusion

In this work, we presented a new methodology for resolving white matter pathways in areas of crossing fibers. Our new method shows good tracking capabilities. Experiment results on the synthetic datasets depict that the proposed method can successfully reveal structure in crossing regions over a broad range of crossing angles and curvatures. It also demonstrates the robustness of the algorithm under different levels of noise. Upon the evaluation to in vivo human brain DTI dataset, the method is possible to trace out white matter pathways that are not obtainable using single-tensor tractography. The proposed algorithm is very fast and needs a small number of gradient directions, making it efficiently for clinical use. However, in spite of these advantages, deterministic tractography is still affected by high noise level. In order to address this problem, our future work will focus on global tractography.

References

1. Hagmann P., Kurant M., Gigandet X., Thiran P., Wedeen V.J., Meuli R., Thiran J.P.: Mapping human whole-brain structural networks with diffusion MRI. *PLoS ONE*, 4(2):e597, (2007)
2. Gong G., He Y., Concha L., Lebel C., Gross D.W., Evans A.C., Beaulieu C.: Mapping anatomical connectivity patterns of human cerebral cortex using in vivo diffusion tensor imaging tractography. *Cereb Cortex* 19, 524–536 (2009)
3. Behrens, T.E., Woolrich, M.W., Jenkinson, M., Johansen-Berg, H., Nunes, R.G., Clare, S., Matthews, P.M., Brady, J.M., Smith, S.M.: Characterization and propagation of uncertainty in diffusion-weighted MR imaging. *Magn. Reson. Med.* 50(5), 1077–1088 (2003)
4. Behrens T.E., Berg H.J., Jbabdi S., Rushworth M.F., Woolrich M.W.: Probabilistic diffusion tractography with multiple fibre orientations: What can we gain? *Neuroimage*, no. 34(1), 144–155 (2007)
5. Zhang, F., Hancock, E.R., Goodlett, C., Gerig, G.: Probabilistic white matter fiber tracking using particle filtering and von Mises–Fisher sampling. *Med. Image Anal.* 13(1), 5–18 (2009)
6. Lifshits S., Tamir A., Assaf Y.: Combinatorial fiber-tracking of the human brain. *NeuroImage*, Vol. 48, No. 3, 532-540 (2009)
7. Qazi A.A., Radmanesh A., O'Donnell L., Kindlmann G., Peled S., Whalen S.: Resolving crossings in the corticospinal tract by two-tensor streamline tractography: Method and clinical assessment using fMRI. *NeuroImage* 47(supplement 2):T98-T106, (2009)
8. Blyth R.: Tractography with multiple fiber directions. In proceeding of ISMRM. (2003)
9. Peled, S., Friman, O., Jolesz, F., Westin, C.F.: Geometrically constrained two-tensor model for crossing tracts in DWI, *Magnetic Resonance Imaging*, vol. 24. 1263-1270 (2006)
10. Basser P.J.: Inferring microstructural features and the physiological state of tissues from diffusion-weighted images. *NMR Biomed.* 8(7-8):333-44 (1995)